Universidade de Aveiro Departamento de Física
2010

Andreia Gerniski Macedo

Nanotubos e nanobastonetes de óxidos de lantanídeos: síntese, processamento, luminescência e propriedades catalíticas

Lanthanide oxide nanotubes and nanorods: synthesis, processing, luminescence and catalytic properties

Universidade de Aveiro Departamento de Física
2010

Andreia Gerniski Macedo

Nanotubos e nanobastonetes de óxidos de lantanídeos: síntese, processamento, luminescência e propriedades catalíticas

Lanthanide oxide nanotubes and nanorods: synthesis, processing, luminescence and catalytic properties

Dissertação apresentada à Universidade de Aveiro para cumprimento dos requisitos necessários à obtenção do grau de Doutor em Física, realizada sob a orientação científica do Doutor Luís Dias Carlos, Professor Catedrático do Departamento de Física e do Doutor João Rocha, Professor Catedrático do Departamento de Química da Universidade de Aveiro

Apoio financeiro SFRH/BD/28433/2006
PTDC/CTM/73243/2006

Dedico este trabalho aos meus pais e sobrinhos.

o júri

presidente

Doutor José Manuel Lopes da Silva Moreira
Professor Catedrático, S. A. Ciências Sociais Jurídicas e Políticas da Universidade de Aveiro

Doutor Hugh Douglas Burrows
Professor Catedrático, Departamento de Química da Universidade de Coimbra

Doutor João Pedro Rodrigues Conde
Professor Catedrático, Instituto Superior Técnico da Universidade Técnica de Lisboa

Doutor João Pedro Esteves de Araújo
Professor Auxiliar, Faculdade de Ciências da Universidade do Porto

Doutor Luís Dias Carlos
Professor Catedrático, Departamento de Física da Universidade de Aveiro

Doutor João Rocha
Professor Catedrático, Departamento de Química da Universidade de Aveiro

agradecimentos

Aos meus pais pelo exemplo, apoio, conselhos e motivação.

À Maria João pela amizade, conversas, valores e pensamentos positivos.

Ao Profº Luís Carlos e Profº João Rocha pela orientação.

À Universidade de Aveiro e FCT pela bolsa.

À Profª Rute Ferreira, Drª Anabela Valente, Profº Tito, Profª Ana Barros, Profº Andrei Kolkhine e Profº Vitor Amaral pelo apoio fundamental no desenvolvimento do trabalho.

Ao centro de microscopia da Universidade de Aveiro: Profº Augusto, Drª Marta e Drº Marc.

Também agradeço aos pesquisadores que em colaboraram nas diferentes etapas do trabalho: Manuel, Igor, Celeste, Esmeralda, Edson, Susana, Rosário, Protima, Patricia Neves, Michel, Paula Brandão, Sónia Nobre, Mário Reis, Nuno João, Z. Lin, Paulo André, Carlos Vicente e Sra Conceição.

Aos amigos, pois a convivência só nos faz crescer enquanto seres humanos: Mariana, Sonia Pinho, Susana, Tânias, Lorena, Ana Maria, Cláudia, Michel, Mohamed, Nadia, Tang, Liu, Sérgio, Paulo, Tiagos, Felipe, Bruno, Daniel, Edilson, João, André, Sandra, Angélica, Alexandre, Gabriel, Christian...

palavras-chave

Nanotubos, lantanídeos, luminescência, termalização anômala, dielectroforese, catálise, compósitos.

resumo

Esta tese relata estudos de síntese, caracterização da estrutura e das propriedades de fotoluminescência e aplicações de nanotubos e nanobastonetes de óxidos de lantanídeos em pontas para microscopia de força atómica, catálise heterogénea e compósitos de base polimérica.

Há um interesse crescente em compreender como o confinamento quântico decorrente da redução do tamanho de partícula pode influenciar a eficiência da luminescência, a dinâmica dos estados excitados, a transferência de energia e os efeitos de termalização de nanoluminóforos. Em nanocristais dopados com lantanídeos (Ln^{3+}), e apesar da localização dos estados 4f, ocorrem efeitos de confinamento quântico via interacção com os modos vibracionais da rede. Em particular, a termalização anómala, descrita para uma variedade de nanocristais dopados com Ln^{3+}, tem sido atribuída à ausência de modos vibracionais de menor frequência. Este nanoconfinamento pode ter impacto na dinâmica da luminescência, bem como na transferência de energia mediada por modos vibracionais e processos de upconversion. Nesta tese, relata-se o estudo deste efeito em nanotubos de Gd_2O_3:Eu^{3+}. A influência de parâmetros como a concentração de európio e as condições de calcinação também foi investigada.

Algumas aplicações destes óxidos de lantanídeos também foram exploradas, nomeadamente a modificação de pontas usadas em microscopia de força atómica com nanobastonetes de Gd_2O_3:Eu^{3+}, lograda através de dielectroforese, técnica que não degrada a emissão de luz (rendimento quântico 0.47). As pontas modificadas são estáveis sob condições de trabalho, podendo ser aplicadas, por exemplo, em microscopia óptica de varrimento de campo próximo (SNOM).

A oxidação em fase líquida do etilbenzendo foi investigada usando como catalisador nanotubos de CeO_2, em presença dos oxidantes hidroperóxido de t-butilo e H_2O_2, e do solvente acetonitrilo, e temperaturas entre 55 e 105 ºC.

Nanobastonetes de Gd_2O_3:Eu^{3+} recobertos com sílica foram preparados pelo método sol-gel. Esta cobertura resultou num aumento, quer do rendimento quântico de emissão, de 0.51 para 0.86 (excitação a 255 nm), quer dos tempos de vida,de 1.43 para 1.80 ms (excitação a 394.4 nm). A superfície dos nanotubos cobertos com sílica foi modificada com o agente de acoplamento metacrilato de 3-(trimetoxissilil)propilo que permitiu a preparação de compósitos através da subsequente polimerização in-situ do estireno por técnicas de miniemulsão e solução.

keywords

Nanotubes, lanthanides, luminescence, anomalous thermalisation, dielectrophoresis, catalysis, composites.

abstract

This thesis reports on the synthesis, characterisation of the structure and photoluminescence properties, and applications of nanotubes and nanorods of lanthanides oxides in atomic force microscopy tips, heterogeneous catalysis and polymer-base composites.

There is a growing interest in understanding how size-dependent quantum confinement affects the photoluminescence efficiency, excited-state dynamics, energy-transfer and thermalisation phenomena in nanophosphors. For lanthanide (Ln^{3+})-doped nanocrystals, and despite the localisation of the 4f states, confinement effects are induced mostly via electron-phonon interactions. In particular, the anomalous thermalisation reported for a handful of Ln^{3+}-doped nanocrystals has been rationalised by the absence of low-frequency phonon modes. This nanoconfinement may further impact on the Ln^{3+} luminescence dynamics, such as phonon-assisted energy transfer or upconversion processes. Here, this effect is investigated in Gd_2O_3:Eu^{3+} nanotubes. The influence of parameters such as europium concentration and calcination procedure is also studied.

Some applications of these lanthanides oxides have been explored, for instance the modification of atomic force microscopy tips with photoluminescent Gd_2O_3:Eu^{3+} nanorods, using dielectrophoresis, a technique which preserves the red emission of the nanorods (quantum yield 0.47). The modified tips are stable under working conditions and may find applications in scanning near-field optical microscopy.

The liquid-phase oxidation of ethylbenzene over CeO_2 nanotubes has been investigated, using tert-butyl-hydroperoxide and H_2O_2 as the oxidising agents, and acetonitrile as the solvent, in the range 55-105 ºC.

Gd_2O_3:Eu^{3+} nanorods have been coated with silica via a sol-gel approach. The silica coating increases both, the Eu^{3+} absolute emission quantum yields from 0.51 to 0.86 (255 nm excitation), and decay times from 1.43 to 1.80 ms (394.4 nm excitation). The silica coating was modified with 3-(trimethoxysilyl) propyl methacrylate and, subsequently, composites have been prepared by in-situ radical polymerisation of styrene via miniemulsion and solution routes.

Index

Publications resulting from this thesis

1. A. G. Macedo, R. A. S. Ferreira, D. Ananias, V. S. Amaral, L. D. Carlos, J. Rocha, Effects of phonon confinement on anomalous thermalisation, energy transfer and upconversion Ln^{3+} doped Gd_2O_3 nanotubes, *accepted* Advanced Functional Materials, 2010

2. A. G. Macedo, S. E. M. Fernandes, A. A. Valente, R. A. S. Ferreira, L. D. Carlos, J. Rocha, Catalytic performance of ceria nanotubes in liquid-phase oxidation reactions with tert-butyl hydroperoxide, *submitted* Molecules, 2010

3. A. G. Macedo, M. A. Martins, S. E. M. Fernandes, A. Barros-Timmons, T. Trindade, L. D. Carlos, J. Rocha, Luminescent SiO_2-coated $Gd_2O_3:Eu^{3+}$ nanorods/poly(styrene) nanocomposites by *in situ* polymerization, *submitted* Optical Materials, 2010

4. A. G. Macedo, D. Ananias, P. S. André, R. A. S. Ferreira, A. L. Kholkin, L. D. Carlos, J. Rocha, Functionalization of atomic force microscope tips by dielectrophoretic assembly of $Gd_2O_3:Eu^{3+}$ nanorods, Nanotech. (2008) 19, 295702

Other publications

5. D. C. Oliveira, A. G. Macedo, N. J. O. Silva, C. Molina, R. A. S Ferreira, P. S. Andre, K. Dahmouche, V. Z. Bermudez, Y. Messaddeq, S. J. L. Ribeiro, L. D. Carlos, Photopaternable di-ureasil-zirconium oxo-clusters organic-inorganic hybrids as cost effective integrated optical substrates, Chem. Mater. (2008) 20, 3696

6. A. G. Macedo, F. Zanetti, A. Mikowski, J. C. Hummelen, C. M. Lepienski, M. G. E. Luz, L. S. Roman, Improving light harvesting in polymer photodetector devices through nanoindented metal mask films, J. Appl. Phys. (2008) 104, 033714

7. A. G. Macedo, R. Valaski, E. A. Vasconcelos, F. Muchenski, E. F. Silva Jr, F. A. Silva, L.S. Roman, Enhanced lifetime in porous silicon light emitting diodes with fluorine doped tin oxide electrodes, Thin Solid Films (2008) 517, 870

8. R. A. S. Ferreira, P. S. Andre, R. Nogueira, C. Vicente, A. G. Macedo, L. J. Q Maia, L. D. Carlos, S. J. L.Ribeiro, Waveguide features in self-patternable amine functionalized organic-inorganic hybrids, SBMO/IEEE MTT-S International Microwave And Optoelectronics Conference, (2007) 1-2, 462-465

9. A. G. Macedo, C. E. Cava, C. D. Canestraro, L. Contini, L. S. Roman, Morphology dependence on fluorine doped tin oxide film thickness studied with atomic force microscopy, Microsc. & Microanal. (2005) 11, supp. 3, 118

Abbreviations List

AAO	Anodic alumina oxide
AFM	Atomic force microscopy
AIBN	2-2'-Azobis(isobutyronitrile)
ATR-FTIR	Attenuated total reflection Fourier transformed infrared
CF	Crystal field
CI	Configuration interaction
DEP	Dielectrophoresis
ED	Electric dipole
EDS	Energy dispersive spectroscopy
ESA	Excited state absorption
ETU	Energy transfer upconversion
FTIR	Fourier transforme infrared spectroscopy
GSA	Ground state absorption
H_C	Hamiltonian of Coulomb interaction
HD	Hexadecane
H_{FI}	Hamiltonian of free ion
H_{SO}	Hamiltonian of spin-orbit interaction
IUPAC	The International Union of Pure and Applied Chemistry
KPS	Sodium persulfate
LB	Langmuir-Blodgett films
LMCT	Ligand to metal charge transfer
Ln	Lanthanides
MD	Magnetic dipole
MPS	3-(trimethoxysilyl) propyl methacrylate
ORMOSIL	Organic modified silicate
QY	Emission quantum yield
PA	Phonon avalanche
PDOS	Phonon density of states
PEG	Poly etilene glycol
PL	Emission luminescence
PLE	Excitation luminescence
PS	Poly(styrene)
S_{bet}	Brunauer, Emmett and Teller superficial area
SDS	Sodium dodecyl sulphate
SEM	Scanning electronic microscopy
SNOM	Near-field scanning optical microscopy
TBHP	Tert-butyl hydroperoxide
TEM	Transmission electronic microscopy
TGA	Thermogravimetry
UC	Upconversion
XRD	X-ray diffraction

Preface

This thesis deals with studies about lanthanide hydroxide and oxide nanotubes/nanorods, their optical properties and applications in different areas, such as: tips for atomic force microscopy (AFM and SNOM), catalysis, polymer nanocomposites and Langmuir-Blodgett films (scheme 1). An overview of the optical properties of lanthanides and size effects is presented in chapter 1.

Chapter 2 reviews the literature, encompassing structure, synthesis and applications of yttrium and lanthanide nanotubes compounds.

Anomalous thermalisation effects observed with $Gd_2O_3:Eu^{3+}$ with nanotubes, nanorods or microcrystals are described and discussed in chapter 3. Room and 11 K excitation and emission photoluminescence techniques were used to probe energy levels, size and form effects on luminescence features. An intense anomalous effect, related with the presence of the $^7F_1 \rightarrow {}^5D_1$ transition lines on 11 K excitation spectra, was observed in the nanotubes, resulting from the Eu^{3+} clusters arrangement after a certain annealing treatment.

This material was also used in the functionalisation of AFM or SNOM tips by dielectrophoresis, results which are summarized in chapter 4.

The catalytic activity of CeO_2 nanotubes was evaluated in the oxidation of ethylbenzene or styrene in liquid-phase reaction, using TBHP or H_2O_2 as oxidising agents, at 55 to 105 ºC, and using acetonitrile as solvent. This work is reported in chapter 5.

Preparation of nanocomposites via *in situ* polymerisation techniques (mini emulsion or solution) are discussed in chapter 6. The surface modification of Y_2O_3 nanotubes with fatty acids (stearic acid) yields aligned structures in Langmuir-Blodgett films.

General conclusions and scope for further word are discussed in chapter 7.

The experimental conditions used for synthesis of gadolinium, yttrium and cerium hydroxide/oxides nanotubes/nanorods are described in appendix A. The general techniques used for characterization are briefly described in appendix B. Equations used for the calculation of the direct and indirect band-gap, from absorption spectra, are presented in appendix C.

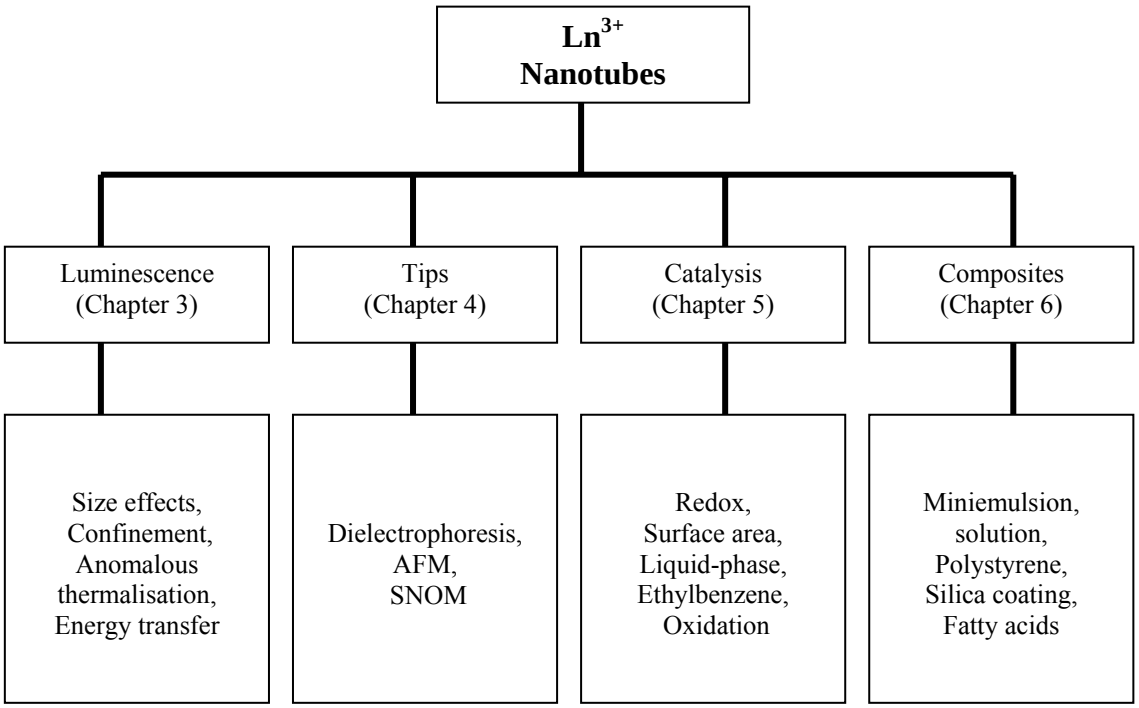

Scheme 1 – Schematic representation of the work I have carried out for this thesis (excluding opening chapters and conclusions).

Chapter 1 – Optical Properties of Lanthanides

1.1 – History, motivation and state of the art

In this thesis luminescence spectroscopy is used to study the optical properties of lanthanide ions in oxide nanotubes hosts (Gd_2O_3:Eu^{3+}, Gd_2O_3:Yb^{3+}/Er^{3+} and CeO_2). According to the IUPAC terminology, lanthanide series comprises the fifteen elements with atomic numbers from 57 (lanthanum) to 71 (lutetium) [1]. The name "rare earths" is sometimes used to describe all the lanthanides together with scandium and yttrium. All lanthanides are f-block elements, corresponding to the filling of the 4f electron shell, except for lutetium which is a d-block lanthanide. The lanthanide ions occupy a special place in the periodic table of the elements. They are situated at the bottom, one row above the actinides. The word 'lanthanide' has a Greek origin (λανυανεω) which means "to lie hidden". This is a very appropriate name since it took more than a century to discover all the lanthanides. At the beginning of the twentieth century, when Bohr developed a new periodic table, the 15 lanthanides were placed in a separate row at the bottom.

The first report on lanthanide ions dates from 1788. B. Geijer [2] reported the analysis of a stone found near Ytterby, Sweden. This mineral was called yttria and its composition was analysed by Gadolin and Arrhenius [3]. It took several scientists and more than a century to discover all 15 lanthanide ions, not only in yttria, but also in ceria, a mineral found in 1803 by Klaproth [4]. Promethium is the only lanthanide that does not occur in nature in a stable form. Only radioactive isotopes are known, and promethium was made artificially in 1941 by irradiating praseodymium and neodymium with neutrons, deuterons and alpha particles.

1.1.1 – Electronic configuration

The trivalent lanthanide ions (Ln^{3+}) have the electronic configuration $[Xe]4f^{N-1}5s^25p^6$ (N is the number of electrons in Ln^{3+} N=1, Ce, and N=14, Lu). The *4f* electrons are not the outermost ones and they are "shielded" from external fields by two electronic shells with larger radial extension (for instance $5s^25p^6$), which explains the "atomic" nature of their spectra. Thus, *4f* electrons are only weakly perturbed by surrounding ligands charges.

Figure 1.1 shows the radial distribution of the wavefunctions from the *4f* and the external 5s5p6s shells in Gd^{3+} ions.

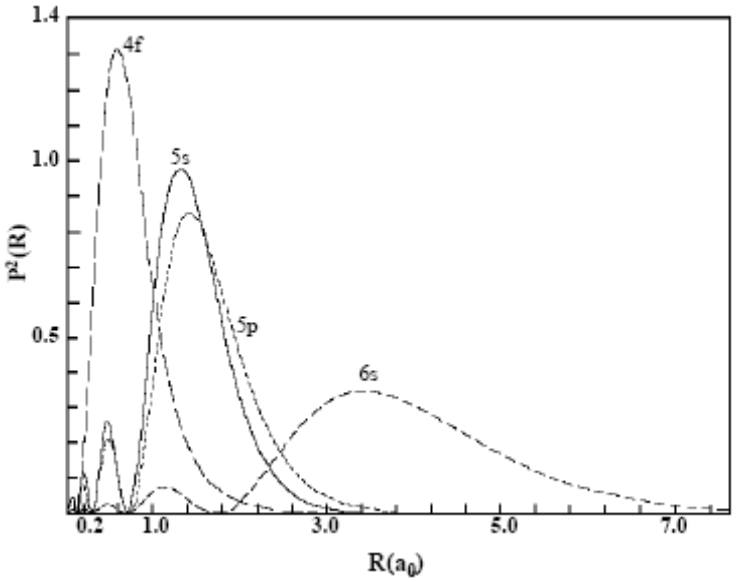

Figure 1.1- Radial densities of the 4f, 5s, 5p and 6s of Gd^{3+} [5].

Considering a specific configuration with N electrons, the total number of states is defined by the number of possible combinations that can be formed relatively to the quantum numbers m_l (z component of the orbital momentum l) and s (spin angular momentum):

$$number\ \ of\ \ states = \frac{[2(2l+1)]\ !}{N\ ![2(2l+1)-N]\ !} \qquad (1.1)$$

For instance, applying the equation (1.1) for the Eu^{3+} $4f^6$ configuration (l=3, N=6) the total number of possible states is equal to 3003, while for Er^{3+} $4f^{11}$ (l=3, N=11) the total number of states is 364.

1.1.2 – The free ion Hamiltonian

In the diagonalization procedure of the free ion Hamiltonian (H_{FI}) the spin-spin, spin-other-orbit and orbit-orbit interactions are of much less importance. Thus, in a first step, the eigenfunctions of H_{FI} may be constructed from the eigenfunctions of the angular momentum operators L^2, S^2, J^2 and J_Z, where L is the total orbital angular momentum, S the total spin angular momentum and J the total angular momentum, J = |L + S|, L+S-1,…|L-S, with $L = \sum_i \ell_i$ and $S = \sum_i s_i$, ℓ and s being monoelectronic orbital and spin angular momentum, respectively. The quantum number J must satisfy the condition $|L - S| \leq J \leq L + S$. For

lanthanide ions an adequate scheme to represent a basis of eigenfunctions is the well-known L - S coupling scheme $|(4f^N)\alpha SLJM_J\rangle$. This notation implies that these eigenstates are pure $4f^N$ states, or, in other words, no configuration interaction (CI) via H_{FI} is taken into account.

In the construction of the $|(4f^N)\alpha SLJM_J\rangle$ eigenstates one frequently finds that they are not unambiguously defined by the S, L, J and M_J quantum numbers. This problem was solved by the use of group theory by Racah [6], who demonstrated that the irreducible representations of certain sub-groups may be used as quantum numbers to classify these eigenstates. This is due to the fact that they form bases for these irreducible representations. Thus, in the above scheme α represents the set of additional quantum numbers necessary to specify the eigenstate. A common procedure in the literature has been to diagonalize the Hamiltonian H_{FI} on a basis formed by the above eigenstates.

The energy levels of a free Ln^{3+} ion are usually interpreted by considering only interactions between the *4f* electrons. Since all the other electronic shells are spherically symmetric, their effect on all the terms of the *4f* configuration is the same in first order. The situation changes if we take into account that the non spherical *4f* shell (because it is nonclosed) can distort the closed spherical shells. Then they can also interact with the *4f* shell. This is, however, a small effect and will be neglected in this treatment [7].

The electronic states of *4f* electrons are obtained by solving the angular part of the Schrödinger equation, and if the symmetry of the problem is known the energy levels may be estimated approximately [11]. This step provides information on the number of energy levels for a certain problem and on their relative ordering, as well as on the selection rules for transitions of various types of radiation. The second part involves calculating the radial part of the wavefunction; this requires knowledge of the exact magnitude of the wavefunctions and is much harder to do.

Having recognized that all the electronic shells, except the *4f* one, are spherically symmetric, and therefore do not contribute significantly to the relative positions of the *4f* energy levels, we can write the Hamiltonian for the *4f* energy levels as:

$$H = -\frac{\hbar^2}{2m}\sum_{i=1}^{N}\Delta_i - \sum_{i=1}^{N}Z^*\frac{e^2}{r_i} + \sum_{i<j}^{N}\frac{e^2}{r_{ij}} + \sum_{i=1}^{N}\zeta(r_i)\vec{s}\cdot\vec{l} \qquad (1.2)$$

where the first term is the kinetic energy of the *4f* electrons, m is mass of electron, $\hbar$ is the reduced Planck constant ($\hbar/2\pi = 1.05\times10^{-34}\ J\cdot s$), Z^*e is the screened charge of the nucleus, r_i is the radial coordenate of the *4f* electron and $\zeta(r_i)$ the spin orbit coupling function:

$$\zeta(r_i) = \frac{\hbar^2}{2m^2c^2r_i}\frac{dU(r_i)}{dr_i} \tag{1.3}$$

where *c* is the velocity of light in vaccum and $U(r_i)$ is the potential in which the electron i is moving. The second term of the equation 1.2 represents the Coulomb interaction of the *4f* electrons with the nucleus. Because there is an interaction with the closed shells that modifies only the magnitude of this term but not its symmetry, we replace the real charge by a screened charge. These two first terms are spherically symmetric and do not remove any degenerescency within the configuration of the 4f electrons.

The next two terms, representing the Coulomb interaction between the *4f* electrons (H_C) and their spin-orbit interaction (H_{SO}), are responsible for the energy level structure of the 4f electrons. When $H_C \rangle\rangle H_{SO}$ we have the so-called Russel – Saunders coupling, where the spin-orbit interaction is only a small perturbation on the energy level structure which has been determined from the diagonalization of H_C. In the case of $H_{SO} \rangle\rangle H_C$ we have the so called $j-j$ coupling scheme. For Ln^{3+} both H_C and H_{SO} are of about equal magnitude, this situation is called intermediate coupling.

The Hamiltonian in the equation 1.2 is solved in a one-electron approximation; that is, electron correlation is neglected. The matrix elements are calculated for the Hamiltonian:

$$H_l = H_c + H_{SO} \tag{1.4}$$

in a set of base functions and then diagonalize the matriz for the specific $4f^N$ configuration. It is common practise to use a basis set of Russel-Saunders configuration. The Hamiltonian H_l is diagonal in J, and therefore the total matrix of energies for a $4f^N$ configuration can be split up into sub-matrices for states with the same J. These states (terms) are then still degenerate in M_J and are a linear combination of states (terms) with different L and S but the same J.

In accordance with the general rule of addition of angular momentum, the total angular momentum J of an atom can take, as mentioned above, the values $L+S \geq J \geq |L-S|$. In the case $L \geq S$, $2S+1$ different values of J are possible, i.e., the term splits into 2S+1 different components. The number 2S+1 is called the multiplicity of the term. In the case $L < S$, the number of components equals to $2L+1$. If the multiplicity of a term $2S+1$ equals 1, the term is called singlet; 2:doublet; 3: triplet; 4:quartet; and so on. Thus the full designation of a term has the form ${}^{2S+1}L_J$. So a term with L=0, S=3/2 and J=3/2 is denoted as ${}^4S_{3/2}$. To the term LS there belong $(2L+1)(2S+1)$ states differing by values of the z-components of orbital and spin

angular momenta M_L and M_s. The spin-orbit interaction does not completely remove this degeneracy. The energy of an isolated atom cannot depend on how the total angular momentum of an atom is oriented in space. Therefore 2J+1 states of the atom, corresponding to the different possible values of the z component of the total angular momentum M, pertain to one and same energy value. In other words, each J component of a term is degenerate with a multiplicity equal to 2J+1 [16]:

$$\sum_J (2J+1) = (2L+1)\,(2S+1) \tag{1.5}$$

i.e., splitting of the term due to spin-orbit interaction does not alter the number of states pertaining to the LS term.

Figure 1.2 shows the energy level distribution of Ln^{3+} doped $LaCl_3$ crystals.

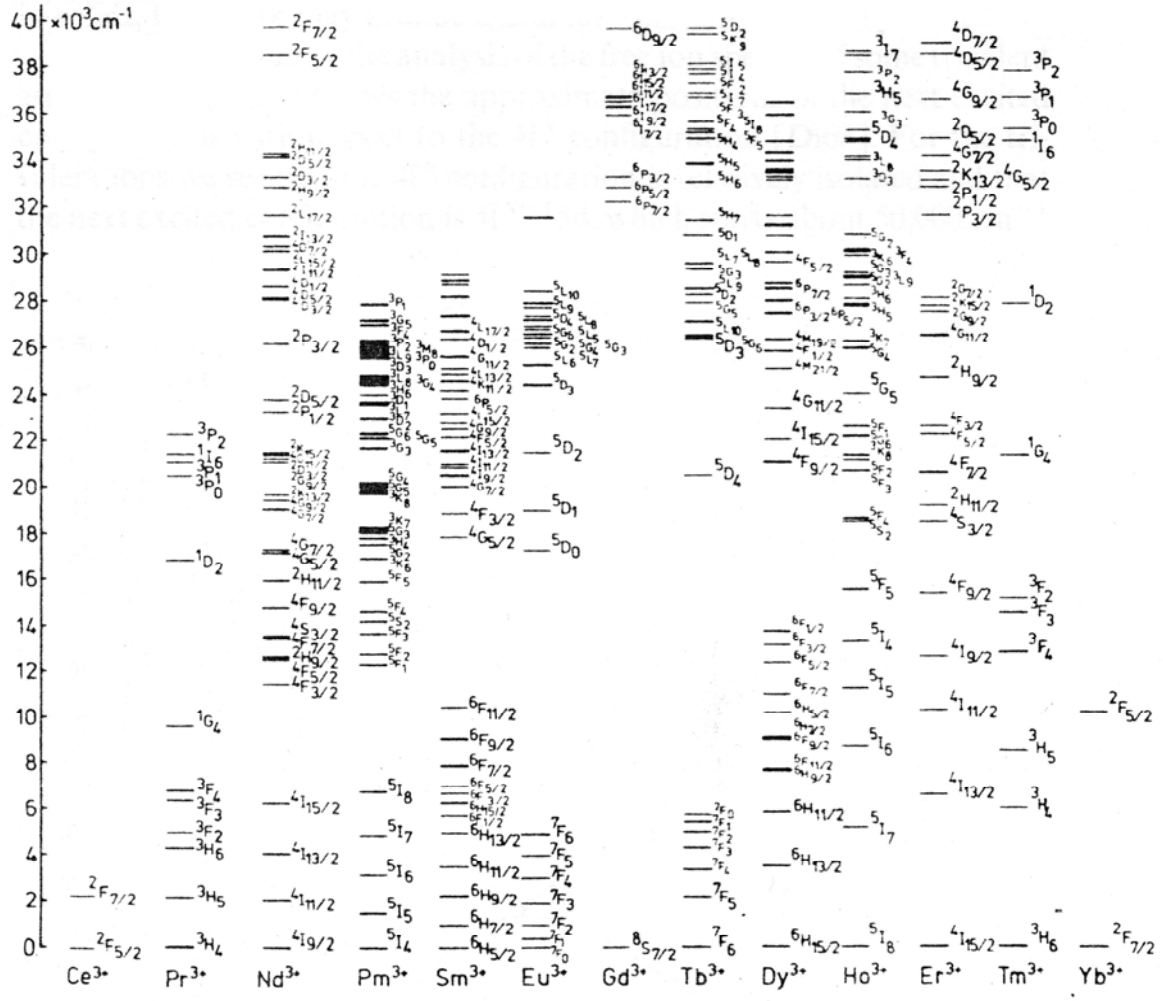

Figure 1.2 – Ln^{3+} energy levels observed in $LaCl_3$ [7]

1.1.3 – The crystal field Hamiltonian

The *4f* shell of Ln^{3+} ions is nonclosed and therefore has a non spherical charge distribution. If the ion is introduced into a host, the ion experiences an inhomogeneous electrostatic field, the so called crystal field (CF), which is produced by the charge distribution in the host. This crystal field distorts the closed shells of the Ln^{3+} ions. The effect on the nonclosed shell *4f* shell is yet more important: it removes to a certain degree (which depends on the crystal symmetry) the M_j degeneracy of the free ion *4f* levels discussed previously, thus producing a major modification of the energy level scheme.

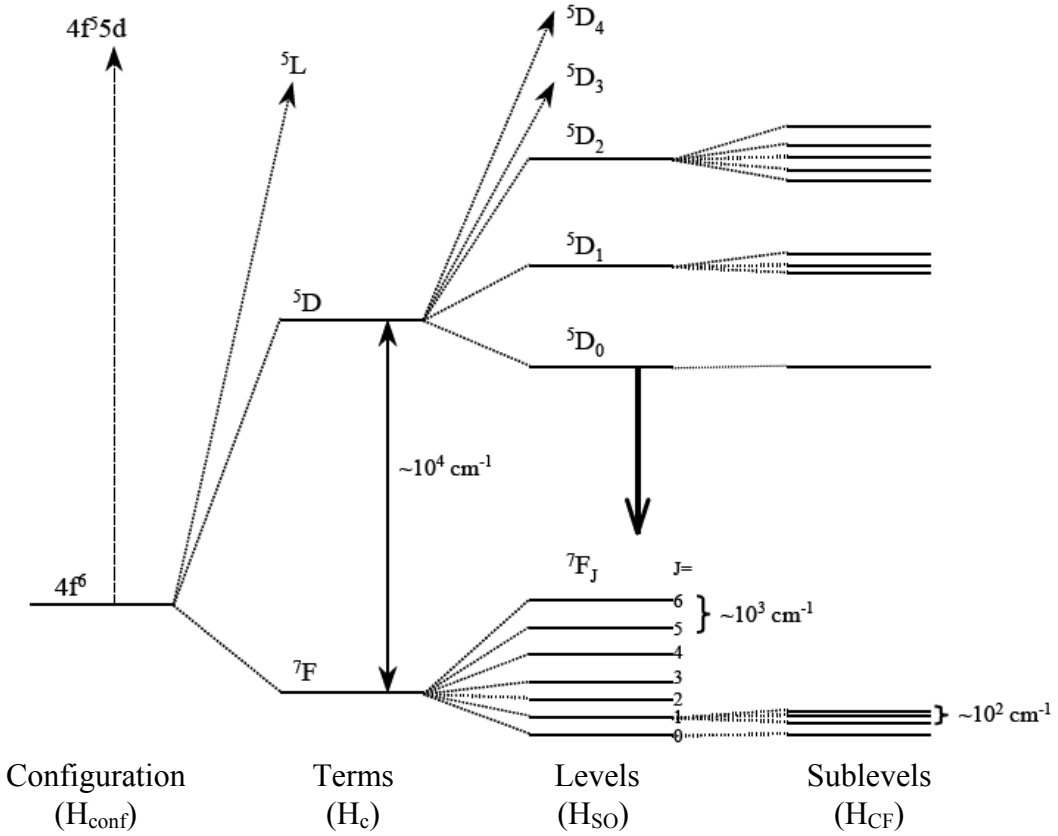

Figure 1.3– Partial diagram of the Eu^{3+} ion displaying an approximated levels distribution for the different Hamiltonians that operate on the $4f^6$ configuration [8]

Thus, crystal field splitting has two aspects: one concerns the symmetry of the problem, namely the number of levels into which the J terms of the free ion are split in a crystal field of a given symmetry; the second concerns the actual magnitude of the crystal field splitting.

A crystal can be considered as built up of point charges at the crystallographic position of ions [**7**]. The potential at the site of the Ln^{3+} ion can be calculated and used to determine the crystal field splitting of the Ln^{3+} free ion terms. This approach, called the point charge model [9,10] , does give the qualitative features of the problem, but actual calculations show that the magnitude of the crystal field splitting is underestimated in this scheme; however it can be used for illustrative purposes. A more realistic model should take into account the spatially extended charge clouds of the individual ions. Considerations of the point charge model ions [11]:

a) The ions are considered static in the crystal (lattice vibration and their effect on the energy levels are neglected).

b) The *4f* electrons of one Ln^{3+} ion are regarded as representative of those of all the Ln^{3+} ions in the crystal and the interaction of *4f* electrons of adjacent Ln^{3+} is neglected.

c) The crystal consists of extended charge distribution. This produces an overlap of the charge distribution of the neighbouring ions and *4f* electrons. In addition, a charge transfer between the *4f* electrons and the electrons of the ligands can take place. Both effects contribute to the crystal field interaction.

d) The *4f* electrons of one ion are considered to be independent of each other; that is correlation effects play no significant role.

With the previous considerations, the crystal potential $\phi(r_i,\varphi_i,\vartheta_i)$ is calculated at the site of the 4f electrons. If the crystal has charge density $\rho(R)$ and the *4f* electrons have radius r_i, this results in:

$$V = -\sum_i \frac{e_i \rho(R)}{|R - r_i|} d\tau = -\sum_{k,i} e_i \int \rho(R) P_k\left(\cos(R, r_i)\right) \frac{r_<^k}{r_>^{k+1}} d\tau \qquad (1.6)$$

where e_i is the electron charge, the parameters $P_k(cos(R,r_i)$ are Legendre polynomials (see eq. 2.3a from ref 7), $r_<$ and $r_>$ are, respectively, the smaller and larger value of R and r_i. The parameters $P_k(cos(R,r_i)$ can be expressed as:

$$P_k\left(\cos(R, r_i)\right) = \frac{4\pi}{2k+1} \sum_q Y_{kq}^*(\vartheta_i, \vartheta_i) Y_{kq}(\vartheta, \varphi) \qquad (1.7)$$

where Y_{kq} are spherical harmonics. Susbstituting eq. 1.7 in 1.6 we have:

$$V = -\sum_{k,q,i} e_i \int \rho(R) \frac{4\pi}{2k+1} (-1)^q Y_{kq}(\vartheta_i, \varphi_i) Y_{k-q}(\vartheta, \varphi) \frac{r_<^k}{r_>^{k+1}} d\tau$$

$$V = -\sum_{k,q,i} e_i \int (-1)^q \rho(R) C_{kq}(\vartheta_i, \varphi_i) C_{k-q}(\vartheta, \varphi) \frac{r_<^k}{r_>^{k+1}} d\tau$$

$$V = -\sum_{k,q,i} B_{kq} C_{kq}(\vartheta_i, \varphi_i) \tag{1.8}$$

where

$$C_{kq} = \left(\frac{4\pi}{2k+1}\right)^{1/2} Y_{kq} \tag{1.9}$$

is called Racah tensor operator [12-13] of rank *k* and the parameters B_{kq} are defined as

$$B_{kq} = -e \int (-1)^q \rho(R) C_{k-q}(\vartheta, \varphi) \frac{r_<^k}{r_>^{k+1}} d\tau \tag{1.10}$$

where they are the so-called cristal field parameters of even rank (k = 2, 4 and 6). The values of k are restricted by parity and triangularity rules for *f* orbitals. The allowed values of *q* depend on the symmetry of the crystal field around the Ln^{3+} ion [14].

Table 1.1– Sublevels observed in each J levels (J integer or semi-integer) for the 32 local symmetry point group[a]

Crystallographic system	J (integer)								
	0	1	2	3	4	5	6	7	8
Cubic	1	1	2	3	4	4	6	6	7
Hexagonal and trigonal	1	2	3	5	6	7	9	10	11
Tetragonal	1	2	4	5	7	8	10	11	13
Triclinic, monoclinic and orthorhombic	1	3	5	7	9	11	13	15	17
	J (semi-integer)								
	1/2	3/2	5/2	7/2	9/2	11/2	13/2	15/2	
Cubic	1	1	2	3	3	4	5	5	
Other local symmetry	1	2	3	4	5	6	7	8	

[a] Cubic: O_h, O, T_d; T_h and T; hexagonal: D_{6h}, D_6, C_{6v}, C_6, D_{3h} and C3h; tetragonal: D_{4h}, D_4, C_{4v}, C_{4h}, C_4, D_{2d} e S_4; trigonal: D_{3d}, D_3, C_{3v}, S_6 e C_3; orthorhombic: D_{2h}, D_2 e C_{2v}; monoclinic: C_{2h}, C_2 e C_s (ou C_{1h}) and triclinic: S_2 (ou C_i) e C_1.

Crystal field increases the degenerescency of the levels in a maximum of 2J+1 sublevels (Stark components) if J is an integer, or J+1/2 if J is a semi integer. The number of

non null parameters depends of the local symmetry around the ion; lower degree of symmetry implicate in higher number of parameters. The maximum number of sublevels or Stark components observed in an energy level, by local field effect, depends of the local point group, (Table 1.1).

1.1.4 – $4f^n \rightarrow 4f^n$ transitions

An oscillating electromagnetic field of appropriate frequency can be used for the excitation of an ion via an electron transition form the ground state to a higher energy level. Transitions between two energy levels can have either electric dipole (ED) or magnetic dipole (MD) character. Higher order transitions, such electric or quadrupole processes, can usually be neglected due to their reduced transition probabilities. Electric dipole transitions require a change of parity of the electron wavefunction. Thus, due to the Laporte selection rule, electric dipole transitions within the *4f*-shell are (parity) forbidden and only magnetic dipole transitions are expected. The electric dipole operator ($\vec{P}$) has odd parity and it is given by [15-16]:

$$P = -e\sum_i \vec{r}_i \qquad (1.11)$$

For Ln^{3+} ions localised in crystalline sites without inversion symmetry, a mixing of opposite-parity states into the $4f^N$ states can occur resulting in a relaxation of the Laporte selection rule. The effect of admixing of states with opposite parity to the *4f*-states has been investigated by Judd and Ofelt [17,18]. These intra-configurational *4f-4f* transitions are observed as forced ED transitions and the selection rules are:

1. $\Delta l = \pm 1$
2. $\Delta S = 0$
3. $\Delta J \leq 2l \leq 6$

Additionally, for lanthanides ions with an even number of electrons the following selection rules are valid:

$J = 0 \leftrightarrow J' = 0$ forbidden

$J = 0 \leftrightarrow J' = 2,4,6,...$ strong

$J = 0 \leftrightarrow J' = 1,3,5,...$ weak

Magnetic dipole induced transitions can occur between states of the same configuration, magnetic dipole operator ($\vec{M}$) has even parity [15-16]. This operator can be represented by:

$$\vec{M} = -\left(\frac{e\hbar}{2mc}\right)\left(\vec{L} + 2\vec{S}\right) \qquad (1.12)$$

Selection rules for magnetic dipole transitions are as follow:

1. $\Delta J \leq 0{,}1$ and $J = 0 \rightarrow J' = 0$ forbidden

1.1.5 – $4f^n \rightarrow 4f^{n-1}$ 5d *(fd)* transitions

The $4f^N \rightarrow 4f^{N-1}5d$ transitions are induced by the electric dipole operator (parity allowed). The *5d* electrons extend spatially farther out than the *4f* electrons, which mean that the crystal field interaction for a *5d* electron is larger than for a *4f* electron; in fact, in comparison to it the spin-orbit interaction can be neglected in first order. For Ce^{3+} and Tb^{3+} ions, this absorption lies in the UV region. The excited *4f-5d* states is strongly influenced by the crystal field which splits the *5d* level into a number of levels, this number varies considerably from a lattice to another. In the case of Tb^{3+}, excitation in the *4f-5d* absorption bands is followed by green emission. As a result of UV absorption, the ion is raised to a $4f^7 5d$ state; it then decays stepwise from this state to the $^5D_3$ or $^5D_4$ state, thereby giving up phonons to the lattice. Because of the large distance between these states and the ^7F levels, the process stops here and the ion then returns to the ground state by emitting radiation (luminescence). Although the position of the *4f-5d* absorption and excitation bands depends to a very great extend on the nature of the lattice, the green emission does not, because it involves transitions between *4f* levels [19].

The situation as far as the Ce^{3+} ion is concerned is entirely different. Excitation in the *4f-5d* absorption bands is followed by emission from the *5d* states themselves. Contrary, to the case of Tb^{3+}, the emission here depends strongly on the lattice.

1.1.6 – Decay curves and lifetimes

The lifetime of an excited state is defined by the average time that the ion spends in the excited state prior to return to the ground state [20]. The luminescence intensity associate with

radiative relaxations of *N* ions (initially in an excited state) to a fundamental state is described as [21,22,24] :

$$I(t) = k_r N(t) \tag{1.13}$$

where k_r represents the probability of radiative relaxation and *N(t)* is given by:

$$N(t) = N_0 e^{-t/\tau_0} \tag{1.14}$$

where N_0 corresponds to number of excited ions at *t=0* and τ the lifetime of the excited state. Thus the luminescence intensity is:

$$I(t) = I_0 e^{-t/\tau_0} \tag{1.15}$$

The experimental lifetime (τ_{exp}) corresponds not only to radiative relaxation process, but also to non radiative relaxation rates, thus [25]:

$$\frac{1}{\tau_{\exp}} = k_r + k_{nr} = \frac{1}{\tau_r} + k_{nr} \tag{1.16}$$

where k_r and k_{nr} are, respectively, the probabilities of radiative and non radiative transitions, and τ_r is the radiative decay time. The quantum efficiency (η) of a state is defined as:

$$\eta = \frac{k_r}{k_r + k_{nr}} \tag{1.17}$$

1.2 – Size effects

Two features are considerably affected in nanophosphors due to size reduction: relaxation mediated via phonons and energy transfer. The first change because in nanomaterials the phonon density of states (PDS) becames discrete and a cut off of low energy phonons is observed. The second one is sensitive to size and environment [26].

The energy gap can change in nanoscopic materials, for instance the *4f5d* states are more sensitive to the crystal fields because the *5d* orbital interacts with the surroundings ligands, thus size effects impacts in the relaxation dynamics for systems having ions like Eu^{2+} or Ce^{3+}. B. Mercier *et al.* [27,28] showed indirectly using spectroscopic measurements that the gap in Gd_2O_3 increases when the size decreases from bulk materials to nanoparticles with average size of 7 nm, Figure 1.4A-B. They monitored the emission at 611 nm and the position of the ligands to metal charge transfer (LMCT) band for nanoparticles with 7, 9, 20 and 50 nm and found two overlapping bands at 250 nm (5 eV) and another band at lower wavelength (~ 230 nm), both were attributed to LMCT. The LMCT shifted to lower wavelength positios as

the particle size decrease. The shift was theoretically estimated in the case of one dimensional confinement and considering a Wannier exciton:

$$\Delta E_g = A \times \frac{R_B}{d} - \frac{B}{\varepsilon d} + \ldots \qquad (1.18)$$

A and B being proportionality factors independent of the material, ε the static dielectric constant and d the diameter of the nanocrystal, the Bohr radius estimated from these measurements was between 1 nm<R_B<1.8 nm. However, detailed calculations (ab initio and/or linear combination of atomic orbitals model, LCAO) for the evolution of the gap in sesquioxide are needed to confirm their estimation of the R_B.

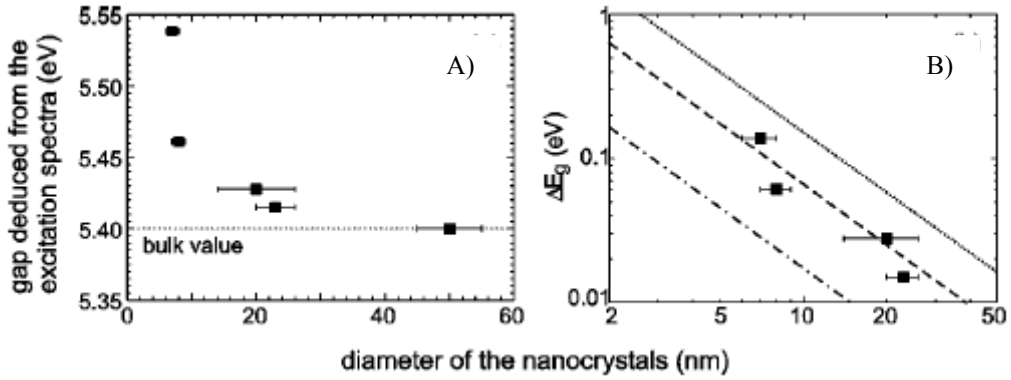

Figure 1.4 - A) Evolution of the gap with size and B) evolution of the measured ΔE_g (filled square) with size compared to silicon (dotted line), ZnO (dashed line) and for Gd_2O_3 considering a Bohr radius of 0.5 nm (dash-dotted line). [27]

The shift of the LMCT states to the higher energy side in nanocrystals, due to different ligands shielding from environment compared with the bulk, has been studied by M. Jia *et al*. and T. Igarashi *et al.* among others [29, 30, 31].

T. Igarashi *et al.* [30] reported the luminescence characterisation of Y_2O_3:Eu^{3+} nanoparticles (61±15 nm in diameter) and microparticles (3.1±1.2 μm in diameter). In the excitation spectra acquired while monitoring at 612 nm ($^5D_0 \rightarrow {}^7F_2$ transition from Eu^{3+} at C_2 local symmetry), the LMCT bands are observed at 255 nm and 260 nm, in nano and microparticles, respectively. This LMCT band is due to the electronic transition from the *2p* orbital of O^{2-} to the *4f* orbital of Eu^{3+} and it is related closely to the covalency degree of the O –Eu bond [30]. The decrease in energy for electron transfer from O^{2-} and Eu^{3+} represents the increase in the covalency, i.e., lower ionicity in the O-Eu bond. Therefore, the blueshift in the

LMCT excitation band showed in nanoparticles means an increase in the ionicity of O-Eu bond.

Also B. Mercier *et al* [28] discussed the LMCT band shift position in terms of the degree of ionicity; by using the effective mass approximation (EMA) they estimated the *R* value of 3.1 nm. These authors suppose that the confinement can occur in the covalent part of the bonds. In a band structure, the extension of conduction and valence bands is proportional to the degree of ionicity of the material. In this model the R parameter is the distance for which the confinement effects on the covalent part of the bonding becomes important.

1.2.1 – Modification of radiative lifetime

The decay time for spontaneous emission from ions excited to the state *i* in a dielectric medium with refractive index *n* is given, in the electric dipole approximation by [32]:

$$\tau = \frac{3\pi\varepsilon_0 \hbar c^3 g_i}{n} \sum_j \frac{1}{\mu_{ij}^2 \mu_{ij}^3 g_j} \tag{1.19}$$

where the sum runs over all terminal states *j*, ε_0 is the permittivity, g_i and g_j are degeneracies of the *i* and *j* states,

$$\mu_{ij} = e\left\langle i\left|\sum_k \bar{r}_r\right|j\right\rangle \tag{1.20}$$

is the matrix element of the electric dipole operator, and $\hbar\omega_{ij}$ is the energy difference between the *i* and *j* states. The quantities g_i, g_j and ω_{ij} are related to ionic properties and depend only on the emitting ions and their nearest neighbors, i. e. ions whitin a distance of 1-10 nm. The index *n*, on the other hand, depends on the modes of a cavity large compared to the wavelength of the emitted radiation and, therefore, on the properties of the medium surrounding the emitting ions whitin a distance of the order of the wavelength. Thus, for a particle much smaller than the wavelength, the refractive index to be considered cannot be the index of this material n_c but rather the index n_m of the medium surrounding the particle. If τ_c is the lifetime of the ions in an infinite medium with index n_c, the lifetime τ_p in a single very small particle in a medium with index n_m is given by [32]:

$$\tau_p = \frac{n_c \tau_c}{n_m} = \frac{\tau_0}{n_m} \tag{1.21}$$

where τ_0 is the lifetime in the small particle in vacuum. For a very small particle the lifetime therefore should be inversely proportional to the index of the surroundings. If the particle is

not much smaller than the excitation wavelength or the particle is part of a powder, it will be necessary to use an effective index with a value somewhere between n_c and n_m. Thus the lifetime for ions in a powder is dependent on particle size and powder density, and the measured value will be between the theoretical value τ_p and the bulk single crystal τ_c.

Thus the dependence of the radiative lifetime on *n* arises from the change in the density of states for photons in the medium of reduced light velocity and the modification of the polarizability of the surrounding medium. In nanoparticles the relation between radiative decay time and *n* is given by the relation [33]:

$$\tau_r = \frac{1}{f(ED)} \frac{\lambda^2}{\left[\frac{1}{3}\left(n_{eff}{}^2 + 2\right)\right]^2 n_{eff}} \tag{1.22}$$

where λ is the wavelength, *f(ED)* is the oscillator strength and n_{eff} is the effective index of refraction given by:

$$n_{eff}(x) = x n_{NP} + (1-x) n_{med} \tag{1.23}$$

where *x* is the "filling factor" that represents the fraction of the volume occupied by the nanoparticles, the use of the n_{eff} is valid when the average size of the nanoparticles is much smaller than the wavelength of light.

1.2.2 – Modification of phonon density of states and confinement on electron–phonon interaction and anomalous thermalisation

No quantum confinement effects are expected for the *4f* configuration because the *4f* electrons are localised in inner shells, however the electron-phonon interaction may change in nanomaterials [26]. Confinement effects on electron-phonon interaction occur due to the phonon density of states that became discrete in nanocrystals and the low-energy acoustic phonon modes are absent. As a consequence of the PDS modification, luminescence dynamics of optical centers in nanoparticles, particularly, the nonradiative relaxations are expected to behave differently from that in bulk materials.

The most essential property of acoustic vibrations in a nanoparticle is the existence of minimum size-quantized frequencies corresponding to acoustic resonances of the particle. In dielectric nanocrystals, the Debye model is not valid for evaluation of PDS if the radius of the nanocrystals is less than 10 nm [26,34,35]. The vibrational modes of a finite sphere were analysed by Lamb [36] and Tamura [37]. A stress-free boundary condition at the surface and a finiteness condition on both elastic displacements and stresses at the center are assumed.

These boundary conditions yield the spheroidal and torsional modes, determined by the following eigenvalue equations [26,37]:

$$2\left\{\eta^2+(l-1)(l+2)\left[\eta\frac{j_{l+1}(\eta)}{j_l(\eta)}-(l+1)\right]\right\}\xi\frac{j_{l+1}(\xi)}{j_l(\xi)}-\frac{1}{2}\eta^4 + \left[\eta^2-2l(l-1)(l+2)\right]\eta\frac{j_{l+1}(\eta)}{j_l(\eta)}+(l-1)(2l+1)\eta^2=0 \quad (1.24)$$

$$\frac{d}{d\eta}\frac{j_l(\eta)}{\eta}=0 \quad (1.25)$$

where for the reduced frequencies of the spheroidal and torsional modes, $\xi=\omega R/\upsilon_l$ and $\eta=\omega R/\upsilon_t$, with ω being the phonon frequency and R the radius of nanoparticles; j_l is the *l*th order spherical Bessel functions; υ_l and υ_t are the sound velocities of longitudinal and transverse modes, respectively. G. K. Liu *et al.* [40] used equations 1.24 and 1.25 to simulate the PDS distribution in Y_2O_2S nanocrystals, Figure 1.5 shows their results.

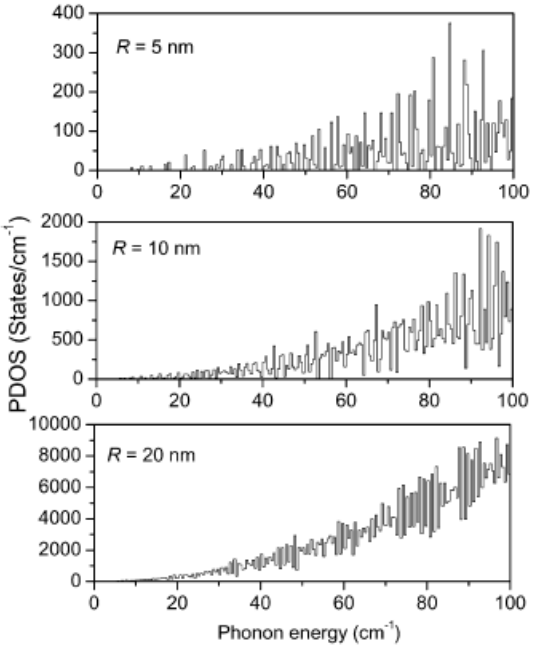

Figure 1.5– Calculated phonon density of states in 5, 10 and 20 nm nanocrystals of Y_2O_2S [40]

Comparing the PDS distribution from 5, 10 and 20 nm Y_2O_2S nanocrystals, presented in Figure 1.5, the authors showed that the low-frequency phonon modes are significantly reduced in the smaller crystals. Furthermore, there is a cut-off frequency ($\eta_{\min}$) in the low frequency side of phonon spectrum below which all phonon modes are intrinsically

eliminated. Thus the luminescence dynamics, especially the phonon-assisted energy transfer processes, in nanocrystals is expected to be different from that in their bulk.

The dependence of $\nu_{\min}$ on the nanoparticle size can be expressed as [37,38]:

$$\nu_{\min} = \frac{\upsilon_t}{2\pi R}\eta_{\min} \tag{1.26}$$

where η_{min} is the minimal reduced frequency determined by the numerical solution of the equations (1.24) and (1.25), these reduced frequencies are determined by the zeros of the spherical Bessel functions [37]. Thus the optical spectrum and luminescence dynamics of an ion in dielectric nanoparticles can be significantly modified through electron-phonon interactions.

It is well known that the population of the energy levels of Ln^{3+} ions generally obeys the Boltzmann distribution characterized by the Boltzmann factor:

$$b_i = \frac{g_i \exp(-E_i / k_B T)}{\sum_j g_j \exp(-E_j / k_B T)} \tag{1.27}$$

where k_B is the Boltzmann constant (1.38 x 10^{-23} J/K or 0.695 cm^{-1}/K) and E_i is the energy of the level. Hence, at low temperature one should generally observe emission or absorption from the lowest level of the initial multiplet on which most ions populate, supposing the energy differences between the lowest level and nearest upper level is much larger than $k_B T$.

Recently, the evolution of the lowest components of the $^4I_{15/2}$ Stark level of Er^{3+} was studied in the low temperatute excitation spectra. The $^4I_{15/2(1,2,3)} \rightarrow {}^4F_{7/2(a)}$ transitions in nanocrystals were monitored at temperatures from 2.2 to 41 K, when pumped with a 10 Hz (5 ns) laser pulse, Figure 1.6A. The hot bands at 492.3 and 492.9 nm had non linear population dependence with the laser power; a possible explaination was attributed to the hot bands arising from the upper Stark components of the $^4I_{15/2}$ overlap with the excitation bands of some defect sites from the lowest level in the ground state.

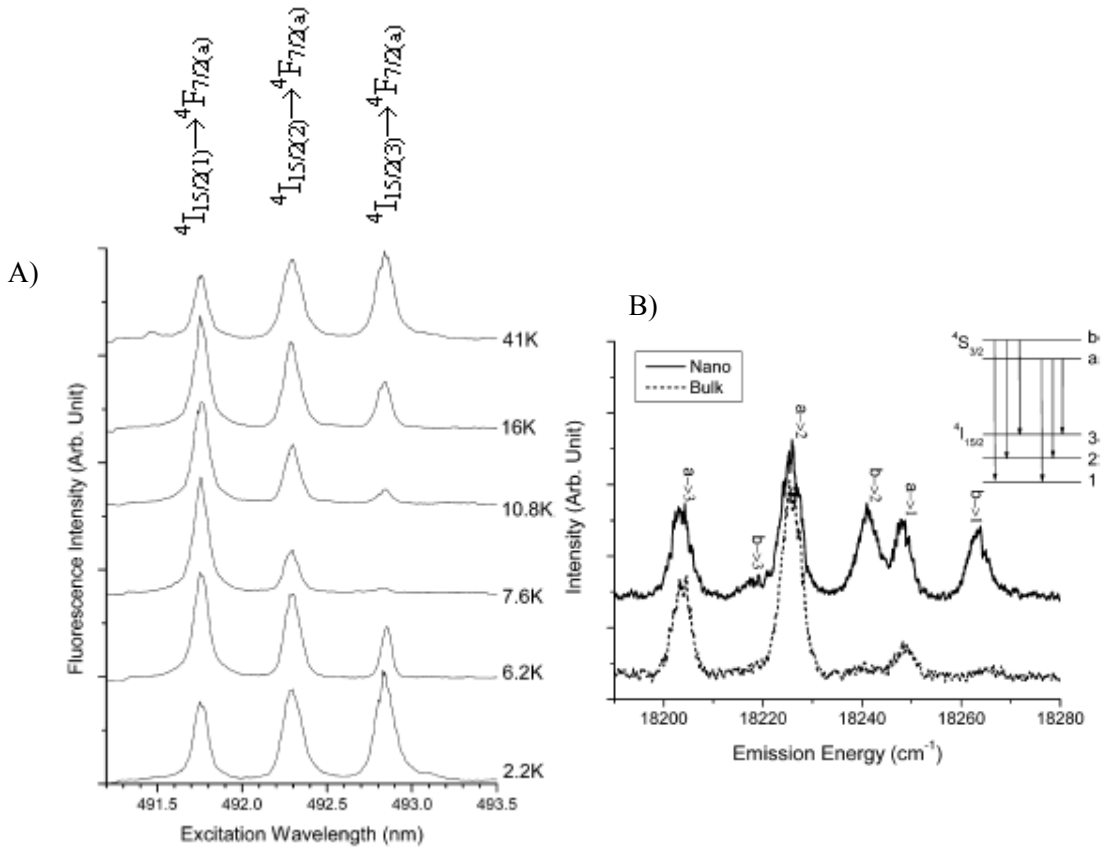

Figure 1.6 – A) Excitation spectra of the $^4I_{15/2(1,2,3)} \rightarrow {}^4F_{7/2(a)}$ transitions in $Y_2O_2S:Er^{3+}$ nanocrystals at temperatures from 2.2 to 41 K [26] and B) emission spectra of the transitions $^4S_{3/2(a,b)} \rightarrow {}^4I_{15/2(1,2,3)}$ in $Y_2O_2S:Er^{3+}$ nanocrystals (solid line) and bulk (dotted line) at 3 K [42].

In the literature, hot bands with energy up to 200 cm^{-1} were reported in the excitation spectra of $Y_2O_2S:Er^{3+}$ nanocrystals at temperatures below 9 K [41,42], for example, the presence of the $^4I_{15/2(4,5)} \rightarrow {}^4F_{7/2(a\text{-}d)}$ transitions (note that the $^4I_{15/2(4)}$ and $^4I_{15/2(5)}$ Stark componentes are 210 cm^{-1} and 224 cm^{-1} above the $^4I_{15/2(1)}$ ground state level, respectively). These same transitions were not observed in the excitation spectra acquire from the bulk sample. Figure 1.6B shows the $^4S_{3/2} \rightarrow {}^4I_{15/2}$ transition in the nanocrystalline and bulk $Er^{3+}:Y_2O_2S$ samples at 3 K.

The pump wavelength is 491.8 nm. Only the emission lines from 546.5 to 550.0 nm were measured for comparison, which correspond to the transitions $^4S_{3/2(a,b)} \rightarrow {}^4I_{15/2(1,2,3)}$ indicated by arrows. Similarly to the situation for the ground state $^4I_{15/2}$, a vast majority of the excited Er^{3+} ions should be in the lower Stark level of $^4S_{3/2}$ at 3 K, since the Boltzmann factor of the upper Stark level (15 cm^{-1} above) is calculated to be only 0.08%. Therefore the normal emission lines of the nanocrystals should be similar to those of the bulk samples with just

three peaks arising from the $^4S_{3/2(a)} \rightarrow {}^4I_{15/2(1,2,3)}$. In fact, as shown in Figure 1.6B, hot bands corresponding to the emission from the upper level $^4S_{3/2(b)}$ are also observed in the emission spectra of nanocrystals at 3 K.

The anomalous thermalisation effect due to absence of low-frequency phonon modes in nanocrystals discussed above should also occur in other systems. Observation of this effect depends on the energy level structure of the luminescent centers, as well as on the sample temperature and crystal size. According to the temperature-dependent multi phonon relaxation rate and the relationship between the cut off frequency and crystal size, anomalous hot bands from the excited states with higher energies will occur in crystals with smaller size.

Mercier *et al.* [43] and Liu *et al.* [44] provide experimental evidence of, respectively, anomalous thermalisation in $Gd_2O_3:Eu^{3+}$ nanoparticles and $Gd_2O_3:Eu^{3+}$ nanotubes. Meltzer *et al.* [46,47] and Tissued *et al.* [48,49] also studied this effect in Eu_2O_3 nanoparticles.

Mercier *et al.* [43] presented two effects resulting from the size reduction of $Gd_2O_3:Eu^{3+}$ nanoparticles in the excitation spectra monitored at 611 nm (whitin the $^5D_0 \rightarrow {}^7F_2$ transition): inhomogeneous line broadening of the $^7F_0 \rightarrow {}^5D_0$ transition and the lowest excited $^7F_1$ Stark component ($^7F_{1a}$ level) of Eu^{3+} as a function of temperature; the particles analised had sizes around 8, 11, 20, 23 and 100 nm; and the smaller the particles, less populated the $^7F_{1a}$ state is. The explanation of this second phenomenon was related with the absence of very low energy phonons in small particles. However, it should be noted that, in order to control the size of these particles, distinct thermal annealings at 900, 1000, 1100, 1200 and 1400 K were performed, respectively. The effect of annealing parameters in the hot bands intensity will be discussed in Chapter 3.

Liu *et al.* [44] reported hot bands originating from the $^7F_{1a}$ level, with energy of 217 cm^{-1}, in the excitation spectrum below 50 K, Figure 1.7A. The temperature dependence of intensity in the excitation spectra was investigated from 10 to 295 K. The integrated intensity ratio of hot bands to normal bands, $(^7F_1 \rightarrow {}^5D_1)/(^7F_0 \rightarrow {}^5D_1)$, as a function of temperature is shown in Figure 1.7B. The calculated ratios are approximately obtained based on equation 1.27 (ΔE = 217 cm^{-1}). At higher temperature (>60 K), the calculated ratios are in good agreement with the measured ones obeying the normal Boltzmann distribution. Below 50 K, the Eu^{3+} population in $^7F_1$ deviates significantly from the Boltzmann distribution. This anomalous thermalisation was also atributed to elimination of low-energy phonon modes.

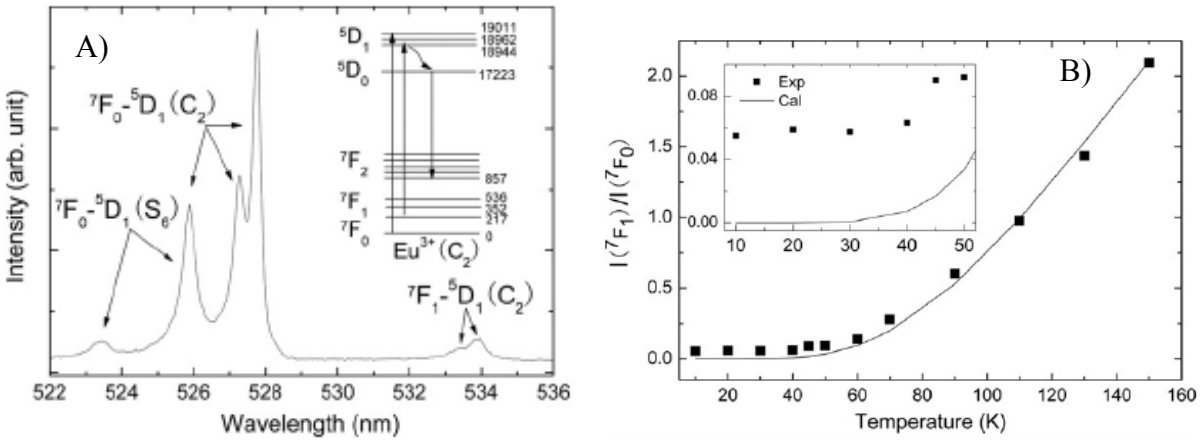

Figure 1.7 – A) Excitation spectrum of Gd_2O_3:Eu^{3+} nanotubes in the region of the $^7F_{0,1}\rightarrow{}^5D_1$ transitions at 10 K, monitoring the $^5D_0\rightarrow{}^7F_2$ (C_2) emission at 611 nm. The schematic diagram of partial energy levels of Eu^{3+} ions is presented and B) Temperature dependence of the integrated intensity ratio of the hot bands to normal bands in $(^7F_1\rightarrow{}^5D_1)/(^7F_0\rightarrow{}^5D_1)$. The scattering dots are observed values, whereas the line denotes the calculated values based on the Boltzmann distribution. [44].

Studies of electron – phonon interactions in insulating Eu_2O_3 performed by R. S. Meltzer et al. [46,47] revealed that the acoustic-phonon modes become discrete in energy with a low-frequency "gap" and the confinement of the vibrational excitations results in a particle-size-dependent amplitude of the motion of the atoms thereby producing a greatly enhanced interaction between the electronic states of the impurity ion and the vibrational modes of the nanoparticle as the particle size is reduced. B. Tissue et al. [48,49] also investigated the low temperature excitation spectra of the cubic and monoclinic Eu_2O_3 nanoparticles (12, 6 and 4 nm in diameter); they reported hot bands arising from the $^7F_1$ level of Eu^{3+} ions, Figure 1.8, an increase in the intensity of hot bands compared to the normal excitation lines occurs as the particle size decreases.

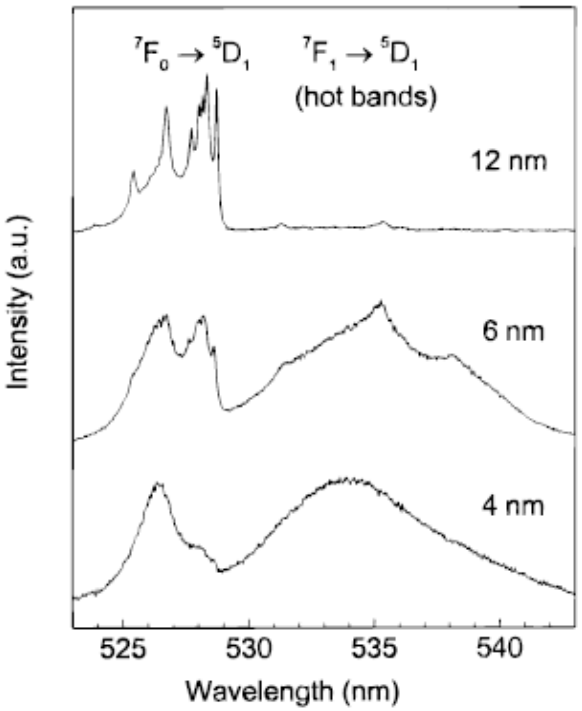

Figure 1.8 – Excitation spectra of nanocrystalline Eu_2O_3 at approximately 12 K showing the $^7F_1 \rightarrow {}^5D_1$ hot-band region. [49]

In order to address all the features of the optical interactions in the nanoparticles, these authors proposed the studies of the location, distribution, or segregation of dopants in nanoparticles; the efficiency of energy transfer across interfaces; effects of quantum confinement or changes in phonon dynamics and electron-phonon interactions on the radiative and nonradiative relaxation rates in localized luminescent dopants.

1.2.3 – Energy transfer and upconversion

Upconversion (UC) refers to nonlinear optical processes characterized by the successive absorption of two or more pump photons via intermediate long-lived energy states followed by the emission of the output radiation at a shorter wavelength than the pump wavelength. This general concept was first recognized and formulated independently by Auzel, Ovsyankin, and Feofilov in the mid-1960s [33,50,51].

The predominant mechanisms of upconversion in nanophosphors are excited-state absorption (ESA), energy transfer upconversion (ETU) and photon avalanche (PA) [52].

The Er^{3+} ions are excited from the ground state to the $^4I_{11/2}$ level by absorbing one 980 nm photon (denoted as ground state absorption process, **GSA**, in Figure 1.9). The ions in the

$^4I_{11/2}$ level sequentially absorb another 980 nm photon and are raised to the $^4F_{7/2}$ level (excited-state absorption process, **ESA1**). Thus the ions in $^4F_{7/2}$ level undergo multi-phonon relaxation to the $^2H_{11/2}$ and $^4S_{3/2}$ levels.

Another process that can populate these levels is labelled **ET1**: $^4I_{11/2} + {}^4I_{11/2} \rightarrow {}^4I_{15/2} + {}^4F_{7/2}$ (a photon arising from the $^4I_{11/2} \rightarrow {}^4I_{15/2}$ transiton is re-absorbed leading to the $^4I_{11/2} \rightarrow {}^4F_{7/2}$ transition). The $^4F_{9/2}$ level can be pumped by nonradiative relaxation trough the excited $^4S_{3/2}$ state (gap of ~3200 cm^{-1}).

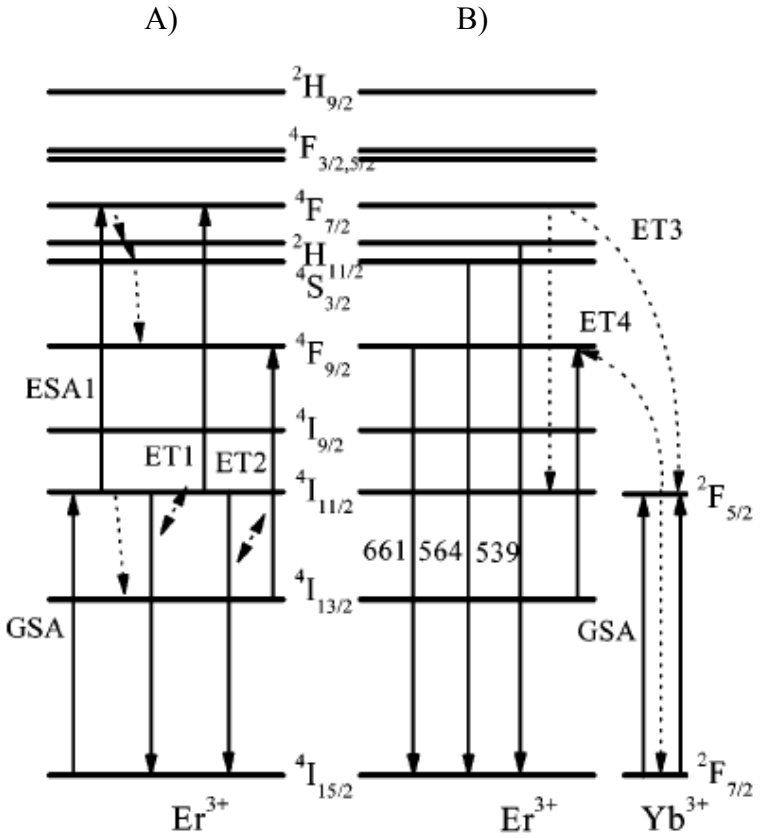

Figure 1.9 – Energy levels and up conversion scheme for the Er^{3+} and Yb^{3+} codoped system [53]. Upconversion and energy transfer processes: ground state absorption (GSA), excited-state absorption process (ESA) and energy transfer (ET). The processes that occur whitin the energy levels of Er^{3+} ions are represented in A) while the energy transfer process between Er^{3+} and Yb^{3+} are depicted in B).

From the reduction of relative intensity of green ($^2H_{11/2}$, $^4S_{3/2} \rightarrow {}^4I_{15/2}$) and red ($^4F_{9/2} \rightarrow {}^4I_{15/2}$) emission with increasing the concentration of Er^{3+} ions from 0 to 6%, Figure 1.10. A, H. Guo et al. [53] assumed another possible path denoted as **ET2**: $^4I_{13/2} + {}^4I_{11/2} \rightarrow {}^4F_{9/2} + {}^4I_{15/2}$

($^4I_{11/2} \rightarrow {}^4I_{13/2}$ transition mediated multi-phonon relaxation, followed by the absorption of a photon arising from the $^4I_{11/2} \rightarrow {}^4I_{15/2}$ leading to the $^4I_{13/2} \rightarrow {}^4F_{9/2}$ transition). The $^4I_{13/2}$ level may be excited through multi-phonon nonradiative process from $^4I_{11/2}$ level and radiative process from $^4S_{3/2}$ level.

For Yb^{3+}/Er^{3+} codoped phosphors, the Er^{3+} ions can be excited from ground-state $^4I_{15/2}$ to the excited state $^4I_{11/2}$ by two processes: ground state absorption and energy transfer from excited Yb^{3+} ions as follow [$^4I_{15/2}$(Er)+ $^4F_{5/2}$(Yb) $\rightarrow {}^4I_{11/2}$ (Er)+ $^4F_{7/2}$(Yb)]. The energy transfer dominates the process because much larger Yb^{3+} absorption cross section as compared with the Er^{3+} [54]. Then the ions in the $^4I_{11/2}$ level are excited to the $^4F_{7/2}$ level by ESA1 process. After that, the ions undergo multi-phonon relaxation to luminescent levels $^2H_{11/2}$ (3-phonon relaxation with single phonon of approximately 400 cm^{-1}) and $^4S_{3/2}$ (3-phonon relaxation with single phonon of approximately 230-240 cm^{-1}).

The **ET3** process occurs to pump the Yb^{3+} to the $^2F_{5/2}$ (under 488 nm laser excitation): $^4F_{7/2}$ (Er^{3+}) + $^2F_{7/2}$ (Yb^{3+})$\rightarrow {}^4I_{11/2}$ (Er^{3+}) + $^2F_{5/2}$ (Yb^{3+}). This process depopulates the excited $^4F_{7/2}$ level and causes the decrease of green emission intensity. **ET4** is a possible way in that the populated $^4I_{13/2}$ level was excited to the $^4F_{9/2}$ level by energy transfer from the excited Yb^{3+} ions: $^4I_{13/2}$ (Er^{3+}) + $^2F_{5/2}$ (Yb^{3+}) $\rightarrow {}^4F_{9/2}$ (Er^{3+}) + $^2F_{7/2}$ (Yb^{3+}).

The UC luminescent efficiency in these three processes varies considerably. ESA is the least efficient UC process. Efficient UC is possible in PA with metastable, intermediate levels that can act as a storage reservoir for pump energy. However, the PA process suffers from a number of drawbacks, including pump power dependence and slow response to excitation (up to several seconds) due to numerous looping cycles of ESA and cross-relaxation processes. In contrast, ETU is instant and pump power independent, and thus has been widely used to offer highly efficient UC (~ two orders of magnitude higher than ESA) over the past decade.

In ref. [53] the authors also showed that green emission intensity decreases with increasing Yb^{3+} concentration while red intensity increases. Figure 1.10 shows the upconversion spectra of the Er^{3+} and Yb^{3+}/Er^{3+} codoped Gd_2O_3 nanoparticles varying the Ln^{3+} concentrations.

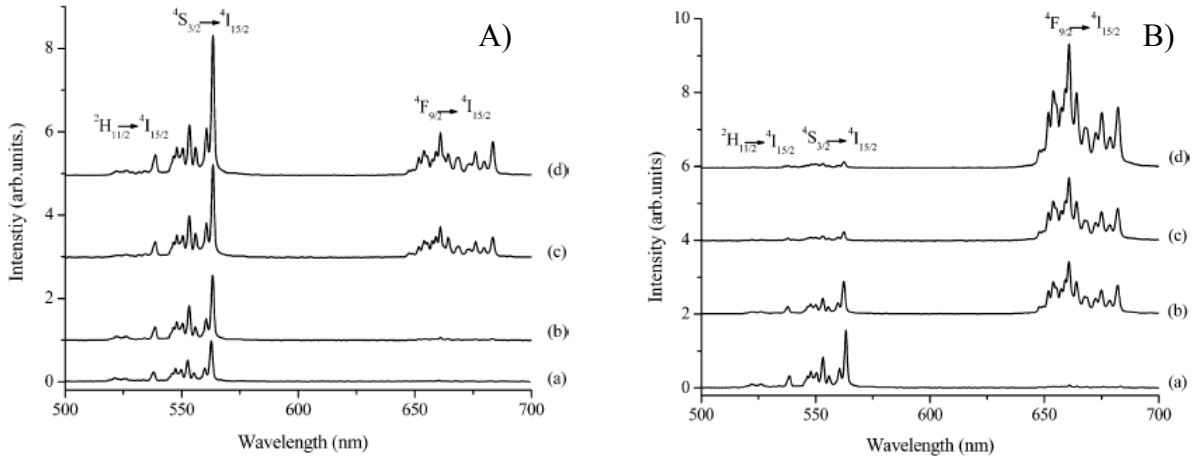

Figure 1.10 – A) Upconversion spectra of doped $Gd_2O_3:Er^{3+}$ nanoparticles with different Er^{3+} concentration: a) 0.5%, b) 1%, c) 3%, d) 6% and B) upconversion spectra of $Gd_2O_3:Er^{3+}/Yb^{3+}$ nanoparticles with different Yb^{3+} concentration: a) 0%, b) 2%, c) 5% and d)10%.[53]

Recently, detailed investigation of nanocrystalline $Y_2O_2S:Er^{3+}$ upconversion phosphors have shown that with 2-4 % at. % Er^{3+}-Yb^{3+} codoping, the nanocrystals (with typical diameters of 20-50 nm) have upconversion efficiencies that are 20-25 % higher that of bulk counterparts [55,56]. Some applications of the upconverting nanophosphors as thermal sensors will be presented at the Chapter 2.

Chapter 2 – Structure, synthesis and applications of lanthanide hydroxide and oxide nanotubes/nanorods

2.1 – Crystal structure

Lanthanide hydroxide nanotubes have a hexagonal crystal structure, for instance $Tb(OH)_3$ is hexagonal $P6_3/m$ with the metal atom, Tb, at 2c (1/3, 2/3, 1/4) [58]. The Tb atomic array can be described as infinite linear chains, parallel to the c-axis, Figure 2.1, in which the distance between each of the two neighbouring Tb (3.6 Å) coincides with the unit-cell parameter *c*. Each chain is surrounded by three other chains, which are displaced by *c*/2 with the respect to the central one, and form hexagonal tunnels where the OH groups are inserted. It is clearly shown that the hexagonal $Tb(OH)_3$ has an anisotropic structure.

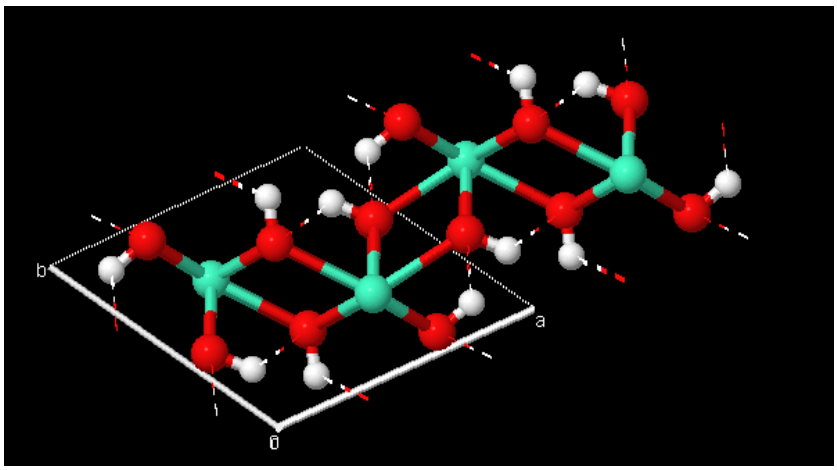

Figure 2.1 – Partial crystal structure of $Ln(OH)_3$, where green balls represent the Ln^{3+} ion, red balls the oxygen and white balls the hydrogen atoms.

Upon thermal annealing the lanthanide hydroxide nanotubes are converted to the lanthanide oxide nanotubes that are binary sesquioxides with the cubic bixbyite structure ($Ia\bar{3}$). Bixbyite can be thought of as an oxygen deficient fluorite (e.g., CeO_{2-x}), where the lattice parameter is doubled and a quarter of the oxygen atoms are removed [59]. Unlike fluorite, there are two unique cation positions due to the ordered arrangement of the oxygen atoms. There are 3 times as many of the so-called 24*d* (C_2) sites as 8*b* (S_6) sites. These sites are conveniently described by considering the cation surrounded by anions occupying six corners of a (fluorite lattice) cube, as illustrated in Figure 2.2. For the 24*d* site, the unoccupied

positions are in the sample plane on opposite corners of one cube face, while for the 8*b* site, the unoccupied positions are diagonally opposed. Furthermore, the 24*d* coordination cube is distorted, with three distinct metal-oxygen distance pairs (conversely for the 8*b* site, the six metal-oxygen distances are equal). The 24*d* distortion originates in the oxygen atoms (labelled 3 and 4) localised below the unoccupied positions in Figure 2.2A, increasing the O3-O-O4 angle. Oxygen atoms labelled 1 and 2 are farthest from the *A* atom, while O atoms in the same plane as the unoccupied positions (labelled 5 and 6 in Figure 2.2A) are nearest to the *A* atom and have the smallest O5-*A*-O6 angle. However, the mean of the three pairs of 24*d* *A*-O distance is practically the same as the 8*b* *A*-O distance. Figure 2.2A-B show also how the symmetries of the two lattice cation sites differ. The 24*d* site is noncentrosymmetric (*C*2 symmetry), while the 8*b* site is centrosymmetric (*S*6 or *C*3*i* symmetry)

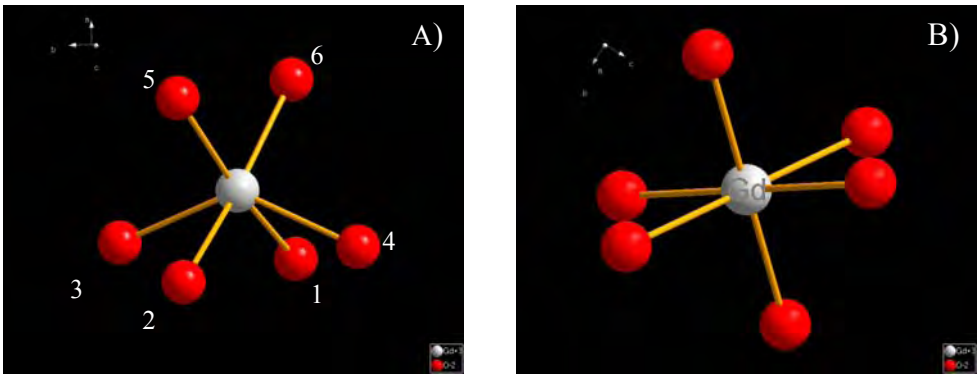

Figure 2.2- The two cation sites of cubic Ln_2O_3 bixbyite, where the white spheres represent Ln^{3+} ion and the red spheres denote oxygen atoms: A) 24*d* (C_2 symmetry) and B) 8*b* (S_6 symmetry) sites.

The controlled synthesis of lanthanide nanotubes depends on the intrinsic structure via phase control, and extrinsic means such as the manipulation of nucleation, growth process and post-treatments [60], or even the self assembly through dipole interactions or oriented attachments [61,62]. The growth directions of $Ln(OH)_3$ nanotubes are reported to be [001] or [100], both reasonable in view of the crystal structures since the former is the growth direction of the rare earth hydroxide nanowires. The axis directions of Ln_2O_3 or CeO_2 nanotubes that are obtained by dehydration from hydroxides vary. The different growth directions assigned to $Ln(OH)_3$ nanotubes should be further analysed taking into consideration the different synthesis conditions and the crystal structures [63]. Atomistic simulation of ceria nanotubes by Parker and co-workers based on the Born model [64] revealed that in multilayer wrapped ceria

nanotubes, polycrystalline behaviour like boundaries, junctions, and dislocations are important to accommodate the strain [65], Figure 2.3.

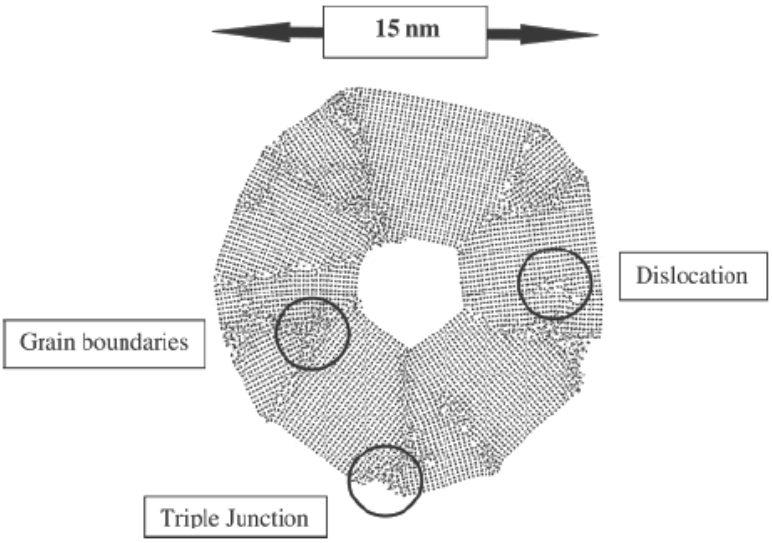

Figure 2.3 – Multilayer wrapped CeO_2 nanotube model showing polycrystalline behaviour. The figure indicates important structural features including boundaries, junction and dislocation [65].

Figure 2.4 shows an example of a continuous feeding (using hydrothermal method) of $Y(OH)_3$ to the seeds (nanorods) surface that would preferentially occur at the circumferential edges of each regular-shape seed because these sites have higher free energies than those of other sites on the surface. As soon as the crystal has grown, mass transportation to the growing regions would lead to under saturation in the central part of the growing faces of each seeds, and that 'two nanotubes' could be grown on each seed at almost the same rate with opposite direction until all $Y(OH)_3$ had been completely consumed, eventually resulted in the formation of nanotube having well-defined hollow interiors.

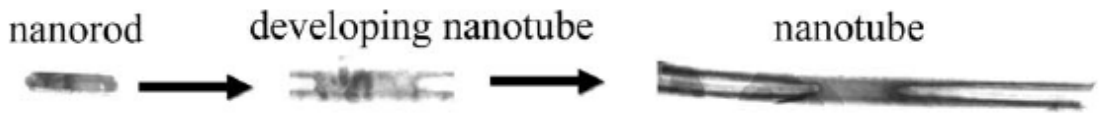

Figure 2.4 – Diffusion-controlled growth of $Y(OH)_3$ nanotube [60]

2.2 – Synthesis

Lanthanide compounds have been extensively utilized as high-performance phosphors, devices, catalysts, and other functional materials based on the electronic, optical, and chemical characteristics arising from their 4f electrons [66-69]. The processing of lanthanide-based materials in nanotubular form [44,70,73-101] affords promising highly functionalized materials as a result of both shape-specific and quantum size effects [41-47].

Nanotubes structures are different from nanowires or nanoplates in topology. If some crystal faces are confined and other crystal faces are allowed to grow, these tubular structures will not be formed directly. Therefore, more complex mechanisms for these structures are proposed. The tubular nanostructures can be classified into thin wall tubes, typically related to compounds with two dimensional structures, and thick-wall tubes, related with three-dimensional compounds. Mechanisms and methods such as scrolling of nanosheets, etching of terminal faces, hard and soft templates effects, and Kirkendall [102] effects for nanorods are suggested for the formation of monocrystalline and polycrystalline nanotubes. [103, 104]

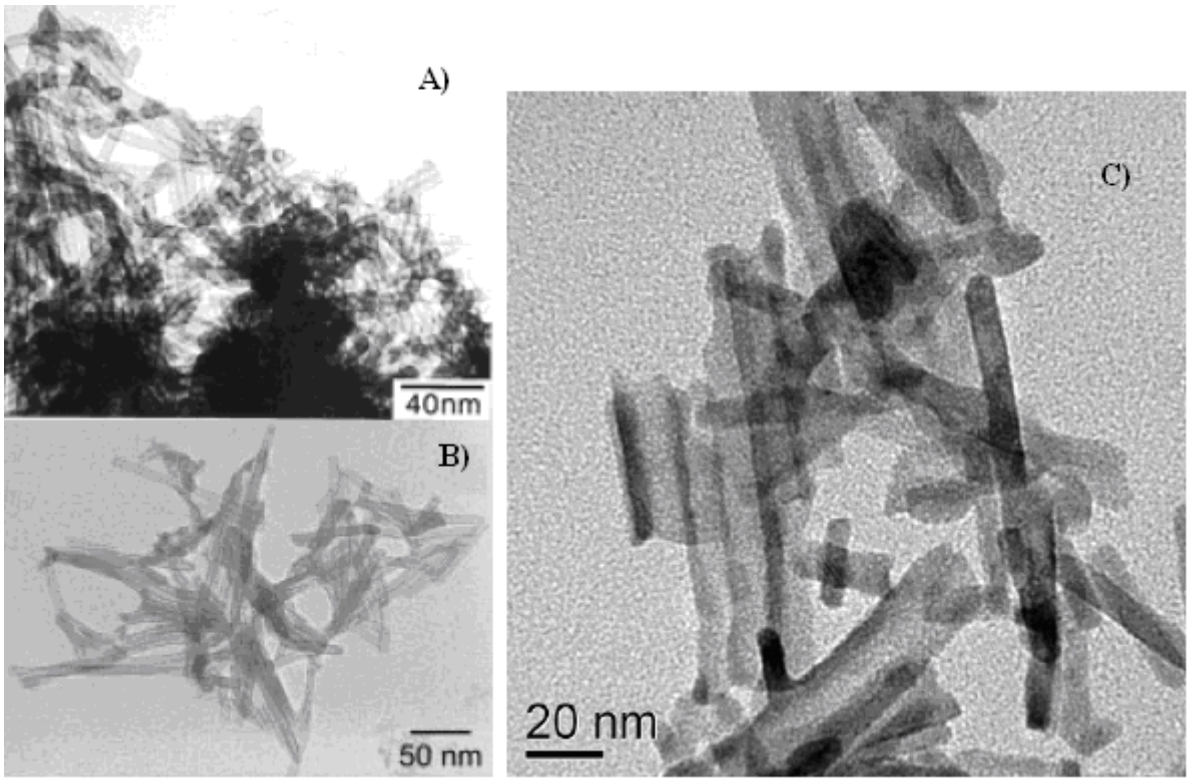

Figure 2.5– A-B) Er oxide nanotubes prepared using SDS surfactant as organic template [78,79] and C) $Gd_2O_3:Eu^{3+}$ prepared trough hydrothermal method [44]

Recently, the synthesis of lanthanide oxide nanotubes has attracted considerable interest as indicated by the increasing number of publications concerning: $Tb(OH)_3$ and $Y(OH)_3$ single crystalline nanotubes synthesized on a large scale by hydrothermal treatment of the corresponding oxides [58].

In reference [77] Tb_2O_3 nanotubes were fabricated by calcination of the precursor $Tb(OH)_3$ nanotubes prepared by a template-assisted hydrothermal route. M. Yada et al [78, 79] described the synthesis of rare-earth oxide nanotubes or hierarchical structures templated by dodecyl sulfate assemblies, realized by homogeneous precipitation with urea and their conversion into a hollow nanotube with an inner diameter of 3 nm after anionic exchange of the surfactant with acetate ions, Figure 2.5A-C.

X. Bai [70,82] have synthesized pure cubic phase $Y_2O_3:Eu^{3+}$ nanotubes as well as nanowires by a hydrothermal method and $Y_2O_3:Eu^{3+}/Y_2O_3$ core-shell composite, a remarkable improvement of photoluminescence was observed for the core-shell composite under both violet and ultraviolet excitations. Also a versatile synthetic method of preparing ordered rare earth nanotubes was proposed based on nitrides and via the sol gel method assisted with porous anodic alumina oxide [83].

Cerium oxide nanotubes were produced by using oxygen-free hydrothermal alkali treatment of anhydrous cerium chloride at high temperature, followed by washing with water and hydrochloric acid [87], large cavity CeO_2 nanotubes were obtained by etching $Ce(OH)_3$ nanotubes/nanorods with H_2O_2 [88] or synthesized with a simple solid-liquid interface reaction route without surfactants employing $Ce(OH)CO_3$ as precursors for micro or nanotubes [89]. A.-W. Xu [91] reported a simple method for direct growth of the first $Dy(OH)_3$ nanotubes by facile hydrothermal treatment of bulk Dy_2O_3 crystals. Pr_6O_{11} single-crystal nanotubes with a typical 3-D crystal structure in the bulk have been successfully obtained through a template-free molten-salt synthetic method [92]. L. Liu [44] reported the synthesis and luminescence related features of $Gd_2O_3:Eu^{3+}$ nanotubes obtained using nitrides precursors and hydrothermal treatment, Figure 2.5C. These and other reports found in the literature are listed in table 2.1, the methods of synthesis are also summarised.

Table 2.1 – Synthesis methods for yttrium and lanthanide hydroxide and/or oxide nanotubes

Compound	Method	Reactants	Ref.
$Gd_2O_3:Eu^{3+}$	hydrothermal	nitrates, NaOH	44
$Gd_2O_3:Eu^{3+}$	homogenous precipitation	oxides, ammonia	73
$Gd_2O_3:Eu^{3+}$	Liquid phase deposition	carbon NT as template	74
Y_2O_3	hydrothermal	oxide, ammonia	75
Y_2O_3	hydrothermal	nitrates, NaOH, PEG-6000	60
Y_2O_3	electrochemical	porous alumina, nitrates, NaC_2O_4	76
$Tb(OH)_3$, $Y(OH)_3$	hydrothermal	oxide	58
Tb_2O_3	organic template	chloride, SDS	77
M_2O_3 (M=Gd, Yb, Er)	surfactant	nitrates, SDS,NaOH	78, 79
$M(OH)_3$ (M= Pr, Sm, Gd, Tb, Dy, Er)	hydrothermal	nitrates, NaOH	80
$M(OH)_3$ (M= La, Pr, Sm, Gd, Tb, Dy, Er, Yb, Tm)	hydrothermal	Oxides, KOH or NaOH	81
$Y_2O_3:Eu^{3+}$	hydrothermal	nitrates, NaOH, calcination	70,82
M_2O_3 (M=Y, Pr, Nd, Sm, Eu, Gd, Tb, Dy, Ho, Er, Yb)	sol-gel	porous alumina as template	83
$Gd_{0.2}Ce_{0.8}O_{1.9}$	dehydration and denitrification	polycarbonate membrane as template	84
CeO_2	Precipitation and aging	nitrates, ammonia	85
CeO_2	liquid phase deposition	porous alumina as template	86,101
CeO_2	hydrothermal	anhydrated chloride	87
CeO_2	hydrothermal and etching with H_2O_2	chlorides, NaOH	88
CeO_2	solid-liquid interface reaction	$Ce(OH)CO_3$ as precursor	89
CeO_2	liquid phase deposition	carbon NT as template	90
Dy_2O_3	hydrothermal		91
Pr_6O_{11}	molten-salt synthetic method		92
Y_2O_3	hydrothermal	nitrates, NaOH, ammonia	93
$Y_2O_3:Er^{3+}$	hydrothermal	nitrates, NaOH	94,95
$Y_2O_3:Eu^{3+}$	Hydrothermal	nitrates, KOH	96
$Y_2O_3:Eu^{3+}$@CNt	solution	nitrates, ammonia	97
$Y_2O_3:Eu^{3+}$	sol-gel	porous alumina as template	98
Eu_2O_3	organic template	oxide and methacrylate	99
Eu_2O_3	sol-gel template approach	porous alumina, nitrate, urea	100

2.2.1 – Methods for nanotubes growth

Growth of lanthanide hydroxide and oxide nanotubes in solution has been successfully achieved [105]. To develop strategies that can guide and confine the growth direction to form one dimensional nanostructures, researchers have used a number of approaches such hydrothermal synthesis [44,58,60,72,75,81], sol-gel combined with porous or 1D templates (porous AAO, polymer membranes or carbon nanotubes) [74,83,84,90,98,100], electrochemical deposition in porous anodic alumina oxide (AAO) [77,101], surfactant assisted growth [77-79,99] and molten salt methods [81].

2.2.1.1 – Hydrothermal synthesis

The hydrothermal process has been used to produce crystalline structures since the 1970's [106]. This is the most frequent method used for the synthesis of yttrium and lanthanide hydroxide and oxide nanotubes. This process begins with an aqueous mixture of a soluble metal salt (metal and/or metal–organic) of the precursor materials. Usually the mixed solution is placed in an autoclave (showed at Figure 2.6) under moderate temperature, and autogeneous high pressure conditions. Typically, the experimental temperature ranges between 100 ºC to 300 ºC and the pressure exceeds 1 atm. The microwave assisted hydrothermal technique [107] leads to some advantages when compared with the use of conventional ovens, for instance: (a) rapid heating to reaction temperature, (b) enhancement of reaction kinetics by one to two orders of magnitudes which also saves reaction time and energy, and (c) formation of smaller particles.

Figure 2.6 – Teflon-lined stain steel autoclave for conventional hydrothermal synthesis

An important parameter that rules the final morphology is the pH of the colloidal suspension obtained after mixing the metal precursor, solvent and base (usually NaOH, KOH or ammonia solution). The effect of pH and reaction temperature on the product size is related to the nucleation and growth of the particles. The shape and size of the products are closely related with the nucleation process, which is strongly affected by the solubility of the product in the precipitating solution. An increase in the OH^- concentration decreases the solubility of the solution and a large amount of nuclei are formed at the same time.

Many studies have reported the synthesis of $Y(OH)_3$ and corresponding Y_2O_3 nanotubes under strong basic conditions [72,60,58,81] using NaOH or KOH as base. N. Li *et al.* [75] investigated the influence of pH and temperature on the morphology of yttrium compounds using NaOH and ammonia solution, and reported a complete phase distribution in the temperature-pH diagram for the NaOH and NH_4OH systems. Using NH_4OH pure hexagonal $Y(OH)_3$ is obtained in the range of 80-220 ºC and pH 11.2-14, while using NaOH the same phase is achieved at 100-220 ºC and pH < 13. It seems that a high pH value leads to the formation of a large amount of nuclei and small particles are favoured due to the suppressed growth of each nucleus. Table 2.2 summarizes the lanthanide hydroxides nanotubes obtained by the hydrothermal method, and their experimental conditions.

Table 2.2 – Hydrothermal experimental conditions for synthesis of yttrium and lanthanide hydroxides and oxide nanotubes

Hydroxide or oxide	Solvent, base	pH	T (ºC)/time (h)	Calcination T (ºC)/time (h)	Ref.
$Gd(OH)_3$	H_2O, NaOH	13	120/15	500/1	44
$Y(OH)_3$	H_2O, NH_4OH	13.5	160/24	600/2	75
$Y(OH)_3$	H_2O, NaOH	12.5	140/24	500/2	60
$Y(OH)_3$ $Tb(OH)_3$	H_2O, NaOH	-	170/48	450/6	58
$Y(OH)_3$	H_2O, NaOH	14	120/12	-	80
$M(OH)_3$ (M= La, Pr, Sm, Gd, Tb, Dy, Er, Yb, Tm)	H_2O, NaOH or KOH	13	120-140/12-24	500/2	81
$Y_2O_3:Eu^{3+}$	H_2O, NaOH	13	150/12	500/2	70,82
CeO_2	H_2O, NaOH	>13	120/72	-	87

2.2.1.2 – Sol-gel and template-assisted synthesis

The synthesis of lanthanide hydroxide or oxide nanotubes arrays assisted by templates has been reported. The outer surface of carbon nanotubes has been used as template.Utilizing periodic structured templates, such as porous AAO [83,98,100] and polymer membranes [84], nanostructures can form inside the confined channels. For example, porous AAO membranes have embedded hexagonally ordered nanochannels. In general, the sol–gel process is associated with a gel composed of sol particles. As the first step, colloidal (sol) suspension of the desired particles is prepared from the solution of precursor ions. The porous anodic alumina oxide template will be immersed into the sol suspension, so that the sol will aggregate on the anodic alumina oxide template surface. With an appropriate deposition time, sol particles can fill the channels and form structures with high aspect ratio. The final product will be obtained after a thermal treatment to remove the gel. These pores can also be filled to form one dimensional nanostructures using electrodeposition method described in 2.2.1.3 topic.

Lanthanide oxide nanotubes (M_2O_3, M=Y, Pr, Nd, Sm, Eu, Gd, Tb, Dy, Ho, Er and Yb) were successfully prepared by the sol-gel method assisted with porous AAO template [83]; an example of Gd_2O_3 nanotubes is shown in Figure 2.7A. In this case, the template received a pre treatment with a phosphoric acid solution for removal of the gases trapped inside the pores. The templates were immersed into the sol (prepared using lanthanide oxides, nitric acid and water bath at 100 ºC, pH 2-3) for 2 h, and then a calcination at 500 ºC for 20 min was performed. It was found that the as prepared lanthanide oxide formed into bamboo-like nanotubes and entirely hollow nanotubes; the sizes are 50-100 nm in diameter and more than 1 μm in length. Large scale $Y_2O_3:Eu^{3+}$ and Eu_2O_3 nanotubes (outer diameter 50-80 nm) have also been prepared by this method but using urea as basic medium and annealing at 700-800 ºC for 8-10 h [98, 100]. SEM images showed nanotubes parallel to each other, vertically oriented to form an array like a replica of the template; and TEM images revealed that these tubes have a thin wall around 5 nm.

$Gd_2O_3:Eu^{3+}$ and CeO_2 nanotubes were prepared by coating the outer surface of carbon nanotubes [74,90]. G. Liu *et al.* [74] adopted a procedure involving the mixture of lanthanide nitrates precursors (Gd and Eu), carbon nanotubes and $CO(NH_2)_2$; followed by the addition of polyvinyl pyrrolidone (PVP) as dispersant and surfactant, this suspension was stirred for 2.5-5 hours at a temperature range of 80-90 ºC. After filtering and drying, the obtained powder was calcined at different temperatures in the range 600-900 ºC. The size of these $Gd_2O_3:Eu^{3+}$ polycrystalline nanotubes could be controlled by changing the reaction time (2.5 h, wall thickness 25-30 nm and 4.5 h, wall thickness 45-50 nm) and concentration of the reactants.

One of the disadvantages of this method is the post synthesis template removal; these authors reported the complete elimination of the carbon nanotubes upon thermal annealing at temperatures from 700 to 900 ºC. Also carbon nanotube assisted synthesis of CeO_2 nanotubes was reported [90], Figure 2.7B, and a similar experimental procedure was used: lanthanide nitrates, carbon nanotubes (previously treated with nitric acid) and a base solution (aqueous NaOH), filtering and drying followed by calcination at 500 ºC for 0.5 h. Even before the calcination the phase identified by XRD was CeO_2 , this occurs because the Ce^{3+} oxidation state is very unstable as compared with the Ce^{4+} oxidation state mainly in alkaline solution and in air. TEM images reveal that the carbon nanotubes are first coated with CeO_2 nanoparticles, the calcination at 450-500 ºC maintain the uniform distribution at the outer surface of carbon nanotube, while annealing at higher temperature collapses the tubular structure with the growth of the particle size.

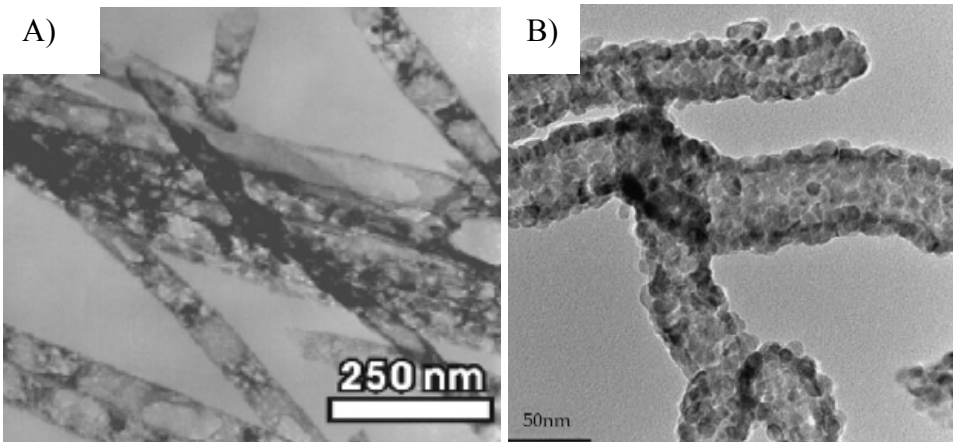

Figure 2.7 – A) Gd_2O_3 nanotubes prepared by using porous AAO membrane as template [83] and B) CeO_2 nanotubes using carbon nanotubes as template [90]

2.2.1.3 – Electrochemical deposition

Electrochemical deposition has not been widely used to fabricate lanthanide hydroxide and oxide nanotubes in porous structures [77,101]. L. Yang *et al.* [76] prepared Y_2O_3:Eu^{3+} nanotubes array by electric field assisted deposition onto porous anodic aluminium oxide substrates, Figure 2.8. The outer diameter of the nanotube was about 60 nm and the thickness of the nanotube wall was about 3 nm.

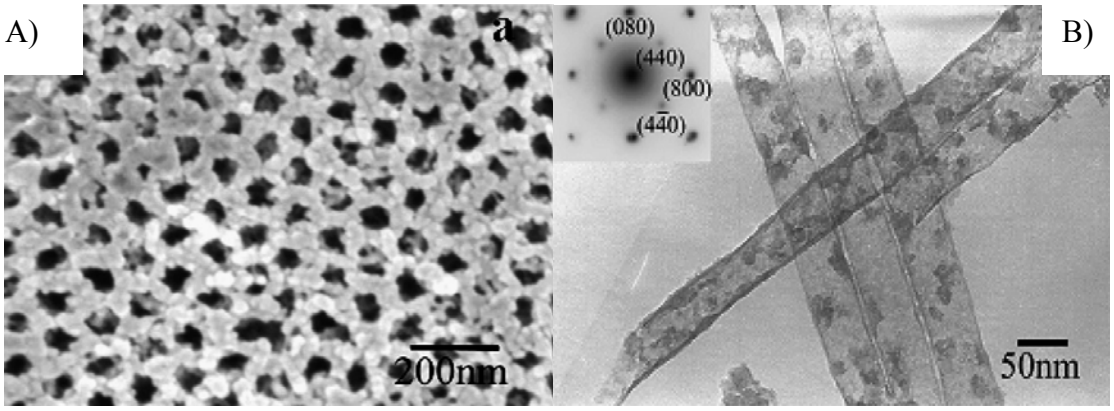

Figure 2.8 – A) SEM and B) TEM images of $Y_2O_3:Eu^{3+}$ nanotubes prepared by electrochemical deposition [76].

Comparing with the sol-gel technique, this method reduces the cost considerably but also improves the efficiency because the electrolyte can be used several times and the final product prepared by this method is a nanotube arrays. No nanowires were found.

2.2.1.4 – Surfactant-assisted growth

Surfactant-promoted anisotropic one-dimensional crystal growth has been considered as a convenient way to synthesize lanthanide hydroxide and oxide nanotubes [77-79,99]. This anisotropic growth is often carried out in a microemulsion system composed of three phases: oil, surfactant and water. In the emulsion system, the surfactants serve as microreactors to confine the crystal growth. To obtain the desired materials, one needs to prudently select the species of precursor and surfactants, and also set the other parameters such as temperature, pH value, and concentration of the reactants. As a result, developing surfactant-assisted systems are a trial-and-error based procedure which requires much effort to choose proper capping agents and reaction environment.

This route of synthesis was adopted by Q. Tang et al. [77] to prepare yttrium hydroxide and oxide nanotubes in the presence of poly-ethylene glycol (PEG); by morphology and FTIR studies they proposed the coordination of PEG molecules to yttrium ions. The oxide phase was obtained during the subsequent calcination.

The most important work related with use of organic molecules in the synthesis of lanthanides hydroxide and oxide nanotubes was reported by M. Yada et al. [78] because of the excellent homogeneity and small size of these tubular structures (~6 nm in diameter). They described the synthesis of rare earth oxide nanotubes (M_2O_3, M= Er, Tm, Yb and Lu) templated by dodecylsulfate assemblies, realized by homogeneous precipitation with urea and

their conversion into a hollow nanotube with an inner diameter of 3 nm after anionic exchange of the surfactant with acetate ions. These lanthanide oxide nanotubes have 6 nm of outer diameter and 1 nm of wall thickness. The specific surface area of 266 m^2g^{-1} for the anion-exchanged form was in close agreement with 256 m^2g^{-1} for the as-prepared one. In reference [79], hierarchical two and three dimensional microstructures composed of rare-earth compound nanotubes were reported. In the presence of SO_4^{2-} (or $H_2PO_2^-$, F^-, HPO_3 and SiO_3^{2-}) it was synthesized as follows: urea, $Yb(NO_3)_3$, Na_2SO_4 and H_2O were mixed in a molar ratio of 1:2:10:1000 and then reacted at 80 ºC for 40 h whilst vigorously stirred. Inspection of the solid obtained indicated the presence of single and double-walled nanotubes with outer diameter of 10-30 nm and a length of several hundred nanometers. The FTIR and X-ray microanalysis indicated that SO_4^{2-} anions are incorporated into the solids. For films preparation, a quartz board and a poly(ethylene terephthalate) film were dipped vertically in a reaction solution and the synthesis of nanotubes was performed without stirring in the presence of SO_4^{2-} ; a precipitate was observed on the substrates. These precipitates were found to be composed of nanotubes, Figure 2.9.

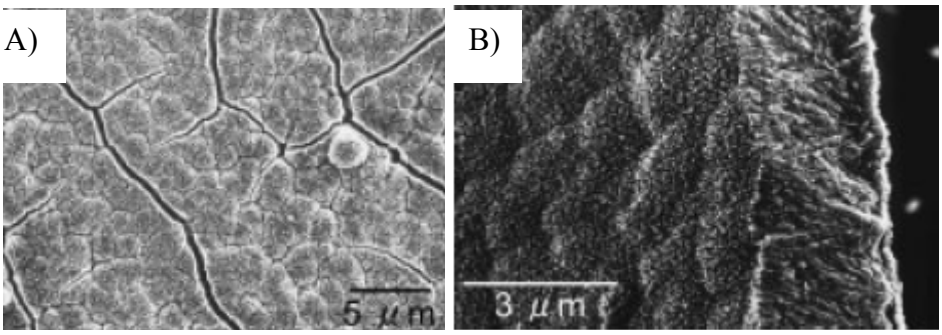

Figure 2.9 – SEM images of the microstructures composed of ytterbium oxide nanotubes formed on the quartz board: A) thin film and B) cross section of the film [79].

2.2.1.5 – Molten salt

Molten salt synthesis is often used to obtain ceramic powders. Molten salts are used as a reaction aid to prepare complex oxides from their constituent oxides. Particulate materials with shape anisotropy are prepared by this technique and used as starting materials for grain-oriented ceramics.

X. Wang *et al* [81] reported the preparation of Pr_6O_{11} nanotubes, via molten salt route, by mixing the Pr_6O_{11}bulk with NaCl followed by calcination at 840 ºC during 3 h. The solidified NaCl-Pr_6O_{11} products obtained were immersed into fresh water for about ten hours to remove NaCl from the Pr_6O_{11} material, during which fresh water was constantly replaced.

The authors discussed the nanotubes formation and thermal stability as a role of the presence of defect clusters such Pr_4O_6. This defect cluster involves the vacant Pr tetrahedron and its six edge-bridging oxygen atoms and is created when an oxygen atom is extracted from the parent fluorite structure PrO_2, which results in two types of Pr cations in the Pr_6O_{11} species: Pr cations participating in the Pr_4O_6 vacancy cluster and those without an oxygen vacancy in their coordination sphere. The result of the cation lattice relaxation is that the intracluster Pr-Pr distances have an average of 4.1 Å, while the intercluster Pr-Pr distances are about 0.4 Å shorter. In other words, the Pr^{3+} ions are crowded into the region between the defect clusters. On the other hand, the dominant chemical force in the rare-earth oxides is ionic in nature, and the electrostatic repulsion between the defect clusters tends to separate them, which may provide the possibility for the exfoliation process of Pr_6O_{11} single-molecule layers from the bulk. By HRTEM images and electron difraction the obtained Pr_6O_{11} nanotubes would grow along $[1\bar{1}0]$ axis. However the esfoliation take place for instance when at 840 °C (the melting point of NaCl is about 808 °C) NaCl will melt and ionize into Na^+ and Cl^- ions, which can attack the crowded $[Pr_x^{3+}O_y^{2-}]^{z-}$ anion and the positively charged $[Pr_4O_6]^{4+}$ vacancy cluster along all directions, so that combinations between layers can be loosened to some extent. Since the interaction between [111] layers is the weakest, exfoliation can occur first along the [111] planes, which can be then stabilized by the high viscosity of the NaCl flux and may lead to the formation of these nanotubes.

2.3 – Applications

Although most research conducted on Ln^{3+} oxide or hydroxide nanotubes has been of a fundamental nature, there is much interest on their potential applications. For example, they have already proven to be extremely stable and resistant in ambient environment and they also rank among the best nano-emitters that are now available. Next, I summarize some of their applications.

2.3.1 – Biomedical applications

Emissive europium hydroxide nanorods (20 nm × 500 nm) functionalized by a surface coating of chromophore containing organically modified silicate (ORMOSIL) layer, have been synthesized and characterized by high-resolution transmission electron microscopy (TEM) [108], Figure 2.10. Low-temperature photophysical characterization of the functionalized nanorods (FENR) demonstrated a strong red $^5D_0$ luminescence both in the solid and in water suspension.

The enhancement of $^5D_0$ emission bands under 390 nm excitation of the functionalised nanorods compared to that of the pristine nanorods was attributed to the energy transfer from the antenna chromophores of the surface functionalized ORMOSIL coating to the Eu^{3+} in the nanorods, Figure 2.11. Furthermore, a larger quantum yield (functionalised nanorods: 0.11; pristine: 0.02) and longer lifetime (functionalised: 1.97 ms; pristine: 0.56 ms) are observed in the solid-state with the same excitation at 390 nm.

The potential of this functionalised nanorods material for live cell imaging has also been assessed. Both the bare and functionalized nanorods are able to enter living human cells with no discernible cytotoxicity. Chromophore-to-Eu^{3+} energy-transfer in the functionalized nanorods enable staining of the cytoplasm of living human cells. This is confirmed by co-staining with fluorescent dextran: the localization of functionalised nanorods was examined with green staining by this commerial cytoplasm marker (fluorescent dextrans Alexa Fluoro 488) with excitation at 488 nm, at which Eu^{3+} cannot be directly excited. The areas presenting red emissrion from Eu^{3+} ions of the functionalised nanorods matched with those areas presenting green emission from the fluorescent dextran marker.

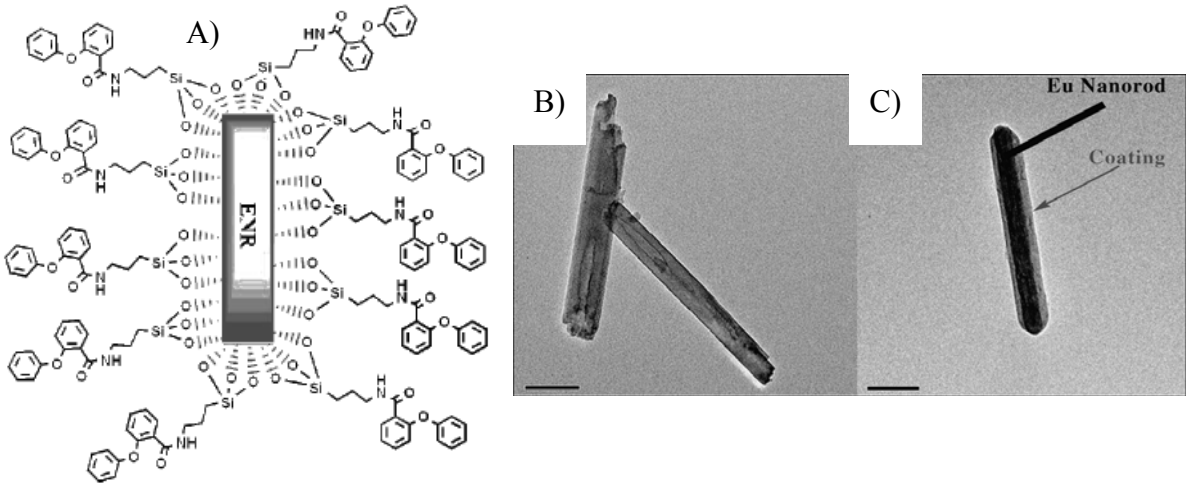

Figure 2.10- A) Surface functionalisation of europium hydroxide nanorods (ENR) with chromophore (methyl phenoxybenzoate)-ORMOSIL coating, B) TEM image of the hydrothermally synthesized ENR (bar) 100 nm); and C) ENR functionalized by an ORMOSIL coating (bar) 50 nm) [108].

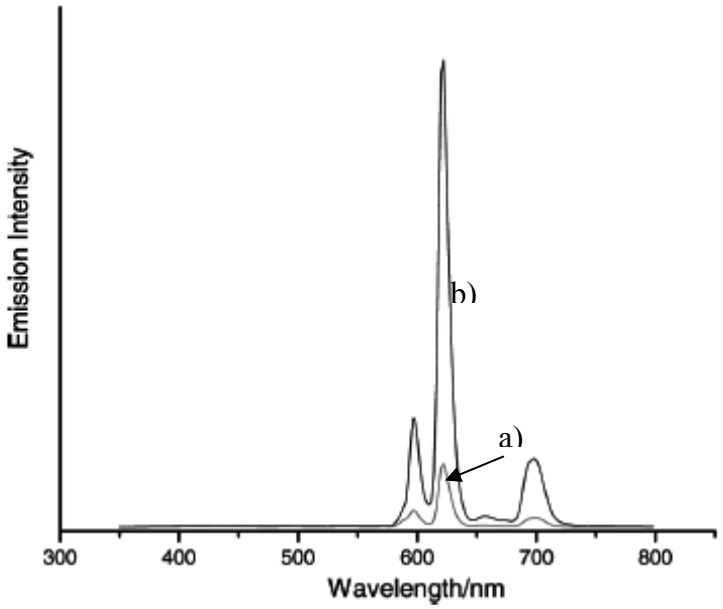

Figure 2.11 – Enhancement of the red $^5D_0$ emission from the europium nanorods (line a) by surface functionalization by sol-gel silica with chemically bound chromophores (line b) (λ_{ex} = 390 nm).

Internalization of the bare and functionalized europium nanorods in human lung carcinoma A549 and Hela cells was studied at the nanorod loading of 10 μg ml-1 over an exposure period from 30 min to 24 h. Cells loaded with these two types of nanorods were excited at 390 and 457.9 nm. For the europium hydroxide nanorods, pale-red luminescence areas were observable in the cytoplasm of a small number of cells after 2 h of exposure. After further 2 h, more cells were found to give pale-red luminescence in the cytoplasm and especially around the nucleus. At an exposure time of up to 6 h, red luminescence was observed around the nucleus of most of the cells. No emission was observed inside cells that were exposed to comparable concentrations of commercial $EuCl_3$ or Eu_2O_3 as controls.

The red chromophore-sensitized luminescence from the internalized nanorods in live human lung carcinoma cells (A549) can be observed by confocal microscopy 2 h after loading and reaches maximal emission after 24 h.

2.3.2 –Optical thermometry

Rare earth doped fluorescent materials have been used as temperature sensors because their absorption and emission properties are temperature dependent. Luminescence intensity ratio based method has the ability to cover a wide range (−196 to 1350 °C) with reasonable measurement resolution. Though the rare earth doped bulk materials for temperature measurements have been discussed by several authors using luminescence intensity ratio

technique [109], the current interest in this is to re-investigate the materials in light of nano-size and its interesting behavior. Nano-sized materials have shown promising properties that are different from their bulk counter parts and led to the 'miniaturization' of tools. Rare earth doped nanocrystalline materials can be used as the temperature sensor in many areas where electrical methods are unpractical such as in biology, optical telecommunications, etc.

Singh *et al.* [110] reported $Gd_2O_3:Yb^{3+}/Er^{3+}$ nanocrystalline phosphor, the intensities of the upconversion fluorescence bands were recorded at different temperatures. It was found that the intensities of all bands decrease with increasing temperatures, however the intensity ratio between the transitions $^2H_{11}\rightarrow{}^4I1_{5/2}$ and $^4S_{3/2}\rightarrow{}^4I1_{5/2}$ increases with the increasing temperature (300 K$\rightarrow$900 K), Figure 2.12, because the energy separation between $^2H_{11}$ and $^4S_{3/2}$ is very small (~ 700 cm^{-1}) and they are thermally coupled each other.

The intensities of the upconversion fluorescence bands were recorded at different temperatures keeping other conditions constant. It was found that the intensities of all the bands decrease with increasing temperature. This could be understood easily from the expression:

$$N(t) = N(0)\exp(-t/\tau) \qquad (2.1)$$

where N(t) is the population in the level at the temperature t and τ is the lifetime of the state.

The inverse of the τ is equal to the sum of the radiative emission rate (R) and the nonradiative relaxation rate (NR). The NR relaxation depends on temperature and therefore in the steady state regime of the excitation and fluorescence detection, the average intensity can be written as:

$$\langle I\rangle = N_i(0)\,\tau_i\,(t)\,\upsilon i\,P_i^r \qquad (2.2)$$

where υ_i is the emission frequency and P_i^r is the spontaneous (radiative) emission rates.

As the temperature increases the value of τ decreases due to the increase of the NR and so a decrease in R. Thus when the temperature increases fluorescence intensity decreases.

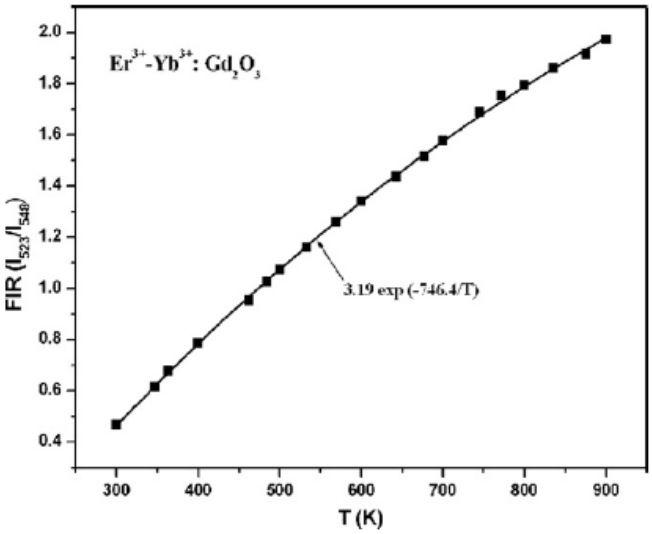

Figure 2.12 – Intensity ratio of green upconversion emissions at 523 and 548 nm relative to the absolute temperature

L. Yang *et al.* [111] reported nonlinear blue upconversion luminescence of Gd_2O_3: Er^{3+}/Yb^{3+} nanowires due to thermalisation effects arising from the laser heating. According to the ratio of $^2H_{11/2}\rightarrow{}^4I_{15/2}$ to $^4S_{3/2}\rightarrow{}^4I_{15/2}$ emission intensity, the temperature of the sample exposed to radiation of 978-nm laser is given, Figure 2.13. A variation from 326 to 422 K was obtained when the laser power increases from 0.2 to 1.2 W. The authors also discussed in detail the processes involved in the upconversion and reported that two 978 nm photons were absorbed in turn in the upconversion luminescence mechanism responsible for populating the $^2H_{11/2}$, $^4S_{3/2}$,$^4F_{9/2}$ and $^2H_{9/2}$ energy levels.

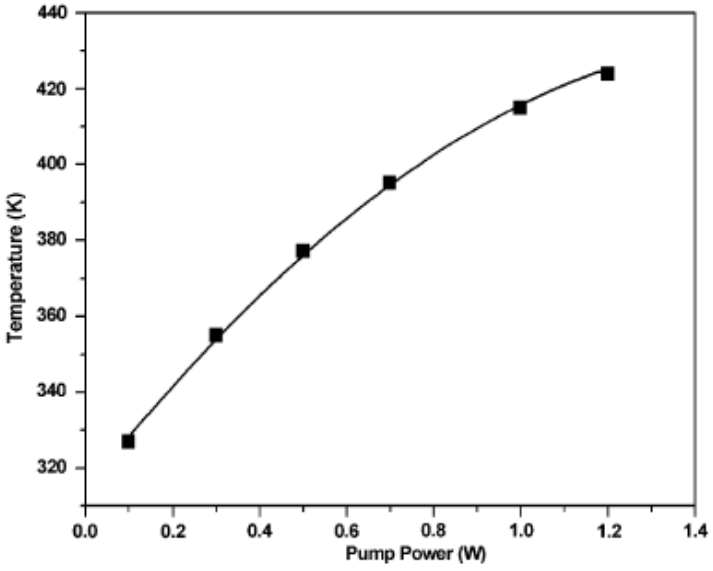

Figure 2.13 - The dependence of sample temperature on pump power estimated from the ratio of $^2H_{11/2}\rightarrow{}^4I_{15/2}$ emission intensity to $^4S_{3/2}\rightarrow{}^4I_{15/2}$ emission intensity [111].

2.3.3 – AFM/SNOM tips

The use of the light-emission features of lanthanide ions is particularly attractive for real-time and on-line sensing or screening applications (even unique as both fluorescent donors and acceptors in FRET experiments) because these ions possess long excited-state lifetimes (10^{-5}–10^{-3} s) and emit in the visible and near-infrared regions with characteristic quasi-atomic narrow lines and strong Stokes shifts. Surprisingly, there are few reports describing the functionalization of AFM tips with lanthanide ions (sub micrometre Er^{3+}/Yb^{3+}-codoped fluoride glass particle glued through a UV polymerized polymer to the end of the tip) and their subsequent use as ANSOM probes [112]. Additionally, these tips were used to acquire images of surface plasmon polaritons (SPP), as well the radiative and evanescent field components (REC), from light transmitted from subwavelength apertures in metallic films [113].

A. Cuche *et al.* [114] prepared SNOM tips with $Y_3Al_5O_{12}:Ce^{3+}$ (YAG matrix doped with cerium atoms in substitution of yttrium ions) via Low Energy Cluster Beam Deposition (LECBD) of YAG:Eu^{3+} target. These clusters do not cover homogenously the tip surface but they aggregate locally under the shape of thin wires, the first clusters deposited on the rough aluminium surface playing the role of nucleation centres. The possibility of working with very small emitting volumes of a stable temporal behaviour makes possible to use these oxide nanoparticles as light sources for active tips. To validate YAG:Ce^{3+} coated tips as active optical tips, NSOM imaging was performed in the transmission mode by using the light emitted in the spectral range of ~ 550 nm over gold discs of 400 nm in diameter deposited over glass substrate, see Figure 2.14.

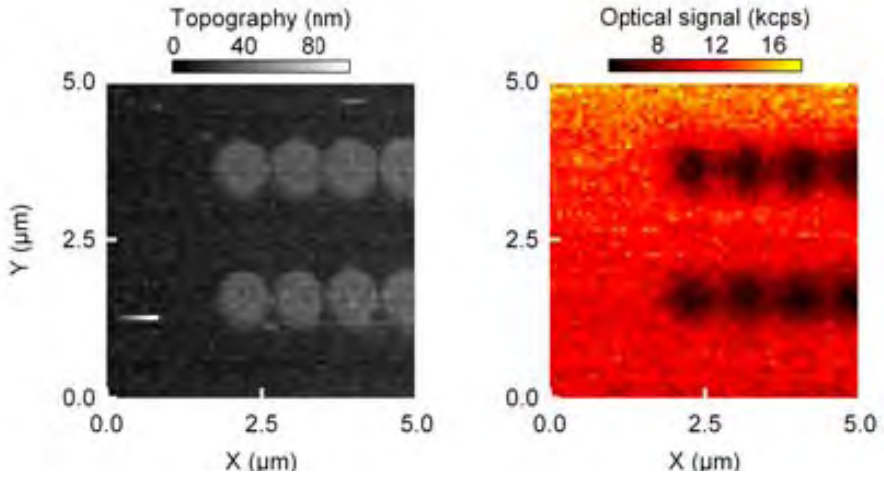

Figure 2.14 - Topography (numerically flattened) and near-field optical images of gold circles (400 nm diameter) on a fused silica cover slip, with a tip functionalized with oxide nanoparticles [114].

2.3.4 –Sensors

Ceria nanowires were used in a humidity sensor [115], Figure 2.15A-B. The sensing properties are controlled by ion-type conductivity. Both the response and recovery times are about 3 s, this fast recovery was explained due the absence of pores, usually the water molecules remain condensed inside pores resulting in higher recovery times. These humidity sensors were fabricated by depositing the CeO_2 nanowires on interdigital electrodes, the fabrication process is described in three steps: (1) the CeO_2 nanowires were dispersed in ethanol by magnetic and ultrasonic stirring; (2) the mixed solution of CeO_2 nanowires was dropped onto interdigital electrodes (3 mm ×3 mm× 0.5 mm); (3) the humidity sensors were annealed at 420 °C for 5 min.

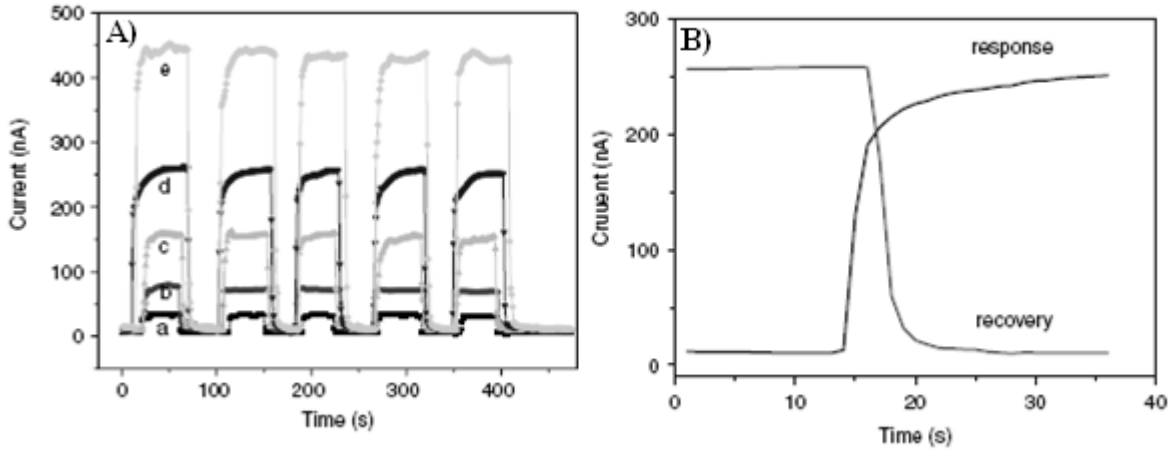

Figure 2.15 – A) Characteristics of the humidity sensor at different humidities at V = 1 V (curve a: 33% RH; curve b: 54% RH; curve c: 75% RH; curve d: 85% RH; and curve e: 97% RH). B) Response and recovery of the humidity sensors of the CeO_2 nanowires.

Humidity sensing is related to a water-adsorption process. Initially, water vapour is chemisorbed on the surface of the CeO_2 nanowires, and then hydroxyl groups can be formed at the surface. In this case, proton transfer occurs among the hydronium ions (H_3O^+). The electrical response depends on the number of water molecules adsorbed on the sensor surface. Usually, there is one monolayer of water of covering at around 20% relative humidity (RH)[1], and more layers at even higher humidity. Further physisorbed layers are formed with increasing humidity. H_3O^+ appears in the physisorbed water and serves as a charge carrier.

The H^+ ions can move freely in the physisorbed water according to the Grotthuss's chain reaction by which an 'excess' proton or protonic defect diffuses through the hydrogen bond network of water molecules or other hydrogen-bonded liquids through the

[1] The relative humidity of an air-water mixture is defined as the ratio of the partial pressure of water vapor in the mixture to the saturated vapor pressure of water at a prescribed temperature.

formation/cleavage of covalent bonds [116]. Electrolytic conduction takes the place of protonic conduction at high humidity. This is further confirmed from the characteristics of the resistance versus relative humidity of the humidity sensoring. The resistance decreases exponentially with increasing humidity, implying ion-type conductivity as the humidity-sensing mechanism.

Columnar ceria based sensors for detection of gaseous ethanol and nitrogen dioxide were also reported [117].

2.3.5 –Catalysis

CeO_2 finds an application as a component in a variety of catalytic systems. The redox properties of ceria (Ce^{4+}/Ce^{3+}) and the high stability of its lattice oxygen are among the most important factors that contribute to the catalytic reactivity in oxidation reactions [118]. Effective utilization of ethylbenzene, available in the xylene stream of the petrochemical industry to more value added products is a promising one in chemical industry. The oxidation products of ethylbenzene are widely employed as intermediates in organic, steroid and resin synthesis. Activity of the catalysts towards liquid phase oxidation of ethylbenzene is also investigated and correlated with different vanadia species on the supported catalysts. The main product obtained was acetophenone. Ceria nanotubes present higher surface area and Ce^{3+}/Ce^{4+} redox that allow its use as catalysts. Tubular shape also allows their use as catalysts nanoparticles support in the inner or outer regions.

L. G. Rovira *et al* [101] reported CeO_2 nanotubes prepared using porous AAO template by electrochemical depositon and their use in CO conversion. The kinetic mechanisms reported for this reaction consider that both the metallic phase and the support play a role in the activation of the CO oxidation. If so, the detailed features of the support structure would be expected to influence the catalytic behavior of these metal/ CeO_2 systems. Therefore, it should be feasible that CeO_2 nanotubes such as those prepared here could show an improved behavior in this catalytic application. Measurements of the catalytic activity of calcined CeO_2 nanotubes within the AAO membrane in the CO oxidation reaction were carried out. Their results obtained in these experiments are presented in Figure 2.16 as a light-off curve.

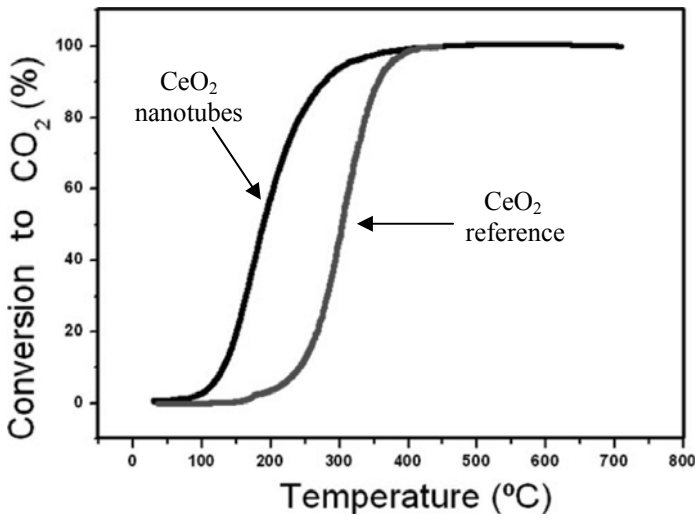

Figure 2.16 - Light-off curve corresponding to CeO_2-NT/AAO and owder CeO_2. Experimental conditions: amount of ceria sample, 10 mg total; flow rate, 100 cm^3 min^{-1}; reaction mixture, 1% CO + 20% O_2 + He balance. Powder CeO_2 was diluted with crushed quartz. [101].

In these curves, the conversion of CO is represented as a function of the reaction temperature. These curves provide qualitative information about the catalytic behavior of the studied material. The so-called light-off temperature (LOT), which is the temperature at which 50% of conversion is reached, is usually employed as an activity evaluation parameter. In brief, the lower the value of this LOT, the better is the catalytic activity of the tested material. Figure 2.16 includes the light-off curve of a powder CeO_2 sample, used as a reference, with 42 m^2 g^{-1} of BET surface area, a value in the same order of magnitude as that corresponding to the CeO_2-NT/AAO system tested in this work, 20 m^2g^{-1}. The LOT observed with the CeO_2-NT/AAO prepared here is 189 °C, while in the case of the conventional powder oxide this temperature is 300 °C. Powder CeO_2 shows negligible activity at temperatures below 200 °C, whereas the nanotube sample prepared here reaches a conversion close to 60% at this temperature. These results confirm that the CeO_2 nanotubes show a much improved catalytic performance. A comparison of the reaction rates observed with the two materials at the same temperature allows a more accurate quantification of the differences in the catalytic performance of the two materials. The catalytic activity values observed at moderate temperature, i.e., 200 °C, are the following (per gram of oxide): 77.2 × 10^{-2} cm^3 CO_2 $(STP)^2/(g{\cdot}s)$ for the CeO_2-NT/ AAO and 0.16 × 10^{-2} cm^3 CO_2 (STP)/(g·s) for the powder CeO_2 oxide. These values indicate that the redox activity of the exposed CeO_2 surface of the

[2] STP - Standard Temperature and Pressure - is defined by IUPAC (International Union of Pure and Applied Chemistry) as air at 0ºC (273.15 K, 32 ºF) and 10^5 pascals (1 Pa = 10^{-6} N/mm^2 = 10^{-5} bar = 0.1020 kp/m^2 = 1.02x10^{-4} m H_2O = 9.869x10^{-6} atm = 1.45x10^{-4} psi (lbf/in^2))

nanotubes is much higher, more than 400 times that of a standard material. Other authors have obtained CeO_2 nanotubes with improved catalytic behavior in the oxidation of CO [89].

Chapter 3 - Effects of phonon confinement on anomalous thermalisation, energy transfer and upconversion in Ln^{3+}-doped Gd_2O_3 nanotubes

3.1– Introduction

Lanthanide containing compounds have been extensively utilized as high-performance phosphors in various devices based on the electronic, optical, and chemical properties of 4*f* electrons [66-69]. Ln^{3+} hydroxide and oxide (Ln=Ce, Pr, Nd, Sm, Dy, Tb, Gd, Yb, Er) nanocrystals, Y_2O_3:Eu^{3+}/Y_2O_3 core-shell composites, Y_2O_3:Eu^{3+} and Gd_2O_3:Eu^{3+} nanotubes, and Gd_2O_3:Yb^{3+},Er^{3+} nanorods have received considerable attention [44,70-101] because they exhibit shape-specific and quantum-size effects [26-29,39-46,49,53,120].

Size-dependent quantum confinement reflects on the radiative and non-radiative electronic transitions in nanoparticles, and tuning the particles structure at the nanometer scale may result in novel optical properties for applications in three-dimensional displays [124,125], light-emitting devices [126] and bioassays [127,128]. Due to the confinement effect in Ln^{3+}-nanocrystals, the PDS becomes discrete, with a cut off on the low-energy side [40-42,46]. Because the low-frequency phonons contribute most effectively to the non-radiative relaxation between closely spaced Stark levels, the lack of these low-frequency modes modifies considerably the Ln^{3+} emission dynamics, relatively to that of bulk materials.

Up to now, anomalous thermalisation due to the absence of low-frequency phonon modes (nanoconfinement effects) has been reported only for a few Ln^{3+}-nanocrystals [40-44,46,49]. In 1998 Tissue *et al.* noticed the presence of broad $^7F_1 \rightarrow {}^5D_1$ hot bands in the excitation spectra of 4-6 nm Eu_2O_3 particles at 12 K. A large increase in the intensity of these hot bands, relatively to the normal excitation lines, was measured for particle size from 12 down to 4 nm [49]. Later, Liu *et al.* reported hot bands of the $^4I_{15/2} \rightarrow {}^4F_{7/2}$ transition (with energies up to 200 cm^{-1} higher than the energy of the zero-phonon line) in the excitation spectra of Y_2O_2S:Er^{3+} nanocrystals (20-40 nm) below 7 K [40,42]. The direct phonon relaxation between the Stark levels of the $^4I_{15/2}$ ground term is restricted due to the lack of low-energy modes and, consequently, the intensity of the hot bands originating from the upper

$^4I_{15/2}$ crystal field levels increases suddenly as temperature decreases below 7 K [41,42]. This interpretation was extended to the above-mentioned anomalous hot bands in Eu_2O_3 particles [46]. Recently, Mercier *et al.* [43] and Liu *et al.* [44] provide experimental evidence of, respectively, anomalous thermalisation in Gd_2O_3:Eu^{3+} nanoparticles and Gd_2O_3:Eu^{3+} nanotubes. Hot bands originating from the lowest $^7F_1$ Stark level, with energy of 217 cm^{-1}, were observed in the excitation spectrum below 50 K. Both groups interpreted this anomalous thermalisation effect in terms of phonon confinement. In 2003, Liu *et al.* [42] suggested that the phonon-confinement effects in Ln^{3+}-containing nanocrystals may further impact on the phonon-assisted energy transfer and upconversion processes.

Herein, I wish to describe the photoluminescence features of Eu^{3+} in Gd_2O_3 nanotubes (0.16, 1.00, 3.30 and 6.60% Eu^{3+} mole content) and nanorods (3.30%) and of Er^{3+} in Yb^{3+},Er^{3+} co-doped Gd_2O_3 nanotubes (5.00% Yb^{3+}, 1.20% Er^{3+} mole content) synthesised using different annealing conditions (Appendix A1). The nanotubes exhibit a remarkable anomalous thermalisation effect (described in chapter 1, item 1.2.2), one order of magnitude larger than that previously reported for similar Gd_2O_3:Eu^{3+} (3.96%) nanotubes [44], which strongly depends on the thermal history and Ln^{3+} content. At 10 K, the Gd_2O_3:Eu^{3+} nanotubes display a unique energy transfer from Eu^{3+} C_2 to S_6 crystallographic sites, while the Gd_2O_3 nanotubes co-doped with Yb^{3+},Er^{3+} exhibit the unexpected $^2H_{11/2}\rightarrow{}^5I_{15/2}$ upconversion green emission.

This chapter is organized in the following way:

a) We start by presenting structural and magnetic data of Gd_2O_3:Eu^{3+} and Gd_2O_3:Yb^{3+},Er^{3+} nanotubes (with the C_2 and S_6 crystallographic Ln^{3+} sites) and its emission, excitation and decay time features, as a function of temperature (11-300 K). For the Gd_2O_3:Eu^{3+} nanotubes the influence of the morphology and annealing conditions on the absolute quantum yields, decay time and $Eu^{3+}(S_6)$-to-$Eu^{3+}(C_2)$ and Gd^{3+}-to-Eu^{3+} (both C_2 and S_6) energy-transfer rates are also addressed.

b) Secondly, the temperature-dependence of the intensity of the $^7F_1\rightarrow{}^5D_1$ and $^2H_{11/2}\rightarrow{}^5I_{15/2}$ transitions is studied as a function of the annealing conditions and Eu^{3+} or Yb^{3+},Er^{3+} contents, respectively.

c) Finally, we demonstrate that this anomalous thermalisation effect induces the unexpected presence, at 10 K, of both, $Eu^{3+}(C_2)\rightarrow Eu^{3+}(S_6)$ energy transfer (Gd_2O_3:Eu^{3+}) and $^2H_{11/2}\rightarrow{}^5I_{15/2}$ upconversion emission (Gd_2O_3:Yb^{3+},Er^{3+}), and may could be rationalised on the basis of the size-dependent discretization of the PDOS.

3.2 – $Gd_2O_3:Eu^{3+}$ and $Gd_2O_3:Yb^{3+},Er^{3+}$ nanotubes

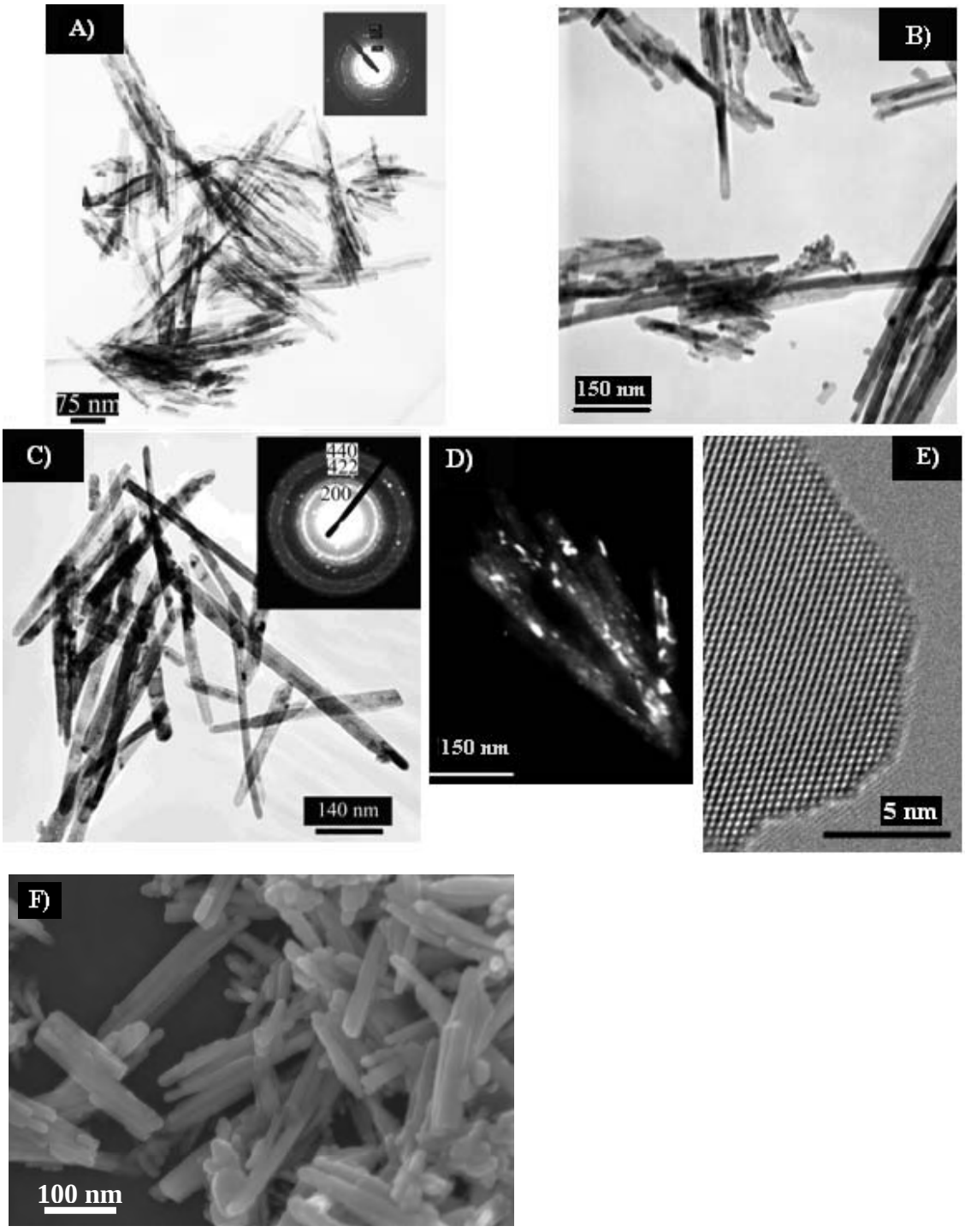

Figure 3.1– TEM images of $Gd_2O_3:Eu^{3+}$. A) Nanotubes (3.30%), annealed at 500 ºC for 1 h. B) Nanotubes (3.30%), annealed at 700 ºC for 3 h. C) Nanorods (3.30%), annealed at 700 ºC for 3 h. D) Dark field image of nanotubes showing nanocrystallites (*ca.* 10 nm), E) HRTEM of nanotubes (3.30%), annealed at 700 ºC for 3 h and F) SEM image of $Gd_2O_3:Yb^{3+},Er^{3+}$.

Transmission electron microscopy (TEM) images (Figure 3.1A-B) show regular cylindrical $Gd_2O_3:Eu^{3+}$ nanotubes with 100–180 nm in length (some even longer) and

diameters of 5-25 nm (Figure 3.2A-B). The structure is cubic, as shown by the electron diffraction pattern (inset in Figure 3.1A). The nanotubes are polycrystalline, as revealed by the dark field images (Figure 3.1D), with nanocrystallites of lateral dimension *ca.* 10 nm (using powder XRD data and the Scherrer equation, it was found that all nanotubes studied have similar sizes, Figure 3.3). The thickness of the nanotubes wall is 5–10 nm. The mean length and diameter (Figure 3.2), of the $Gd_2O_3:Eu^{3+}$ nanorods shown in C are much less well defined but tend to be larger than those of the nanotubes in Figure 3.1A-B. The morphology of the $Gd_2O_3:Yb^{3+},Er^{3+}$ nanotubes is similar, Figure 3.1F.

Powder X-ray diffraction (XRD) patterns of the as-prepared $Gd_2O_3:Eu^{3+}$ (or Yb^{3+},Er^{3+}) were indexed to a pure hexagonal $Gd(OH)_3$ structure (PDF 83-2037), while the patterns of the annealed samples are characteristic of the Gd_2O_3 cubic phase [131]. The cubic cell lattice parameter (*a)* is 10.81944 Å (nanotubes), 10.81692 Å (nanorods) and 10.8162 Å (microcrystals). No lattice parameter change was detected due to different annealing conditions or aging time. Considering the Gd^{3+} first coordination sphere, the gadolinium oxide has a bixbyite structure $Ia\bar{3}$ with two crystallographically unique cation sites, in C_2 (non centrosymmetric) and S_6 (centrosymmetric) local symmetry, on a 3:1 population ratio. Minor interstitial sites may occur [132].

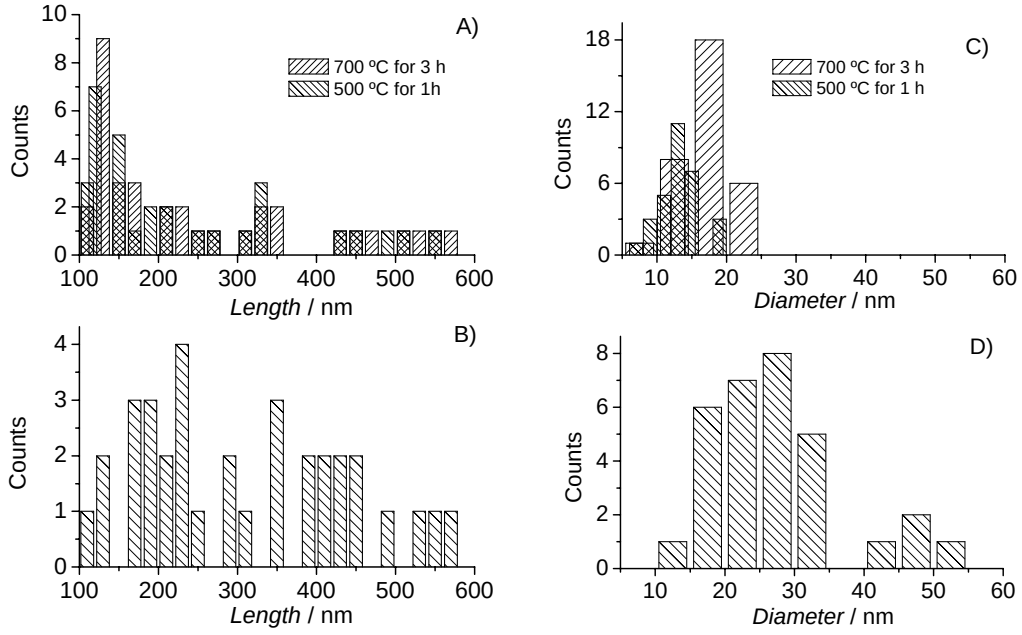

Figure 3.2 - Average length and diameter distribution of $Gd_2O_3:Eu^{3+}$ nanotubes (3.30%) annealed at 700 ºC for 3 h and 500 ºC for 1 h (A and C) and nanorods (3.30%) annealed at 700 ºC for 3 h (B and D).

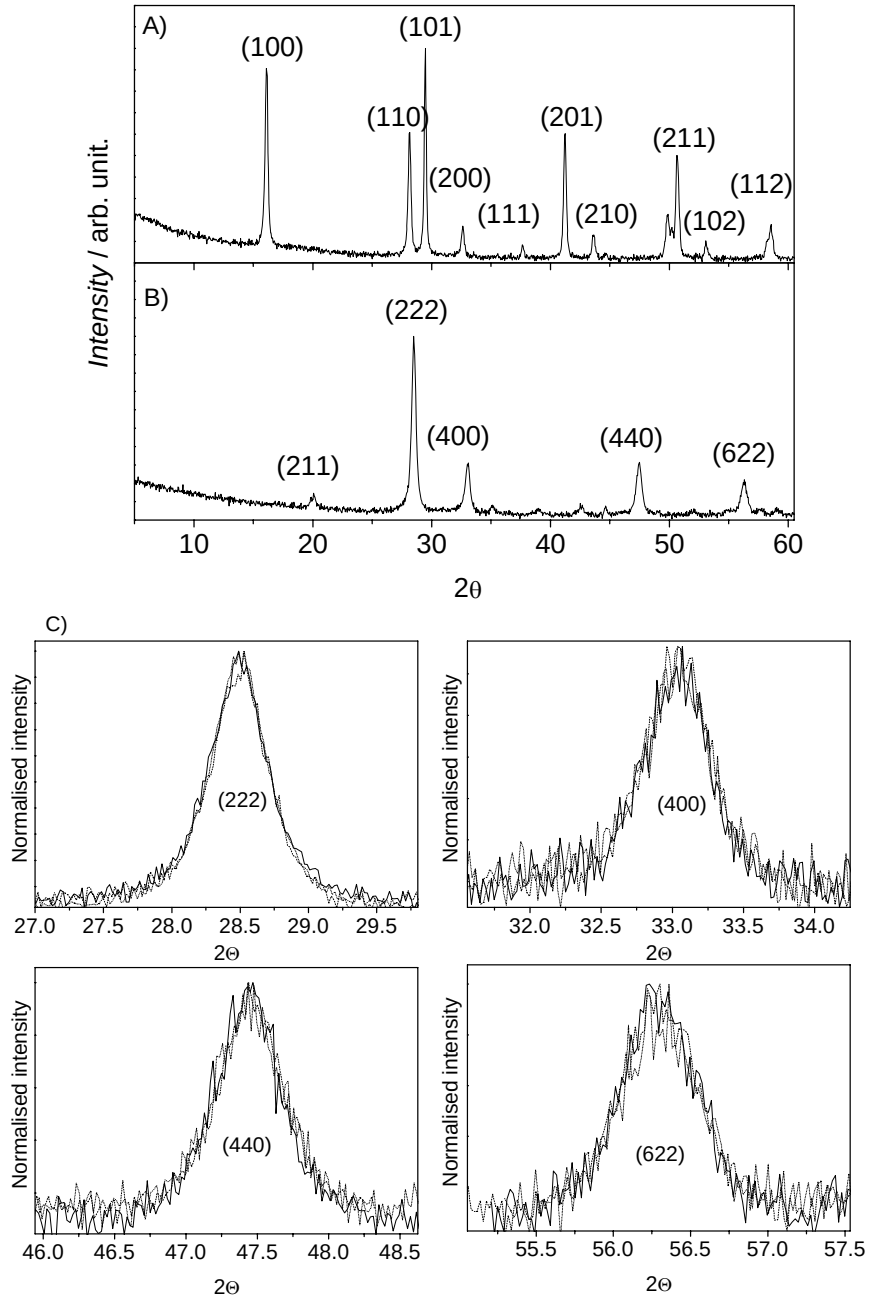

Figure 3.3 - Typical XRD patterns from A) $Gd(OH)_3:Eu^{3+}$ (or $Gd(OH)_3:Yb^{3+},Er^{3+}$) as obtained sample and B) $Gd_2O_3:Eu^{3+}$ (or Gd_2O_3: Yb^{3+},Er^{3+}) obtained after thermal treatment of hydroxide sample and C) Selected reflections of $Gd_2O_3:Eu^{3+}$ nanotubes (3.30%): fresh annealed at 700 ºC for 3 h (solid) and 650 ºC for 3 h (dashed) and annealed at 700 ºC for 3 h and aged for 60 days (dotted line).

In chapter 2 the symmetries of the two lattice cation sites were discussed. The 24*d* site is non centrosymmetric (C_2 symmetry), while the 8*b* site is centrosymmetric (S_6 or C_{3i}

symmetry). Due to different symmetries, 24*d* cations are expected to have spectroscopic signatures that are distinct from 8*b* cations.

Although the crystalline structure exhibits the same phase transitions under annealing, the nanocrystals display thermogravimetry curves with distinct dehydration dynamics when compared with the microcrystals, Figure 3.4. Around 8 % weight loss is observed between 326-362 ºC, at this point, the $Gd(OH)_3$ hexagonal structure loses one water molecule and rearranges in a monoclinic phase, $Gd(OH)_3 \rightarrow Gd(OOH)+H_2O$ [134-135]. Another mass loss stage is observed between 450-570 ºC. At this stage hydroxyl, nitrate and carbonate groups are eliminated, generating oxide (Gd_2O_3) from the hydroxide phase. For the nanocrystals (nanotubes and nanorods) complete monoclinic to cubic phase conversion require temperatures until 635 ºC.

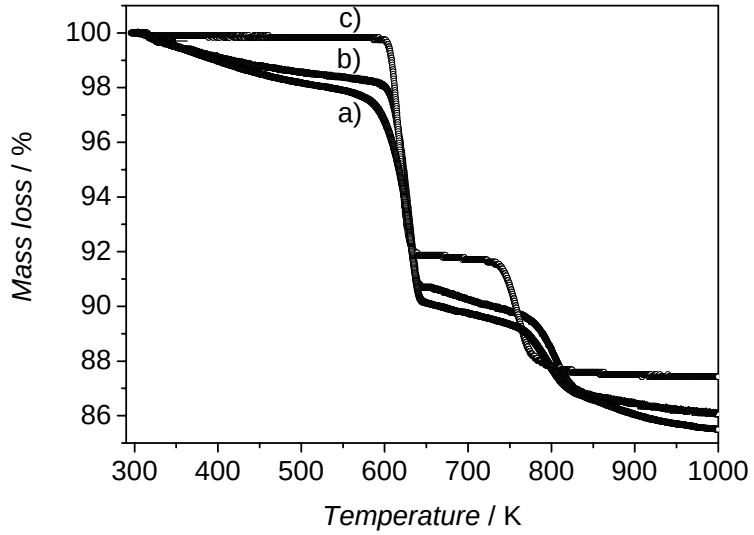

Figure 3.4– Thermogravimetry curves from the a) nanotubes (3.30%), b) nanorods (3.30%) and c) microcrystals (3.65%).

Elemental analysis revealed that Eu^{3+} ions incorporated at Gd_2O_3 host correspond to the concentrations (in units of mass %) of 0.16, 3.30 and 6.60 the nanotubes, and 3.30 in the nanorods and 3.65 in the microcrystal.While the Yb^{3+} Er^{3+}ions incorporated at Gd_2O_3 host correspond to the concentrations (in units of mass %) of 5.00 and 1.20.

The vibrational modes were probed trough Raman spectroscopy, all the modes observed in the microcrystal were also observed in the nanocrystals, but with reduced intensity, Figure 3.5.

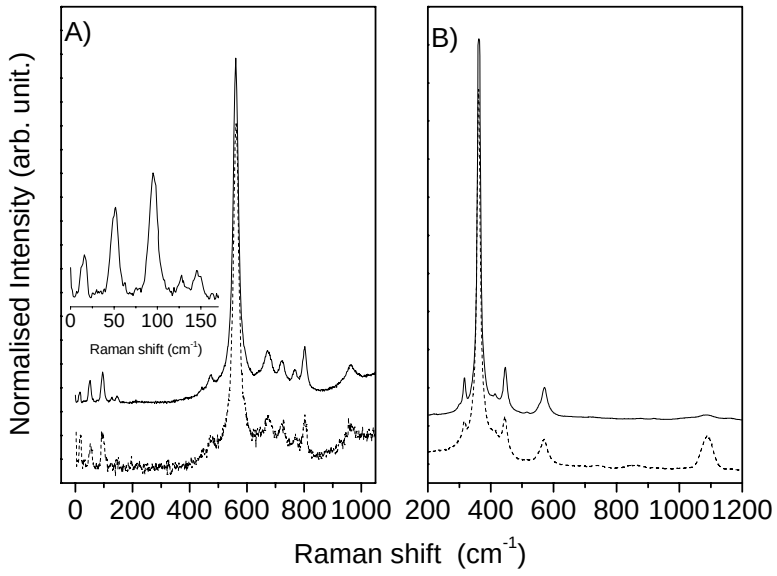

Figure 3.5- Room-temperature micro-Raman spectra of microcrystals (solid line) and nanotubes (dashed line) upon wavelength excitation at A) UV, 325 nm and B) green, 520 nm. All samples were calcined at 700 ºC by 3 h. Inset shows the magnification of the low frequency modes (0-170 cm^{-1} region).

DC magnetic susceptibility was measured as a function of temperature, Figure 3.6. From this result it is possible to extract the paramagnetic effective moment $p_{eff} = g\sqrt{J(J+1)}\,\mu_B$ and the paramagnetic Curie temperature θ_p. For example, the p_{eff} of the Gd_2O_3:Eu^{3+} nanotubes with 3.30% and annealing at 973 K during 3 h is 7.1±1 μ_B, lower than the theoretical value 7.8 μ_B (considering 3.30% of non-magnetic Eu^{3+} ions, J=0). Using polarized-neutron experiments to measure the temperature dependence of the susceptibility of the Gd^{3+} ions at the two different C_2 and S_6 sites in cubic Gd_2O_3, Moon and Koehler showed the formation of antiferromagnetic clusters of $Gd^{3+}(C_2)$ ions, reducing therefore the susceptibility of these ions [136,137]. The temperature dependence below 10 K of the magnetic susceptibility of the Gd^{3+} ions at both sites was explained considering the effects of short-range magnetic order (within those clusters) on the susceptibility of $Gd^{3+}(C_2)$ and $Gd^{3+}(S_6)$ ions. Thus, we consider cluster formation extended for a wide range of temperature a possible explanation for the reduction of the paramagnetic effective moment (see Ref. [136] for further details).

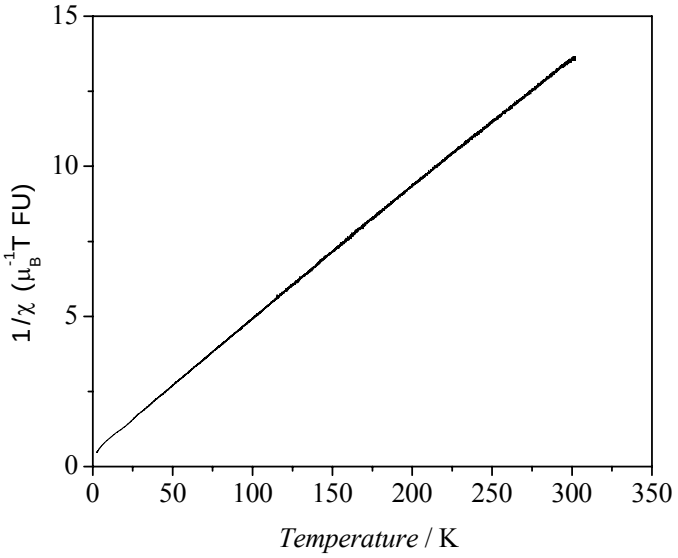

Figure 3.6 - Inverse DC magnetic susceptibility as a function of temperature

3.2.1 – Optical characterisation

3.2.1.1 – Photoluminescence (PL/PLE) of the $Gd_2O_3:Eu^{3+}$ nanotubes, nanorods and microcrystals

Figure 3.7 (curve a) shows the 11K emission spectrum of the $Gd_2O_3:Eu^{3+}$ microcrystals under UV excitation, displaying the typical Eu^{3+} $^5D_0 \rightarrow {}^7F_{0\text{-}4}$ transitions. Varying the excitation wavelength induces changes in the relative intensity of the Stark components, indicating the presence of more than one Eu^{3+} local environment. Moreover, 5 Stark components are observed for the $^5D_0 \rightarrow {}^7F_1$ transition, whose maximum allowed splitting is 3. In accordance with the structural data, the two Eu^{3+}-local environments are characterised by C_2 and S_6 local symmetry groups. The Eu^{3+} ions at S_6 local symmetry groups are localised in a centre of inversion, therefore, both the electrical dipole transitions and the $^5D_0 \rightarrow {}^7F_0$ transition are forbidden, being the emission essentially ascribed to the $^5D_0 \rightarrow {}^7F_1$ magnetic transition. For the Eu^{3+} ions with C_2 local symmetry group, it is expected that the $^5D_0 \rightarrow {}^7F_2$ electric-dipole transition dominates, typical of a distorted site with low symmetry. Therefore, based on the excitation wavelength dependence of the emission lines the corresponding assignment of the Stark components arising from the Eu^{3+} ions at S_6 and C_2 sites was performed. In particular, two excitation wavelengths 523.5 and 527.6 nm that favours the emission from the Eu^{3+} ions at S_6 and C_2 sites, respectively were used.

The emission dependence on the Eu^{3+} concentration was evaluated for the nanotubes with 0.16, 3.3 and 6.6 %. The major changes are observed in the $^5D_0 \rightarrow {}^7F_{0,1}$ transitions, as shown in Figure 3.7B where the contributions from Eu^{3+} (S_6) and Eu^{3+} (C_2) are clearly identified. Increasing the Eu^{3+} concentration induces a decrease in the intensity ratio between the Eu^{3+} (S_6) and Eu^{3+} (C_2) emission lines. This observation indicates an increasing rate of energy transfer on increasing the concentration [139]. We will return to this point latter.

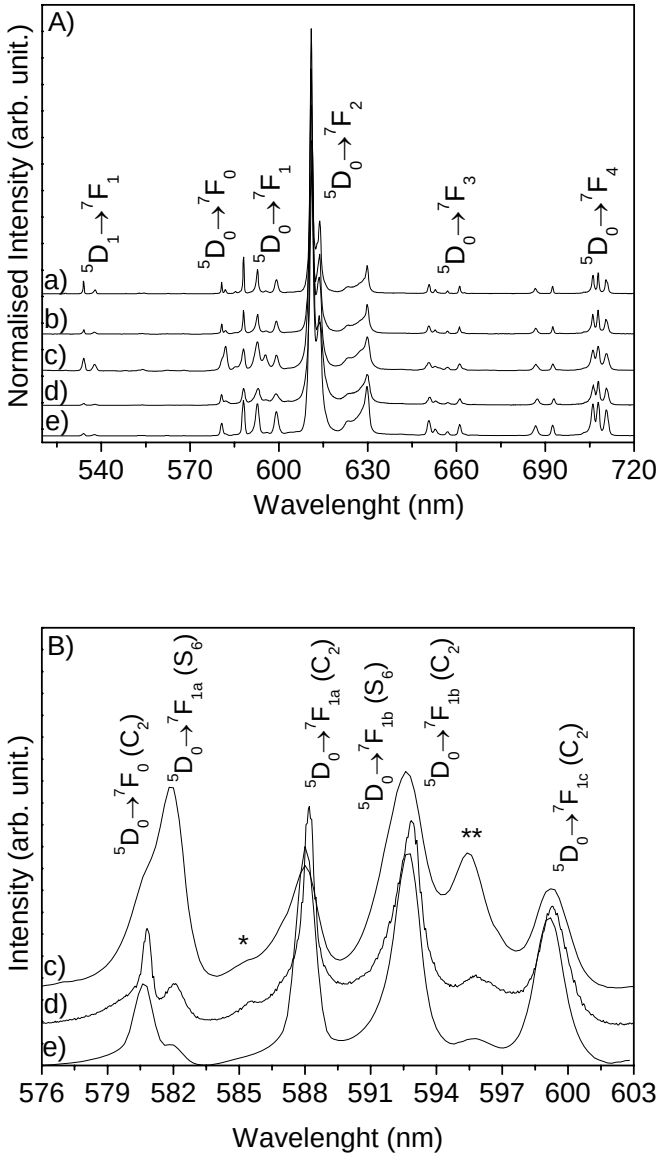

Figure 3.7 - A) Emission spectra (11 K) of Gd_2O_3:Eu^{3+} microcrystals (3.65%) (a), nanorods (3.30 %) b), and nanotubes c) 0.16%, d) 3.30% and e) 6.65%, under 274.4 nm excitation and B) Magnification of $^5D_0 \rightarrow {}^7F_{0,1}$ spectral region .

Figure 3.8 shows a magnification of $^5D_0 \rightarrow {}^7F_{0,1}$ spectral region for the $Gd_2O_3:Eu^{3+}$ microcrystal (3.65 %) and the respective assignment of the emission lines from Eu^{3+} ions at S_6 and C_2 sites, based on the 523.5 and 527.6 nm excitation wavelength dependence that favours the emission from the Eu^{3+} ions at S_6 and C_2 sites, respectively. The two lines marked with asterisks in Figure 3.8, already identified by Hunt et al. [138] and Buijs *et a.l* [139], and also observed for the nanorods (not shown), are attributed to electron/phonon interaction caused from the coupling between the $^5D_0 \rightarrow {}^7F_{1a}(C_2)$ and $^5D_0 \rightarrow {}^7F_{1b}(S_6)$ transitions and vibracional modes. The line at 585.4 nm (*ca.* 78 cm^{-1}) is favoured by selective $Eu^{3+}(C_2)$ excitation, whereas the line at *ca.* 595.6 nm (*ca.* 106 cm^{-1}) is favoured by selective $Eu^{3+}(S_6)$ excitation. These two vibrational modes are observed in the FT-Raman spectrum, see the Figure 3.5A. These modes were observed both in the microcrystal and nanocrystals.

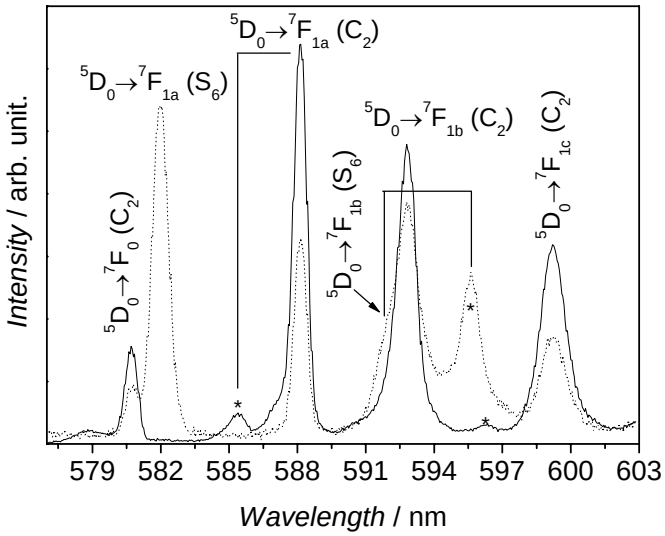

Figure 3.8 –Partial 11 K emission spectra recorded from the microcrystal (3.65%) upon wavelength excitation at 527.6 nm ($Eu^{3+}(C_2)$, solid line) and 523.5 nm ($Eu^{3+}(S_6)$, dotted line), sample calcined at 700 ºC for 3 h. Due to the very efficient $S_6 \rightarrow C_2$ energy transfer the vibronic component associated to the $^5D_0 \rightarrow {}^7F_{1b}(S_6)$ transition is faintly discerned at 596.4 nm in the C_2 emission spectrum.

For all the samples (microcrystals and nanocrystals) increasing the temperature up to 300 K, induces a blue-shift of the $^5D_0$ level from 17221 cm^{-1} to 17226 cm^{-1}, ascribed to the Eu^{3+} ions with C_2 local coordination group and no changes are observed for the emission arising from the Eu^{3+} ions at S_6 local symmetry, Figure 3.9. The theory of phonon induced

relaxation process has been extensively studied and the theory has recently extended to successfully explain the thermal behaviour of widths and positions of *4f* ions in crystal and the manifested effects of phonon perturbation on the optical spectra [140].

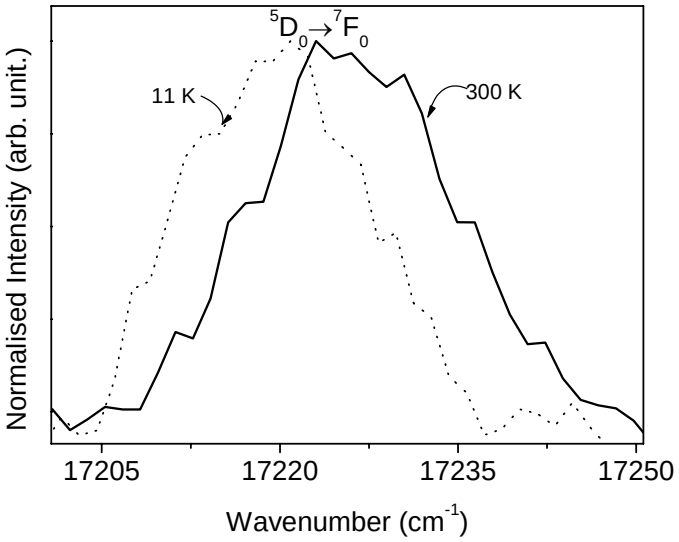

Figure 3.9 - Blue-shift of the $^5D_0$ level from 17220 cm^{-1} to 17226 cm^{-1}, ascribed to the Eu^{3+} ions with C_2 local coordination group, λ_{exc}= 527 nm (C_2).

The emission spectra of the Gd_2O_3:Eu^{3+} nanorods and nanotubes are identical to that of the microcrystal, apart from an increase in the emission full width at half maximum (fwhm). For instance, the fwhm value of the transition at 582 nm ($^5D_0 \rightarrow {}^7F_{1a}$ line of the Eu^{3+} at S_6 local symmetry) are 29.1 ± 0.4 cm^{-1} (nanotubes), 23.3 ± 0.9 cm^{-1} (nanorods) and 17.93 ± 0.3 cm^{-1} (microcrystal). We may suggest that this increase in the fwhm can be attributed to the reduced crystallinity degree and also to the presence of a superficial layer of the amorphous material in the nanocrystals.

Figure 3.10 shows the excitation spectra (11 K) of the Gd_2O_3: Eu^{3+} nanotubes, nanorods and microcrystals recorded by selectively monitoring the $^5D_0 \rightarrow {}^7F_2(C_2)$ and $^5D_0 \rightarrow {}^7F_1(S_6)$ emissions at 611 and 582.4 nm, respectively. The strong broad band *ca.* ~250 nm is ascribed to O→Eu LMCT transitions [141]. Beside the Eu^{3+} intra-$4f^6$ lines, $^7F_0 \rightarrow {}^5D_{4\text{-}0}$, $^5L_6$, $^5G_{2\text{-}6}$, the spectra exhibit the Gd^{3+} intra-$4f^7$ lines, $^8S_{7/2} \rightarrow {}^6I_{7/2\text{-}17/2}$, $^6P_{3/2\text{-}7/2}$, showing for C_2 and S_6 sites efficient Gd^{3+}-to-Eu^{3+} energy transfer [139,142]. The energy difference between the maximum intensity peaks of the LMCT transitions for the two monitored wavelengths (248 and 255 nm, for S_6 and C_2, respectively) is due to shorter Eu-O bond length of S_6 sites [131].

The excitation spectra of the Eu^{3+}:Gd_2O_3 nanocrystals resemble that of the microcrystals although a blue-shift of the LMCT band relatively to the bulk materials is observed. As it was discussed in Chapter 1, section 1.2, this effect has been previously studied, for instance, Igarashi *et al.* [143] reported that the reduction of particle size causes lattice distortion and the lattice parameter to be larger; such a change of crystallinity increases the ionicity of Eu–O bonds shifting the LMCT excitation peak towards the higher-energy side

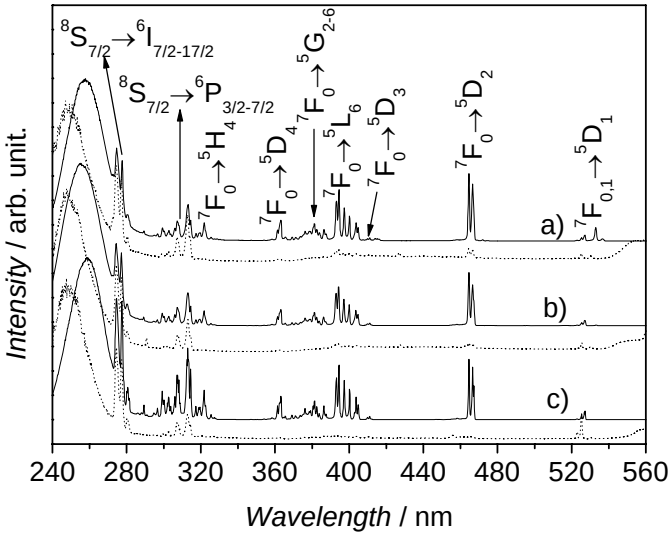

Figure 3.10 - Excitation spectra (11 K) of Gd_2O_3:Eu^{3+} microcrystals a), nanorods b), and nanotubes (3.30%) c) monitoring the $^5D_0\rightarrow{}^7F_2$ emission (C_2) at 611 nm (solid line) and the $^5D_0\rightarrow{}^7F_1$ emission (S_6) at 582.4 nm (dotted line).

Based on the emission and excitation spectra at 11 K (Figure 3.8 and Figure 3.10), the assignment of the energy levels below 30000 cm^{-1} was performed (Scheme 3.1). The energy levels of the C_2 site are similar to those reported for analogous Gd_2O_3:Eu^{3+} nanotubes [44], nanorods [120,121] and microcrystals [139]. For Eu^{3+}(S_6), only the $^5D_{1a,b}$ levels can be unambiguously assigned (energies in accordance with those reported by Buijs *et. al.* [139]), the $^7F_0\rightarrow{}^5D_{1a,b}$ and $^5D_0\rightarrow{}^7F_{1a,b}$ transitions are the only ones allowed by the site symmetry selection rules.

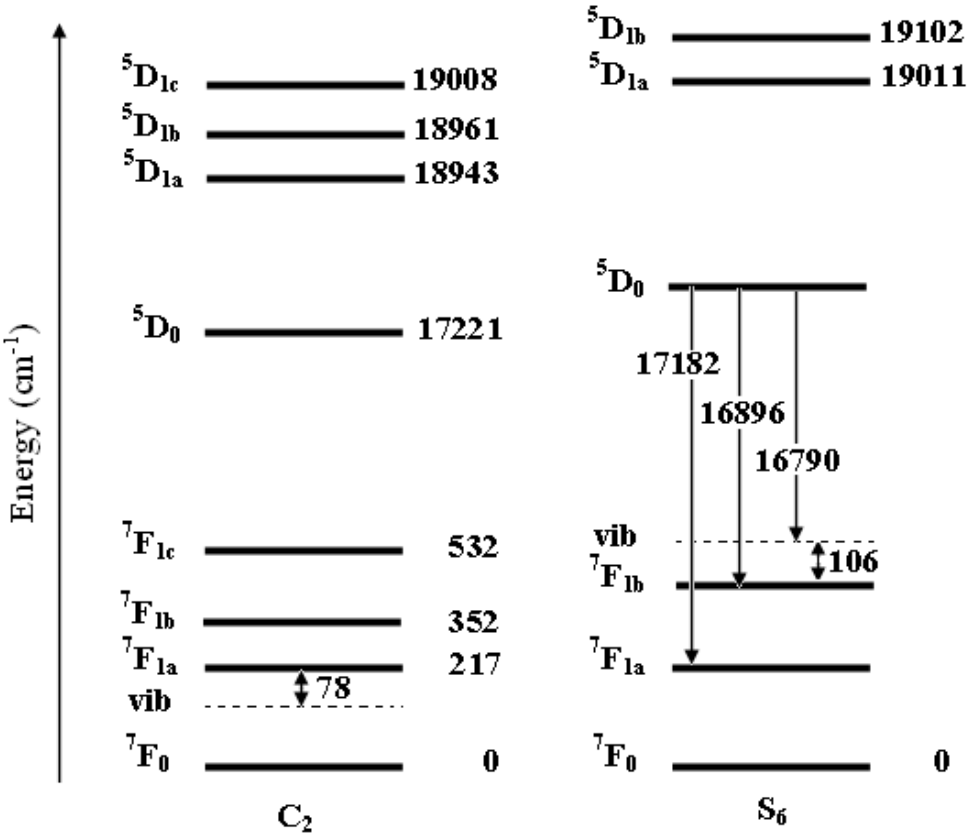

Scheme 3.1- Partial E\u^{3+} energy level diagram for the C_2 and S_6 sites of Gd_2O_3:Eu^{3+} nanotubes/nanorods. Error 7 cm^{-1}.

The $^5D_0$ emission decay curves ascribed to the $Eu^{3+}(C_2)$ and $Eu^{3+}(S_6)$ were monitored within the $^5D_0 \rightarrow {}^7F_2$ and $^5D_0 \rightarrow {}^7F_1$ transitions, respectively, at 11 K, under 394 nm excitation wavelength. The $^5D_0$ emission decay curves ascribed to the $Eu^{3+}(S_6)$ site strongly depend on the Eu^{3+} concentration, in such that a single exponential behaviour is only observed for the low concentrated nanotubes (0.16 and 1 %), yielding lifetime values of 1.09 ms and 0.54 ms, respectively. For higher concentrated samples, the emission decay behaviour deviates from a single exponential function due to the higher influence of the $S_6 \rightarrow C_2$ energy transfer [139]. These emission decay curves have been modelled using dipole-dipole, dipole-quadrupole and superexchanging interactions for Gd_2O_3:Eu^{3+} crystals [139]. These detailed analysis lies beyond the scope of the present work.

The low-temperature (11K) $^5D_0$ emission decay curves ascribed to the $Eu^{3+}(C_2)$ site are well described by a single exponential function, for Eu^{3+} concentrations higher than 3.30 %, yielding the $^5D_0$ lifetime values gathered in Table 3.1. For the nanotubes with Eu^{3+} concentration of 0.16 and 1.00 % the emission decay curves display a rise time followed by an exponential decay behavior. Similar emission decay curves have already been observed in

Y_2O_3:Eu^{3+} crystals with Eu^{3+} concentrations between 0.5 and 25.0 %, in a large temperature range [144]. The presence of a rise time was assigned to the submicron nonradiative decay between the $^5D_1$ level from Eu^{3+} ions at S_6 local symmetry to the $^5D_0$ level of the Eu^{3+} ions with C_2 local symmetry. In this context, these emission decay curves can be approximated by a simple rise and decay time model of the form:

$$I = A \times \left(1 - C \times e^{-(t/\tau_{rise})}\right) \times e^{-(t/\tau_{5D0})} \quad (3.1)$$

where A and C are constants, τ_{rise} and τ_{5D0} stands for the rise time constant and $^5D_0$ lifetime values, respectively. The emission decay curves monitored for the nanotubes with Eu^{3+} concentration of 0.16 and 1.00 % were fitted using equation (3.1) (Figure 3.11) yielding to the τ_{rise} and τ_{5D0} values listed in Table 3.1. The estimated rise time values decrease with the increase of the Eu^{3+} concentration (from 75 to 48 μs for the nanotubes with Eu^{3+} concentration of 0.16 and 1.00 %, respectively). These values are smaller than those reported for bulky Y_2O_3:Eu^{3+} [144] and Gd_2O_3:Eu^{3+} [139].

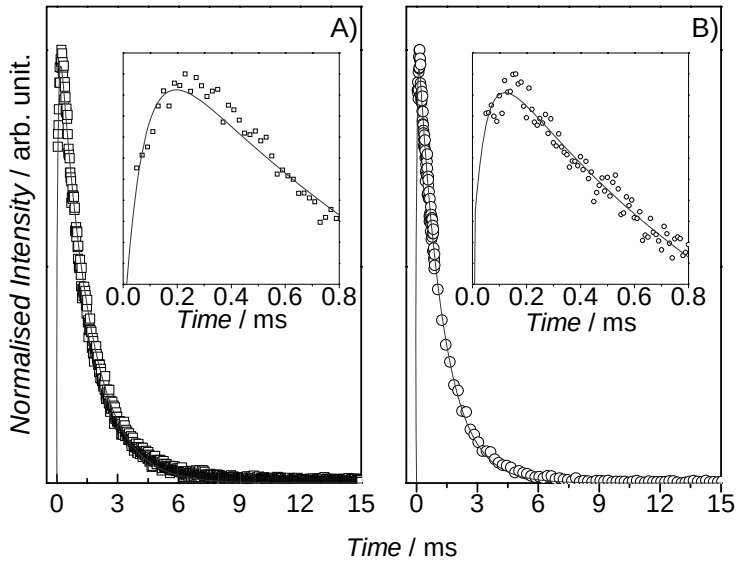

Figure 3.11 - Emission decay curves for the nanotubes with A) 0.16 and B) 1 % of Eu^{3+}. The solid lines correspond to the data best fit using Eq. (3.1).

The $^5D_0$ (C_2) lifetime value depends on the increase of the Eu^{3+} concentration (0.16-6.65 %). It is observed a maximum and a minimum value for the $^5D_0$ (C_2) lifetime values for Eu^{3+} concentrations of 1.00 % (1.20 ms) and 3.30 % (1.76 ms), respectively Table 3.1.

The dependence of the $^5D_0$ (C_2) lifetime values both on the Eu^{3+} concentration and calcination temperature can be discussed considering that the 11K lifetime value corresponds to the radiative lifetime (τ_{RAD}). In this context, the radiative $^5D_0$ (C_2) decay time dependence

on the Eu^{3+} concentration and thermal treatment may be rationalised in terms of the equation 1.22 from Chapter 1 [44,145]. The effective index of refraction is given by:

$$n_{eff} = n_{Gd_2O_3}x + (1-x)n_{med} \quad (3.2)$$

where x is the filling factor and n_{Gd2O3} (equal to 1.976) or n_{med} (equal to 1) are the index of refraction of the Gd_2O_3 and the medium, respectively. The estimated filling factor values are listed in Table 3.1 and Figure 3.12.

Table 3.1 - $^5D_{0,\,1}$ lifetime (τ_{5D0}, τ_{5D1}, respectively), rise time (τ_{rise}) obtained under excitation at 394.4 nm in the temperature interval 11-300 K for the nanotubes, nanorods with different Eu^{3+} concentration and distinct calcination time and temperature and for the microcrystal. The filling factors (x) for the nanotubes and nanorods are also shown. The error in the lifetime values is ~ 1.5 %.

Sample	Eu^{3+} (%)	*calcination T (ºC)/ time (h)*	C_2						S_6	x
			11 K	300 K	11 K	300 K	11 K	300 K	11 K	
			τ_{rise} (μs)	τ_{rise} (μs)	τ_{5D0} (ms)	τ_{5D0} (ms)	τ_{5D1} (μs)	τ_{5D1} (μs)	τ_{5D0} (ms)	
Nanotubes	0.16	700 / 3	75.20	35.45	1.44	1.63	169	63	1.09	0.76
	1.00	700 /3	48.80		1.20	1.53	109	64	0.54	0.86
	3.30	650 / 3			1.38	1.45				0.78
		650 / 6			1.50	1.32				0.74
		700 / 3			1.76	1.45	64	38		0.66
		700 / 6			1.50	1.48				0.74
		750 / 3			1.58	1.32				0.71
		750 / 6			1.16	1.41				0.91
	6.65	700 / 3			1.50	1.37	54	35		0.74
Nanorods	3.30	700 / 3			1.46	1.46	71	39		0.75
Microcrystals	3.65	700 / 3			1.00	1.00	66	21		

The emission decay curves for the $^5D_0$ (S_6) level were not acquired due to the overlap between the $^5D_0 \rightarrow {}^7F_0$ (C_2) and $^5D_0 \rightarrow {}^7F_1$ (S_6) transitions, due to the thermal induced broadening of the emission lines.

The comparison of the $^5D_0$ lifetime values with those in the literature is not straightforward, as the lifetime depends both on the concentration, morphology and synthesis parameters, such as calcination time and temperature.

Increasing the temperature up to 300 K, marked changes are observed in the $^5D_0$ emission decay curves. The monitoring and excitation wavelengths were the same as the ones used at 11K. For the Eu^{3+} at C_2 local site, all the emission decay curves are well reproduced by a single exponential function, except for the low-concentrated nanotubes (0.16 %), whose emission decay curve display a rise time component. The fit results concerning the τ_{rise} and τ_{5D0} values are listed in Table 3.1. The decrease of the τ_{rise} value with the temperature variation from 11 to 300 K indicates an increase in the time scale behind the cross-relation between the $^5D_1$ level from Eu^{3+} ions at S_6 local symmetry to the $^5D_0$ level of the Eu^{3+} ions with C_2 local symmetry. The monotonic decrease of the τ_{5D0} value as the Eu^{3+} concentration varies from 0.16 to 6.65 %, may be interpreted based on the radiative and nonradiative processes active at room-temperature [45]. In particular, similarly to that previously observed for Eu^{3+}:Gd_2O_3 crystals, due to the cross relaxation $Eu^{3+}(^5D_1)+ Eu^{3+}(^7F_0) \rightarrow Eu^{3+}(^5D_0) + Eu^{3+}(^7F_3)$ which is enhanced at higher Eu^{3+} doping concentrations [45].

The lifetime associated with the $^5D_1$ excited state was determined for the Eu^{3+} ions at C_2 local symmetry by monitoring the $^5D_1 \rightarrow {}^7F_1$ transition under 394 nm excitation wavelength in the temperature range 11-300 K. The emission decay curves for the $^5D_1$ (S_6) level could not be recorded as no emission from this excited state could be monitored. All the emission decay curves display a single exponential behaviour (not shown), whose fit procedure lead to the lifetime values gathered in Table 3.1. Similarly, to that mentioned for the $^5D_0$ lifetime values, the comparison of the $^5D_1$ decay rates with those in the literature is not straightforward, as the lifetime depends both on the concentration, morphology and synthesis parameters, such as calcination time and temperature. Nevertheless, the $^5D_1$ values reported here, are similar to the ones of Eu^{3+}:Y_2O_3 nanotubes with 1 % of Eu^{3+} (68 μs, at 300 K) [70] being higher than the values of Eu^{3+}:Gd_2O_3 crystals with Eu^{3+} concentration of 0.1 % (124 μs) [139] and Gd_2O_3 nanotubes with 4 % of Eu^{3+}(47 μs) acquired at low temperature [44].

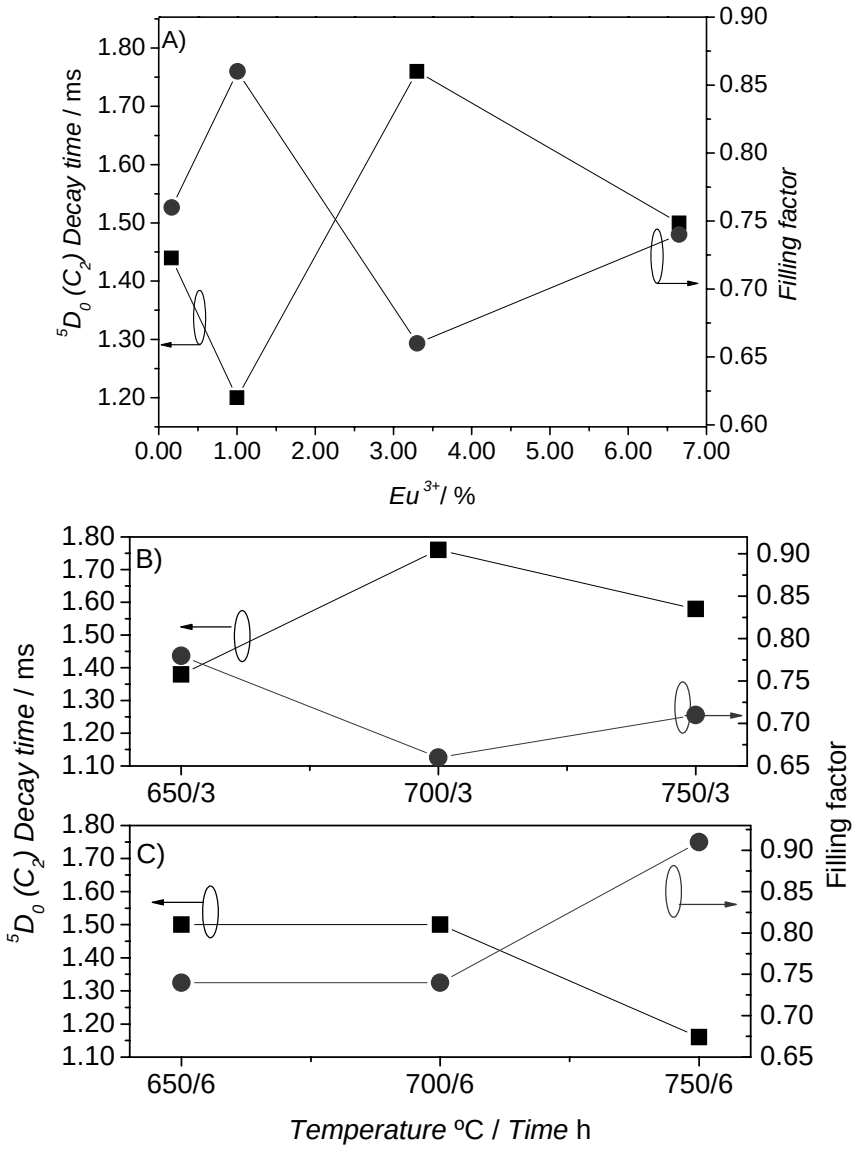

Figure 3.12 - $^5D_0$ (C_2) radiative decay time (squares) and filling factor values (balls): A) Effect of the Eu^{3+} concentration, samples calcined at 700 ºC by 3 hours, and the same parameters from nanotubes with 3.30 % of Eu^{3+}concentration calcined B) 650, 700 or 750 ºC by 3 h and C) 650, 700 or 750 ºC by 6 h. The lines are visual guide lines.

Independently of the Eu^{3+} concentration, higher values were found at 11 K, relatively to the ones acquired at 300 K, pointing the presence of thermal activated non-radiative mechanisms. Both at 11 and 300 K, the increase in the Eu^{3+} concentration is responsible for a decrease in the $^5D_1$ time decay rate, which may be assigned to the above mentioned cross relaxation path ($Eu^{3+}(^5D_1)$+ $Eu^{3+}(^7F_0) \rightarrow Eu^{3+}(^5D_0)$ + $Eu^{3+}(^7F_3)$) [45].

For the nanotubes with 3.3 % Eu^{3+} concentration, the effect of the calcination temperature (650-750 ºC), time (3-6 hours) and morphology on the $^5D_0$ (C_2) emission decay curves was studied, using the same experimental condition above mentioned (monitoring at

the $^5D_0 \rightarrow {}^7F_2$ transition and exciting at 394 nm). It was found that despite the typical exponential behaviour the $^5D_0$ emission decay curves depend on the calcination temperature and on the morphology. In particular, the morphology variation from nanotubes to nanorods induces a decrease in the $^5D_0$ radiative lifetime value, which may be explained by the smaller size of the nanotubes relatively to that of the nanorods [44].

The $^5D_0$ lifetime value acquired for the nanorods is independent of the temperature, as reported for Eu^{3+}:Y_2O_3 microcrystals. The variation of both the calcination time and temperature is also responsible for alterations in the time scale behind the $^5D_0$ (C_2) and $^5D_1$ (C_2) depopulation. At 11 K, for a calcination time of 3 hours, the maximum τ_{5D0} value occurs at 700 ºC, whereas for a calcination time of 6 hours the τ_{5D0} value remains constant as the temperature increases from 650 to 700 ºC, being smaller at 750 ºC. It should be pointed out that the radiative lifetime (τ_{5D0} acquired at 11 K) dependence on the calcination temperature and time displays the same evolution with the filling factor as the one above discussed for the radiative lifetime dependence on Eu^{3+} concentration.

Attending to the fine relation between the synthesis methods and parameters with the intrinsic time scales behind the depopulation of the $^5D_0$ and $^5D_1$ excited levels, we also measured the respective lifetime values for the microcrystal by monitoring the $^5D_0 \rightarrow {}^7F_2$ (C_2) and $^5D_1 \rightarrow {}^7F_1$ (C_2) transitions, respectively, under 394 nm excitation wavelength in the temperature interval 11-300 K (not shown). The curves are well reproduced by single exponential functions yielding to $^5D_0$ and $^5D_1$ lifetime values smaller than those reported for the nanomaterials (Table 3.1); in good agreement with the lack of quantum confinement in the crystal. The $^5D_0$ lifetime values are independent of the temperature similarly to that reported for Eu^{3+}:Gd_2O_3 microcrystals, with approximately the same lifetime [139].

Figure 3.13 shows the excitation spectra (11 K) in the region of the $^7F_0 \rightarrow {}^5D_1$ transition (520–540 nm) by monitoring, respectively, the $^5D_0 \rightarrow {}^7F_2$ (C_2) emission at 611.0 nm and the $^5D_0 \rightarrow {}^7F_1$($S_6$) emission at 582.4 nm. The high-energy $^5D_1$ Stark component ($^5D_{1c}$) of C_2 site and the low-energy $^5D_1$ Stark component ($^5D_{1a}$) of S_6 are superimposed. The presence of the $^7F_0 \rightarrow {}^5D_{1a,b}$ (S_6) transitions in Fig. 4A (respectively *ca.* 523.5 and 526 nm) points to an efficient Eu^{3+}(S_6)-to-Eu^{3+}(C_2) energy transfer mechanism.

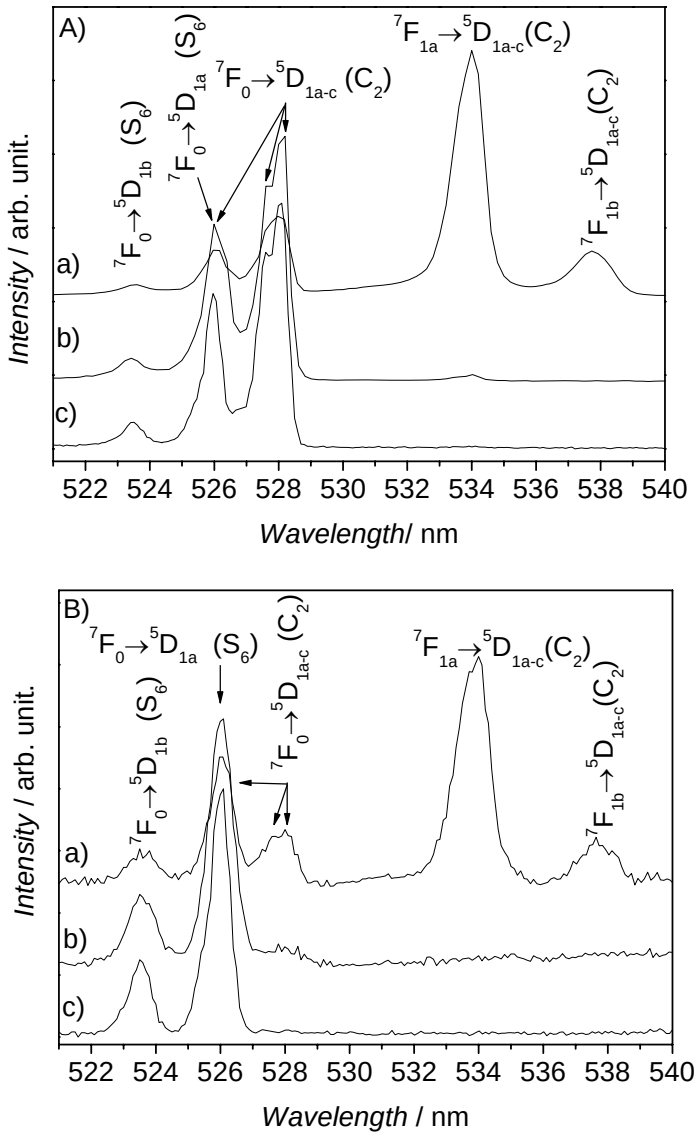

Figure 3.13 - 11 K excitation spectra of Gd_2O_3:Eu^{3+} expanded in the spectral region of the $^7F_{0,1}\rightarrow{}^5D_1$ transitions monitoring the A) $^5D_0\rightarrow{}^7F_2$ emission (C_2) at 611.0 nm and B) $^5D_0\rightarrow{}^7F_{1a}$ emission (S_6) at 582.4 nm from a) nanotubes (3.30%), b) nanorods (3.30%) and c) microcrystals (3.65%), samples annealed at 973 K during 3 h. The spectral resolution is 1 nm (the slits used are 0.4 mm and the reciprocal linear density of the monochromator is 2.6 $nm.mm^{-1}$).

The total emission intensity originated from the excited $Eu^{3+}(S_6)$ ions, *I(S₆)*, is proportional to the amount of isolated and radiatively decaying $Eu^{3+}(S_6)$ centres and can be calculated from the spectrum recorded at 11 K and excited at 523.5 nm, $^7F_0\rightarrow{}^5D_{1b}(S_6)$ line, Figure 3.14. This intensity allows to estimate the critical $Eu^{3+}(S_6)\rightarrow Eu^{3+}(C_2)$ energy-transfer distance R_0 assuming, for any $Eu^{3+}(S_6)\rightarrow Eu^{3+}(C_2)$ pair, that the $Eu^{3+}(S_6)$ ions will decay

radiatively if their separation is larger than R_0 and $S_6 \rightarrow C_2$ transfer will occur if it is smaller than R_0.

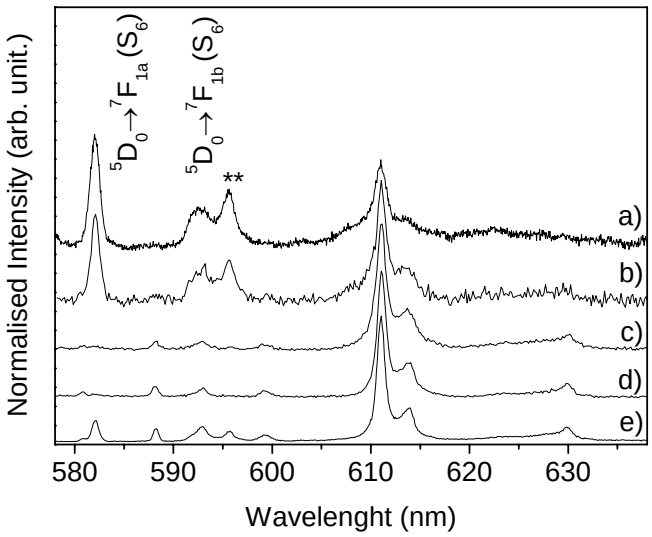

Figure 3.14 - Part of the emission spectrum (11 K) from Gd_2O_3:Eu^{3+} (a-d 0.16, 1.00, 3.30 and 6.60 % of Eu^{3+}) and (line "e") microcrystal (3.65 % of Eu^{3+}), excited at 522.6 nm ($^7F_1 \rightarrow {}^5D_0$ line of the Eu^{3+} ions in the S_6 local symmetry).

According to Buijs *et al.* [139] if each $Eu^{3+}(S_6)$ has *n* neighbouring Gd^{3+} sites within R_0 that can be occupied by a $Eu^{3+}(C_2)$, thus the probability for the Eu^{3+} (S_6) ion to be isolated in Gd_2O_3 host is given by:

$$(100 - C)^n = \frac{I(S_6) \times 100}{I(S_6) + I(C_2)} \qquad (3.3)$$

where *C* is the Eu^{3+} molar concentration. Given the *n* value and the structural Gd_2O_3 data [131], R_0 will be estimated. Figure 3.15 A-C display the $I(S_6)$, *n* and R_0 values for Gd_2O_3:Eu^{3+} nanotubes (0.16, 1.00, 3.30 and 6.60%), nanorods and microcrystals. For similar Eu^{3+} content (3.30–3.65%), the intensity of the $Eu^{3+}(S_6)$ emission of the nanotubes is lower than the emissions of nanorods and microcrystals, suggesting that the number *n* of neighbouring Gd^{3+} sites within R_0 that may be occupied by $Eu^{3+}(C_2)$ ions is larger for nanotubes with the consequent increase of the critical $S_6 \rightarrow C_2$ energy transfer distance R_0 (from 14.2 and 14.9 Å, in the microcrystals and nanorods, respectively, to 15.8 Å in the nanotubes). The intensity ratio of $Eu^{3+}(S_6)$ and $Eu^{3+}(C_2)$ emission lines decreases on increasing the Eu^{3+} content in the Gd_2O_3:Eu^{3+} nanotubes (Figure 3.15A). This observation, already reported for the bulk material by Buijs *et al.* [139], indicates an increasing rate of $Eu^{3+}(S_6) \rightarrow Eu^{3+}(C_2)$ energy transfer with

the subsequent increase of the *n* neighbouring Gd^{3+} sites within R_0 that may be occupied by $Eu^{3+}(C_2)$ ions (Figure 3.15B) and of the critical $S_6 \rightarrow C_2$ energy transfer distance R_0 (Figure 3.15C).

As far as we know, no data are available for Gd_2O_3:Eu^{3+} nanocrystals, thus not allowing the comparison of $I(S_6)$, *n*, and R_0 values. However, for microcrystals, the $I(S_6)$ value measured in this work (9.5%) is smaller than that reported for analogous materials (11%) [139], despite the smaller amount of incorporated Eu^{3+} (3.65 against 5%). Thus, in spite of the smaller number of active Eu^{3+} centres in the microcrystals synthesised in this work, the number *n* of neighbouring Gd^{3+} sites within R_0 that may be occupied by $Eu^{3+}(C_2)$ ions and the R_0 values are larger than those previously reported [139], which suggests a clustering of Eu^{3+} ions at C_2 sites.

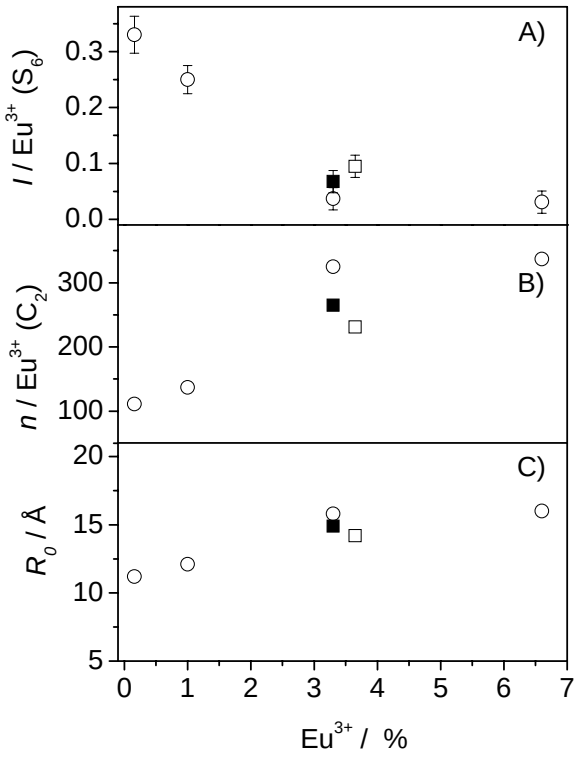

Figure 3.15 - a) I (S_6), b) number of Gd^{3+} neighbours at C_2 local symmetry and c) R_0 as function of concentration. The point of Eu^{3+} (%) equal to 3.6 % corresponds to microcrystal sample.

Table 3.2 lists the room-temperature emission quantum yield (QY) values measured for Gd_2O_3:Eu^{3+} nanotubes, nanorods and microcrystals, upon excitation at 255 nm (LMCT band), 274.4 nm ($^8S_{7/2} \rightarrow {}^6I_{7/2\text{-}17/2}$ Gd^{3+} lines) and 394.4 nm ($^5D_0 \rightarrow {}^7L_6$ $Eu^{3+}(C_2$) lines). Among

the Gd_2O_3:Eu^{3+} nanocrystals, those annealed at 750 ºC for 3 h display the maximum emission QY, 0.58-0.59. Changing the annealing parameters (time, temperature or pH), induces small variations in the emission quantum yields.

In general lanthanide-based nanomaterials present lower emission quantum yields than their bulk counterparts due to the increase of nonradiative transition channels mediated via a high surface-to-volume ratio [147,148]. Although other optically-active inorganic nanomaterials show this effect, the quantum-yield response versus size or shape depends on the emission mechanism. For example, the quantum yield of CdSe quantum dots is enhanced after water molecules surface passivation [149], while the same process is less important for bulk CdSe. In contrast, water molecules (or hydroxyl groups) at the Gd_2O_3:Eu^{3+} nanorods surface include additional vibracional mechanisms and non-radiative depopulation paths.

Table 3.2– Emission quantum yield of the Gd_2O_3:Eu^{3+} nanotubes, nanorods and microcrystals

Annealing	λ_{exc} = 255 nm			λ_{exc} = 274 nm			λ_{exc} = 394 nm		
	NT	NR	MC	NT	NR	MC	NT	NR	MC
650 ºC 3 h	0.51	0.44		0.32	0.28		0.07	0.06	
650 ºC 6 h	0.51	0.46		0.31	0.32		0.05	0.09	
700 ºC 3 h	0.51	0.50	0.70	0.30	0.28	0.65	0.04	0.06	0.21
700 ºC 6 h	0.54	0.56		0.32	0.32		0.08	0.08	
750 ºC 3 h	0.59	0.58		0.38	0.36		0.05	0.09	
750 ºC 6 h	0.54	0.53		0.29	0.33		0.08	0.08	

As can be observed in Table 3.2, there are variations in the QY measured upon different wavelength excitations, for instance, the QY values reduces when the wavelength excitation changes from the LMCT, Gd^{3+} to the Eu^{3+} transition lines. The explanation for these results is still an open question.

3.2.1.2 – Photoluminescence (PL/PLE) of the Gd_2O_3:Yb^{3+},Er^{3+} nanotubes

Figure 3.16a,b shows the 300 and 11 K excitation spectra by monitoring the main emission lines at 978 nm ($^2F_{5/2}\rightarrow{}^2F_{7/2}$ transition lines from Yb^{3+}) and 1534 nm ($^4I_{13/2}\rightarrow{}^4I_{15/2}$ transition lines from Er^{3+}). A weak broad band localised at 300 nm (300 K) and at 250 nm (11 K) has been also attributed to a charge transfer band related with Yb^{3+} [146]. In the excitation spectra by monitoring at 1534 nm ($^4I_{13/2}\rightarrow{}^4I_{15/2}$ transition lines from Er^{3+}), Figure 3.16c,d, the

most intense excitation peaks belong to the hypersensitive transitions to $^4G_{11/2}$ and $^2H_{11/2}$. Clearly, there exists energy transfer from Yb^{3+} to Er^{3+}, by utilizing the enhanced energy transfer from Yb^{3+} to Er^{3+} and multi photon absorption the upconversion emission effect is observed in this material.

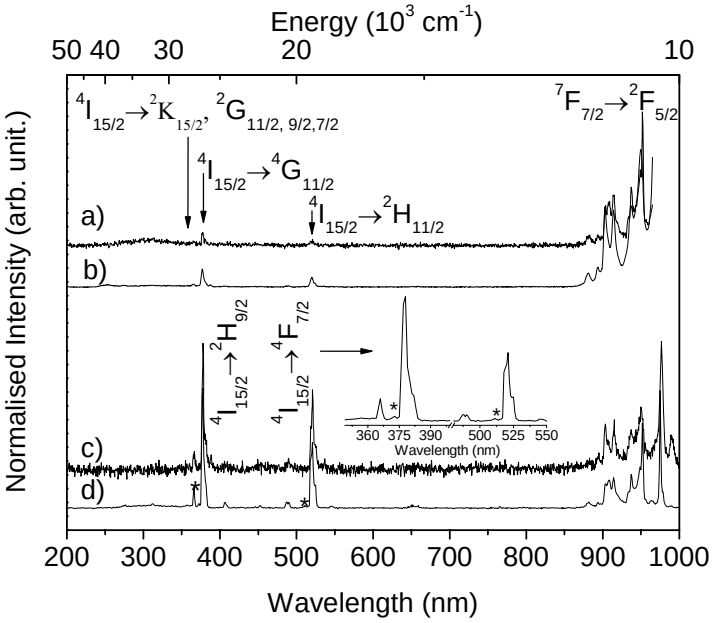

Figure 3.16 – Excitation spectra by monitoring the emission at 978 nm ($^2F_{5/2}\rightarrow{}^2F_{7/2}$ transition lines from Yb^{3+}) recorded at a) 300 K and b) 11 K; and by monitoring at 1534 nm ($^4I_{13/2}\rightarrow{}^4I_{15/2}$ transition lines from Er^{3+}) recorded at c) 300 K and d) 11 K. The inset showns the magnification of the $^4I_{13/2}\rightarrow{}^4I_{15/2}$ region and the asterisks depict the vibronic lines.

The two peak marked by asterisks correspond to the phonon side band due M process [150,151] (M process is characterised by the electron-phonon coupling with an infrared-active, or ungerade, vibrational modes) for the hypersensitive transitions from the ground state to the $^4G_{11/2}$ and $^2H_{11/2}$ states, respectively.

At 11 K and 300 K the near-infrared region emission spectra of Gd_2O_3:Yb^{3+} Er^{3+} shows the typical transitions $^4I_{11/2,\ 13/2}\rightarrow{}^4I_{15/2}$ at 980 nm and 1550 nm of Er^{3+} and $^2F_{5/2}\rightarrow{}^2F_{7/2}$ between 978-1100 nm of Yb^{3+}, Figure 3.17. The energy levels of Yb^{3+} Er^{3+} are depicted in the Scheme 3.2.

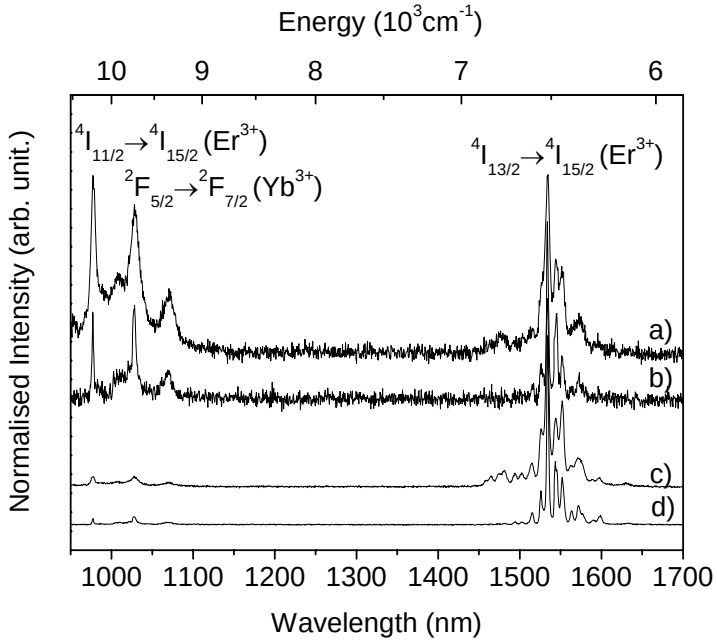

Figure 3.17 – Near-infrared emission spectra of the $^2F_{5/2}\rightarrow{}^2F_{7/2}$ (Yb^{3+}) and $^4I_{11/2,\ 13/2}\rightarrow{}^4I_{15/2}$ (Er^{3+}) transition lines acquired at following temperature and wavelength excitation: a) 300 K, 250 nm, b) 11 K, 313 nm, c) 300 K, 377 nm and d) 11 K, 377 nm, respectively.

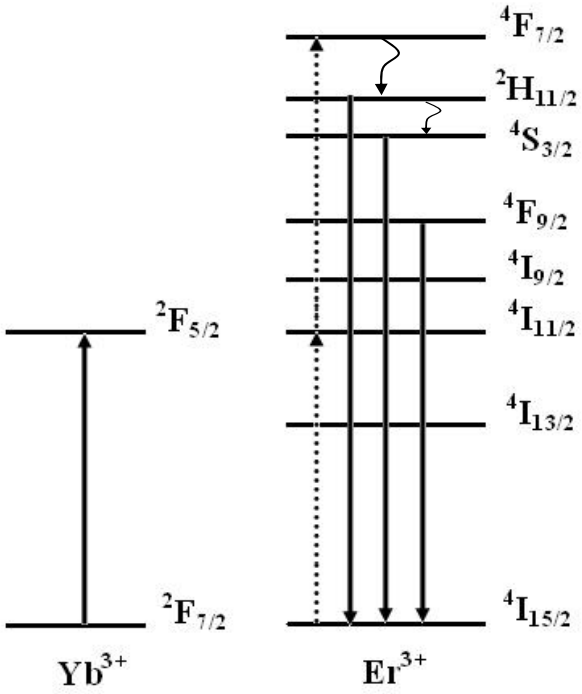

Scheme 3.2 – Partial Yb^{3+} and Er^{3+} energy level diagram in Gd_2O_3 nanocrystals. Dotted line represents the photon absorption involved in the up conversion process and curved lines are the de-population paths trough non radiative relaxation by multi-phonons emission.

3.2.1.3 – Upconversion

The upconversion spectra were acquired in the 500-720 nm wavelength regions upon 980 nm excitation, Figure 3.18. At 300 K, series of sharp lines are observed at 523 nm, 548 nm and 660 nm; they are assigned to the transitions between the Stark components of the $^2H_{11/2}$, $^4S_{3/2}$ and $^4F_{9/2} \rightarrow {}^4I_{15/2}$ levels from Er^{3+} ions (energy level depicted at Scheme 3.2). Lines arising from $^4F_{9/2} \rightarrow {}^4I_{15/2}$ transitions are dominant in the upconversion spectrum, comparing the intensity ratio of the integrated area of emission lines arising from $^2H_{11/2}$, $^4S_{3/2} \rightarrow {}^4I_{15/2}$ and $^4F_{9/2} \rightarrow {}^4I_{15/2}$ the result is 0.011.

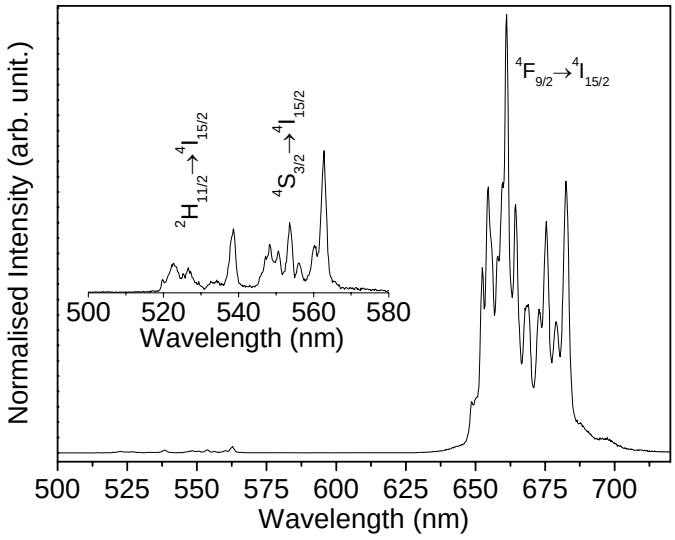

Figure 3.18 – Green and red upconversion emission spectra measured at 300 K. Inset the magnification of the $^2H_{11/2}$, $^4S_{3/2} \rightarrow {}^4I_{15/2}$ transitions region.

3.2.1.4 – Influence of the laser power

To understand the upconversion mechanisms, the intensity (*I)* of the upconversion emission was measured as a function of the laser power (*P)*. For the upconversion process, *I* is proportional to the n^{th} power of *P*, that is:

$$I \propto P^n \tag{3.4}$$

where *n* is the number of pump photons absorbed per upconverted photon emitted. A plot of log *I* versus log *P* yields a straight line with slope *n*. The result is shown in Figure 3.19 for $^2H_{11/2} \rightarrow {}^4I_{15/2}$, $^4S_{3/2} \rightarrow {}^4I_{15/2}$ and $^4F_{9/2} \rightarrow {}^4I_{15/2}$ transitions at 300 and 11 K.

These results show that the two-photon process is responsible for green and red upconversion at room temperature. This result is in accordance with *n* values previously reported for the Yb^{3+},Er^{3+} codoped Gd_2O_3 nanocrystals compounds [152,153].

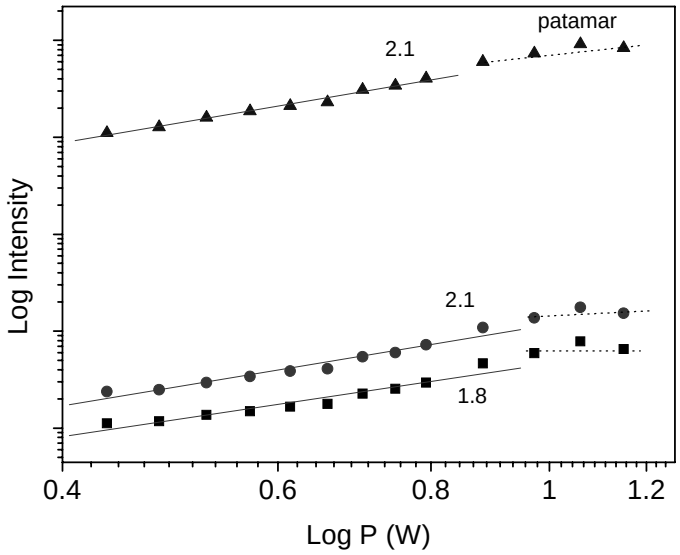

Figure 3.19- Dependence of the upconversion emission intensity on excitation power, Eq. (3.7), from ■ - $^2H_{11/2}\rightarrow{}^4I_{15/2}$, ● - $^4S_{3/2}\rightarrow{}^4I_{15/2}$ and ▲ - $^4F_{9/2}\rightarrow{}^4I_{15/2}$ transitions.

3.2.2 - Anomalous photoluminescence features of Gd_2O_3:Eu^{3+} and Gd_2O_3:Yb^{3+},Er^{3+} nanotubes

In what follows we discuss the intriguing and unprecedent anomalous thermalisation of the $^7F_{1a,b}$ (Eu^{3+}) and $^2H_{11/2}$ (Er^{3+}) levels, in Gd_2O_3:Eu^{3+} and Gd_2O_3:Yb^{3+},Er^{3+} nanotubes, respectively, that induces C_2-to-S_6 energy transfer (Eu^{3+}) at 11 K and $^2H_{11/2}\rightarrow{}^4I_{15/2}$ upconversion emission (Er^{3+}), both clearly unexpected. We stress that the photoluminescence measurements were all carried out within a week after preparing fresh samples. When the samples are kept in ambient atmosphere degradation of these anomalous properties started after *ca.* 7 days and after *ca.* 70 days no $^7F_{1a,b}$ population was observed at 11 K. Re-calcination of the samples, using the synthesis conditions used for preparing the parent samples, recovers the anomalous behaviour.

3.2.2.1 – $^7F_{1a,b}$ and $^2H_{11/2}$ population

An interesting aspect observed in the excitation spectra of Gd_2O_3:Eu^{3+} nanotubes (3.30%, annealed at 700 ºC for 3 h) is the presence of the $^7F_{1a,b}\rightarrow{}^5D_1$ lines at temperatures below 80 K (Figure 3.20A). For Gd_2O_3:Yb^{3+},Er^{3+} nanotubes (5.00% Yb^{3+} and 1.20% Er^{3+}, calcined at 700 ºC for 3 h) it is also remarkable to observe the $^2H_{11/2}\rightarrow{}^4I_{15/2}$ upconversion emission in the entire 11-300 K temperature range (Figure 3.21B).

The ratio of the populations of the $^7F_1$ and $^7F_0$ levels (C_2 or S_6 sites) normally follows a Boltzmann distribution:

$$\frac{^7F_1\rightarrow{}^5D_1}{^7F_0\rightarrow{}^5D_1}\propto\exp(-\Delta E/kT) \quad \text{and} \quad \frac{^2H_{11/2}\rightarrow{}^4I_{15/2}}{^4S_{3/2}\rightarrow{}^4I_{15/2}}\propto\exp(-\Delta E_2/kT) \qquad (3.5)$$

where k is the Boltzmann constant, T the temperature and ΔE_1 and ΔE_2 the energy differences between the $^7F_0$ and the $^7F_1$ and the $^2H_{11/2}$ and $^4S_{3/2}$ levels (Scheme 3.1 and 3.2). Thus, the $^7F_1$ and $^2H_{11/2}$ populations should be close to 0 at 11 K, as indeed observed for nanorods and microcrystals (Figure 3.20B-C) and for Gd_2O_3:Yb^{3+},Er^{3+} nanotubes calcined at 650 ºC during 3 h, (Figure 3.21A) and by Liu *et al.* for analogous Gd_2O_3:Eu^{3+} nanorods (5% Eu^{3+}, annealed at 700 ºC for 1 h [121]). However, for the nanotubes the $^7F_1\rightarrow{}^5D_1$ lines dominate the 11 K excitation spectra of Figure 3.20A and the $^2H_{11/2}\rightarrow{}^4I_{15/2}$ upconvertion emission in Figure 3.21B displays intensity similar to that of the $^4S_{3/2}\rightarrow{}^4I_{15/2}$ lines.

Although this anomalous thermalisation effect has been previously reported for Gd_2O_3:Eu^{3+} nanotubes [44] and Y_2O_2S:Er^{3+} nanocrystals [42], it is one order of magnitude stronger for our best samples (0.16% Eu^{3+} annealed at 650 ºC for 6 h, 3.30% at 700 ºC for 3 h and 6.60% at 850 ºC for 6 h, see below). Moreover, as far as we know, there are no previous reports illustrating anomalous thermalisation effects in high-energy $^7F_1$ Stark components (352 cm^{-1} above $^7F_0$) and in the $^2H_{11/2}$ Er^{3+} excited level.

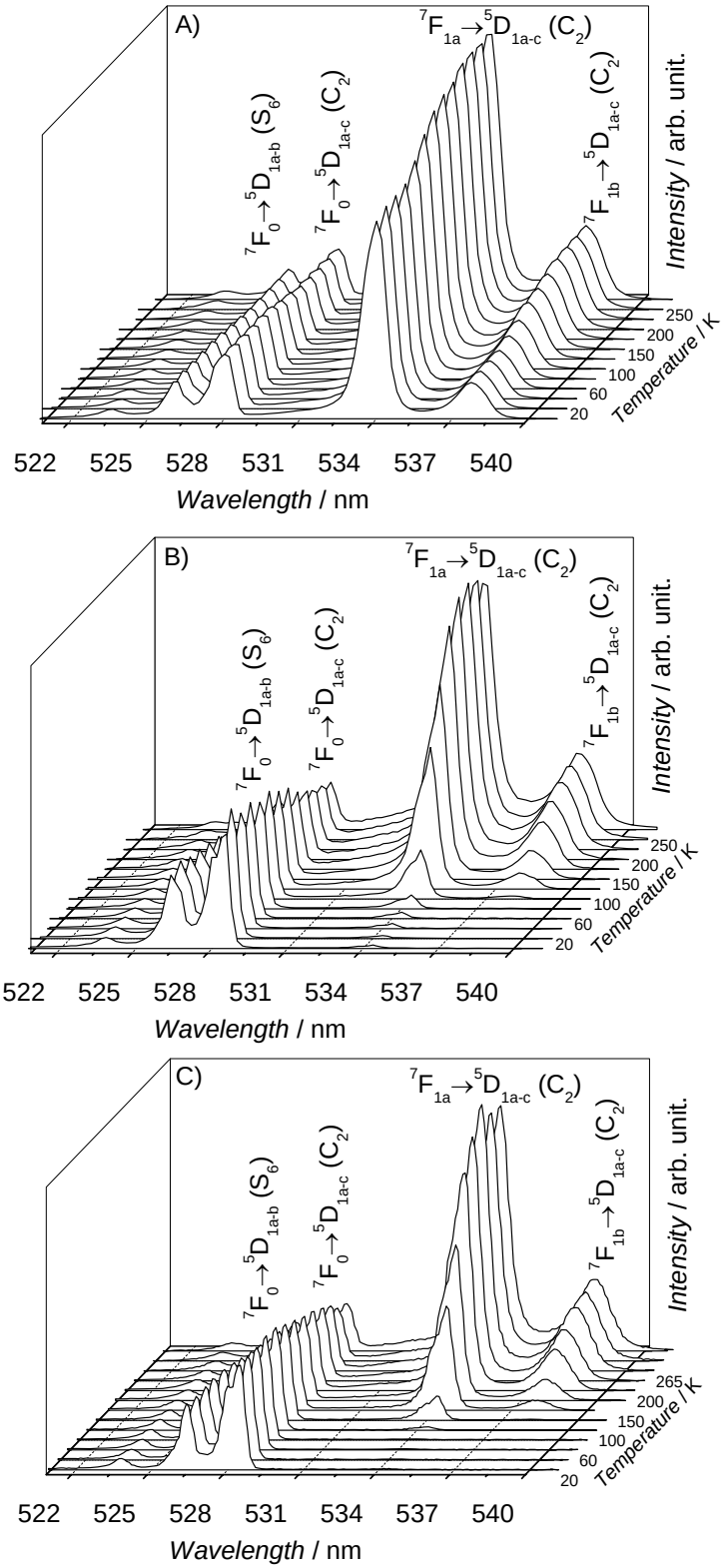

Figure 3.20 - Expanded $^7F_{0,1}\rightarrow{}^5D_1$ excitation spectra acquired monitoring the $^5D_0\rightarrow{}^7F_2$ emission (C_2) at 611 nm from A) nanotubes (3.30%), B) nanorods (3.30%) and C) microcrystals (3.65%) as function of temperature; samples annealed at 700 ºC for 3 h.

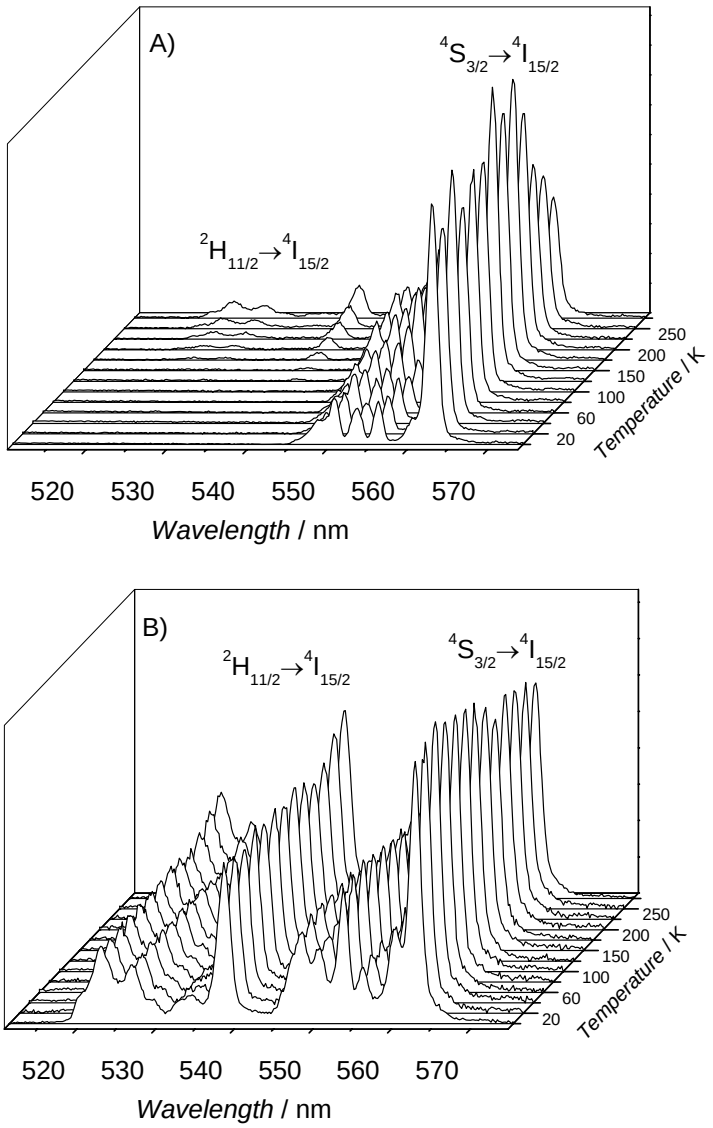

Figure 3.21 - Expanded upconversion emission spectra upon laser excitation (980 nm, set at 0.8 W) in the $^4S_{3/2}$, $^2H_{11/2}\rightarrow{}^4I_{15/2}$ region from Gd_2O_3:Yb^{3+}, Er^{3+} (5.00% Yb^{3+} and 1.20 % Er^{3+}) calcined at A) 650 ºC by 3 h and B) 700 ºC by 3 h.

To ensure that the spectra of nanotubes, nanorods and microcrystals were measured in identical experimental conditions and at the same temperature of 11 K the following procedure was adopted:

a) Thin (<0.5 mm), same size, pellets of Gd_2O_3:Eu^{3+} nanotubes and microcrystals (or nanorods) (3.30 % of Eu^{3+} concentration annealed at 700 ºC for 3 h) were placed 0.3 mm apart in the same cryostat holder and cooled to 11 K.

b) Excitation spectra of both pellets were recorded, monitoring the $^7F_2\rightarrow{}^5D_0$ lines of the Eu^{3+} C_2 sites (611 nm), by moving the cryostat horizontally. In this way, the $^7F_1\rightarrow{}^5D_1$

transition lines were detected for the nanotubes and not detected for microcrystals, Figure 3.22. Thus, excluding the possibility that the samples were at elevated temperature inside the cryostat. The latter is also supported by the fact that the intensity ratio of hot-to-normal bands remains unchanged when the incident power of the Xe lamp is attenuated by inserting neutral density filters.

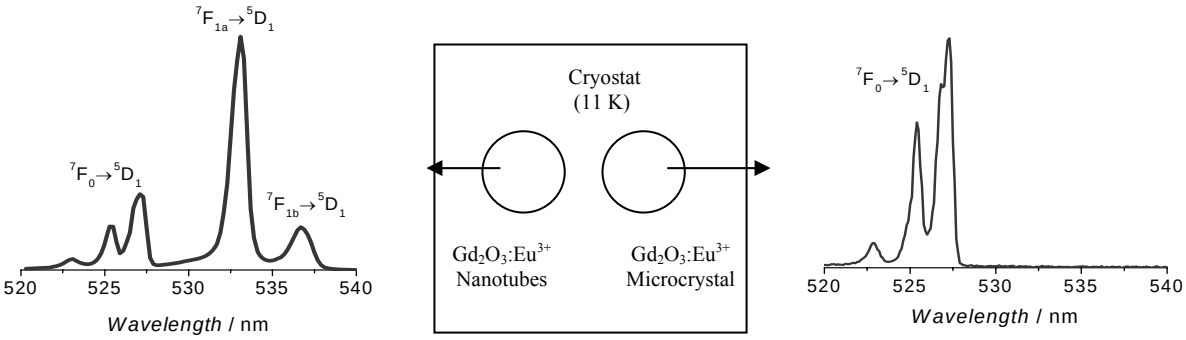

Figure 3.22 - Scheme of the experimental set-up made to ensure the low temperature environment.

The temperature dependence of the integrated intensity ratio of hot-to-normal bands as a function of the annealing conditions is shown in Figure 3.23 and Figure 3.24 for the Gd_2O_3:Eu^{3+} (3.30% Eu^{3+}) and Gd_2O_3:Yb^{3+},Er^{3+} nanotubes (5.00% Yb^{3+} and 1.20% Er^{3+}), respectively. The integrated intensities are calculated fitting the Eu^{3+} $^7F_{0,1a,1b}\rightarrow{}^5D_1(C_2)$ transitions (acquired monitoring the $^5D_0\rightarrow{}^7F_2(C_2)$ emission at 611 nm) and the Er^{3+} upconversion $^2H_{11/2}\rightarrow{}^4I_{15/2}$ and $^4S_{3/2}\rightarrow{}^4I_{15/2}$ lines using Gaussian functions.

The temperature dependence of the $^2H_{11/2}\rightarrow{}^4I_{15/2}/{}^4S_{3/2}\rightarrow{}^4I_{15/2}$ integrated intensity ratio of the nanocrystals calcined at 700 ºC during 3 h is rather anomalous and constant between 10 and 250 K. In contrast, the temperature dependence of this ratio for the nanotubes calcined at 650 ºC displays the expected Boltzmann distribution with ΔE ($^2H_{11/2}\rightarrow{}^4S_{3/2}$)=700 cm^{-1}. The intensity ratio between the $^2H_{11/2}\rightarrow{}^4I_{15/2}$ and $^4S_{3/2}\rightarrow{}^4I_{15/2}$ transitions remains essentially unchanged as the power of the diode laser increases from 0.4 to 1 W indicating negligible thermal effects arising from the excitation laser.

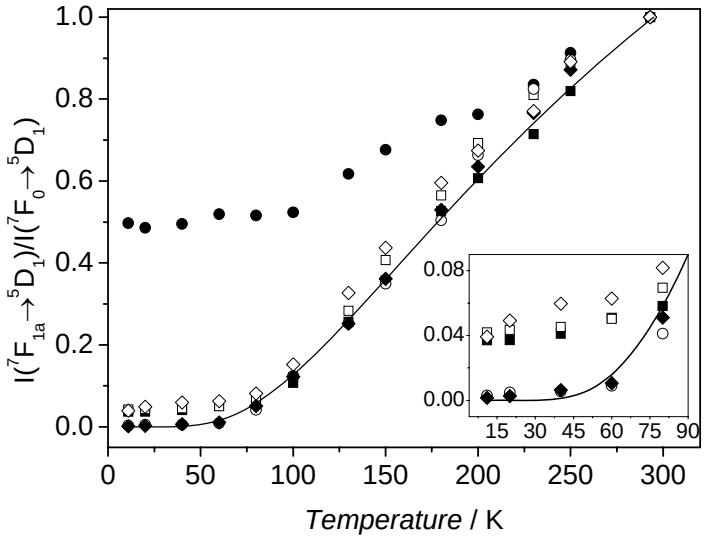

Figure 3.23 - Normalised relative intensity ratio between the $^7F_{1a}\rightarrow{}^5D_1$ and the $^7F_0\rightarrow{}^5D_1$ transitions recorded from Gd_2O_3:Eu^{3+} nanotubes (3.30%), monitored at 611 nm ($^5D_0\rightarrow{}^7F_2$ line of the Eu^{3+} ions in the C_2 local symmetry), versus temperature. Annealing parameters: ■ – 650 ºC during 3 h; □ – 650 ºC during 6 h; ● – 700 ºC during 3 h; ○ – 700 ºC during 6 h; ◆ – 750 ºC during 3 h; ◇ – 750 ºC during 6 h. The inset shows a magnification of the low temperature region for all the samples with the exception of that calcined at 700 ºC during 3 h. The full lines are Boltzmann distributions, Eq. 3.5, considering $\Delta E = 217$ cm^{-1} ($^7F_{1a}\rightarrow{}^7F_0$, C_2).

The temperature dependence of the $^7F_{1a}\rightarrow{}^5D_1/{}^7F_0\rightarrow{}^5D_1$ ($^7F_{1a}$ at 217 cm^{-1} above $^7F_0$) integrated intensity ratio (R_a) of the samples calcined at 650 ºC, during 3 and 6 h, and at 750 ºC, during 6 h, is similar to that previously quoted by Liu *et al.* [44], intensity ratio at 11 K of ~0.03. However, the sample calcined at 700 ºC during 3 h exhibits an abnormal temperature dependence for R_a ratio, being almost constant below 115 K and one order of magnitude larger (~0.49) than those of the other samples.

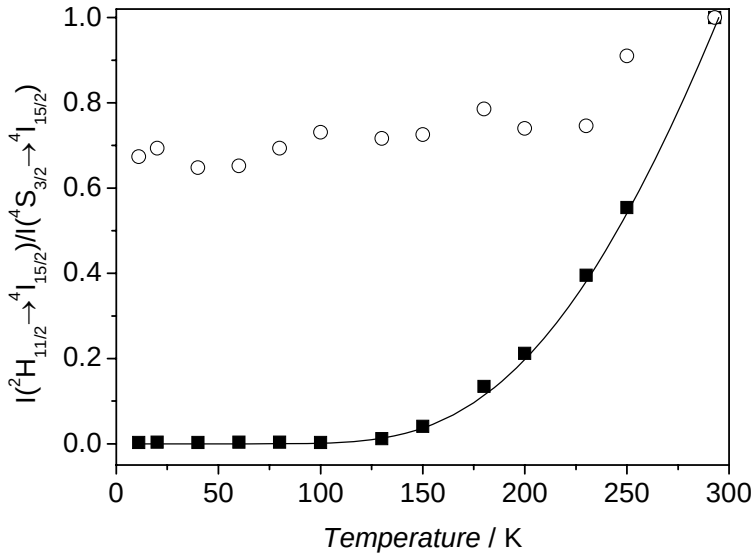

Figure 3.24- Normalised relative intensity ratio between the $^2H_{11/2}\rightarrow{}^4I_{15/2}$ and $^4S_{3/2}\rightarrow{}^4I_{15/2}$ transitions in Gd_2O_3:Yb^{3+}, Er^{3+} nanotubes (5.00% Yb^{3+} and 1.20 % Er^{3+}), excited at 980 nm via Yb^{3+}-to-Er^{3+} energy transfer, versus temperature. Annealing parameters: ■ – 650 ºC during 3 h; ○ – 700 ºC during 3 h. The full line is a Boltzmann distribution, Eq. (3.5), considering ΔE =700 cm^{-1}($^2H_{11/2}\rightarrow{}^4S_{3/2}$).

For each Eu^{3+} nanotubes concentration the maximum value for the 11 K R_a ratio depends on the annealing conditions (time and temperature) and it may even be zero. The temperature dependence of these maxima is shown for three Eu^{3+} concentrations in Figure 3.25A. Figure 3.25B exhibits the temperature dependence of the $^7F_{1b}\rightarrow{}^5D_1/{}^7F_0\rightarrow{}^5D_1$ intensity ratios (R_b) for the same set of samples showing in Figure 3.23.

It is quite remarkable that the $^7F_{1b}$ level (at 352 cm^{-1} above $^7F_0$) is still populated at low temperatures also displaying an anomalous thermalisation effect. However, the R_b ratio at 11 K is lower than the corresponding R_a (for instance ~0.32 for the sample calcined at 700 ºC during 3 h, Figure 3.25B). The temperature range where it is almost constant is also slightly lower (~90 K). For the other represented samples the $^7F_{1b}$ population is thermalized and R_b follows the expected Boltzmann trend.

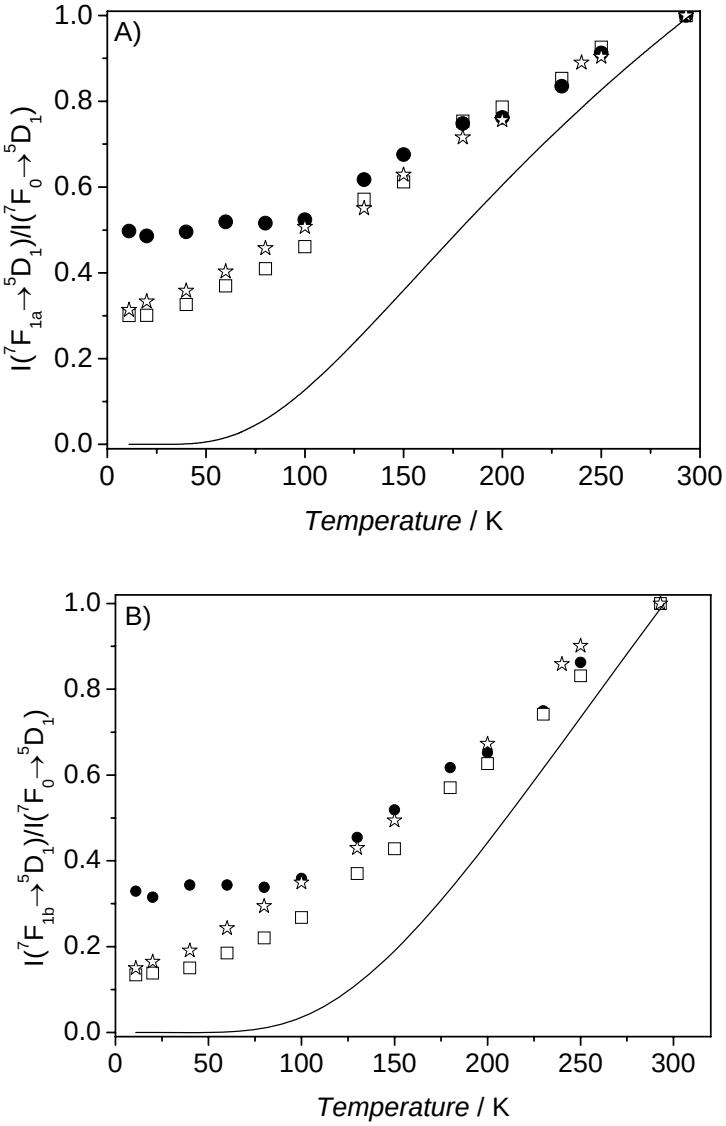

Figure 3.25- Influence of Eu^{3+} concentration on the maximum values of normalised relative intensity ratio of the A) $^7F_{1a}\rightarrow{}^5D_1$ and $^7F_0\rightarrow{}^5D_1$ lines or B) $^7F_{1b}\rightarrow{}^5D_1$ and $^7F_0\rightarrow{}^5D_1$ lines in Gd_2O_3:Eu^{3+} nanotubes. (□, 0.16% annealed at 650 ºC for 6 h; ●, 3.30% at 700 ºC for 3 h and ☆, 6.60% at 850 ºC for 6 h). The full lines are Boltzmann distributions, Eq. (3.5), considering ΔE =217 cm^{-1}, $^7F_{1a}\rightarrow{}^7F_0(C_2)$ (A) and ΔE =352 cm^{-1}, $^7F_{1b}\rightarrow{}^7F_0(C_2)$ (B).

3.2.2.3 – Eu^{3+} (C_2) to Eu^{3+} (S_6) energy transfer at 11 K

In contrast with a previous report,[44] for Eu^{3+} contents above 3.30% and samples annealed at 700 ºC for 3 h, back transfer from $Eu^{3+}(C_2)$-to-$Eu^{3+}(S_6)$ occurs efficiently in the Gd_2O_3:Eu^{3+} nanotubes at 11 K, as shown by the three groups of transitions observed at *ca.* 527-528 ($^7F_0\rightarrow{}^5D_1(C_2)$), 533-535 ($^7F_{1a}\rightarrow{}^5D_1$) and 537-539 nm ($^7F_{1b}\rightarrow{}^5D_1$) arising from

$Eu^{3+}(C_2)$ ions, site-selective excitation spectra of Figure 3.10B and Figure 3.26 monitored the $D_0 \rightarrow {}^7F_1$ (S_6) emission at 582.4 nm.

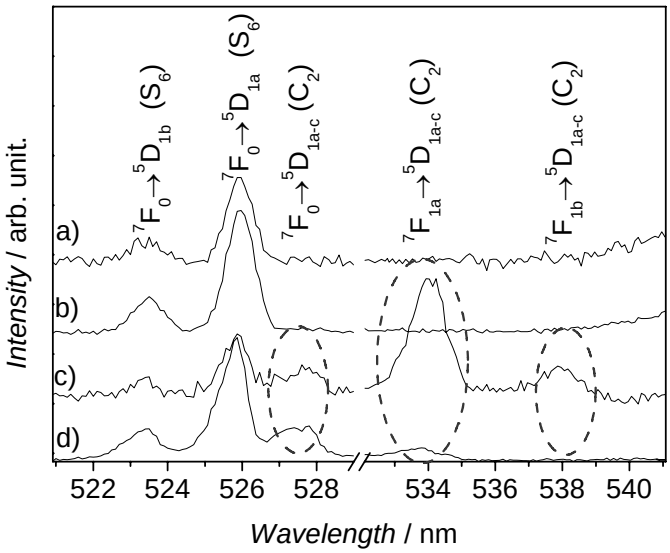

Figure 3.26- Expanded 11 K excitation spectra recorded monitoring the $^5D_0 \rightarrow {}^7F_{1a}$ emission (S_6) at 582.4 nm of $Gd_2O_3:Eu^{3+}$ nanotubes a) 0.16, b) 1.00, c) 3.30, and d) 6.60%; samples annealed at 700 ºC K for 3 hours.

The band at *ca.* 530-532 corresponds to the transition between the vibronic component associated to the $^5D_0 \rightarrow {}^7F_{1a}$ (C_2) transition (*ca.* 78 cm^{-1}) to the $^5D_1$ levels. We note that nanorods also exhibit the $Eu^{3+}(C_2)$-to-$Eu^{3+}(S_6)$ energy transfer, although much weaker (faint $^7F_0 \rightarrow {}^5D_1$ line, Figure 3.13B). Because the energy difference between the $^5D_0$ levels of Eu^{3+} in both sites (*ca.* 100 cm^{-1} for microcrystals[]) can not be bridged thermally at 11 K, some other mechanism must be operative. As both $^7F_{1a,b}$ (C_2) levels are populated at low temperatures, transitions to the $^5D_1(C_2)$ levels become possible, allowing then subsequent energy transfer to the resonant $^5D_{1a}$ (S_6) excited state (Scheme 3.1)

3.2.2.3 – Rationalizing the anomalous PL features

We now attempt to rationalise the anomalous thermalisation effect on the basis of phonon confinement in nanocrystals [28-41,44]. We start by stressing that TEM and XRD did not indicate any significant differences in the morphology (diameter, wall thickness and nanocrystallite size) and crystal structure of samples exhibiting or not anomalous

thermalisation. The PDS in nanocrystals is discrete and the low-frequency acoustical phonons cutoff (ν_{min}) depends on the particles radius *R* as [41]:

$$\nu_{\min} = 2.05\frac{v_s}{2\pi R} \quad (3.6)$$

where v_s is the sound velocity (5000 ms^{-1} in Gd_2O_3). Eq. (3.6) is related to the classical approach of Lamb in which an isolated spherical nanoparticle of diameter *d* cannot support internal vibrations at frequencies less than the so-called Lamb mode frequency $\nu_L = \frac{2\pi v_s}{d}$ [27,40]. Considering a one-dimensional phonon confinement *perpendicular* to the nanotubes wall with a thickness of ~5 nm the phonon cutoff frequency is estimated based on Eq. (3.6) as ~23 cm^{-1} [44]. Thus, it is expected that the PDS should also be discrete at ~220 cm^{-1} and, as a result, the $^7F_{1a}$ and $^7F_{1b}$ levels of the Gd_2O_3:Eu^{3+} nanotubes are not depopulated, the direct phonon relaxation is restricted (much less in the $^7F_{1b}$ level at ~350 cm^{-1}). This explanation seems adequate to rationalise the anomalous thermalisation effect measured by us in the samples with lower R_a (3.30%, calcined at 650 ºC, during 3 and 6 h, and at 750 ºC, during 6 h) and also by Liu *et al.* in analogous Gd_2O_3:Eu^{3+} nanotubes (3.96%, annealing at 500 ºC, 1 h) [44]. However, in the Gd_2O_3:Eu^{3+} nanotubes with 0.16%, annealed at 650 ºC for 6 h, 3.30%, 700 ºC for 3 h and 6.60%, 850 ºC for 6 h, the effect we observe is *ca.* 10–16 times larger and, thus, the phonon cutoff frequency resulting from the (above-mentioned) one-dimensional phonon confinement *perpendicular* to the nanotubes wall does not fully account for it. Moreover, the anomalous thermalisation of the $^2H_{11/2}$ level in the Gd_2O_3:Yb^{3+},Er^{3+} nanotubes also could not be rationalise based only on the one-dimensional phonon confinement *perpendicular* to the nanotubes wall that restrict the direct phonon relaxation from the $^2H_{11/2}$ level to the $^4S_{3/2}$ one, involving a 3-phonon process with single phonon energy around 230-240 cm^{-1} [42] (intriguingly a value similar to the $^7F_0$–$^7F_1$ energy difference previously discussed).

As a further effect from this confinement the discrete features of the PDS – approximately modelled by a sequence of discrete sharp peaks [41-42] – may play a crucial role in the $^7F_{1a,1b}$ thermal populations. The energy matching between the available phonons frequency and the Eu^{3+} and Er^{3+} electronic levels provides a route to their thermalisation (depopulating process). Slight changes in the structure of the nanotubes (for instance due to thermal treatment or modifications in the Eu^{3+} or Yb^{3+}/Er^{3+} contents) may induce considerable changes in the discrete PDS, thus modifying completely the energy resonance conditions and the intensity ratio values. For sizes of *ca.* 5 nm, for instance, abrupt changes of more than one

order of magnitude from PDS maxima to almost zero values with small changes of phonon energy are profuse in the PDS discrete spectra of Y_2O_2S nanocrystals (Fig. 2 of Ref. [41]).

Moreover, the different values obtained for the R_{1a} and R_{1b} ratios of $Gd_2O_3:Eu^{3+}$ nanotubes may also be explained by this extra resonant effect, indicating that the two $^7F_{1a,1b}$ electronic levels have distinct anomalous thermalisations. For R_{1b} the effect of PDS discretization is less effective, because the PDS spectra exhibit a baseline at higher energies.

In principle, the exposure of the nanotubes to the ambient moisture would produce an amorphous layer at the nanotube' surfaces increasing the effective wall thickness and broadening the PDS spectra. Eventually this would destroy the nanoconfinement conditions and therefore the thermalisation behaviour of the $^7F_1$ level will be similar to that of the $Gd_2O_3:Eu^{3+}$ nanorods.

A quantitative analysis of this effect (beyond the scope of the present thesis) should take into account the presence of nanometer-size clusters (smaller than 5 nm) in the walls of the Gd_2O_3 nanotubes which may reduce the phonons cutoff frequency.

Although Ln^{3+}-rich nanometer-size clusters may, in principle, also form in $Gd_2O_3:Eu^{3+}$ and $Gd_2O_3:Yb^{3+},Er^{3+}$ nanorods and microcrystals, the anomalous thermalisation effect is absent because the clusters are embedded in extended three-dimensional Gd_2O_3 domains, where no specific direction for one-dimensional phonon confinement may be defined, with the ensuing modifications in the phonon density of states (the three-dimensional Gd_2O_3 regions behave as a thermal bath depopulating the $^7F_1$and $^2H_{11/2}$ levels) .

3.3 – Conclusions

$Gd_2O_3:Eu^{3+}$ (0.16, 1.00, 3.30 and 6.60% Eu^{3+} mole content) and $Gd_2O_3:Yb^{3+},Er^{3+}$ (5.00% Yb^{3+}, 1.20 % Er^{3+}) nanotubes, $Gd_2O_3:Eu^{3+}$ nanorods (3.30%) and $Gd_2O_3:Eu^{3+}$ microcrystals (3.65%) have been obtained by hydrothermal synthesis using different annealing conditions, 650 to 850 ºC and times interval ranging from 3 to 6 h. For nanotubes, the role of the ion-phonon interaction on the photoluminescence features and excited state dynamics is completely different from the role for nanorods and microcrystals, due to the absence of low-frequency phonon modes. Hot bands arising from the two lowest-lying $^7F_1$ Eu^{3+} crystal-field levels are observed in the excitation spectra of $Gd_2O_3:Eu^{3+}$ nanotubes with higher intensity than the corresponding bands originated in the $^7F_0$ ground state between 300 and 11 K. For $Gd_2O_3:Yb^{3+},Er^{3+}$ nanotubes, hot bands arising from the $^2H_{11/2}$ Er^{3+} level are also discerned in the emission spectra measured in that same temperature range with similar intensities than the ones originated in the $^4S_{3/2}$ low-energy level. These remarkable anomalous thermalisation

effects, which are strongly dependent on the thermal history of the samples and on the Eu^{3+} or Yb^{3+}/Er^{3+} concentrations, is one order of magnitude larger than previously reported for similar $Gd_2O_3:Eu^{3+}$ (3.96%, annealing at 500 ºC, 1 h) nanotubes.

The anomalous thermalisation may be rationalized in the theoretical framework of ion-lattice interaction considering both, the one-dimensional phonon confinement *perpendicular* to the nanotubes wall (as previously proposed for $Gd_2O_3:Eu^{3+}$ nanotubes), and the discrete features of the phonon density of states. The energy matching between the frequency of the available phonons and the $^7F_{1a,1b}$ and $^2H_{11/2}$ electronic levels provides a route to their thermalisation (depopulating process). Minor changes in the structure of the nanotubes (due to thermal treatment or Ln^{3+} concentration) may induce considerable changes in the discrete phonon density of states, entirely modifying the energy resonance conditions and the intensity ratio values.

The confinement on electron-phonon interaction in nanocrystals impacts other aspects of the luminescence dynamics of lanthanide ions that depend on the low-energy phonon modes of the lattice (*e.g.* in phonon-assisted energy transfer and upconversion processes). Therefore, a fundamental understanding of the effects of phonon confinement on the luminescence features is crucial, particularly in systems such as $Gd_2O_3:Eu^{3+}$ and $Gd_2O_3:Yb^{3+},Er^{3+}$ nanotubes that have been used as fluorescent markers in a variety of immunosensing applications.

Chapter 4 – Modification of AFM tips with $Gd_2O_3:Eu^{3+}$ nanocrystals

4.1 – Introduction

Scanning probe microscopy (SPM) is one of the most important tools in nanoscale characterisation (see description of this technique in Appendix B5). In addition to providing excellent resolution and sensitivity, the tip (the central component of the SPM) is a nanoprobe that may be functionalized to measure various properties depending on the mode of operation. In particular, to improve the resolution of atomic force microscopy (AFM) images, the tips have been intentionally modified by different methods. Often, the resolution gain has been attributed to the specific geometry of the modified tips [154]. Recent examples include the controlled fabrication of carbon nanotubes (CNTs) probe tips for tapping-mode AFM imaging [154] and high-resolution magnetic force microscope probes using preformed Ni and Co magnetic nanowires [156] or CoFe-film-coated CNTs.

In addition, the physical or chemical properties may be modified, transforming the AFM tip into a local probe sensitive to a specific interaction/property. For example, optically active tips have been developed for high-resolution scanning near-field optical microscopy (SNOM), namely apertureless SNOM (ANSOM) [157-161]. Alternatively, the luminescence of commercial AFM tips may be used for the combination of optical and conventional force microscopies. Si_3N_4 are frequently used in liquid cells [162-163] and high resolution optical imaging based on the photoluminescence of commercial Si_3N_4, Si and high-density C-based AFM tips (which scatter incident green light as in ANSOM) has been reported [158,159]. The AFM tip acts as a tiny light source, which may be scanned to produce an image. This idea has also been implemented using a fluorescent porous silicon particle as the light source [164]. However, due to their low spring constant values (<1 Nm^{-1}), the Si_3N_4 tips have limited use in fluids, as well as in tapping AFM, whereas porous silicon is very sensitive to fast oxidation and chemical contamination.

In this chapter, a new approach towards the use of the light-emission features of lanthanide ions in real-time imaging applications is reported: the functionalization of an AFM and SNOM tips with $Gd_2O_3:Eu^{3+}$ nanorods achieved by DEP [170–173], see a scheme of DEP deposition in Scheme 4.1. To the best of our knowledge, this is the first report on the fabrication of AFM tips coated with lanthanide-containing nanorods using this technique. DEP

has been used to assemble Ni and Co nanowires on the tip of a commercial AFM cantilever [156], CNTs into micro-electrodes and submicrometre diameter fibrils [170], and to fabricate short CNT tips [173]. The unique geometry and properties of nanostructures such as Gd_2O_3:Eu^{3+} nanorods and CNTs make them attractive building blocks for new functional imaging devices, such as high-resolution SNOM probes [112,113]. Moreover, DEP may efficiently manipulate, align and assemble the Gd_2O_3:Eu^{3+} nanorods, allowing the fine control of their position, as well as the homogeneity and thickness of the coating layer, increasing the layer-to-tip adhesion and affording optically active AFM tips.

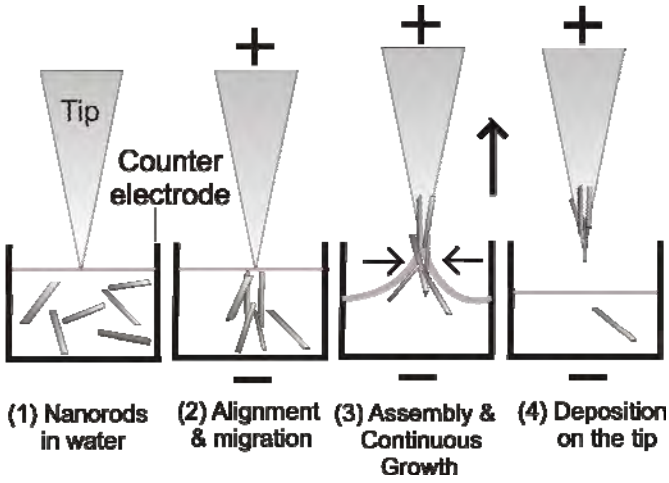

Scheme 4.1- Experimental set up used for DEP deposition

4.2 – Phenomenological definition DEP

The term "dielectrophoresis" was coined by H. A. Pohl (1951) [165,166], who performed experiments with small plastic particles suspended in insulating dielectric liquids and found that the particles would move in response to the application of a nonuniform AC or DC electric field. The phenomenological bases of his definition are listed below:

a) Particles experiment a DEP force only when the electric field is nonuniform;
b) The DEP force does not depend on the polarity of the electric field and is observed with AC, as well as DC excitation;
c) Particles are attracted to region of stronger electric field when their permittivity ($\varepsilon_{particles}$) exceeds that of the suspension medium (ε_m), i. e., when $\varepsilon_{particles} > \varepsilon_m$;
d) Particles are repelled from regions of stronger electric field when $\varepsilon_{particles} < \varepsilon_m$;
e) DEP is most readily observed for particles with diameters ranging from approximately 1 to 1000 μm.

DEP involves the translation motion of a neutral matter caused by the polarization effect in a nonuniform electric field lines and differs from electrophoresis process where a charged particle is attracted to electrode with opposite polarity in a uniform or nonuniform applied field. This gradient field must be created using metallic tips as electrode, by the dielectrophoretic process the nanorods will be deposited or stay concentrates next to surface of these materials. This behaviour is also dependent on experimental parameters, such as bias applied, frequency, size and length of the electrodes.

4.2.1 – Dielectrophoretic force [167]

Two distinct types of electromechanical interactions may be identified: imposed field and mutual particle interaction. Imposed field interaction reign when a single particle, or an ensemble of non interacting particles, is influenced by an externally imposed field. Mutual particle interactions occur where particles are so closely spaced that the local field of a particle influences its neighbours.

Let us start to estimate the net force on a small dipole, Figure 4.1.

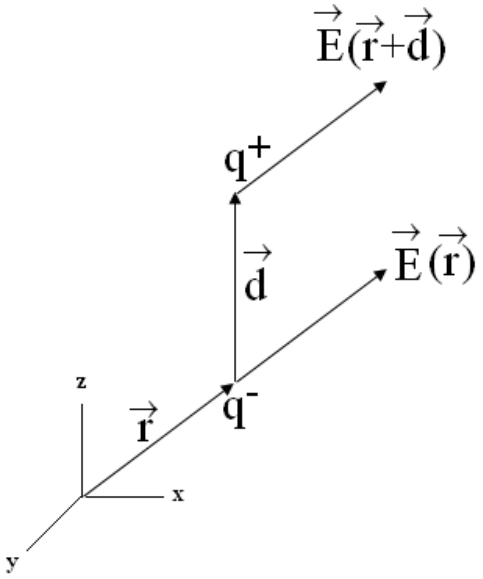

Figure 4.1 – Representation of the net force on a small dipole of strength $|\vec{p}| = q|\vec{d}|$ in a non uniform field.

In a non uniform electric field, the two charges (+q and –q) will experience different values of the vector field $\vec{E}$ and the dipole will experience a net force. Performing a sum of the forces on the particle, we have:

$$\vec{F} = q\vec{E}(\vec{r}+\vec{d}) - q\vec{E} \qquad (4.1)$$

where $\vec{r}$ is the position vector of –q. If $|\vec{d}|$ is small compared to the characteristic dimension of the electric field nonuniformity, the electric field can be expanded using a Taylor series:

$$\vec{E}(\vec{r}+\vec{d}) = \vec{E}\left(\vec{r}\right) + (\vec{d}\cdot\nabla)\vec{E}\left(\vec{r}\right) + \ldots \tag{4.2}$$

Thus

$$\vec{F}_{dipole} = (q\vec{d}\cdot\nabla)\vec{E} + \ldots \tag{4.3}$$

If the limit $|\vec{d}| \to 0$ is considered, the force on an infinitesimal dipole is given by:

$$\vec{F}_{dipole} = (\vec{p}\cdot\nabla)\vec{E} + \ldots \tag{4.4}$$

This approximation, referred as dielectrophoretic approximation, is adequate for imposed field interaction because the dimensions of the electrodes are much larger than the particles. Similarly, the torque is $\vec{T}_{dipole} = \vec{p}\times\vec{E}$.

Consider a particle suspended in a fluid of permittivity ε_m upon a z- direction electric field. The electrostatic potential ($\phi_{dipole} = p_{eff}\cos\theta/(4\pi\varepsilon r^2)$) satisfies Laplace's equation every where because of the divergence and curl free properties of the electrostatic field. The assumed solution for the potential outside (ϕ_1) and inside (ϕ_2) the particle takes the form [167]:

$$\phi_1(r,\theta) = -Er\cos\theta + \frac{A\cos\theta}{r^2},\ r > R \tag{4.5}$$

$$\phi_2(r,\theta) = -Br\cos\theta,\ r < R \tag{4.6}$$

where A and B are unknown coefficients to be determined using the boundary conditions. The boundary conditions are applied at r=R, the surface of the particle. First, the electrostatic potential must be continuous across the particle-fluid boundary:

$$\phi_1(r=R,\theta) = \phi_2(r=R,\theta) \tag{4.7}$$

Second, the normal component of the displacement flux vector must be continuous across the boundary:

$$\varepsilon_1 E_{r1}(r=R,\theta) = \varepsilon_2 E_{r2}(r=R,\theta) \tag{4.8}$$

where $E_{r1} = -\partial\phi_1/\partial r$ and $E_{r2} = -\partial\phi_2/\partial r$ are the normal electric field components in the fluid and particle, respectively. Combining the Eqs. 4.5, 4.6 and Eqs. 4.7, 4.8 results in:

$$A = \frac{\varepsilon_{particle} - \varepsilon_m}{\varepsilon_{particle} + 2\varepsilon_m} R^3 E \text{ and } B = \frac{3\varepsilon_m}{\varepsilon_{particle} + 2\varepsilon_m} E$$

with this a general relationship between the effective moment and the coefficient A is obtained:

$$p_{eff} = 4\pi\varepsilon_m A \tag{4.9}$$

For the case of the homogeneous, dielectric particle, the expression for the effective dipole moment is:

$$p_{eff} = 4\pi\varepsilon_m K R^3 E$$

The net dielectrophoretic force acting upon a lossless dielectric particle of permittivity $\varepsilon_{particle}$ and length a, suspended in a medium of permittivity ε_m and subjected to an electric field E, is:

$$\vec{F}_{DEP} = 2\pi\varepsilon_m a^3 K \nabla E^2$$

where the expression for the force has been rewritten using the Clausius-Mossoti function K (this provides a measure of strength of the effective polarization of a particle as function of $\varepsilon_{particle}$ and ε_m):

$$\vec{F}_{DEP} = 2\pi a^3 \varepsilon_m \left[\frac{\varepsilon_{particle} - \varepsilon_m}{\varepsilon_{particle} + 2\varepsilon_m} \right] \nabla E^2 \tag{4.10}$$

However, when an AC field is used, these equations must be adapted assuming that the constants in the expressions for the potential functions ϕ_1 and ϕ_2 are complex.

A close examination of Equation 4.10 reveals important features of the dielectrophoretic effect exhibited by lossless dielectric particles in lossless media. For reference, these are enumerated below:

a) F_{DEP} is proportional to particle volume;

b) F_{DEP} is also proportional to ε_m, the dielectric permittivity of the medium in which the particle is suspended;

c) The DEP force vector is directed along the gradient of the electric field intensity $\nabla(E^2)$, which, in general, is not parallel to the electric field vector $\vec{E}(r)$.

d) The DEP force depends upon the magnitude and sign of K, the Clausius-Mossoti function.

Considering the items c) and d) it is possible to distinguish between positive and negative dielectrophoresis effect:

Positive DEP: K>0 (or $\varepsilon_2>\varepsilon_1$). Particles are attracted to electric field intensity maxima and repelled from minima.

Negative DEP: K<0 (or $\varepsilon_2<\varepsilon_1$). Particles are attracted to electric field intensity minima and repelled from maxima.

For time-average DEP force, by using the Equation 4.10 to replace the complex effective dipole moment, we have:

$$\vec{F}_{DEP} = 2\pi a^3 \varepsilon_m \,\mathrm{Re}\left[\frac{\varepsilon_{particle} - \varepsilon_m}{\varepsilon_{particle} + 2\varepsilon_m}\right]\nabla E_{rms}^2 \qquad (4.11)$$

where E_{rms} still a function of position, is the root-mean-square magnitude of the imposed AC electric field.

Since the response of materials to alternating fields is characterized by a complex permittivity, it has real and imaginary parts, in the following way:

$$\varepsilon(\omega) = \varepsilon'(\omega) + i\varepsilon''(\omega) \qquad (4.12)$$

ε' is the real part of the permittivity, which is related to the stored energy within the medium. ε'' is the imaginary part of the permittivity, which is related to the dissipation (or loss) of energy within the medium.

In a lossy medium, the total current density has contribution from conduction and displacement density currents, thus $J_{tot} = J_{co} + J_{dis} = \sigma E - i\omega\varepsilon' E = -i\omega\varepsilon'' E$. By considering this relation, the complex permittivity has the following dependence with the frequency of the electric field [168]:

$$\varepsilon''(\omega) = \varepsilon'(\omega) - \frac{i\sigma}{\omega} \qquad (4.14)$$

where σ is the conductivity and ω is the frequency of the AC electric field.

4.3 – Calculus of the DEP force on $Gd_2O_3:Eu^{3+}$ nanorods:

Permittivities of the $Gd_2O_3:Eu^{3+}$ nanorods, in pellet and in aqueous suspension, were monitored versus electric field frequency as follows:

a) The capacitance (C_p) and parallel resistance (R_p) were measured at the frequency interval of 75 KHz – 30 MHz using a HP 4285A Precision LCR meter (75 KHz-300MHz) coupled to a HP 1645 Dielectric test fixture, applied voltage equal 1 V.

b) The distance between the electrodes was checked for each test, this distance corresponds to the thickness of the $Gd_2O_3:Eu^{3+}$ nanorods pellet or, in the case of the suspension, the thickness of the suspension drop.

c) The C_p and R_p parameter are related with the static dielectric constant (ε_s) by:

$$\varepsilon_s = \varepsilon_0 \varepsilon_r \qquad (4.15)$$

where ε_0 is the space permittivity ($\varepsilon_0 = 8.85 \times 10^{-12} F/m$) and ε_r is the relative dielectric constant of test material.

Experimentally the value of ε_s is obtained by:

$$\varepsilon_s = \frac{t}{A} C_p \tag{4.16}$$

where t is the thickness (m) and A is the area of the electrode (equal to 19.6 μm^2). Combining the equations (4.15) and (4.16), the $\varepsilon_r^{'}$ parameter, corresponding to the real part, is given by:

$$\varepsilon_r^{'} = \frac{t}{A} \cdot \frac{C_p}{\varepsilon_0} \tag{4.17}$$

the imaginary part, denoted by $\varepsilon_r^{''}$, is given by:

$$\varepsilon_r^{''} = \left(\frac{t}{2\pi \ \omega \ A \ \varepsilon_0} \right) \tag{4.18}$$

The evolution of the DEP force versus electric field frequency was calculated by considering our experimental parameters such: dimension of electrodes (metallic ring with 1 cm in diameter and metallic tip with 200 nm in diameter), a coaxial geometry was considered to obtain the distribution of the gradient of the electric field lines around the tip, average length of the nanorods (~1 μm) and permittivity values (distilled water as medium and $Gd_2O_3:Eu^{3+}$ nanorods as particles). The curve generated by this calculus reveals forces with intensity in the range of 34-39 nN, Figure 4.2.

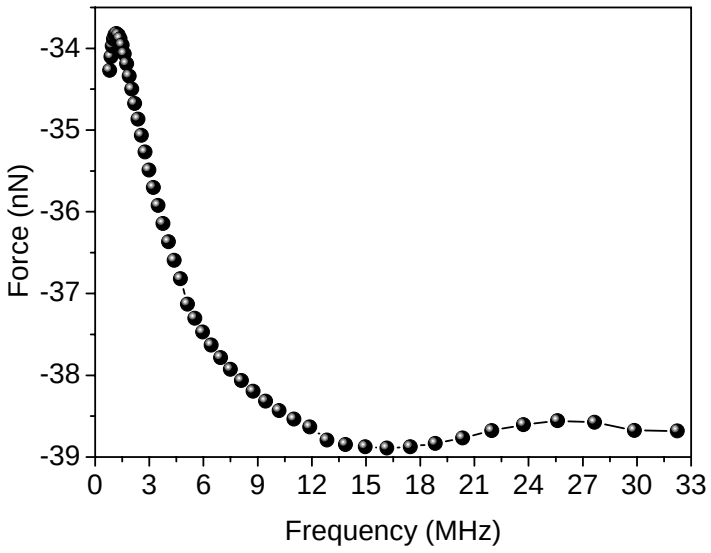

Figure 4.2 - DEP force versus electric field frequency

Figure 4.2 reveals that the magnitude of the DEP force is not constant in this frequency interval, being more intense at frequencies around 1-6 MHz. Therefore, for the DEP deposition, we selected electric field frequencies whitin of this range.

4.4 - Coating of the AFM or SNOM tips with $Gd_2O_3:Eu^{3+}$ nanorods by DEP

The dielectrophoresis set-up is similar to that reported previously for assembly of Ni and Co nanowires and CNTs [169-173] (see Scheme 4.1). As the process requires a conducting electrode the deposition was performed on a Cr–Au-coated Si AFM tip (NSC18/Cr–Au, MikroMasch Spain with tip diameter <100 nm) or tungsten wire (aperture less SNOM tip, diameter 200 nm), using 0.5 ml of an 0.01 mg mL^{-1} distilled water suspension of $Gd_2O_3:Eu^{3+}$ nanorods previously placed into a stainless steel ring support with a Teflon® base (diameter: 1 cm, depth: 0.5 cm, wall thickness: 0.1 cm). The metallic ring and tip electrodes were connected to the AC power supply (Agilent 33250A 80 MHz Function Arbitrary Waveform generator), the AC applied voltage and frequency ranging from 5 to 10 V and 2 to 4 MHz, respectively. Under the guidance of an optical microscope coupled to a CCD, the Cr–Au-coated Si cantilever (or tungsten wire) was translated horizontally, using a motorized translation stage, to contact the suspension surface followed by a gradual withdrawal under the AC field until the AFM tip was coated. A picture of the experimental setup is showed at Figure 4.3.

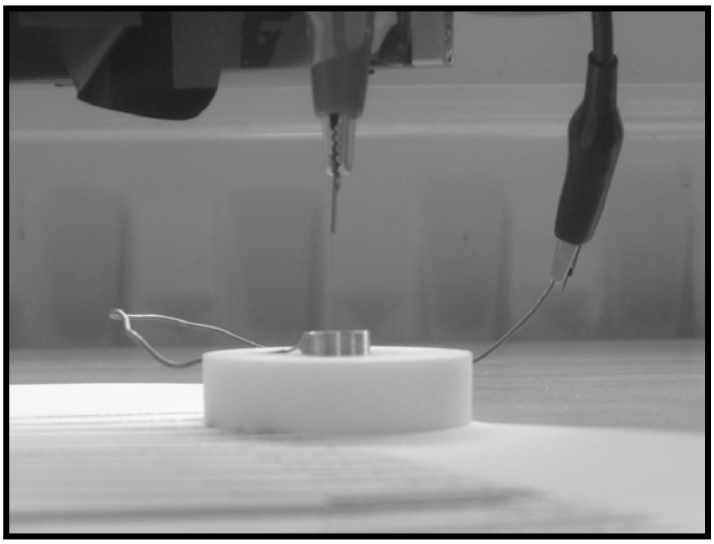

Figure 4.3 - Experimental setup for dielectrophoresis deposition: Teflon support, metallic ring and tungsten wire electrode.

4.5 – Morphology and optical properties of $Gd_2O_3:Eu^{3+}$ modified AFM tips

The SEM images of the AFM tip coated with $Gd_2O_3:Eu^{3+}$ nanorods by DEP deposition before and after (respectively, Figure 4.4A-B) use (see below) reveal that: (i) nanorods-modified region is homogeneous and extends *ca.* 2.5 μm up from the tip apex; (ii) the tip is stable under working conditions. The effective diameters of the pristine- and nanorods modified-tips seem to be similar in both cases (minimum of *ca.* 110 nm). For comparison the Figure 4.4 also presents a SEM image of the AFM tip before the deposition (Figure 4.4B, bottom). The coated region is stable in air, and preserves the chemical, structural and optical properties of the $Gd_2O_3:Eu^{3+}$ nanorods.

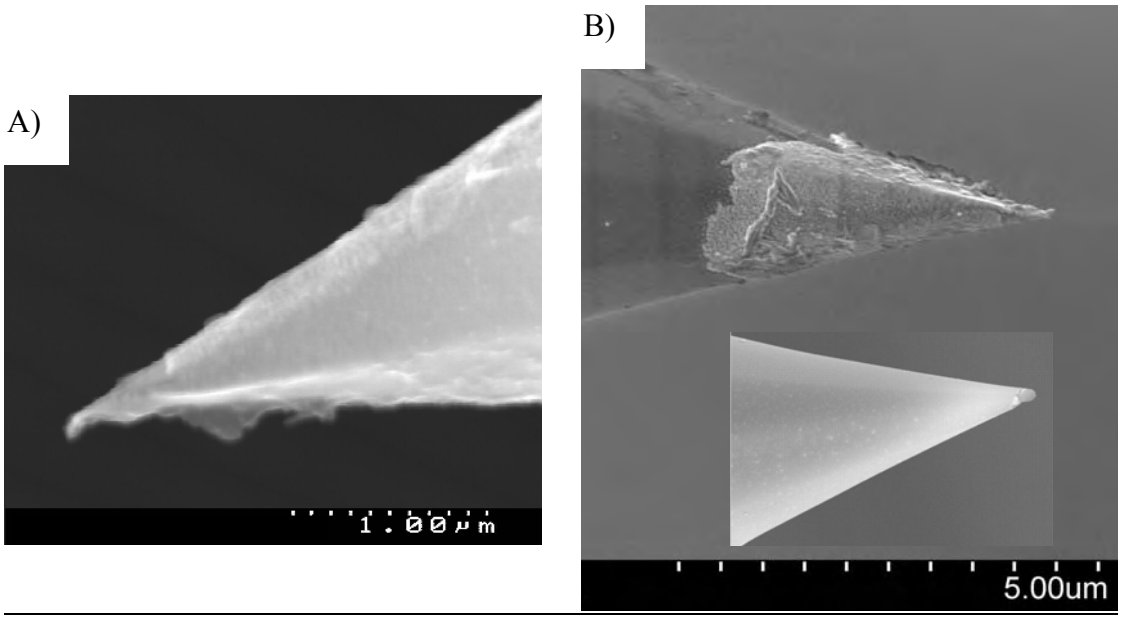

Figure 4.4 - SEM images from commercial Cr-Au coated Si AFM tip that was modified with $Gd_2O_3:Eu^{3+}$ nanorods by the dielectrophoresis technique, being: a) image taken before the use of this modified tip as probe in AFM image recording procedure and b) after. The inset depicts the same tip before the deposition treatment.

Upon UV excitation (254 nm) the modified tips (before and after use) display an emission spectrum identical to that of the $Gd_2O_3:Eu^{3+}$ nanorods (Figure 4.5). Slightly broader lines of the modified tips are due to the increase of the monochromator slits width (from 0.1 to 0.5 mm), in order to enhance the signal. The excitation, emission and absolute quantum yield (Table 3.2) features from the parent $Gd_2O_3:Eu^{3+}$ nanorods were presented in Chapter 3.

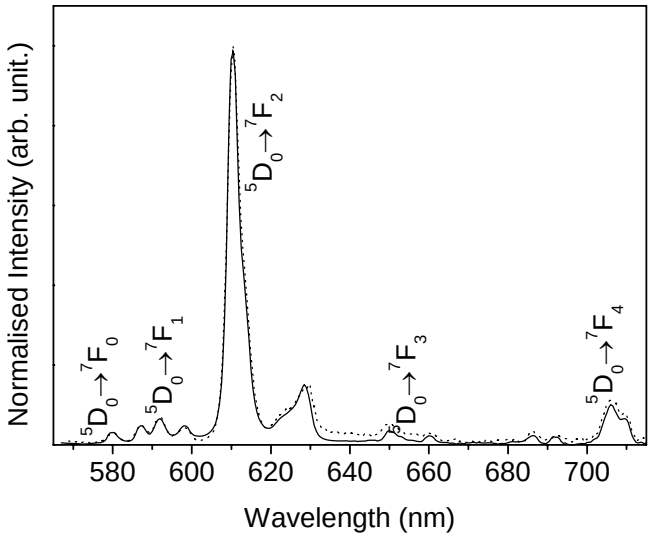

Figure 4.5 – Emission spectra recorded before (solid line) and after (dashed line) the use of this modified tip as probe in AFM image recording procedure.

4.6 – Performance of the $Gd_2O_3:Eu^{3+}$ modified AFM tips

The imaging performances of pristine and nanorods-modified AFM tips were tested in AFM experiment. The two tips were used to characterize the morphology of a grating written in an organic-inorganic methacrylate Zr-based oxo-cluster and poly(oxyethylene)/siloxane hybrid [175,176]. The grating morphology is characterized by a periodic pattern arising from a refractive index variation with a period of 480 nm as presented schematically in Scheme 4.2.

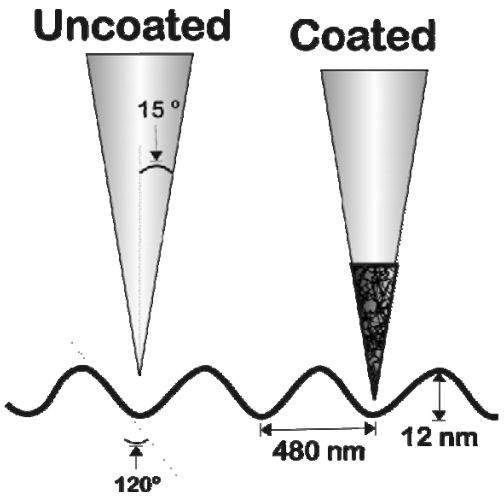

Scheme 4.2 - Cross-section profile representation and differences in the depth measured with pristine and modified tips.

Good quality AFM images were obtained with the Au-pristine and nanorods modified Cr-Au tip, Figure 4.6A-B.

Close inspection of the depth profiles acquired with Cr-Au pristine, nanorods modified Cr-Au, and silicon tips, Figure 4.7A-C respectively, reveals considerable differences in the apparent depth of protrusions. For the modified tip, the profile is significantly deeper than for the uncoated one.

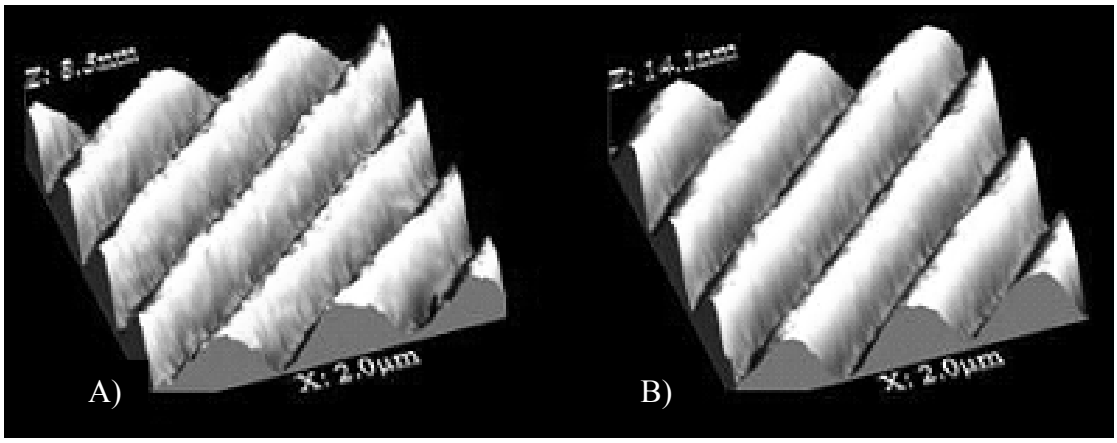

Figure 4.6 - 3D representation of height AFM images from a grating written in an organic-inorganic methacrylate Zr-based oxo-cluster and poly(oxyethylene)/siloxane hybrid recorded using: A) commercial Cr-Au coated Si AFM tip (pristine) and B) the same tip modified with $Gd_2O_3:Eu^{3+}$ nanorods

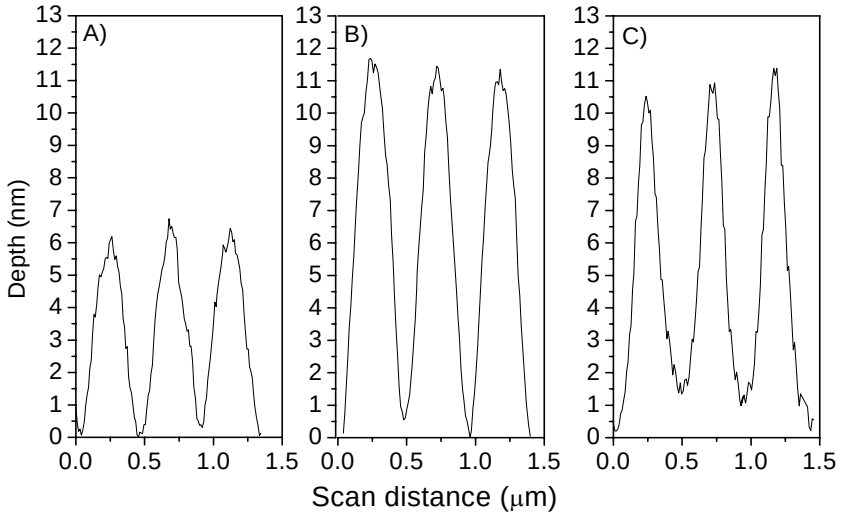

Figure 4.7 - AFM depth profiles taken from images acquired using A) commercial Cr-Au coated Si AFM tip (pristine), B) the same tip modified with $Gd_2O_3:Eu^{3+}$ nanorods and C) commercial Si AFM tip (effective diameters of ca. 20 nm, height AFM image not shown)

This means that the contact forces are significantly different for functionalized and Au-coated tips. This is demonstrated in Figure 4.8 where force-distance curves are shown for comparison. Au-coated tips are less adhesive to the surface and cause significant deformation of test organic-inorganic structures. Nanorods-modified tips show stronger adhesion and do not modify the surface during imaging. Similar results were achieved with images recorded in tapping and contact modes.

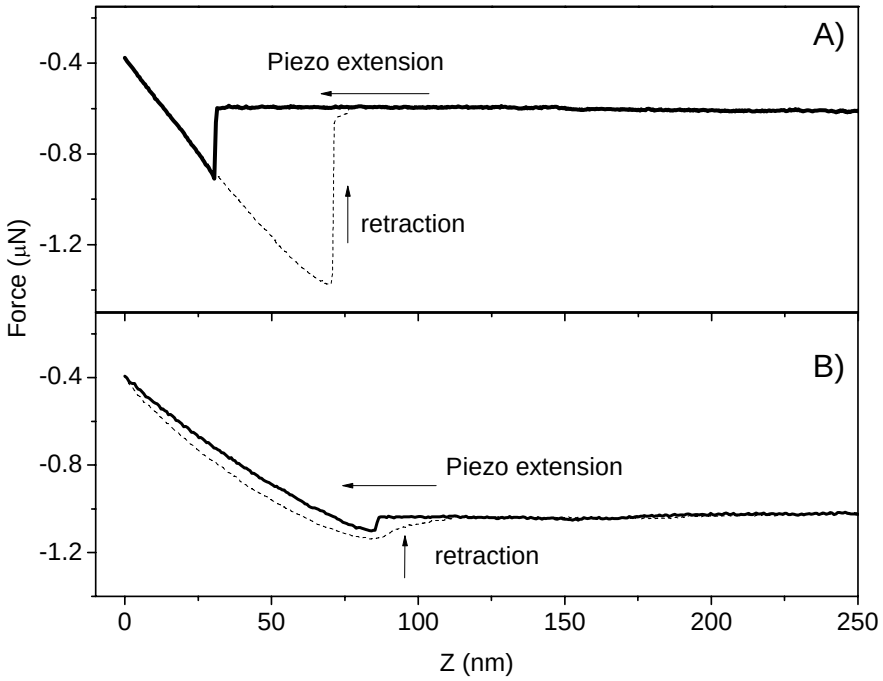

Figure 4.8 - Extension (dashed line) and retraction (solid line) force curves between the hybrid surface sample obtained using: A) commercial Cr-Au coated Si AFM tip, modified with Gd_2O_3:Eu^{3+} nanorods, and B) the same unmodified (pristine) tip.

Using an AFM grating (hard surface-aluminum steps on a silicon wafer) the measured topography profiles were almost the same for coated and uncoated tips, which contrasts with results obtained for the grating written in the organic-inorganic hybrid material. For the latter, the observed difference in depth profiles cannot be solely attributed to the geometric factor contribution, since the diameters of the modified and pristine tips seem to be close to each other and the angle of analyzed sample channel aperture (120º) is much bigger than the tip angle (30º). However, the shape of the force-distance curve indicates significant modification of the surface (strong adhesive force and possible indentation of the material) for pristine tip while relatively small adhesion is observed using Gd_2O_3:Eu^{3+} modified tips where the real

profile of the surface of organic-inorganic hybrid test samples could be obtained. Similar effects were observed in 1,4-benzene-dimethanethiol layer where large attractive force inhibits reliable AFM probing [177]. Using etched Si tips allowed decreasing the adhesion force and very reliable data acquisition. Similarly, it can be concluded that $Gd_2O_3:Eu^{3+}$ coating can be used to decrease the adhesion force between the tip and the soft organic-inorganic hybrid surface making possible regular topography imaging on hybrid test samples.

4.7 – $Gd_2O_3:Eu^{3+}$ modified SNOM tips

Our contribution to SNOM technique concerns the preparation and characterisation of the new emitting tips prepared by DEP. The tips are illuminated in transmission mode with a focused laser beam excitation (Argon λ=457nm), (spot size <1µm). The tip is moved with a piezo stage and the laser illuminates the tip. The tips are oriented from bottom to top as indicated in the Figure 4.9A. Emission is collected with a bandpass filter in the range 580-640nm. Figure 4.9B shows the emission collected from the tip and the localisation of the nanorods at the tip end. These measurements were performed by Dr. Lyonel Aigouy at University Pierre & Marie Curie, Paris.

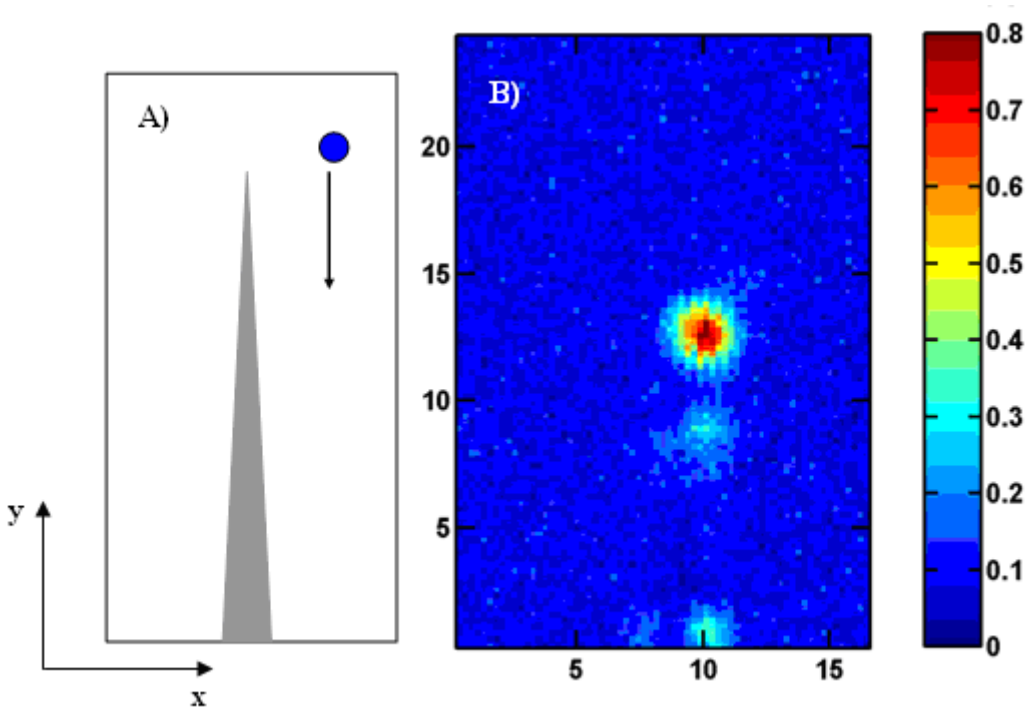

Figure 4.9 – A) Diagram ilustrating the selective position of tip and Argon laser to acquire the luminescence of $Gd_2O_3:Eu^{3+}$ modified SNOM tip, B) The light emission distribution acquired upon conditions described in a). The x,y and color scale are in µm units.

Red emission is acquired mainly from the tip end region, indicating adequate localisation of the $Gd_2O_3:Eu^{3+}$ nanorods deposited by DEP and thus allowing its uses as SNOM tip. However, the wavelength excitation at 457 nm is not proper because it does not match the intra *4f* transitions lines of the Eu^{3+} ions, thus the sign intensity can be enhanced, for instance, using wavelength excitation at 465-467 nm ($^7F_0 \rightarrow {}^5D_2$ transition lines of Eu^{3+}) or 522-527 nm ($^7F_0 \rightarrow {}^5D_1$ transition lines of Eu^{3+}).

4.8 – Conclusions

We developed a simple method for the functionalization of AFM and SNOM tips with $Gd_2O_3:Eu^{3+}$ nanorods. The resulting tips remain sharp, retaining the benefits of AFM imaging while possessing photophysical properties of the attached nanorods, high efficiency, sharp emission lines and long lifetimes (ms). Emitting probes with various emission colours can be prepared and easily tailored for specific applications. Regular topography imaging on test hybrid organic-inorganic samples was improved by using functionalized tips.

Chapter 5 – Catalytic performance of ceria nanotubes

5.1 – Introduction

Cerium oxide has attracted much attention for catalytic and environmental applications, such as depollution of noxious compounds from gaseous streams originating from industrial productions and from automobiles, the (industrial) gas-phase catalytic dehydrogenation of ethylbenzene to styrene, and the degradation of organic pollutants in wastewater through catalytic wet oxidation [178]. The interest arises from its remarkable Ce^{3+}/Ce^{4+} redox and oxygen storage capacity properties. According to the literature the reduction of the ceria is controlled by the nature of oxygen vacancies, albeit the mechanism of creation of these favourable defects and their roles in the activation mechanisms, reducibility and activity of nanosized ceria at the atomic level is still lacking [179]. Cerium oxide has also been used in reactions for therapeutic applications to avoid reactive oxygen intermediates (ROI, like hydrogen peroxide) that increases retinal neurons degeneration (cerium nanoparticles were effectively used to scavenge these ROI within to retinal cells and inhibit the progressive degeneration) [180].

The preparation route determines structural and surface properties of cerium oxide and there is a growing interest in controlling the morphology to obtain cerium oxide nanotubes. Very recently, cerium oxide nanotubes have been produced by hydrothermal alkali treatment [87], precipitation method [181], simple solid-liquid interface reaction route [89], by etching $Ce(OH)_3$ nanotubes/nanorods with H_2O_2 [88] or using carbon nanotubes as templates by a liquid phase deposition method [90].

Here cerium oxide nanotubes/nanorods (synthesis described in Appendix A2) were tested as catalyst in liquid phase reactions for oxidation of ethylbenzene as substrate using *tert*-butyl hydroperoxide (*t*-BuOOH) or H_2O_2 as oxidising agent. The role of the Ce^{3+}/Ce^{4+} redox on the reaction mechanism is discussed. Additionally, the ultraviolet–visible absorption and luminescence techniques were used as probe to study the presence and environment of Ce^{3+} in the samples before and after exposure to *t*-BuOOH or H_2O_2. The fluorescence of Ce^{3+} activated compounds is widely studied [182]. Usually, the Ce^{3+} emission consists of the

allowed electric dipole $5d \rightarrow 4f$ transitions, since the Ce^{3+} has a $4f$ configuration; the ground states have a doublet with an energy separation around 2000 cm^{-1} ($^2F_{5/2}$ *and* $^2F_{7/2}$). The lower excited states are the crystal field components of the 5*d* configuration. Also a broad band in a lower energy position has been attributed to the Ce4$f \rightarrow$O2p charge transfer.

5.2 – Structural data of ceria nanotubes

The powder XRD patterns of CeNT, CeNT-BuOOH, CeNT-H_2O_2 and CeNT recovered after catalysis (CeNT-PhEt-BuOOH-run2) are indexed to cubic fluorite-type CeO_2 (JCPDS34-394) (Figure 5.1).

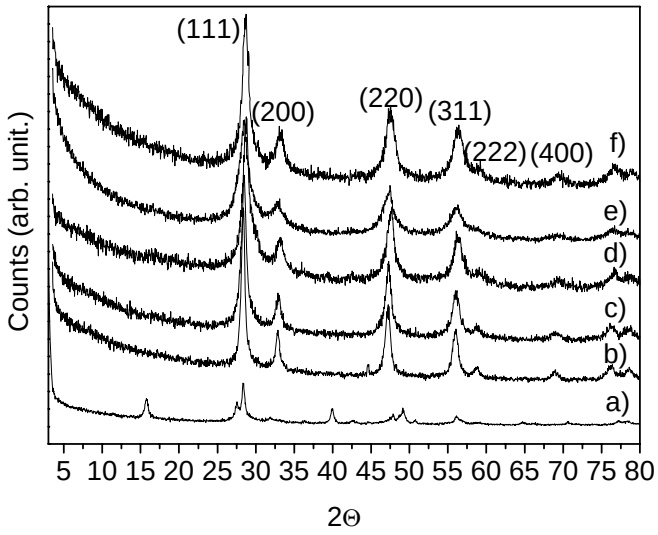

Figure 5.1 – Powder XRD patterns of a) freshly $Ce(OH)_3$, b) CeNT, c) CeNT-PhEt-BuOOH, d) CeNT-BuOOH, e) CeNT-H_2O_2 and f) CeT.

The TEM shows that CeNT consists of nanotubes (and a few nanorods) with a few tens of diameter and lengths of up to several hundreds of nanometers. Some fragmentation of the nanotubes and formation of small 6-8 nm spherical nanoparticles occurred for CeNT-PhEt-BuOOH and CeNT-BuOOH and is much more significant for CeNT-H_2O_2 and CeNT-PhEt-H_2O_2 (Figure 5.2); this is consistent with ref. [181]. The formation of small nanoparticles is consistent with the broadening of the powder XRD reflections, which is clear in the case of CeNT-H_2O_2 (Figure 5.1).

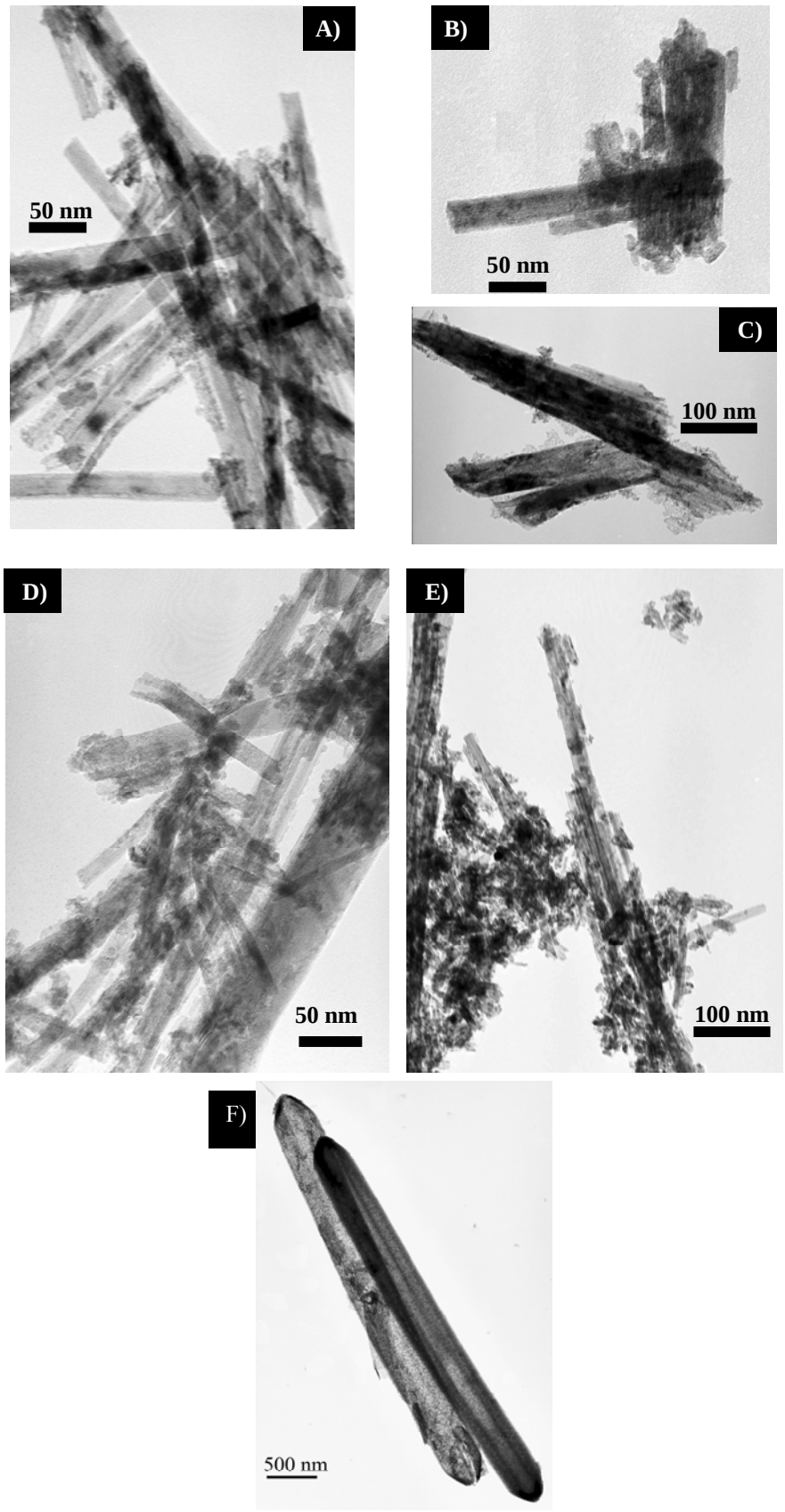

Figure 5.2 - TEM images of A) CeNT, B) CeNT-BuOOH, C) CeNT-H_2O_2, D) CeNT-PhEt-BuOOH, E) CeNT-PhEt-H_2O_2 and F) CeT

The nitrogen adsorption-desorption isotherm (77 K) of CeNT shows a substantial increase in the uptake of nitrogen at relative pressures greater than *ca.* 0.8, which is accompanied by hysteresis, possibly due to condensation/evaporation of nitrogen in/from the mesoporous network (Figure 5.3). The BET surface area is 78 m^2/g (Table 5.1), and the PSD curve is rather broad with maximum pore widths of 16 - 20 nm (Figure 5.3). It is worth mentioning that the PSD curve calculated from the adsorption branch is not well-defined. Nevertheless, the results obtained from the desorption branch are somewhat consistent with the TEM images (Figure 5.2).

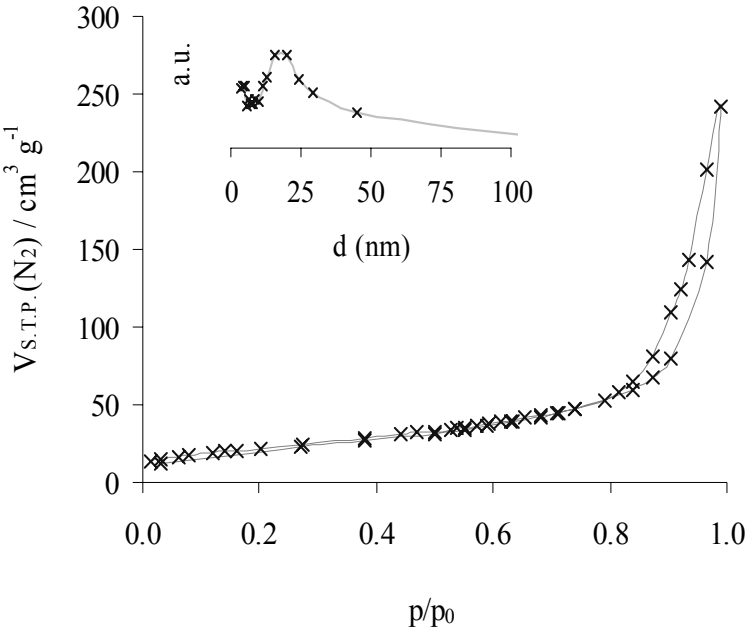

Figure 5.3 - CeNT (77 K) N_2 adsorption-desorption isotherm and (inset) pore-size distribution curve calculated for the desorption branch, using the Barrett-Joiner- Halenda method.

Table 5.1. BET specific surface area

Sample	S_{BET} (m^2/g)
CeNT	78
CeNT-BuOOH	55
CeNT- H_2O_2	90

5.3 – Catalytic oxidation of ethylbenzene

The liquid-phase oxidation of ethylbenzene was carried out under air and autogeneous pressure, in the temperature range 55-105 ºC, using a micro reactor equipped with a valve for sampling, a magnetic stirrer and immersed in a thermostated oil bath. The micro vessel was loaded with 30 mg of catalyst, 1.5 mmol of substrate, 3 mmol of oxidant (70% aq. *tert*-butyl hydroperoxide or 30% aq. H_2O_2) and 1.5 cm^3 of acetonitrile as solvent. The reaction mixture was cooled in an ice bath during 30 seconds prior to opening the valve for sampling, which was performed under stirring. Cyclohexanol and cyclohexene were also tested as substrates. Samples were analysed using a Varian 3800 gas chromatograph equipped with a DB-5 30 m × 0.25 mm capillary column and a flame ionisation detector, using decane as internal standard added to the withdrawn samples. The reaction products were identified by GC-MS (HP 5890 Series II GC; HP 5970 Series Mass Selective Detector) using He as carrier gas.

5.3.1 – General

CeNT promotes the liquid-phase oxidation of ethylbenzene (PhEt), using *tert*-butyl hydroperoxide (*t*-BuOOH) as the oxidant and acetonitrile (CH_3CN) as the solvent, at 55 - 105 ºC. At 55 ºC, 1-phenylethyl *tert*-butyl-peroxide (PhEtOOT) is the only reaction product until 51% conversion (reached after 120 h) (Figure 5.4): no reaction takes place without a catalyst. To the best of our knowledge, the formation of PhEtOOT in the catalytic oxidation of PhEt with *t*-BuOOH has not yet been reported. Syntheses procedures for PhEtOOT are based on the reaction of α-phenylethyl bromide with potassium salt of *t*-butyl hydroperoxide [184]. In the range 70-105 ºC, PhEtOOT selectivity decreases with PhEt conversion, while that to acetophenone increases (Figure 5.4B).

These results suggest that acetophenone is formed from PhEtOOT. On the other hand, the PhEtOOT selectivity tends to decrease with the reaction temperature, while the acetophenone selectivity increases reaching 70% at 89% conversion, at 105 ºC (Figure 5.4, Table 5.2). Aromatic ring oxidation products were never detected revealing excellent regioselectivity of this catalytic system towards the side-aliphatic chain oxidation. The absence of carboxylic acids (which could be formed in consecutive oxidations) was checked by analysing derivatized samples by GC-MS.

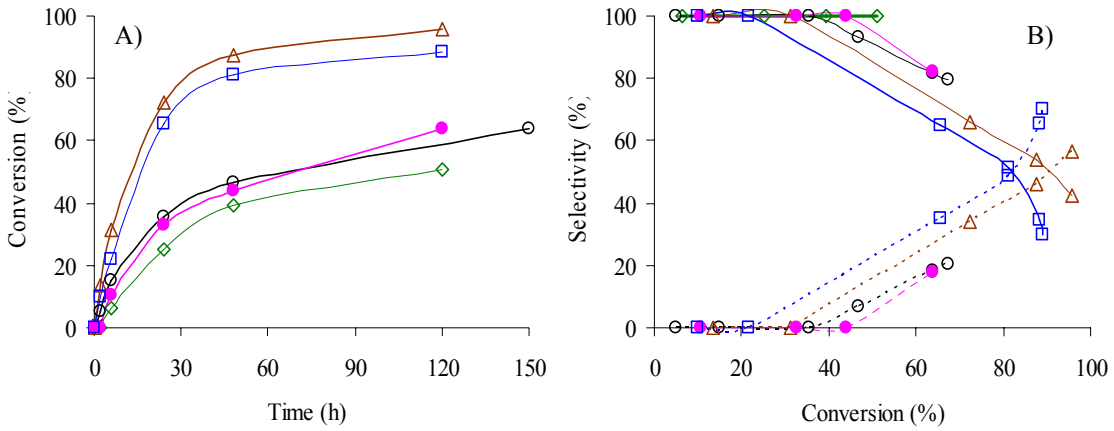

Figure 5.4 - A) - Ethylbenzene oxidation with *t*-BuOOH, in the presence of CeNT, at 55 ºC (◊), 70 ºC (run 1 - (O); run 2 - (•)), 90 ºC (Δ), 105 ºC (□), using acetonitrile as solvent. B) - Dependence of selectivity to PhEtOOT (solid lines) and acetophenone (dashed lines) on conversion for the reactions conditions indicated in A) - the same symbols were used for each reaction.

Table 5.2: Catalytic oxidation of PhEt with *t*-BuOOH, in the presence of the cerium-based catalysts.

Catalyst	Temperature (ºC)	Conversion 6/120 h	PhEtOOT Selectivity 6/120 h	PhEt=O Selectivity 6/120 h
CeNT	55	6/51	100/100	0/0
CeNT (run 1)	70	15/64 [a]	100/82 [a]	0/18 [a]
CeNT (run 2)	70	11/64	100/82	0/18
CeNT-BuOOH	70	16/97 [a]	100/34 [a]	0/64 [a]
CeNT-H_2O_2	70	10/78	100/71	0/29
CeNT	90	31/96	100/43	0/57
CeNT	105	22/88	100/35	0/65
$Ce(SO_4)_2.9H_2O$	70	0/15	-/66	-/34

[a] Calculated at 150 h.

Increasing the temperature from 55 ºC to 90 ºC enhances the reaction rate: conversion at 6 h/120 h increases from 6%/51%, at 55 ºC, to 31%/96%, at 90 ºC (Figure 5.4A, Table 5.2). Increasing the temperature above 90 ºC does not further increase the PhEt conversion. For the reaction carried out at 105 ºC, the conversion of PhEt at 6 h/120 h is 22/88% and after 120 h remains nearly constant (89% at 175 h). Probably, the thermal decomposition

(disproportionation) of *t*-BuOOH becomes a major competitive reaction for PhEt oxidation at high temperatures (see section 5.3.3) [185].

When a radical scavenger (2,6-di-*tert*-butyl-4-methyl-phenol) is added to the reaction of PhEt with *t*-BuOOH in the presence of CeNT, at 70 ºC, no reaction takes place, in contrast to that observed without the radical scavenger. These results indicate that a radical-chain process is involved. The initial induction periods of at least 120 min and 10 min observed for the reactions carried out at 55 ºC and 70 ºC, respectively (at higher temperatures no induction periods were detected), may be due to mechanistic factors. Possibly, the CeNT material acts as an initiator in the homolysis of *t*-BuOOH into free alkoxy (*t*-$BuO^{\bullet}$) and alkylperoxy radicals (*t*-$BuO_2^{\bullet}$) via the net redox reaction represented in eq. 5.1: Ce^{4+} is a relatively strong one-electron oxidant, and the resulting Ce^{3+} species may be re-oxidized by *t*-BuOOH [186]. The *t*-$BuO^{\bullet}$ radical can abstract a proton from the substrate to give the corresponding radical ($PhEt^{\bullet}$), eq. 5.2 [187], which reacts with *t*-$BuO_2^{\bullet}$ radicals to give PhEtOOT (eq. 5.3). It has been reported for the liquid-phase oxidation of arylbenzene compounds in homogeneous phase, in the presence of cerium ammonium nitrate/$KBrO_3$ that radicals of the substrates may reduce Ce^{4+} into Ce^{3+} species, forming intermediate carbocations, which are subsequently oxidized [188]. Accordingly, cerium ions may promote the introduction of the alkylperoxy group of *t*-BuOOH into $PhEt^{\bullet}$ via the net redox reaction represented in eq. 5.4. The reactions represented by equations 5.5-5.6 are typically involved in radical chain processes of oxidation of hydrocarbons, using *t*-BuOOH as oxidant [186]. A control experiment showed that the oxidation of PhEt in the presence of CeNT in the absence of *t*-BuOOH does not take place. Hence, the autoxidation of the substrate with molecular oxygen may be neglected (ethyl benzene hydroperoxide was not detected in the reaction mixtures by GC-MS): the observed induction periods may be due to intermediate rate limiting elementary steps.

The PhEtOOT product may be transformed into acetophenone (PhEt=O) plus *t*-BuOH via radical intermediates [184, 187] (eq. 5.7). This hypothesis is supported by the fact that when CeNT is filtered from the reaction mixture after 24 h, at 70 ºC (at this point PhEtOOT is the only product), and the obtained solution is left to react in the absence of CeNT until 48 h, at the same temperature, the formation of acetophenone is observed. On the other hand, the addition of a radical scavenger to the reaction of PhEt with *t*-BuOOH in the presence of CeNT, after 24 h, at 70 ºC, not only inhibits the reaction of PhEt, but also no acetophenone is formed after 48 h, in contrast to that observed without a radical scavenger.

$$2\ t\text{-BuOOH} \rightarrow t\text{-BuO}_2^{\bullet} + t\text{-BuO}^{\bullet} + H_2O \quad (5.1)$$

$$t\text{-BuO}^{\bullet} + \text{PhEt} \xrightarrow{[Ce^{3+}/\ Ce^{4+}]} t\text{-BuOH} + \text{PhEt}^{\bullet} \quad (5.2)$$

$$\text{PhEt}^{\bullet} + t\text{-BuO}_2^{\bullet} \rightarrow \text{PhEtOOT} \quad (5.3)$$

$$\text{PhEt}^{\bullet} + t\text{-BuOOH} \xrightarrow{[Ce^{4+}/\ Ce^{3+}]} \text{PhEtOOT} + H^{+} \quad (5.4)$$

$$t\text{-BuO}^{\bullet} + t\text{-BuOOH} \rightarrow t\text{-BuO}_2^{\bullet} + t\text{-BuOH} \quad (5.5)$$

$$2\ t\text{-BuO}_2^{\bullet} \rightarrow 2\ t\text{-BuO}^{\bullet} + O_2 \quad (5.6)$$

$$\text{PhEtOOT} \dashrightarrow \text{PhEt=O} + t\text{-BuOH} \quad (5.7)$$

5.3.2 – Stability of CeNT in the liquid-phase oxidation reaction

In order to get some insight into the stability of the CeNT under the applied oxidizing conditions, the solid was recovered from the reaction of PhEt with *t*-BuOOH, using acetonitrile as solvent, at 70 ºC and used in a second batch run. The solid was separated from the reaction medium by centrifugation, washed consecutively with *n*-hexane, dichloromethane and acetone, and finally dried at room temperature prior to reuse (giving CeNT-PhEt-BuOOH). The kinetic curves for runs 1 and 2 are roughly coincident as well as the dependence of products selectivity on conversion (Figure 5.4, Table 5.2). The powder XRD patterns of CeNT and CeNT-PhEt-BuOOH are similar (Figure 5.1). The TGA analyses of the fresh and used solids gave similar weight losses between 30 ºC and 600 ºC (*ca.* 8 wt. %), under air, and therefore coking is negligible. These results suggest that CeNT is fairly stable under the applied oxidizing conditions.

Carrying out the reaction of PhEt in homogeneous phase in the presence of the precursor used for preparing CeNT, *i.e.*, cerium sulphate (using the same mass as CeNT), at 70 ºC, gives 15% conversion after 120 h, and PhEtOOT and acetophenone are formed in 34% and 66% selectivity, respectively (Table 5.2). The reaction is much faster in the presence of CeNT than of $Ce(SO_4)_3.9H_2O$, under similar reaction conditions.

In order to assess the homo/heterogeneous nature of the catalytic reaction in the presence of CeNT, the solid was separated by filtration (Whatman 0.2 μm PVDF w/GMF membrane) after 6 h reaction, at 70 ºC, and the obtained solution was left to react at this temperature until 48 h. Conversion between 6 h and 48 h was approximately a third of that observed in the presence of CeNT (11% *vs.* 32%): possibly, the reaction proceeds in homogeneous phase due to (i) free radicals formed prior to catalyst filtration and/or (ii) due to active CeNT, which were not separated by filtration. Hypothesis (i) is supported by the fact that when a similar experiment was performed in the presence of the radical scavenger, no

PhEt conversion was observed in the same time interval, as could be expected from the above mechanistic considerations. Hypothesis (ii) is ruled out by two experiments. The solid was separated from the reaction medium after 120 h by filtration at 70 ºC, and the obtained solution was analysed by ICP-AES for cerium, which was not detected (detection limit *ca.* 5 ppb). Nevertheless, the obtained solution was evaporated to dryness and to the same vessel PhEt, *t*-BuOOH and CH_3CN were added in the same amounts as those used for the first batch run: after stirring this mixture during 150 h, at 70 ºC, no PhEt reaction was observed, indicating that the 'residue' obtained after evaporation did not contain active cerium compounds. Based on these results, it seems clear that CeNT performs as a heterogeneous redox catalyst for generating free radicals, accounting for a radical chain process in the homogeneous phase.

When pristine CeNT was heated up to 600 ºC in air no structural modifications were observed for the resulting solid (denoted CeNT600), as ascertained by powder XRD. However, CeNT600 is inactive in the reaction of PhEt with *t*-BuOOH, at 70 ºC. The solid recovered (washed and dried) from the reaction of PhEt with *t*-BuOOH in the presence of CeNT, during 150 h, at 70 ºC, was heated at 280 ºC, during 3 h, under static air, giving a solid denoted CeNT-280. The reaction of PhEt with *t*-BuOOH in the presence of CeN-280, at 70 ºC, is slower that that observed for CeNT and CeNT-PhEt-BuOOH, and PhEtOOT is the only product until 54% conversion, reached after 120 h. Thermal treatments seem to gradually destroy the active sites, which may be defect sites in the original material. It has been reported in the literature that defect sites of the type Ce^{3+}-O-Ce^{4+} are responsible for activating PhEt using N_2O as oxidant, at 325 ºC, and increasing temperature of H_2 treatment from 300 ºC to 350 ºC led to a drastic decrease in concentration of these defect sites [189]. UV-vis and photoluminescence studies revealed the presence of both Ce^{3+} and Ce^{4+} in CeNT before and after it exposure to *t*-BuOOH, as discussed ahead.

5.3.3 – Oxidant effect

When H_2O_2 (30% aq.) is used as oxidant instead of *t*-BuOOH, no PhEt reaction is observed in the presence of CeNT during 150 h, at 70 ºC. It was previously reported for a ceria possessing a cubic crystal structure of the fluorite type (67 $m^2.g^{-1}$, 12 nm crystallite size), used as catalyst in the oxidation of PhEt with H_2O_2 and acetonitrile as solvent, that the reaction is sluggish giving *ca.* 4% conversion after 6 h, at 60 ºC, and benzaldehyde and acetophenone were the only products [118]. The decomposition of H_2O_2 has been used as a test reaction for investigating the redox properties of ceria materials. In the case of the

CeNT/H_2O_2 system, the poor catalytic results may be due to the relatively fast 'non-productive' decomposition of H_2O_2 by CeNT. In order to investigate this hypothesis, iodometric titrations were performed for the reactions of CeNT with H_2O_2 or *t*-BuOOH (without PhEt) after 4 h, at 70 ºC. These results revealed that H_2O_2 was totally consumed, whereas *t*-BuOOH conversion after 4 h was negligible, supporting the above hypothesis. It is worth mentioning that acetamide, which may be formed from the reaction of CH_3CN with H_2O_2 via the intermediate formation of the correspondent peroxyimidic acid was not detected in the reaction mixtures [190]. According to the literature, CeNT may undergo morphological changes in the presence of H_2O_2 [88]. A similar destructive effect of H_2O_2 has also been reported for cerium-containing SBA-15, in that cerium was removed from the silica framework, forming fine CeO_2 crystallites on the surface (no cerium leaching was detected during catalytic oxidation reactions) [191].

To the best of our knowledge, the influence of *t*-BuOOH on the physico-chemical properties of CeNT has not been reported. In order to get some insight into the effect of the oxidant on the catalytic activity, the solids used in the reactions of PhEt with *t*-BuOOH or H_2O_2, at 70 ºC, were recovered after 120 h in a similar fashion to that described above for the catalyst recycling experiments, and subsequently characterized: the resulting solids are denoted CeNT-PhEt-BuOOH and CeNT-PhEt-H_2O_2, respectively. On the other hand, for comparative studies, CeNT was treated with H_2O_2 or *t*-BuOOH, in the absence of PhEt, in an ultrasonic bath, as described in the experimental part, giving CeNT-H_2O_2 and CeNT-BuOOH, respectively. The TEM images of CeNT-BuOOH and CeNT-PhEt-BuOOH show some fragmentation of the nanotubes and the formation of 6-8 nm spherical particles, and this effect is major for CeNT-H_2O_2 and CeNT-PhEt-H_2O_2 (Figure 5.2). The ATR-FTIR spectra of CeNT-BuOOH and CeNT-H_2O_2 are similar to that of CeNT in the region 1300-1600 cm^{-1}, with the main difference being that the band at ca. 1640 cm^{-1} assigned to H-O-H bending vibration is very weak in the case of CeNT-BuOOH (not shown).The powder XRD patterns of CeNT-H_2O_2 and CeNT-BuOOH are similar to that of CeNT (see section 5.2), albeit the peaks are slightly broader, especially in the case of CeNT-H_2O_2 (Figure 5.1).

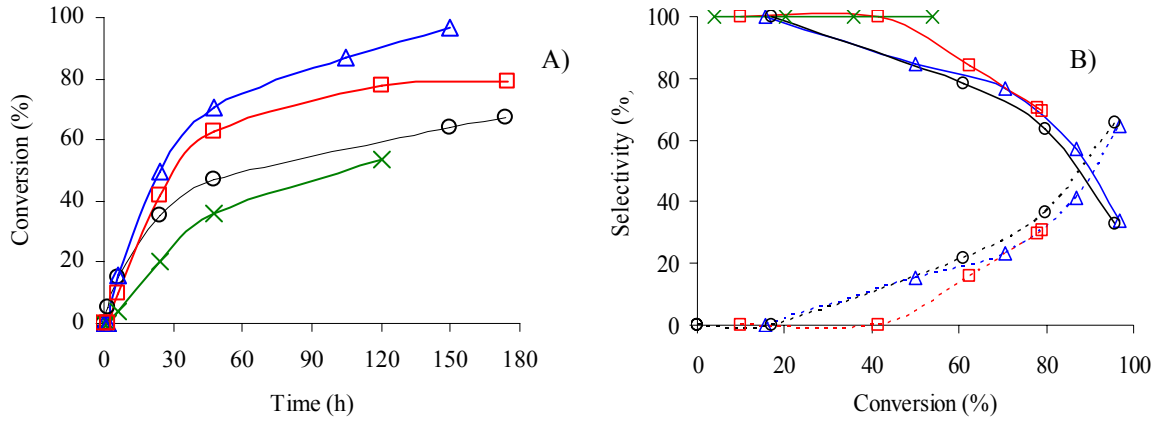

Figure 5.5 - A) - Ethylbenzene oxidation with t-BuOOH, at 70 ºC, using acetonitrile as solvent, in the presence of CeNT (O), CeNT calcined at 280 ºC (×), CeNT pre-treated with H_2O_2 (□) or *t*-BuOOH (Δ). B) - Dependence of selectivity to PhEtOOT (solid lines) and acetophenone (dashed lines) on conversion for the reactions conditions indicated in A) - the same symbols were used for each reaction.

In order to assess the effect of the oxidizing pre-treatment on the reaction of PhEt, the CeNT-H_2O_2 and CeNT-BuOOH materials were tested as catalysts in the oxidation of PhEt with *t*-BuOOH, at 70 ºC. No major differences in products selectivity were observed between the pre-treated solids and CeNT, at least until *ca.* 70% conversion, suggesting that a similar reaction mechanism is involved (Figure 5.5).

However, the reaction rate (based on conversion at 24 h/120 h) is higher for the pre-treated materials than for CeNT, increasing in the order CeNT (35%/~60%) < CeNT-H_2O_2 (42%/78%) < CeNT-BuOOH (50%/~90%), Table 5.2. Altogether, the results support the hypothesis that CeNT is not effective in the reaction of PhEt with H_2O_2 because of its effectiveness in H_2O_2 disproportionation. The reaction of *t*-BuOOH on the surface of CeNT may primarily involve the coordination of the oxidant to defect sites (possibly co-ordinately unsaturated cerium), followed by redox reactions to form radical species, according to the above mechanistic considerations. Based on the XRD patterns and TEM images combined with UV-Vis one may postulate that when the oxidant is H_2O_2 instead of *t*-BuOOH the formation of defect sites is enhanced. Accordingly, a higher catalytic activity could be expected for CeNT-BuOOH in comparison to CeNT-H_2O_2, which was not observed. Other factors which may be responsible for the observed differences in catalytic performances may be the morphology, Ce^{3+}/Ce^{4+} ratio and corresponding redox potentials (a distribution may exist for each sample).

5.4 – Oxidation of different substrates

CeNT was further tested as catalyst in the oxidation of cyclohexene and cyclohexanol, at 55 ºC, during 24 h (Table 5.3). For both substrates, when H_2O_2 was used as oxidant, conversions were negligible, similar to that observed for PhEt. These results contrast with those reported for mesoporous Ce-SBA-15 in the oxidation of cyclohexene and cyclohexanol with H_2O_2, under similar conditions to those used in the present work: 40% cyclohexene conversion was reached after 10 h, at 50 ºC, forming the epoxide as the main product (other products included the 1,2-diol, -en-1-ol and -en-1-one) and, on the other hand, the reaction of cyclohexanol with H_2O_2 gave a maximum of ca. 15% conversion after 7 h, at 60 ºC [191]. The competitive 'non-productive' decomposition of H_2O_2 is probably less important for the referred supported ceria catalyst than for CeNT.

Table 5.3: Oxidation of different substrates with *t*-BuOOH, in the presence of CeNT, using acetonitrile as solvent, during 24 h, at 55 ºC.

Substrate	Conversion (%)	Product	Selectivity (%)
Ethylbenzene 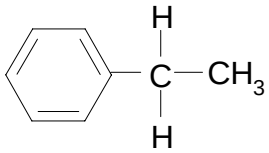	25	1-phenylethyl *tert*-butyl-peroxide 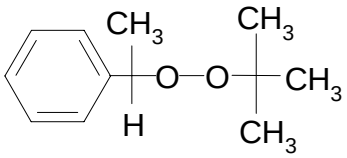	100
Cyclohexene 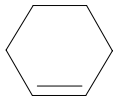	22	1-(*tert*-butylperoxy)-2-cyclohexene 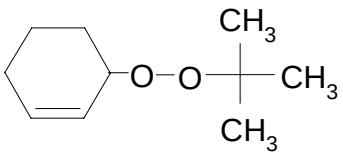	86[a]
Cyclohexanol 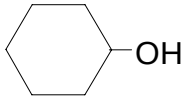	33	Cyclohexanone 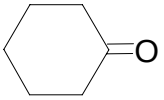	100

[a] By-products are mainly 2-cyclohexen-1-one and minor amounts of 2-cyclohexen-1-ol.

When *t*-BuOOH is used instead of H_2O_2, the reaction of cyclohexanol gives cyclohexanone as the only product in 33% yield, after 24 h, at 55 ºC (when no catalyst is added, cyclohexanone yield is 11%), Table 5.3. When the substrate is cyclohexene, conversion after 24 h is 22% and the main product is 1-(*tert*-butylperoxy)-2-cyclohexene (86% selectivity): by-products include 2-cyclohexen-1-one and minor amounts of 2-cyclohexen-1-ol (when no catalyst is added, no reaction is observed). The products selectivity for cyclohexene somewhat parallels that obtained for PhEt, in that for both substrates the major product is a *tert*-butylperoxy (alkyl or aryl) compound, and saturated C-H bonds are preferentially activated over the unsaturated ones. The 1-(*tert*-butylperoxy)-2-cyclohexene product has been identified in the oxidation of cyclohexene with *t*-BuOOH via radical reactions in the presence of free and alumina-supported transition metal complexes bearing Schiff base ligands [192-194]. For all substrates, CeNT-600 gave negligible conversions, similar to that observed for PhEt.

5.5 – UV-Vis Spectroscopy

Figure 5.6 displays the UV/Vis absorbance spectra of the as-prepared CeNT, CeNT-BuOOH, and CeNT-H_2O_2 powders.

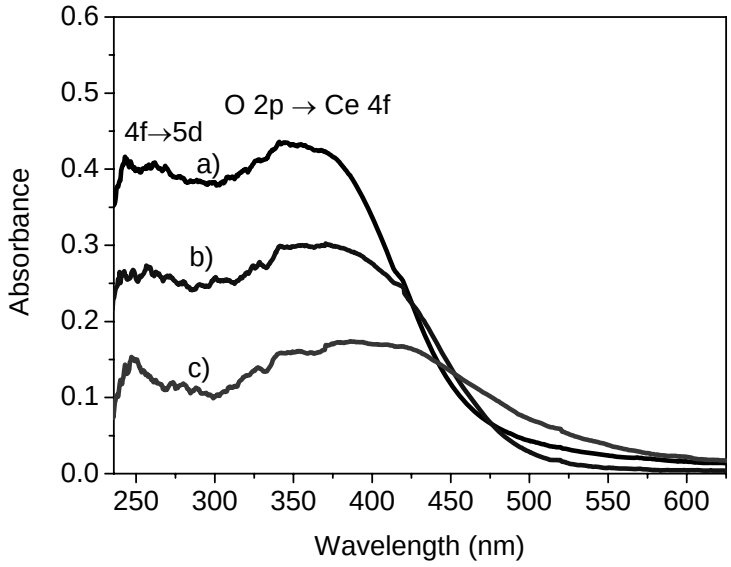

Figure 5.6 - UV-Vis absorbance spectra of a) CeNT, b) CeNT-BuOOH and c) CeNT-H_2O_2 powders.

The peaks attributed to the $4f \rightarrow 5d$ transitions of Ce^{3+}, at 220-320 nm, are observed in all spectra. A broad band (cut-off wavelength 480-550 nm) is also observed due to charge

transfer transitions from O 2*p* to Ce 4*f* [195-200]: a broadening of this band is observed especially in the case of CeNT-H_2O_2 relative to CeNT possibly due to the increasing number of surface defects [183].

The optical energy gap, ε_d, of CeNT ethanol suspension was determined using the Davis and Mott equation [130-203]:

$$\alpha h\nu \approx B(h\nu - \varepsilon_d)^n \tag{5.9}$$

where $h\nu$ is the photon energy, α the absorption coefficient and *B* a constant (related with the reduced mass and the refractive index of the material and with the oscillator strength of the transition), for allowed transitions *n*=1/2. Figure 5.7A shows a plot of $(\alpha h\nu)^2$ versus $(h\nu)$. The extrapolation of the linear region to $(\alpha h\nu)^2 = 0$ results in ε_d=3.1 eV. The indirect energy gap, ε_i, for transitions involving large change in the momentum mediated by phonon absorption is given by [203]:

$$\alpha \propto \frac{\left(h\nu - \varepsilon_i + \varepsilon_p\right)^2}{e^{\varepsilon_p / k_B T} - 1} \tag{5.10}$$

where $\varepsilon_p = h\nu_p$ corresponds to the phonon energy, k_B is the Boltzmann constant and *T* is the temperature, for allowed transitions *n*=2. From the linear region of the plot of $(\alpha^{1/2})$ versus $(h\nu)$ (Figure 5.7B), an indirect band gap, ε_i, may be obtained by extrapolating the straight line to $\alpha = 0$. The ε_i value obtained for CeNT using this procedure is ~2.5 eV. Since no confinement effects on the band gaps are observed for the range of CeNT particle size the obtained ε_d and ε_i values are in accord with the band gaps of ceria bulk [197,204]. The band gap values were not estimated for Ce-BuOOH and CeNT-H_2O_2 due their low dispersion and stability in suspension. However, the similarity of the absorption spectra measured for the CeNT and CeNT-BuOOH powders suggest that the energy gaps of both materials may be comparable, albeit may differ somewhat from that of CeNT-H_2O_2.

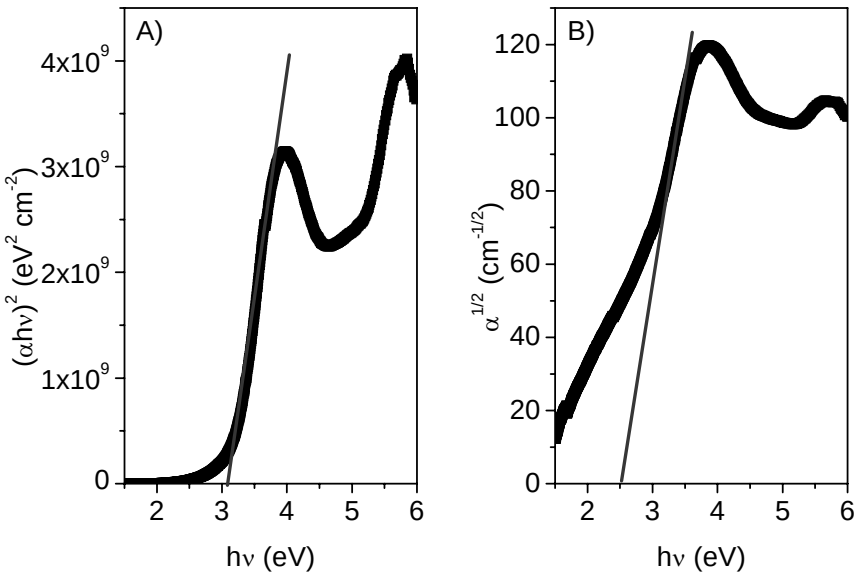

Figure 5.7 - Plots of A) $(\alpha h\nu)^2$ versus $(h\nu)$ and B) $\alpha^{1/2}$ versus $(h\nu)$ for the CeNT ethanol suspension.

5.6 – PLE and PL spectroscopy of ceria nanotubes

Excitation spectra of CeNT at 11 K were acquired monitoring at 370.2, 390.2 nm or 450 nm. Transitions observed between 300 and 340 nm are assigned to the *4f* $^2F_{5/2}$*→5d* transitions (Figure 5.8). The band at 269.7 nm (37078.23 cm^{-1}) observed in both spectra is also assigned to a *4f→5d* transition of Ce^{3+}. Excitation spectrum monitored at 450 nm does not show the Ce^{3+} *4f→5d* transitions and displays only a broad band below 290 nm.

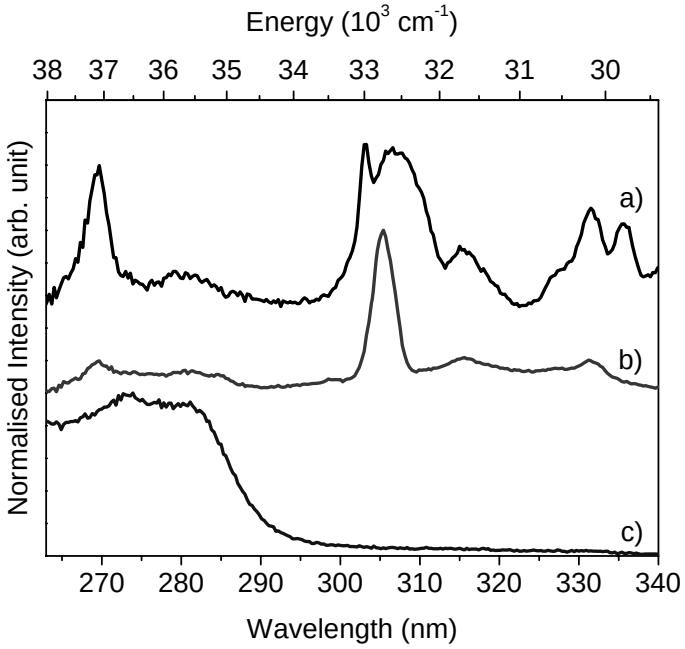

Figure 5.8 - 11 K excitation spectra of CeNT monitoring at a) 370.1 nm, b) 390.2 nm and c) 450 nm

The emission spectra of CeNT (excitation at 332 nm), CeNT-H_2O_2 and CeNT-PhEt-BuOOH (excitation at 316.2 and 332 nm) display two overlapping broad bands at *ca.* 375 and 410 nm, exemplified for CeNT-H_2O_2 by spectral deconvolution (inset of Figure 5.9). In constrast to that observed for CeNT-H_2O_2, in the case of CeNT and CeNT-PhEt-BuOOH, superimposed, are a group of sharp peaks at *ca.* 370.1, 375.8, 380.6, 386.3 and 390.5 nm. Whereas the two broad bands are unequivocally (because their energy separation is 2270 cm^{-1}) attributed to Ce^{3+} $5d \rightarrow {}^2F_{5/2,7/2}$ transitions [205,206], the nature of the sharp peaks is still open to discussion (some authors suggest that the peaks are attributed to the hopping from localized Ce^{3+} states or different defect levels to the *O 2p* band [207]). Furthermore, for the three samples, upon excitation at 282 nm, these peaks are absent and the emission spectrum is dominated by another broad band (380-520 nm) ascribed to *Ce 4f→O 2p* transitions [195,208], Figure 5.9c. The emission spectra clearly show the presence of Ce^{3+} ions in the inorganic matrix of the three materials, which may be in the bulk region or in surface defects [189].

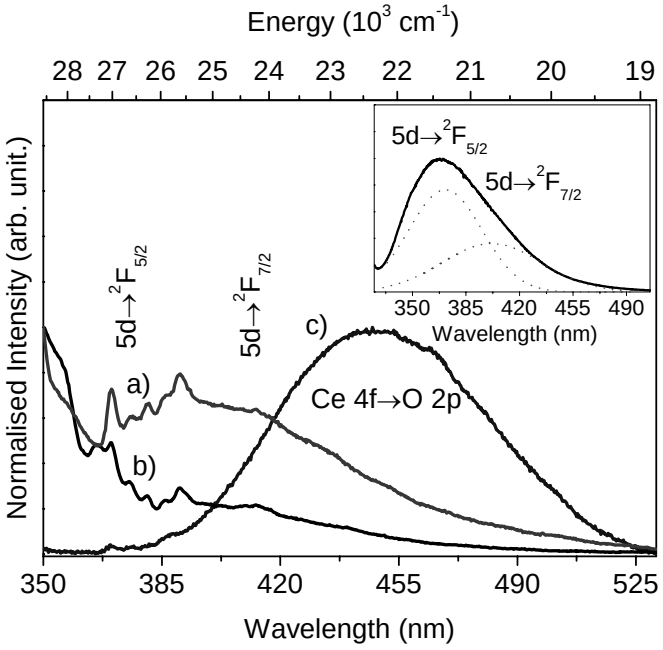

Figure 5.9 - 11 K emission spectra of CeNT upon excitation at a) 316 nm, b) 332 nm and c) 282 nm. The inset shows the emission spectra of CeNT-H_2O_2 (solid line) excited at 316 nm; the dotted lines represent spectral deconvolution using two Gaussian functions attributed to the $5d\rightarrow^2F_{5/2,7/2}$ transitions.

The emission spectrum of CeNT-PhEt-BuOOH also displayed the same sharp lines in the 360-400 nm spectra region upon excitation at 316 and 332 nm, indicating unaltered crystalline environment after its use as catalysts. Upon excitation of CeNT-PhEt-BuOOH at 282 nm (spectrum not shown) the $Ce^{3+}5d\rightarrow^2F_{5/2,7/2}$ transitions were overlapped with the *Ce 4f→O 2p* ones: the corresponding spectrum for CeNT-H_2O_2 also showed the broad bands attributed to the $Ce^{3+}5d\rightarrow^2F_{5/2\ 7/2}$ and *Ce 4f→O 2p* transitions indicating the presence of Ce^{3+} ions, probably in defects. The emission spectra of CeNT600 are similar (not shown).

At room temperature, CeNT material does not emit. Several reasons have been put forward to explain the quenching of luminescence including the thermally-excited interconfigurational system crossing, energy transfer from *4f* level to nearby centres, electron transfer or photoionization [209]. Emission spectra were acquired as a function of temperature, wavelength excitation of 282 nm, and the evolution of the integrated emission is depicted in Figure 5.10. Between 11 and 100 K the CeNT emission intensity remains constant and then it decreases markedly, almost disappearing at *ca.* 220 K. This could be the result of defects (including oxygen vacancies site in the crystal) with electronic energy levels between the O*2p* and 4*f* bands. The number of these defects is temperature dependent [210-212]. This

behaviour can be described by a thermally-activated non-radioactive mechanism modelled by the Mott Seitz equation [213,214]:

$$I = \frac{I_0}{1 + a\exp^{(-\Delta E/k_B T)}} \qquad (5.11)$$

where a is a constant and ΔE is the activation energy that corresponds to the energy gap between the *4f* level and that of the de-excitation states.

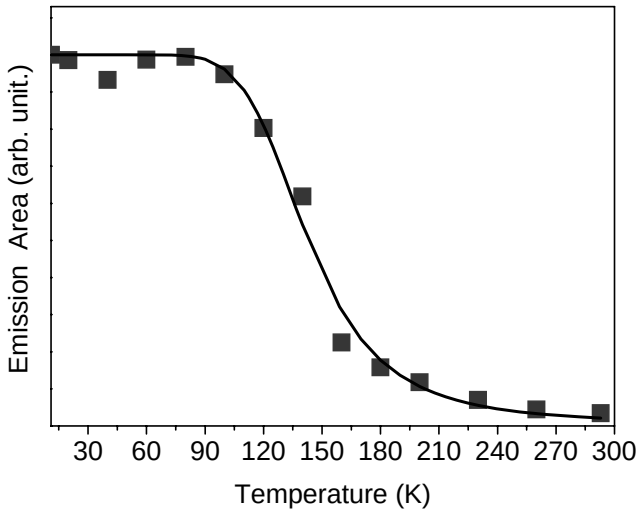

Figure 5.10- Emission intensity as a function of temperature of CeNT (squares) and the Mott-Seitz fitting (solid line) using Eq. (5.11)

A fit of the experimental values by Eq. 5.11 (Figure 5.10) yields activation energy of *ca.* 651 cm^{-1} (81 meV). This value is consistent with a previous report where the defect levels are located in the range of 1 eV below the Ce *4f* band [211, 212].

5.7 – Conclusions

CeO_2 nanotubes (CeNT) have been shown to promote the oxidation of cyclohexene, cyclohexanol and ethylbenzene with *t*-BuOOH, at temperatures as low as 55 ºC. Mechanistic considerations have been put forward based on experimental evidence and literature data. The liquid-phase oxidation catalysis with CeNT/*t*-BuOOH is most likely associated with the Ce^{3+}/Ce^{4+} inter-conversion in the one-electron redox processes mediating the formation of *tert*-butyl(per)oxy radicals: UV-Vis and photoluminescence studies reveal the existence of both oxidation states of cerium in CeNT before and after its exposure to *t*-BuOOH or H_2O_2.

The radical-chain process generates mainly *tert*-butylperoxy products in the reactions of cyclohexene and ethylbenzene most likely via the homolytic addition of *tert*-butylperoxy radicals. The reaction of PhEt at 55 ºC forms 1-phenyl ethyl *tert*-butyl-peroxide as the only product (39% yield after 48 h). This result contributes to the list of the main applications of *t*-BuOOH as a source for tertiary-butyl derivatives, including alkyl peroxides.

Above 55 ºC, PhEtOOT is converted into acetophenone (used as ingredient in perfumes and as a chemical intermediate in the production of pharmaceuticals, resins and flavouring agents) in increasing amounts: for the reaction carried out at 105 ºC, acetophenone selectivity is 70% at 89% conversion. Leaching tests and ICP-AES indicate that CeNT is fairly stable towards leaching of cerium and the catalytic results obtained for the used CeNT are similar to those observed in the first batch run. The conversion of PhEt may be further improved by using an oxidizing pre-treatment with H_2O_2 or *t*-BuOOH to CeNT. When H_2O_2 is used instead of *t*-BuOOH, no conversion is observed for all the investigated substrates (cyclohexene, cyclohexanol, ethylbenzene, cyclohexane), most likely because CeNT is very effective in H_2O_2 disproportionation. Pre-treatment of CeNT with H_2O_2 or *t*-BuOOH prior to reaction of PhEt with *t*-BuOOH leads to faster reaction than CeNT. Ultraviolet-visible and photoluminescence spectroscopy confirm the presence of both Ce^{3+} and Ce^{4+} in the samples (with or without pre-treatment), albeit exposure to H_2O_2 seems to give a more defective material than that with *t*-BuOOH. The catalytic activity does not seem solely related to the number of defect sites, posing importance on other possible factors such as morphology, Ce^{3+}/Ce^{4+} ratio and corresponding redox potentials (a distribution may exist for each sample).

Chapter 6 – Composites

6.1 – Introduction

The synthesis and potential applications of inorganic lanthanide (Ln^{3+}) nanotubes and nanorods have been the subject of several studies [58-70,215]. To process Ln^{3+} nanotubes/nanorods, it is desirable to functionalize their surface, thus producing derivatives that are compatible with solvents and which can further react with organic molecules or make them biocompatible [216]. F. Söderlind *et al.* [217] have reported the direct surface modification of gadolinium oxide with carboxylic acids as citric acid or fatty acids (oleic and stearic) for biomedical purposes, for instance as a possible substitute for boron containing compounds commonly used in neutron capture therapy for local treatment of cancer tumours. The authors also showed that these molecules were coordinated to the surface via the carboxylate group.

Alternatively to direct surface functionalization with organic molecules, coating of lanthanide nanorods with a silica shell is a useful strategy. Besides providing protection from the surrounding environment and increasing the hydrophilic character of the surface, the silica shell confers two main advantages. The first one is the controlled functionalization with different molecules, since silica may be derivatized with organic organoalkoxysilanes containing reactive groups such as amines, thiols, isothiocianates and (meth)acrylates. These functional groups can act as anchorage sites for chromophores, biomolecules or polymer chains. The second advantage of coating the surface of Ln^{3+} nanorods with silica is the improvement of their photoluminescence properties due to the considerable reduction of the number of surface Ln-OH groups. K. L. Wong *et al.* have anchored (methyl phenoxybenzoate) chromophore onto silica-coated europium hydroxide nanorods surface via amine and carboxylate groups; this material was used in live cell imaging [216]. Z. Chen used nanoparticles with free surface carboxylic acid groups for conjugation of biomolecules such as streptavidin and biotin, and then used it for DNA detection [218]. Besides grafting small molecules, appropriate surface modification of silica shells has been widely used to prepare polymer based nanocomposites as a strategy to process nanoparticles and/or yield materials with enhanced properties [219].

Polymer based nanocomposites containing silica coated Bi_2S_3 fibres have been previously prepared by emulsion and suspension polymerization [220]. *In situ* emulsion polymerization afforded nanocomposites in which the nanofibers were coated with polymer spheres, whilst suspension polymerization yielded a homogeneous polymer layer coating.

Here, we report the preparation of SiO_2-coated Gd_2O_3:Eu^{3+} nanorods and subsequent preparation of the corresponding poly(styrene) (PS) based nanocomposites. Firstly the Gd_2O_3:Eu^{3+} nanotubes were prepared using the procedure reported by L.Q. Lin *et al.* [221], followed by the coating with a thin silica layer [222], and subsequent surface modification with 3-methacryloxypropyl-trimethoxysilane (MPS). Finally, styrene was polymerized *in situ* via miniemulsion and solution routes [223] (Scheme 6.1) using two different polymerization techniques. Miniemulsion offers the advantage of using aqueous media although the length of the nanorods is not compatible with the size of the oil drops formed. However, based on previous works [220] it is speculated that the surfactant used can stabilize not only the monomer droplet and the polymer growing particles but also the MPS modified nanorods providing a hydrophobic environment where polymerization can occur. Alternatively, the preparation of the nanocomposites was carried out via solution polymerization using toluene as solvent. The morphology of the ensuing Gd_2O_3:Eu^{3+}/SiO_2/MPS/PS nanocomposite obtained from the two *in situ* polymerization techniques used was distinct and will be compared and discussed. The optical properties of the materials obtained were study by photoluminescence spectroscopy and the effect of successive encapsulation with silica and subsequently with poly(styrene) is discussed.

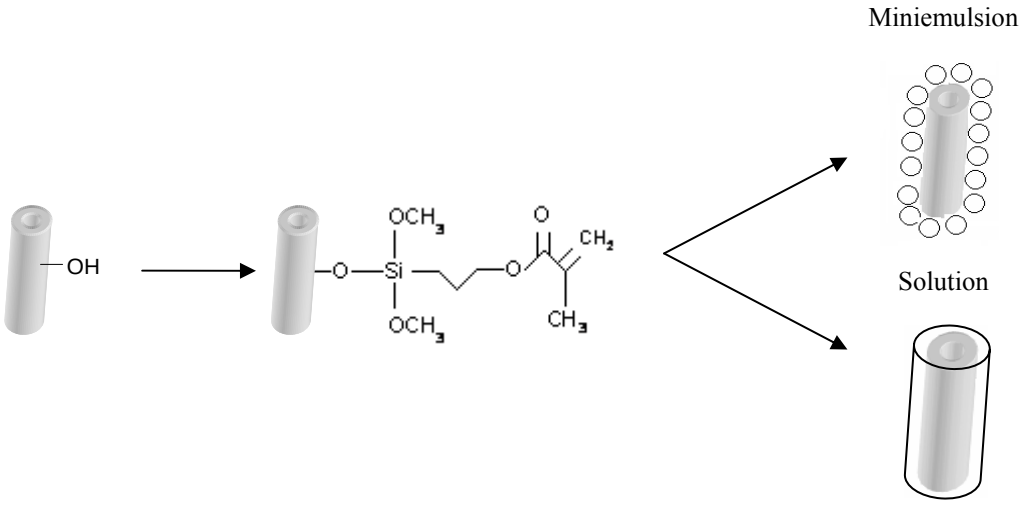

Scheme 6.1 – Preparation of Gd_2O_3:Eu^{3+}/SiO_2/MPS/poly(styrene) composites by miniemulsion and solution routes

In another approach, W. Li *et al.* [72] reported the synthesis of double bond-grafted yttrium-hydroxide nanotube core-shell structures with methyl methacrylate (MMA) molecules. The covalent functionalization involved the irreversible esterolysis of MMA, and the formation of Y(III)–O bonds on the hydrophilic surface of nanotubes in water. This leads to amphipathic composite nanotubes by the attachment of carbon–carbon double-bonds chains

to the surface. Both the forming of the nanotube and MMA attachment were achieved in a single step during the hydrothermal synthesis.

Here, we also report the surface modification of Y_2O_3 nanotubes with stearic acid and, due the induced hydrophobic character of the outer surface; this procedure allows the preparation of aligned films by the Langmuir-Blodgett technique. First, we provide evidences of the effective grafting of the stearic acid molecules onto the nanotubes surface via FTIR and SEM analysis; then we briefly describe the Langmuit-Blodgett technique and the preparation of hydrophobic substrates with stearic acid and Zn^{2+} solutions. Aligned films of stearic acid modified Y_2O_3 nanotubes were prepared onto these hydrophobic substrates. Also the mixed film method (in presence of stearic acid and Zn^{2+} solutions) was utilized.

6.2 – Surface modification and polymerisation by miniemulsion and solution methods

6.2.1. Chemicals

Styrene (Aldrich, 99%) was purified over a column of neutral aluminium oxide to remove the inhibitor prior to use. The water was purified using Sation 8000 and Sation 9000 purification units. 3-(trimethoxysilyl) propyl methacrylate (MPS, Acros Organic, 98%), sodium persulfate (KPS, Acros, 98%), 2-2'-Azobis(isobutyronitrile) (AIBN, Fluka, 98%), hexadecane (HD, Aldrich, 99%), toluene (Aldrich, 99.8 %) and dodecyl sulfate sodium salt (SDS, Aldrich) were used as purchased.

6.2.2. Synthesis of europium doped gadolinium oxide $Gd(OH)_3:Eu^{3+}$ nanorods

See Appendix A1. The surface area of the nanorods determined by BET N_2 adsorption at 77 K was S_{bet} 28 m^2/g.

6.2.3. Europium doped gadolinium oxide nanorods coated with silica ($Gd_2O_3:Eu^{3+}$ / SiO_2)

$Gd_2O_3:Eu^{3+}$ nanorods were obtained by calcination of the $Gd(OH)_3:Eu^{3+}$ in air at 700 ºC during 3 h (heating rate of 5 ºC/minute). Immediately after the calcination, 380 mg de $Gd_2O_3:Eu^{3+}$ nanorods were added to 50 mL of absolute ethanol and dispersed with ultrasonic stirring for 10 minutes, in ice bath. A volume of 30 mL ammonium hydroxide (25 %, Riedel-de Haën) and 1 mL of tetraethyl orthosilicate [$Si(OC_2H_5)_4$), Aldrich, 98%] were added to this suspension. The resulting mixture was stirred with an ultrasonic probe for 2 h, in ice bath. The final product was centrifuged, washed three times with absolute ethanol and dried in air in a ventilated oven at 60 ºC, for 12 hours. This powder was calcined at 700 ºC for 3 h.

6.2.4. Surface modification of SiO_2 coated $Gd_2O_3:Eu^{3+}$ with coupling agent ($Gd_2O_3:Eu^{3+}$/ SiO_2/ MPS)

The coupling agent, 3-(trimethoxysilyl) propyl methacrylate, was used for the modification of the $Gd_2O_3:Eu^{3+}$ / SiO_2. Coating with MPS was achieved by stirring a mixture of $Gd_2O_3:Eu^{3+}$ / SiO_2 (0.2g), MPS (28 μL) and ultra- pure distilled water (20 mL) for four days at room temperature. The pH was adjusted to *ca.* 8 by adding ammonium hydroxide (25 %, Riedel-de Haën). MPS was added in excess: 20 μmol of coupling agent per square meter of silica. The relative amount of MPS and silanol surface concentration was estimated considering the silanol groups density at SiO_2 surface to be *ca.* 8 μmol/ m^2 reported in the literature [224] and the S_{bet} of 28 m^2/g determined for the $Gd_2O_3:Eu^{3+}$ nanorods. Excess MPS was removed by dialysis against water. Typically, 20 mL of the suspension were introduced in a membrane and dialysed against distilled water (1500 mL) to remove the unreacted MPS for four days. The dialysed solution was removed every 24 h and replaced by an equal volume of distilled water. The dialysed solution was monitored by UV spectroscopy using the maximum absorption band of MPS is at 203.5 nm. Free MPS was no longer detected after two days.

6.2.5. Miniemulsion radical polymerization. ($Gd_2O_3:Eu^{3+}$ / SiO_2/ MPS/PS)

Typically styrene (1.95 mL) and the hydrophobe HD (51 μL) were mixed under magnetic stirring for 20 minutes. Separately, sodium hydrogen carbonate (43 mg), SDS (30 mg) were dissolved in an aqueous suspension containing and 20 g of $Gd_2O_3:Eu^{3+}$ / SiO_2 / MPS. The resulting dispersion was added to the first one under magnetic stirring for 30 minutes, followed by ultrasonic probe stirring (amplitude 80 %, power 20W, Sonics-Vibracel Sonifier) for 10 minutes, in an ice bath. The resulting stable miniemulsion was transferred to a jacketed polymerization reactor equipped with a thermostatic bath, a condenser, and a mechanical stirrer and was left under mechanical stirring (300 rpm) and N_2 flow for 20 min, after which it was heated up to 70 ºC. Once the temperature was stabilized 1 mL of an aqueous solution of KPS (9.6 mg/mL) was added to the reaction medium setting the zero time of the polymerization. The polymerization was carried out for 4 hours at 300 rpm. The $Gd_2O_3:Eu^{3+}/SiO_2$/MPS/PS nanocomposite was isolated by three successive centrifugation/re-dispersion cycles using water in order to remove free polymer particles. The purified precipitate was dried in a ventilated oven at 60 ºC.

6.2.6. Conventional radical polymerization in situ and in solution

In a two neck 50 mL round bottom flask fitted with condenser $Gd_2O_3:Eu^{3+}/SiO_2$/MPS (190 mg) were dispersed in 20 mL of toluene. Styrene (4 mL) and AIBN (0.02 g, 0.5 w/w % relative to monomer) were added next. The mixture was degassed under N_2 flow for 20 minutes using an ice bath under magnetic upon which it was heated up to 70 ºC. The polymerization was carried out for 6 hours. Upon cooling to room temperature it was added drop-wise to methanol to precipitate the nanocomposite which was collected by centrifugation and dried in a ventilated oven at 60 ºC.

6.2.7. Extraction of the free PS

In a 25 mL round bottom flask fitted with condenser $Gd_2O_3:Eu^{3+}/SiO_2$/MPS/PS (20 mg) were dispersed in 20 mL of toluene. This mixture was heated up to 110 ºC, in oil bath and magnetic stirring, during 5 h. While the mixture was warm (temperature around 60 ºC), the $Gd_2O_3:Eu^{3+}/SiO_2$/MPS/PS were recovered by filtration using a membrane filter (pore size 0.2 μm, Aldrich).

6.3 – Morphology and FTIR

As reported by Lin *et al.* [221], $Gd_2O_3:Eu^{3+}$ cylindrical particles formed easily due to the isotropic growth along the *c* crystallographic axis. TEM images (see Chapter 3, Figure 3.1) show nanostructures consisting mainly of nanorods, with some nanotubes also present. The electron diffraction pattern indicates a cubic lattice. Closer examination by HRTEM reveals a thin amorphous layer at surface of the nanoparticles. The bright field image showed the polycrystalline character of the specimens: the white regions highlight the contours of small grains.

TEM analysis using several images shows that the sample is predominantly composed of $Gd_2O_3:Eu^{3+}$ nanorods having external diameters between 10 and 60 nm and the length between 100 and 500 nm. Although in lesser amount, $Gd_2O_3:Eu^{3+}$ nanotubes, with walls about 5 to 12.5 nm thick and inner channels about 5-10 nm wide, were also observed.

Coating of $Gd_2O_3:Eu^{3+}$ nanorods with a thin layer of SiO_2 were achieved using the Stöber procedure [222]. A homogeneous silica coating was obtained trough annealing at 700 ºC for 3 hours, this coating was confirmed by TEM (Figure 6.1), which clearly shows a homogeneous shell layer with thickness of 5-10 nm.

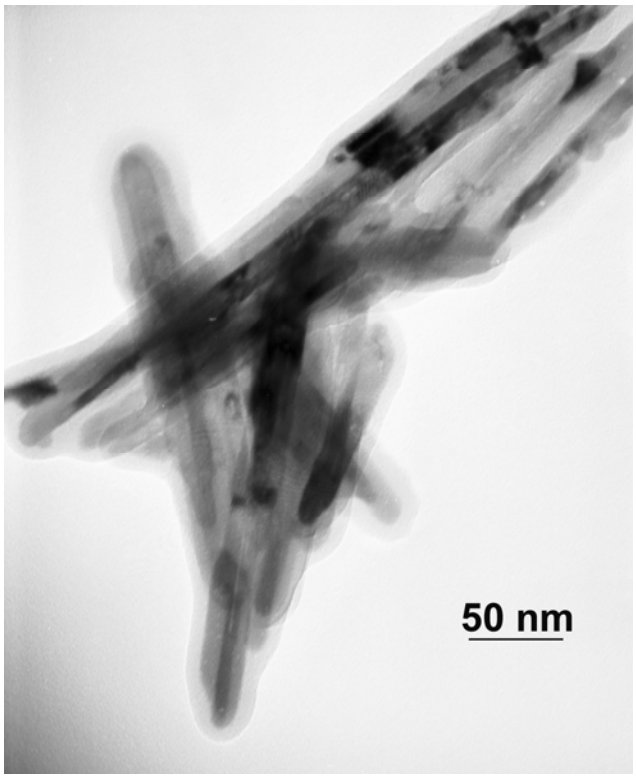

Figure 6.1- TEM images of silica coated $Gd_2O_3:Eu^{3+}$ nanorods ($Gd_2O_3:Eu^{3+}/SiO_2$).

The presence of silica was also confirmed by FTIR spectroscopy (Figure 6.2b). The parent nanotubes exhibit bands characteristic of cubic Gd_2O_3 at 303, 336, 386, 431 and 538 cm^{-1}, which are assigned to the Gd-O stretching modes [225]. $Gd_2O_3:Eu^{3+}/SiO_2$ nanorods give a band at 472 cm^{-1} due to Si-O-Si vibration contribution, and peaks at 800 and 950 cm^{-1} ascribed to Si-O-H stretching. The intense bands near 1100 cm^{-1} are assigned to the asymmetric stretching of the Si–O–Si bridge of the siloxane link [226]. The Si–O–Gd bond should appear below 400 cm^{-1}, which is beyond the capability of our instrument. Zeta potential measurements of pristine $Gd_2O_3:Eu^{3+}$ and silica coated nanorods in aqueous medium at pH 9.5 were -19 and -30.4 mV, respectively.

Following well established procedures described in the literature, $Gd_2O_3:Eu^{3+}/SiO_2$ nanorods were modified with MPS to promote covalent bonding between the nanorods surface and the polymer chains [220,224]. The methoxy groups of the MPS coupling agent hydrolyse in water, under basic conditions, via condensation with silanol groups, forming siloxane bonds (Si-O-Si) with the silica surface. On the other hand, the methacrylate groups allow co-polymerisation with other monomers, in the present case styrene. Removal of unreacted MPS was carried out by dialysis and monitored by UV spectroscopy as described in the experimental section. MPS grafting was confirmed by FTIR spectroscopy. As it can be

observed in Figure 6.2c), after grafting, the typical MPS bands for stretching vibrational modes at 1723 cm^{-1} (C=O), 1635 cm^{-1}(C=C), 2840 cm^{-1} (CH_2) and 2950 cm^{-1} (CH_3) [227] can be detected confirming that the nanorods have been modified. Grafting of MPS was also confirmed by contact angle measurements of $Gd_2O_3:Eu^{3+}$, $Gd_2O_3:Eu^{3+}/SiO_2$ and $Gd_2O_3:Eu^{3+}/SiO_2$/MPS surfaces were 28º , 16º, and 78º, respectively, confirming the hydrophobicity of the functionalized nanotubes upon MPS grafting.

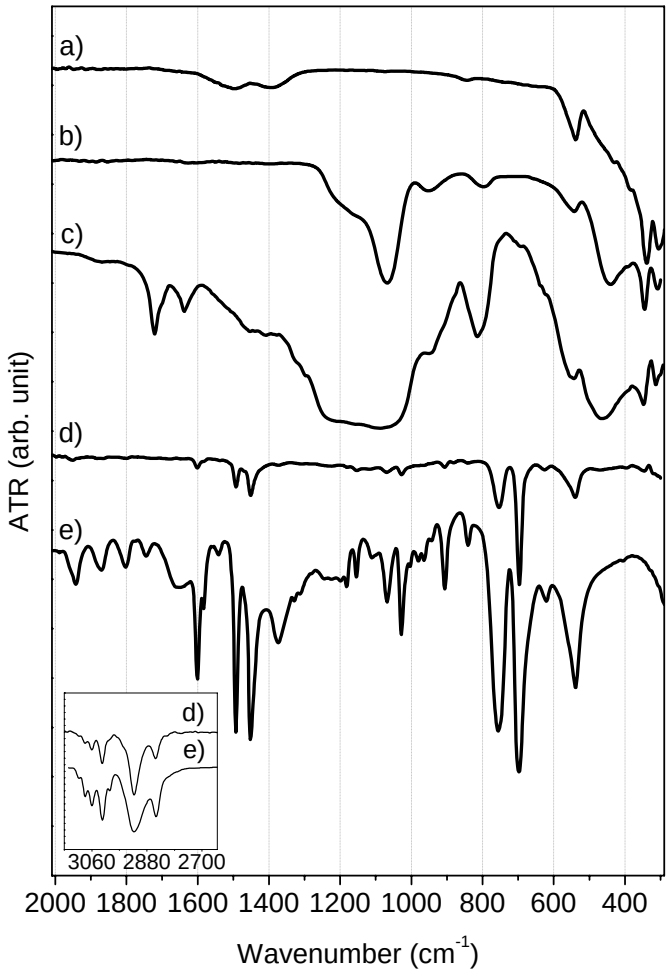

Figure 6.2 – ATR-FTIR spectra from a) $Gd_2O_3:Eu^{3+}$ nanorods, b) SiO_2-coated $Gd_2O_3:Eu^{3+}$ nanorods ($Gd_2O_3:Eu^{3+}/SiO_2$), c) $Gd_2O_3:Eu^{3+}/SiO_2$/MPS, d) SiO_2-coated $Gd_2O_3:Eu^{3+}$ nanorods / poly (styrene) nanocomposite ($Gd_2O_3:Eu^{3+}$ / SiO_2 / MPS / PS) and e) poly(styrene). Inset the expansion of the 2650-3100 cm^{-1} region from spectra d) and e).

$Gd_2O_3:Eu^{3+}/SiO_2$/MPS/PS nanocomposites were then prepared by conventional *in situ* radicalar polimerisation of styrene using the miniemulsion and solution polymerization techniques as illustrated in Scheme 6.1. As it is well known that a significant amount of free polymer is formed under these reaction conditions [228], nanocomposites were isolated by successive centrifugation/redispersion cycles using water in the case of materials prepared by

miniemulsion and ethanol in the case of solution polymerization. The precipitates were dried in a ventilated oven at 60 ºC. The band of the benzene ring folding appears at 700 cm^{-1}, C–H bending of the benzene ring at 759 cm^{-1} [229], as well bands at 3027 cm^{-1} assigned to the C–H stretching of phenyl group and of the bands in the range 1400–1600cm^{-1} characteristic of the C=C stretching of poly(styrene) as well as C-H bending of PS main chain [230] in the FTIR spectra of the $Gd_2O_3:Eu^{3+}$ / SiO_2 / MPS / PS nanocomposites confirm the presence of PS as it shown in Figure 6.2

The FTIR spectrum acquired from $Gd_2O_3:Eu^{3+}/SiO_2$/MPS/PS after extraction of the free PS, Figure 6.3b, the characteristic bands of the PS (at 700, 759, 1400-1600 and 3027 cm^{-1}) are also observed, although with reduced intensity relative to the other bands.

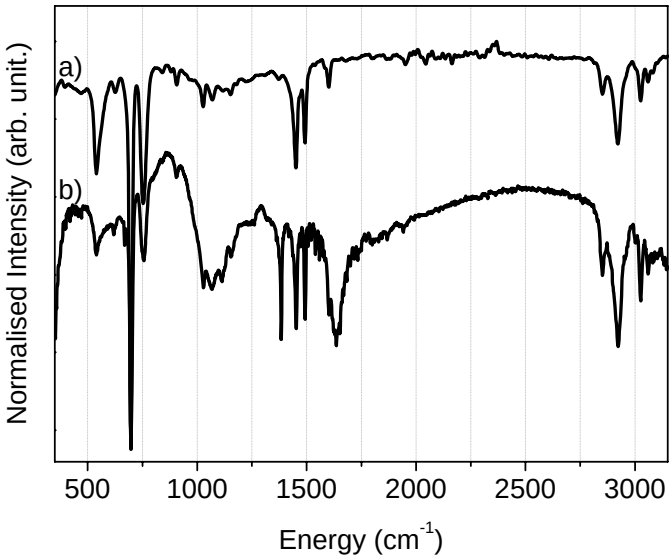

Figure 6.3 – FTIR spectra from $Gd_2O_3:Eu^{3+}/SiO_2$/MPS/PS a) as prepared and b) after extraction of the free PS.

The morphology of the precipitates collected was investigated by SEM and TEM which revealed that the polymerization technique used has a significant influence on the morphology of the polymer coating. Images of the materials prepared by miniemulsion are shown in Figure 6.4A-C. Poly(styrene) spheres (< 100 nm) appear attached to the nanorods surface, indicating that the co-polymerization between the MPS methacryloyl end group and the carbon double bond of the styrene monomer provided a bridge between the polymer chains and the $Gd_2O_3:Eu^{3+}$ / SiO_2 surface. MPS modified nanorods being hydrophobic are stabilized by the surfactant creating a hydrophobic environment capable of capturing active

oligomers produced in the aqueous phase which co-polymerize with the methacrylate group of MPS.

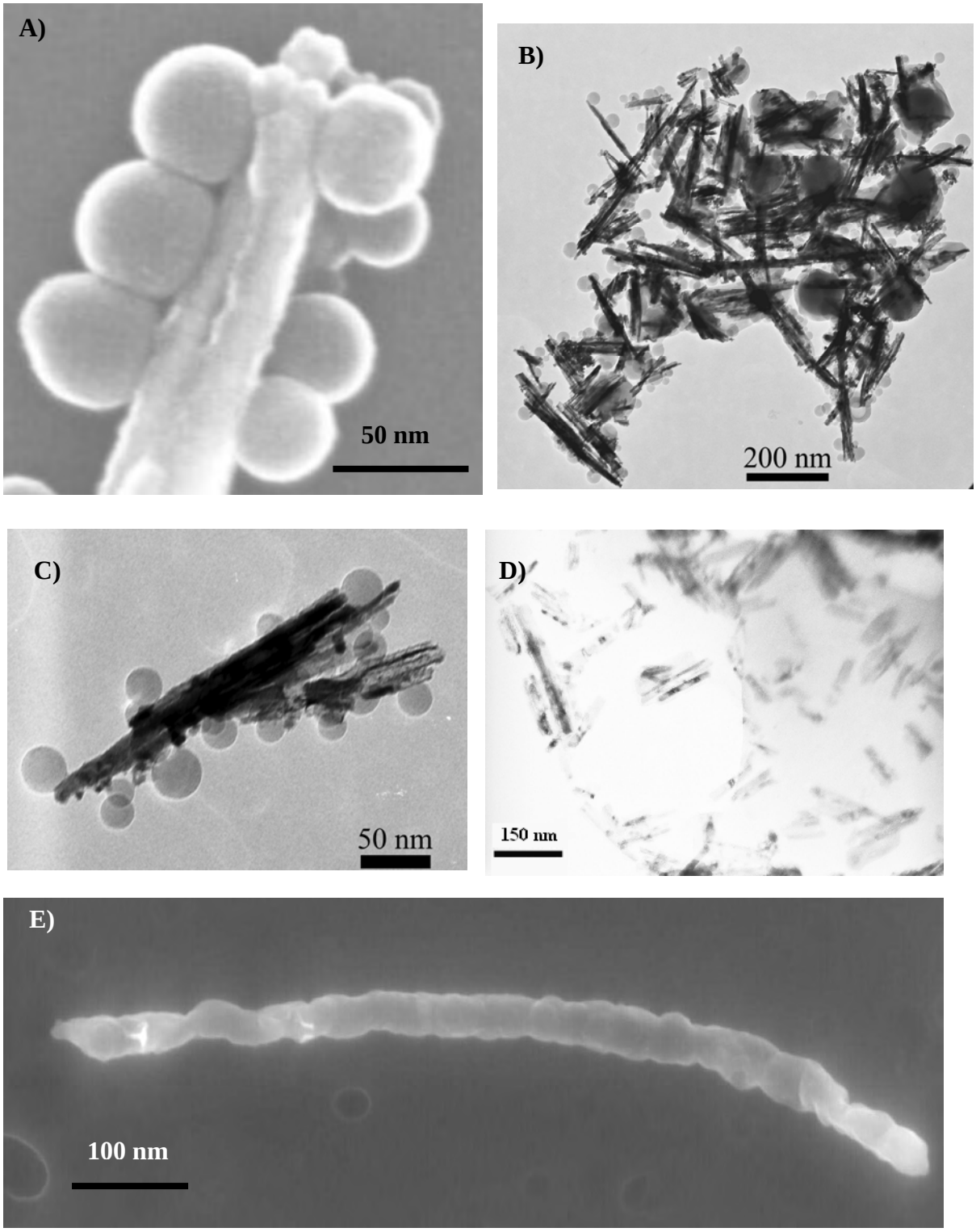

Figure 6.4 – A) SEM and B-C) TEM images of $Gd_2O_3:Eu^{3+}$ / SiO_2 / MPS / PS nanocomposite prepared by miniemulsion, D) TEM from nanocomposite prepared by solution technique and E) SEM after extraction of the free PS.

As shown in previous works from Esteves *et al.* and Reculusa *et al.* [220,231] the morphology of polymeric coating on silica surfaces is associated with the grafting density of MPS which depends on a variety of parameters including surface activation, amount of MPS used and pH of the reaction medium. Although the silica surface was activated by annealing at 700 ºC and an excess amount of MPS was used, the pH was kept around 7 to prevent secondary reactions as discussed elsewhere. Therefore, the grafting may not have been sufficient despite the fact that the surface became significantly more hydrophilic upon MPS grafting. In contrast, the nanocomposites prepared by the solution technique yielded nanorods dispersed in a poly(styrene) matrix as shown in Figure 6.4D. As the polymerization occurs in organic media and under reflux both the interfacial tension problems are reduced. Moreover, in the presence of the organic solvent the polymer chains formed are allowed to expand and wrap around the nanorods surface and/or neighbouring polymer chains yielding a homogeneous coating. The synthetic strategy studied offers a simple processing method to prepare, for example, thin films and can be used with a variety of polymeric materials. Figure 6.4E shows the PS onto the nanorods surface even after the extraction of the free PS, this result indicate the effective MPS/PS bond.

6.4 – PLE and PL of the composites:

The excitation spectra of $Gd_2O_3:Eu^{3+}$ and SiO_2 coated nanorods are shown in Figure 6.5. As presented in Chapter 3, the excitation spectrum from $Gd_2O_3:Eu^{3+}$ nanorods while monitored at 611 nm ($^5D_0 \rightarrow {}^7F_2$ of the Eu^{3+} ions at C_2 local symmetry) transition has a broad band at *ca.* 255 nm ascribed to LMCT. After silica coating, the excitation spectra did not change. However, styrene polymerization slightly shifts the LMCT band from 259 nm to 248 nm (miniemulsion, inset of Figure 6.6) and 253 nm (solution, not shown). These changes are probably associated with the blue emission band (400-600 nm) that appears after styrene polymerisation displaying excitation paths superimposed with the LMCT band (Figure 6.6).

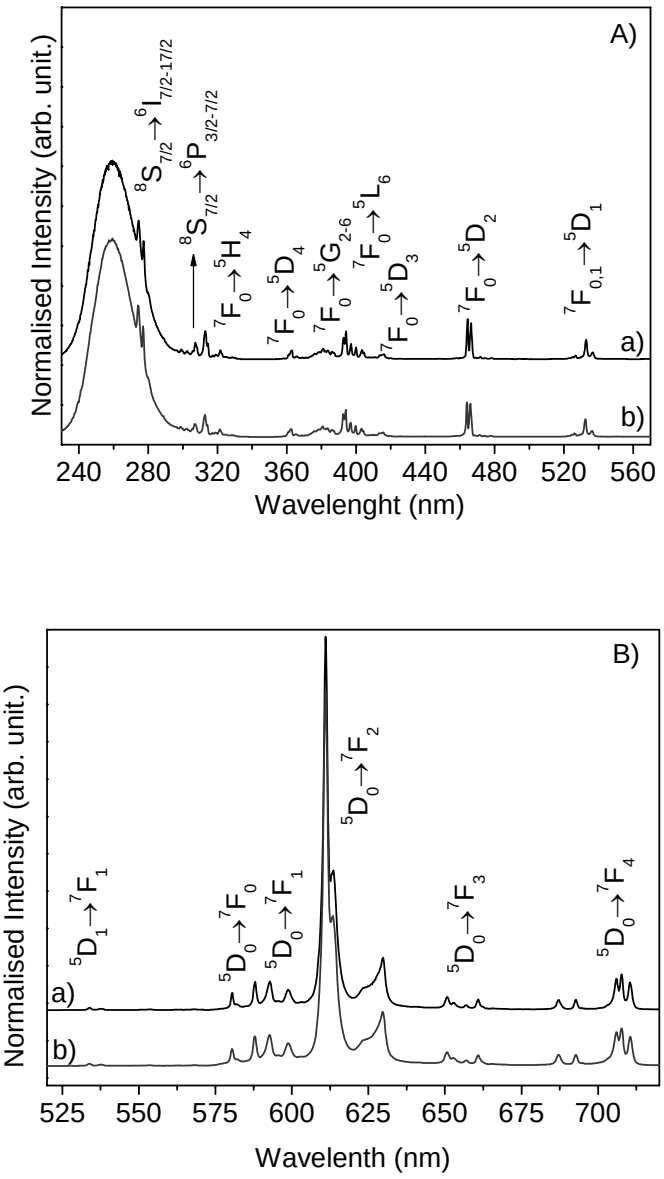

Figure 6.5 - A) Excitation spectra monitored within the Eu^{3+} $^5D_0 \rightarrow {}^7F_2$ (C_2) and B) emission spectra upon excitation at 255 nm, of Gd_2O_3:Eu^{3+} nanorods a) and SiO_2-coated Gd_2O_3:Eu^{3+} nanorods (Gd_2O_3:Eu^{3+}/SiO_2), b).

The same Eu^{3+} intra-configurational emission lines were observed in the spectra of Gd_2O_3:Eu^{3+} and Gd_2O_3:Eu^{3+} / SiO_2 nanorods and poly-styrene nanocomposites. The emission spectra were also described in Chapter 3. The similarity between them confirms that the coating does not change the local symmetry of the (bulk) Eu^{3+} ions.

The emission QY of Gd_2O_3:Eu^{3+} (showed at Table 3.2, Chapter 3) and Gd_2O_3:Eu^{3+}/SiO_2 nanorods were measured upon excitation on the LMCT band (255 nm), Gd^{3+} (274 nm) and Eu^{3+} (394.4 nm) energy levels, we obtained the QY values of 0.86, 0.74 and 0.14, respectively. Remarkably, after silica coating the emission QY of nanorods

increased for all excitation wavelengths, reached a maximum for 255 nm excitation (35% increased when compared with the pristine one) and they were even larger than the values measured for $Gd_2O_3:Eu^{3+}$ bulk microcrystals (for excitation at 255 nm and 274.4 nm).

A blue emission band appears after styrene polymerisation in samples prepared trough miniemulsion or solution (Figure 6.6). Using similar experimental conditions for the spectra acquisition, no emission was detected from the reagents, thus, the hypothesis of this band arises from the non reacted chemicals was disregarded.

H. M. Lee *et al.* reported a similar blue emission from poly(styrene) spheres after electron irradiation [234]. The irradiation induced the creation of radicals, including aryl, main chain, chain-end and phenyl, and these radicals can make bonds with each other forming new molecular structures, for instance aromatic hydrocarbons such biphenyl, p-terphenyl, substituted naphthalene or phenanthrene. Such molecules can be also produced, in minor amounts, during the radical initiated miniemulsion and solution polymerizations of styrene and therefore we tentatively ascribed the blue emission of Figure 6.6 to these radicals.

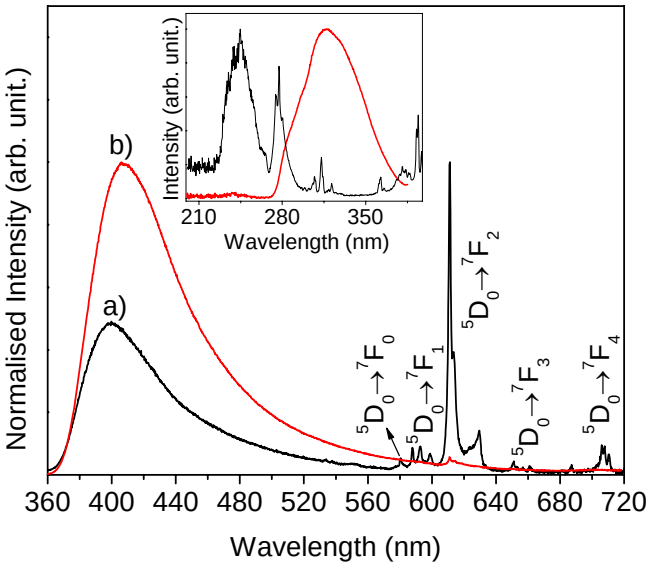

Figure 6.6 – Emission spectra of SiO_2-coated $Gd_2O_3:Eu^{3+}$ nanorods/poly(styrene) nanocomposites prepared by miniemulsion upon excitation at a) 274.4 nm (black line) and b) 317 nm (red line). The inset shows the excitation spectra monitored at 409 nm (red line) and 611 nm (black line). The spectra of the nanocomposites prepared by solution polymerization are similar.

The $^5D_0$ decay curves monitored at 611 nm show an increase of the decay time after silica coating (Figure 6.7). Using an excitation wavelength of 394.4 nm, the decay curves of $Gd_2O_3:Eu^{3+}$ and $Gd_2O_3:Eu^{3+}/SiO_2$ nanorods are well fitted using single exponentials yielding lifetimes of 1.43 ± 0.01 and 1.80 ± 0.01 ms, respectively. The increase of the decay time is related with the reduction of the non-radiative relaxation due the removal of Eu-OH groups upon silica coating, as previously observed for $Y_2O_3:Eu^{3+}/Y_2O_3$ core-shell composites.

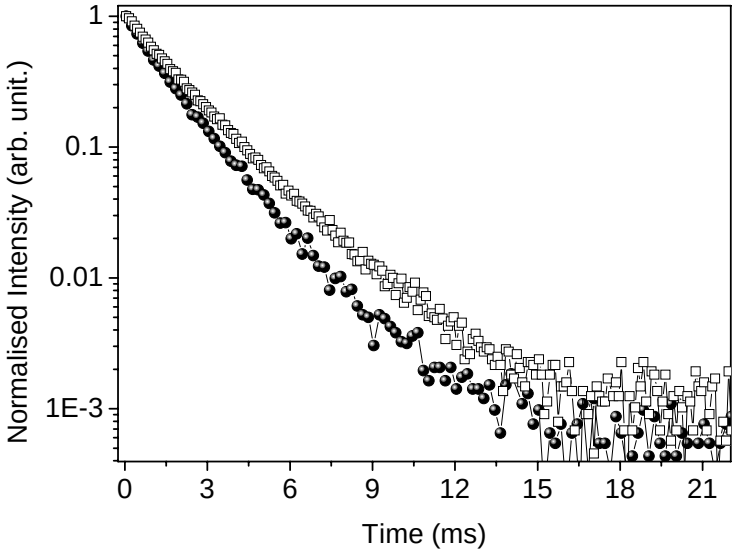

Figure 6.7 – 300 K decay curves of $^5D_0$ level monitored at 611 nm ($^5D_0 \rightarrow {}^7F_2$ lines at C_2 local symmetry) from $Gd_2O_3:Eu^{3+}$ nanotubes (*spheres*) and SiO_2-coated $Gd_2O_3:Eu^{3+}$ nanotubes (*squares*) acquired upon excitation at 394.4 nm.

6.5 – Surface modification of Y_2O_3 nanotubes with fatty acids

6.5.1-Y_2O_3 nanotubes synthesis

Y_2O_3 nanotubes were prepared by micro-oven or conventional hydrothermal synthesis (see Appendix A3).

6.5.2 - Stearic acid surface functionalization (SA/Y_2O_3)

81 mg of Y_2O_3 nanotubes powder were dispersed in 15 mL of toluene by ultrasonic stirring during 10 minutes. After, 161 mg of stearic acid was added and submitted to ultrasonic stirring in ice bath during 20 minutes. In a next step, in nitrogen atmosphere and

reflux, using magnetic stirring this suspension was heated until 110 ºC during three hours. The precipitates were collected by centrifugation, washed with isopropanol at least three times and dried at 60 ºC during 12 hours.

6.5.3 - Langmuir-Blodgett (LB) films

The LB films were transferred onto pre treated glass slides (1 cm^2) or freshly cleaved mica substrates (1 cm^2) in a NIMA model equipment. The glass slides were cleaned by immersion in concentrate nitric acid solution during 15 min, and then washed with ultra pure water, acetone and acetate ethyl, respectively.

A monolayer of stearic acid was deposited onto substrates in order to obtain hydrophobic surfaces. Firstly, the pressure sensor was calibrated and the water solution having Zn^{2+} ions (4 x 10^{-4} M) was added into the sink accessory, an isotherm was acquired to insure the absence of impurities, pressure lower than 1 mN/m was achieved. Subsequently, the substrate was translated until to be immersed into the Zn^{2+} solution, with the barriers closed the solution of stearic acid in chloroform (0.2 mg/ml, 150 μL) was dropped, immediately the barriers were opened in order to spread the material. An interval of 15 minutes was adopted for the complete chloroform evaporation. The pH around 6 was maintained by adding Na_2CO_3 solution (5 x 10^{-5} M).

During the deposition of the stearic acid monolayer at an air/water interface, the target surface pressure was kept constant at 28 mN/m, barrier speed 100 cm^2/mim, and using the vertical dipping method with dipping speed equal to 10 mm/min. These substrates were dried at room temperature and harvested in a humidity free environment.

LB films of SA/Y_2O_3 nanotubes were obtained using the following procedure: ultra pure water was added into the sink equipment, the cleanness was checked by the isotherm and pressure lower than 1 mN/m. Subsequently, the hydrophobic substrate was moved until it was immersed in the ultra pure water, with the barriers closed the solution of stearic acid functionalised Y_2O_3 nanotubes in chloroform (0.2 mg/ml, 850 μL) was dropped, immediately the barriers were opened in order to spread the material. After 15 minutes, deposition was performed with the target surface pressure kept constant at 40 mN/m, barrier speed 100 cm^2/mim and number of layer equal 1.

For mixed films the Zn^{2+} solution was used, stearic acid solution (0.2 mg/ml) and SA/Y_2O_3 nanotubes solution (0.2 mg /ml) were mixed; a volume of 100 μl was utilized. The deposition was performed with the target surface pressure kept constant at 28 mN/m, barrier speed 100 cm^2/mim and number of layer equal 1.

The resulting LB films were analysed by SEM.

6.6 – Morphology and FTIR

Surface modification was performed using stearic acid, which has a linear chain with length around 2.1 nm, Figure 6.8, and thus migration of molecules to the inner region is also possible. TEM and SEM of Y_2O_3 nanotubes are displayed in Figure 6.9A-C.

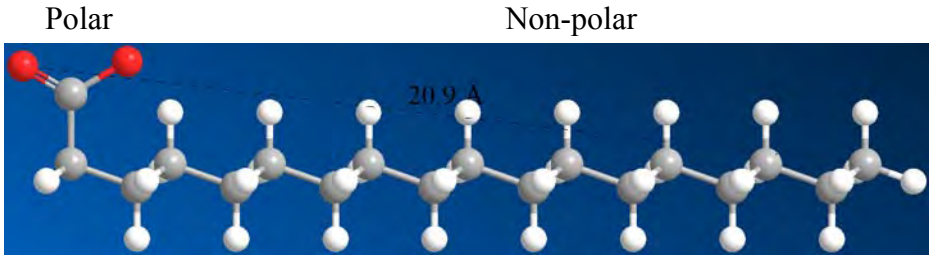

Figure 6.8 – Stearic acid molecule: oxygen, carbon and hydrogen atoms are represent by red, gray and white balls, respectively.

Nitrogen adsorption revealed no changes in pore size distribution (PSD) after surface functionalisation. However, reduction of the volume occupied by the pores points out that some nanotubes were blocked by fatty acid molecules.

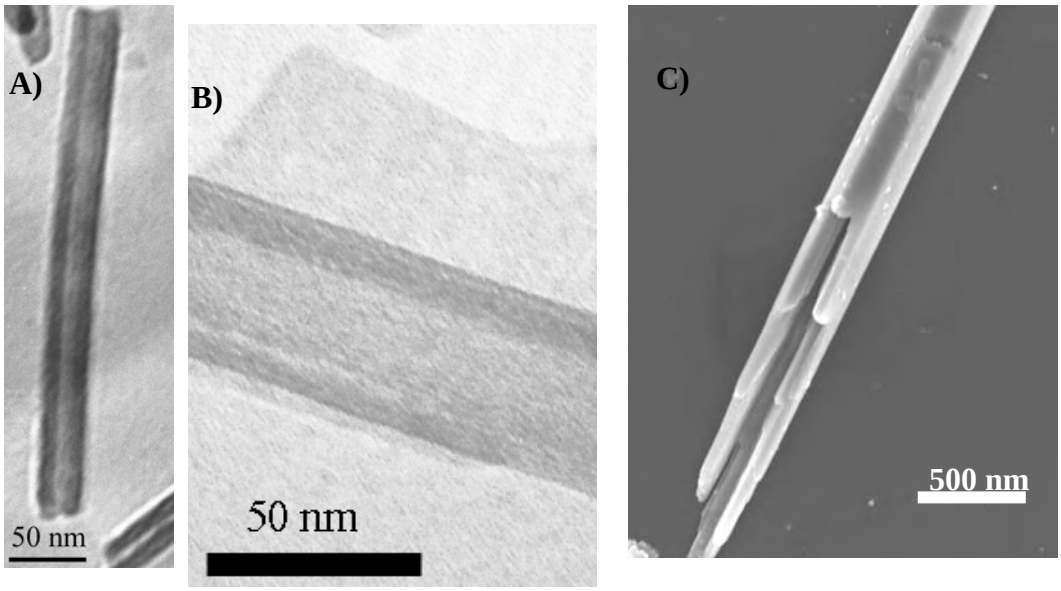

Figure 6.9 – A-B) TEM and C) SEM images from Y_2O_3 nanotubes

The colloidal stability of the stearic acid functionalised Y_2O_3 nanotubes was verified. Distilled water, ethanol and toluene were tested as solvents. Dispersion in water was not possible due the presence of the aliphatic chain of the grafted molecules. In ethanol and

toluene media, after ultrasonic stirring, a homogeneous dispersion was immediately obtained. The precipitation rate was visually faster in ethanol than in toluene medium. These results indicate that the modification from hydrophilic to hydrophobic character of the nanotubes surface was achieved. Moreover, SEM images reveal a slightly irregular surface after the derivatization, indicating the presence of the stearic acid, Figure 6.10.

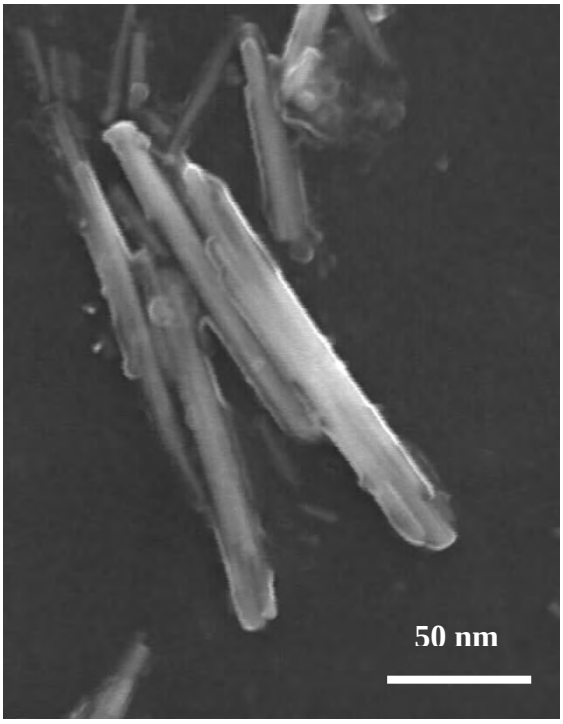

Figure 6.10 – SEM image from SA/Y_2O_3 nanotubes

ATR-FTIR spectra from SA and SA/Y_2O_3 nanotubes are displayed at Figure 6.11a-b, respectively. In the spectra (a) the peak at 1698 cm^{-1} is attributed to carboxyl groups (COOH) of stearic acid. Figure 6.12 shows four possible mechanisms to bridge stearic acid chain in nanotubes surface: (A) monodentate binding mode ν_2 (C=O), (B) and (C) carboxyl has shifted and split into a doublet indicating a weakening of the double bond to a carboxylate asymmetric stretch and the presence of two different bonding modes and (D) carboxylate group bidentate bond (1465 cm^{-1}) [235-237].

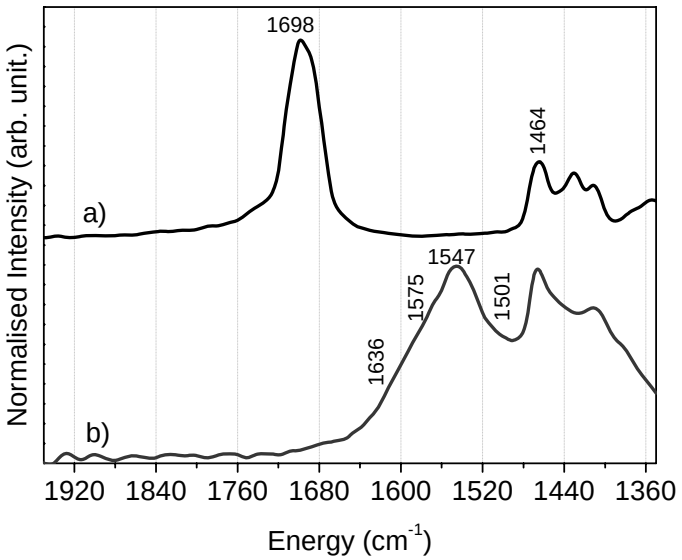

Figure 6.11 - ATR-FTIR of a) SA and b) SA/Y_2O_3 nanotubes

The intense peak observed at 1698 cm^{-1} (C=O stretch) in the Figure 6.11a (from pure stearic acid) has shifted to 1440-1650 cm^{-1} region and split into a doublet in the spectra of SA/Y_2O_3 nanotubes, Figure 6.11b, indicating a weakening of the double bond to a carboxylate (asymmetric stretch). The peak at 1464 cm^{-1} can be attributed to the symmetric bonding mode of a carboxylate group. Peaks at 1636 and 1501 cm^{-1} and a doublet at 1575 and 1547 cm^{-1} shown in spectra are indicative of a surface with mixed strength of bidentate binding. The peaks at 2300-3000 cm^{-1} region (not shown) correspond to symmetric and asymmetric stretch from CH_2 groups; steric hindrance effect resulted in an overall shift (~3 cm^{-1}) to higher energy position in the spectra from SA/Y_2O_3 nanotubes

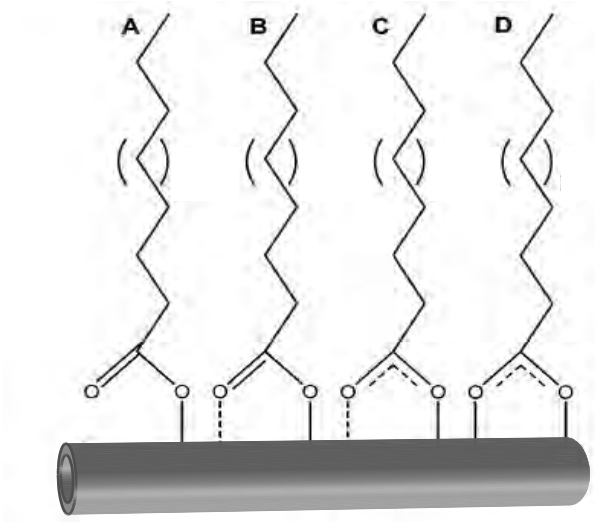

Figure 6.12 - A) monodentate binding mode ν_2 (C=O) at 1698 cm^{-1}, B) and C) carboxyl has shifted and split into a doublet indicating a weakening of the double bond to a carboxylate asymmetric stretch and the presence of two different bonding modes and D) carboxylate group bidentate bond (1465 cm^{-1})

6.7 – Langmuir-Blodgett (LB) films

Langmuir films consist of surface active agents or 'surfactants' trapped at the interface between two dissimilar phases, either liquid-liquid or liquid-gas) [237]. Surfactants are molecules which are amphiphilic; composed of a hydrophilic part and a hydrophobic part. Hydrophilic groups consist of groups such as carboxylic acid, sulphates, amines and alcohols. These are all attracted to polar media such as water and the forces acting upon them are predominantly Coulomb type ($1/r^2$). Hydrophobic (or oleophilic) groups such as a hydrocarbon chain, fats and lipids are much less (if at all) water soluble and the forces acting upon them are predominantly van der Waal's type ($1/r^{12}$ and $1/r^6$). Amphiphilic molecules are trapped at the interface because they posses these two very different types of bonding within the one molecular structure. When surfactants, dissolved in a non-aqueous volatile solvent, are introduced into a polar liquid surface, the solvent evaporates leaving the surfactants oriented at the liquid-gas interface. The hydrophilic 'head' groups pull the molecule into the bulk of the water and the hydrophobic 'tail' groups point into the air. A surface monolayer will only be achieved if the amphiphatic balance of the molecule is correct; that is the balance between hydrophobic and hydrophilic parts.

Sweeping a barrier over the water surface causes the molecules to come closer together and eventually to form a compressed and ordered monolayer. The film produced by such a method is known as a Langmuir film.

Langmuir-Blodgett films consist of mono-molecular layers stacked sequentially onto a solid substrate. A solid substrate is lowered into the water, breaking through the Langmuir film and, provided that certain criteria have been met, the Langmuir film attaches itself to the substrate, coating it with a mono-molecular layer. In this way, a monolayer of stearic acid was deposited in order to obtain the substrate with hydrophobic charater:

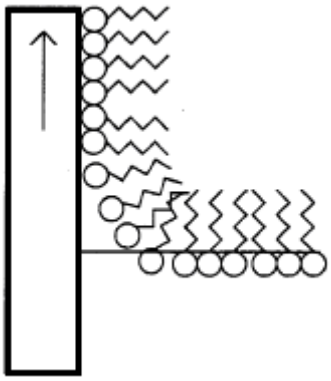

Scheme 6.2 - Deposition of the first monolayer onto a hydrophilic substrate

Molecules or particles in a suspension are subject to attractive forces; in the bulk of the suspension these forces are equal. However, at a surface or interface the forces are unequal and the net effect is to pull the peripheral molecules into the bulk of the suspension. This effect gives rise to surface tension. The surface tension can be defined as “the work required to expand the surface isothermally by unit area”. The tendency of surface-active molecules to accumulate at interfaces favours expansion of the interface and hence lowers the surface tension. Such behaviour makes it possible to monitor the surface pressure as a function of the area occupied per molecule provided that the number of molecules deposited on the surface is known. The isotherm can usually be seen to consist of three distinct regions: gas, liquid and solid regions, depending of the degree of organization of the molecules or particles upon the action of the barriers:

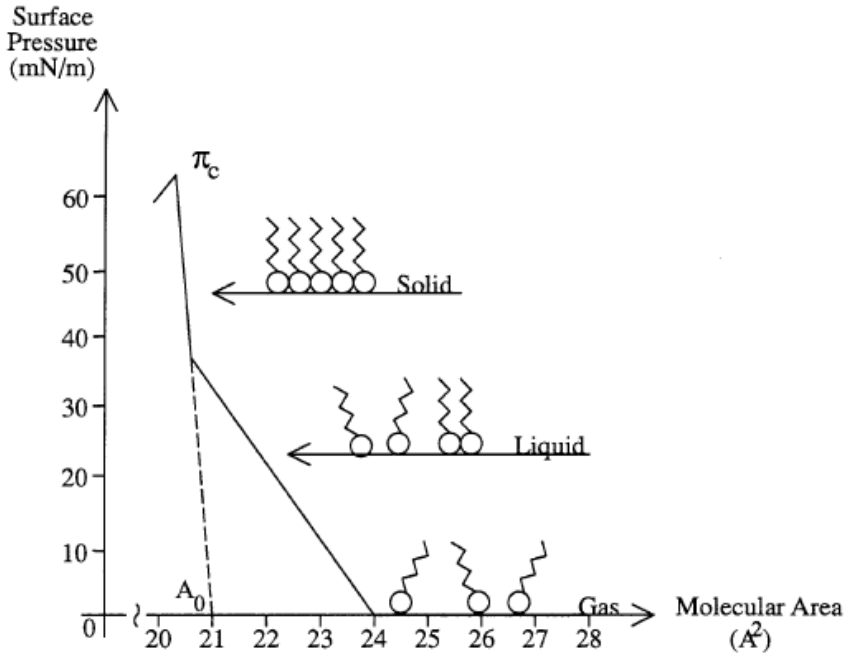

Scheme 6.3 – Regions of stearic acid isotherm on pure water [237].

Usually measures are taken to exclude any contaminants from the subphase as the introduction of ions into pure water can dramatically affect the monolayer properties. For example, the repulsion between adjacent ionised acid groups can be reduced by the addition of divalent metal ions into the water. Introducing zinc ions (Zn^{2+}) into the water results in following reaction taking place:

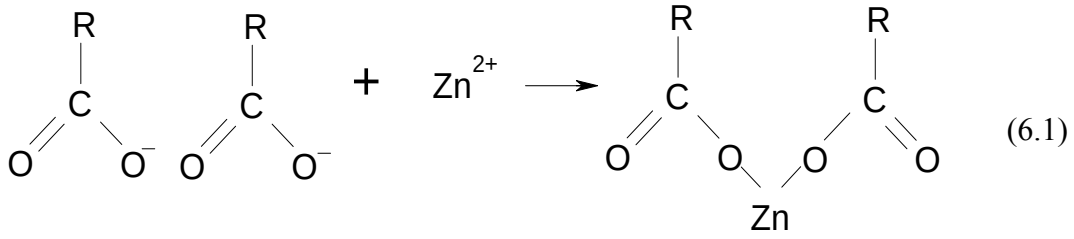

(6.1)

This reaction benefits the organization of the stearic acid in the Langmuir films, for instance, isotherms acquired from stearic acid solution and stearic acid with Zn^{2+} solution, Figure 6.13a-b, respectively, confirm that the presence of Zn^{2+} ions increased the surface tension. Moreover, the transition between liquid and solid regions is better discerned at Figure 6.13b.

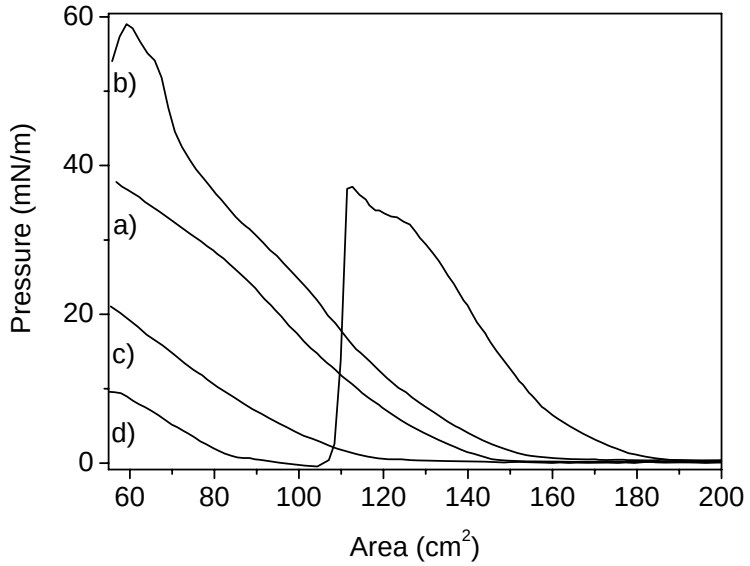

Figure 6.13 - Isotherms from a) SA, b) SA and Zn^{2+} solution, c) SA/Y_2O_3 nanotubes and d) SA/Y_2O_3 nanotubes mixed with free SA and Zn^{2+} solutions (mixed film method).

To achieve a Langmuir-Blodgett assembly, it is necessary that Y_2O_3 or lanthanide oxide nanotubes were rendered hydrophobic and monodispersed in organic solution (chloroform). As discussed previously, this hydrophobic character was achieved by grafting the stearic acid molecules directly onto the surface. The isotherms acquired from SA/Y_2O_3 nanotubes, Figure 6.13c, indicate such organization; however, much better organization was achived by using the mixed film method by adding, simultaneously, free stearic acid and Zn^{2+} solutions, the corresponding isotherm is showed as Figure 6.13d.

Well aligned nanostructures of the modified nanotubes were prepared using the Langmuir-Blodgett technique; Figure 6.14A-D. The LB films, Figure 6.14A prepared from the SA/Y_2O_3 nanotubes solution, presents dispersed and aligned distribution of the nanotubes; while the LB films, Figure 6.14B-D prepared by the mixed films method, presents aggregated and aligned distribution of the nanotubes.

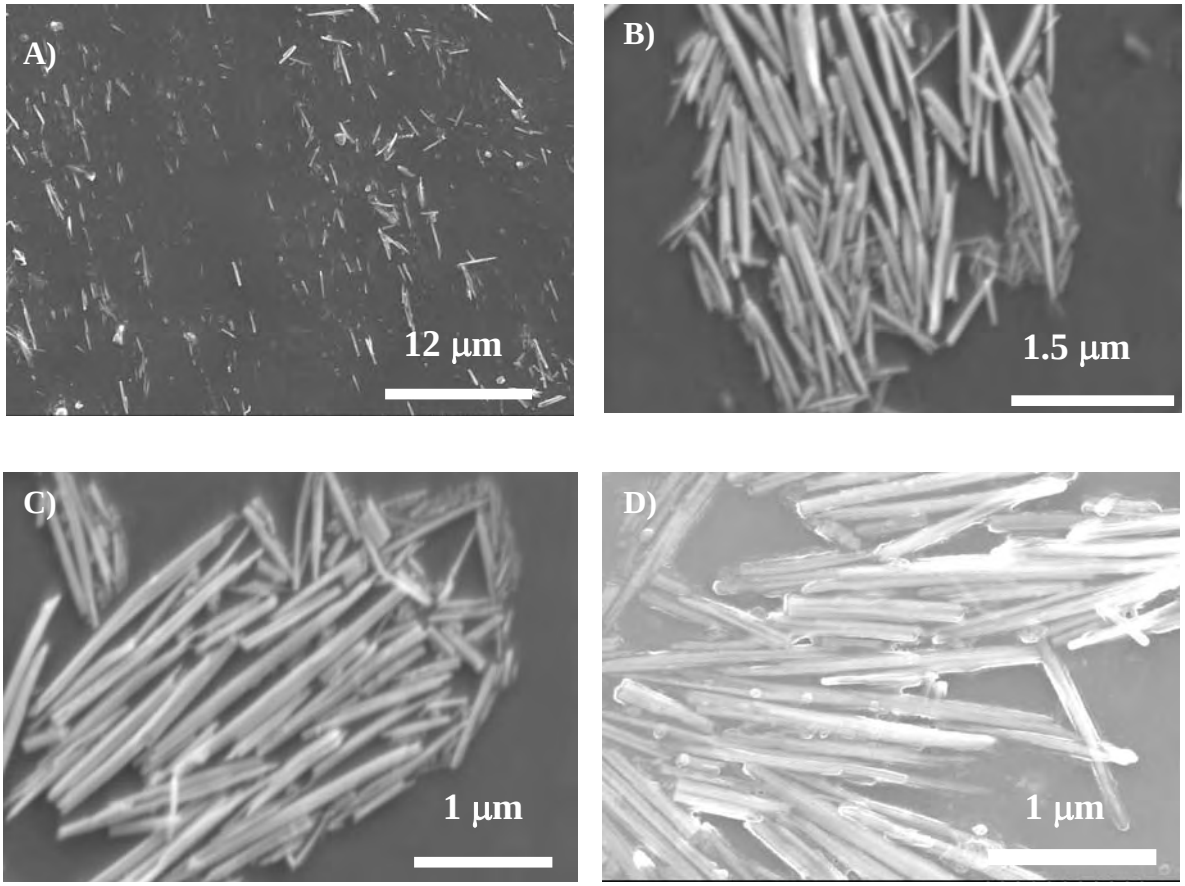

Figure 6.14 - SEM images of films of A) SA/Y_2O_3 nanotubes and B-D) SA/Y_2O_3 nanotubes mixed with free stearic acid and Zn^{2+} solutions (mixed film method).

6.8 – Conclusions

Gd_2O_3:Eu^{3+} / SiO_2 / MPS / PS nanocomposites were prepared by conventional *in situ* radical using the miniemulsion and solution polymerization techniques. Thermal annealing at 700 ºC was important to both transform gadolinium hydroxide into the oxide and to activate the nanorods surface, in order to obtain a regular silica coating. In aqueous suspension, bare Gd_2O_3:Eu^{3+} and silica coated nanorods are negatively charged (zeta potentials of, respectively, -19 and -30.4 mV, at pH 9.5). After silica coating, no differences were observed in the excitation and emission spectra, but the styrene polymerization caused a slight shift of the LMCT band. Blue emission arising from aromatic hydrocarbons is observed in the final nanocomposites. The decay time and emission quantum yield increased considerably after silica coating and are was even larger than those measured for bulk Gd_2O_3:Eu^{3+} crystals. The co-polymerization between methacryloyl end group of the coupling agent (MPS) and the vinyl bond group of the styrene monomer allowed the grafting of the polymer chains to the the surface of Gd_2O_3:Eu^{3+}/SiO_2 nanorods. Depending on the polymerization technique used,

the nanorods were coated with poly(styrene) spheres or by a homogeneous polymer coating. Although the polystyrene coating reduced the optical properties of these nanorods the synthetic strategy studied offers a simple processing method to prepare, for example, thin films and can be used with a variety of polymeric materials, which can either enhance the optical properties or, at least, not affect them.

The outer surface of Y_2O_3 nanotubes has been modified with stearic acid under reflux. Films with aligned Y_2O_3 nanotubes were prepared using the Langmuir-Blodgett technique. Using SA/Y_2O_3 suspention, films having dispersed and aligned nanotubes distribution were obtained, while using the SA/Y_2O_3 suspension and the mixed film method (with SA and Zn^{2+} solution), films of aggregated and aligned nanotubes were obtained.

Chapter 7

Conclusions

Partial conclusions were presented at the end of each chapter. Here, I summarize general conclusions and perspectives for future work concerning synthesis and technological applications of lanthanides oxides nanotubes/nanorods.

This thesis reports on the preparation of lanthanide oxides nanotubes/nanorods, their structural and optical characterization (PL, PLE, life time and QY) as well application in AFM or SNOM tips, liquid-phase catalysis or in the preparation of polymer-based composites.

The first challenge of this work was to obtain lanthanides oxides with tubular morphology. Using conventional hydrothermal synthesis and tuning parameters such as pH, temperature and reaction time I was able to obtain $Gd_2O_3:Eu^{3+}$, $Gd_2O_3:Yb^{3+}Eu^{3+}$ and CeO_2 materials samples often composed of a mixture of nanorods and nanotubes, 10-50 nm outer diameter and less than 1 μm in length. Some nanotubes were also observed in Y_2O_3 samples synthesized by hydrothermal synthesis upon microwave heating. Larger tubes with 500 nm outer diameter and 5 μm length were obtained. For instance, $Y_2O_3:Eu^{3+}$ tubes were prepared by conventional hydrothermal synthesis and rigorous control of pH with ammonia. Multi-step solid-liquid interface reaction using $Ce(OH)CO_3$ as the precursor also resulted in regular CeO_2 tubes. Considering these results I conclude that hydrothermal synthesis parameters such as pH *ca.* 13, low temperatures (*ca.* 120 ºC) and short times of reaction (15-20 h) benefit the formation of nanotubes, although some nanorods are almost always also obtained.

Regarding the optical properties, a strong anomalous thermalisation effect was observed for $Gd_2O_3:Eu^{3+}$ and $Gd_2O_3:Yb^{3+}Eu^{3+}$ nanotubes; not detected in nanorods and microcrystals due to the absence of nanoconfinement effects.

Hot bands arising from the two lowest-lying $^7F_1$ Eu^{3+} crystal-field levels are observed in the excitation spectra of $Gd_2O_3:Eu^{3+}$ nanotubes with intensity larger than the intensity of the corresponding bands originated in the $^7F_0$ ground state, between 300 and 11 K. For $Gd_2O_3:Yb^{3+},Er^{3+}$ nanotubes, hot bands arising from the $^2H_{11/2}$ Er^{3+} level are also observed in the emission spectra measured in these temperature range with intensities similar to the intensities the bands originated in the $^4S_{3/2}$ low-energy level. These remarkable anomalous thermalisation effects, which are strongly dependent on the thermal history of the samples and

on the Eu^{3+} or Yb^{3+}/Er^{3+} concentrations, is one order of magnitude larger than previously reported for similar $Gd_2O_3:Eu^{3+}$ (3.96%, annealing at 500 ºC, 1 h) nanotubes.

The anomalous thermalisation may be rationalized in the theoretical framework of ion-lattice interaction considering both, the one-dimensional phonon confinement *perpendicular* to the nanotubes wall (as previously proposed for $Gd_2O_3:Eu^{3+}$ nanotubes), and the discrete features of the phonon density of states. The energy match between the frequency of the available phonons and the $^7F_{1a,1b}$ and $^2H_{11/2}$ electronic levels provides a route to their thermalisation (depopulating process). Minor changes in the structure of the nanotubes (due to thermal treatment or Ln^{3+} concentration) may induce considerable changes in the discrete phonon density of states, entirely modifying the energy resonance conditions and the intensity ratio values.

The confinement on electron-phonon interaction in nanocrystals impacts other aspects of the luminescence dynamics of lanthanide ions that depend on the low-energy phonon modes of the lattice (*e.g.* in phonon-assisted energy transfer and upconversion processes). Therefore, a fundamental understanding of the effects of phonon confinement on the luminescence features is crucial, particularly in systems such as $Gd_2O_3:Eu^{3+}$ and $Gd_2O_3:Yb^{3+},Er^{3+}$ nanotubes that have been used as fluorescent markers in immunosensing applications.

We developed a simple method for the functionalization of AFM and SNOM tips with $Gd_2O_3:Eu^{3+}$ nanorods using the dielectrophoresis technique. The resulting tips remain sharp, retaining the benefits of AFM imaging while possessing the photophysical properties of the attached nanorods, high efficiency, sharp emission lines and long lifetimes (ms). Emitting probes with various emission colours can be prepared and easily tailored for specific applications. Regular topography imaging on test hybrid organic-inorganic samples was improved by using functionalized tips.

Catalytic activity was observed in CeO_2 nanotubes (CeNT), they have been shown to promote the oxidation of cyclohexene, cyclohexanol and ethylbenzene with *t*-BuOOH, at temperatures as low as 55 ºC. Mechanistic considerations have been put forward based on experimental evidence and literature data. The liquid-phase oxidation catalysis with CeNT/*t*-BuOOH is most likely associated with the Ce^{3+}/Ce^{4+} inter-conversion in the one-electron redox processes mediating the formation of *tert*-butyl(per)oxy radicals: UV-Vis and photoluminescence studies reveal the existence of both oxidation states of cerium in CeNT before and after its exposure to *t*-BuOOH or H_2O_2. The radical-chain process generates mainly *tert*-butylperoxy products in the reactions of cyclohexene and ethylbenzene most likely via the homolytic addition of *tert*-butylperoxy radicals. The reaction of PhEt at 55 ºC

forms 1-phenyl ethyl *tert*-butyl-peroxide as the only product (39% yield after 48 h). This result contributes to the list of the main applications of *t*-BuOOH as a source for tertiary-butyl derivatives, including alkyl peroxides.

Above 55 ºC, PhEtOOT is converted into acetophenone (used as ingredient in perfumes and as a chemical intermediate in the production of pharmaceuticals, resins and flavouring agents) in increasing amounts: for the reaction carried out at 105 ºC, acetophenone selectivity is 70% at 89% conversion. Leaching tests and ICP-AES indicate that CeNT is fairly stable towards leaching of cerium and the catalytic results obtained for the used CeNT are similar to those observed in the first batch run. The conversion of PhEt may be further improved by using an oxidizing pre-treatment with H_2O_2 or *t*-BuOOH to CeNT. When H_2O_2 is used instead of *t*-BuOOH, no conversion is observed for all the investigated substrates (cyclohexene, cyclohexanol, ethylbenzene, cyclohexane), most likely because CeNT is very effective in H_2O_2 disproportionation. Pre-treatment of CeNT with H_2O_2 or *t*-BuOOH prior to reaction of PhEt with *t*-BuOOH leads to faster reaction than CeNT. Ultraviolet-visible and photoluminescence spectroscopy confirm the presence of both Ce^{3+} and Ce^{4+} in the samples (with or without pre-treatment), albeit exposure to H_2O_2 seems to give a more defective material than that with *t*-BuOOH. The catalytic activity does not seem solely related to the number of defect sites, posing importance on other possible factors such as morphology, Ce^{3+}/Ce^{4+} ratio and corresponding redox potentials (a distribution may exist for each sample).

$Gd_2O_3:Eu^{3+}$ / SiO_2 / MPS / PS nanocomposites were prepared by conventional *in situ* radical polymerization using the miniemulsion and solution polymerization techniques. Thermal annealing at 700 ºC was important to both, transform gadolinium hydroxide into oxide, and to activate the nanorods surface, in order to obtain a regular silica coating. In aqueous suspension, bare $Gd_2O_3:Eu^{3+}$ and silica-coated nanorods are negatively charged (zeta potentials of, respectively, -19 and -30.4 mV, at pH 9.5). After silica coating, no differences were observed in the excitation and emission spectra, but the styrene polymerization caused a slight shift of the LMCT band. Blue emission arising from aromatic hydrocarbons was observed in the final nanocomposites. The decay time and emission quantum yield increased considerably after silica coating and were even larger than those measured for bulk $Gd_2O_3:Eu^{3+}$ crystals. The co-polymerization between the methacryloyl end group of the coupling agent (MPS) and the vinyl bond group of the styrene monomer worked as bridge to graft the polymer chains to the surface of $Gd_2O_3:Eu^{3+}$ / SiO_2 nanorods. Depending on the polymerization technique used, the nanorods were decorated with PS spheres or embedded in a homogeneous polymer coating. Although the polystyrene coating reduced the optical

properties of these nanorods the synthetic strategy studied offers a simple processing method to prepare, for example, thin films and can be used with a variety of polymeric materials.

The outer surface of Y_2O_3 nanotubes was modified with stearic acid under reflux. Well aligned nanostructures of the modified nanotubes were prepared using the Langmuir-Blodgett technique.

Scope for further study

a) Preparation of lanthanides nanotubes by using anodic porous alumina template

New experiments should be performed in order to prepare samples essentially pure in nanotubes (not contaminated with nanorods) and with less size dispersion. The use of periodic structured templates, such as porous anodic porous alumina template or polymer membranes, seems to be a suitable route. In this method, nanostructures form inside the confined channels by simple liquid phase deposition or induced by electrochemical deposition.

b) Studies and simulation of PDS in lanthanide nanocrystals

I found that the anomalous thermalisation effect depends on the annealing parameters and Eu^{3+} concentration that can slightly changes the nanotubes structural parameters (the walls thickness, for instance). These minor changes (hardly observed by XRD and TEM) may induce considerable changes in the discrete PDS, modifying consequently the energy resonance between the frequency of the available phonons and the electronic levels and the intensity ratio values between normal and hot bands. The evaluation of the PDS in the Gd_2O_3 compound considering these minor structural changes can quantitatively support those changes in energy matching and intensity ratio.

c) Applications of the lanthanide nanocrystals - SNOM modified tips in imaging.

I propose to further explore the use Gd_2O_3:Eu^{3+} or Yb^{3+},Er^{3+} modified SNOM tips as nano sources for visible light in aperture-less SNOM equipments. We showed that dielectrophoresis is an adequate technique for the tips preparation, that these probes were mechanically stable and that the luminescence features (sharp lines, high QY, long lifetime, energy transfer…) may be used to exploit the interactions over different surfaces during the scanning.

Therefore, I conclude that the lanthanides nanotubes compounds exploit novel fascinating physical and chemical phenomena and they constitute a promising research area in nanotechnology, providing functional nano-objects for light emission, imaging, catalysis, nanocomposites and biomedical applications.

Appendix A – Experimental conditions used for the Ln^{3+} hydroxide or oxide nanotubes/nanorods synthesis

A1) $Gd_2O_3:Eu^{3+}$

$Gd_2O_3:Eu^{3+}$ nanotubes, nanorods and microcrystals were obtained trough hydrothermal synthesis. In a typical synthesis, 15 mL of aqueous solution containing 0.19 mmol of $Eu(NO_3)_3 \cdot 5H_2O$ (Aldrich, 99.99 %) and 4.2 mmol of $Gd(NO_3)_3 \cdot 6H_2O$ (Aldrich, 99.99 %) was prepared, in order to obtain an Eu^{3+} concentration of 3.30 (nanotubes and nanorods) and 3.65% (microcrystals). Then, approximately 13 mL of NaOH solution (1 M) was added (final pH adjusted to 12.5-13 using a pH meter model HD8705) and the mixture was stirred for 1 h. The resultant white gel was transferred to a Teflon® autoclave (inner volume 42 mL) and placed in a furnace at 120 ºC during 15 h (nanotubes), 150 ºC during 48 h (nanorods) and 230 ºC during 48 h (microcrystal). White precipitates were then filtered (filter papers, Whatman nº 43), washed with distilled water, and dried in air at 60 ºC. Dried powder (from nanotubes or nanorods ~1.8 g) was divided in six portions (ca. 0.3 g), placed into the zirconia crucibles, each of which was calcined independently in air 650, 700 or 750 ºC during 3 or 6 h, in a muffle furnace pre-heated at 40 ºC and with a heating rate of 5 ºC/min. Nanotubes with an Eu^{3+} mole content of 0.16, 1.00, and 6.60% were also prepared and thermally treated in the same conditions previously described to the sample having 3.30%. Furthermore the sample with 6.60 % of Eu^{3+} mole content received an addition annealing at 850 ºC during 6 h.

A2) CeO_2

a) CeO_2 nanotubes/nanorods

In a typical reaction, 0.6 g of of $Ce(SO_4)_3.9H_2O$ (Aldrich, 99.9%) was dispersed in 35 mL of NaOH (12 M). This mixture was stirred during 1 h, then transferred to a Teflon® autoclave (inner volume 42 mL) and placed in a pre-heated furnace at 135 ºC for 15 h. The yellowish precipitates were then filtered, washed and dried in air at 60 ºC in nitrogen atmosphere.

The cerium nanotubes (CeNT) material was partially oxidized in air for 24 h and then dispersed in distilled water and treated ultrasonically for 2 h with 70% aqueous tert-butyl hydroperoxide (t-BuOOH) or 15% aqueous hydrogen peroxide to give CeNT-BuOOH and CeNT-H_2O_2, respectively. No thermal treatment was required to transform the as obtained $Ce(OH)_3$ to CeO_2 compound, this oxidation occurred at room temperature and in air atmosphere.

b) CeO_2 tubes

Following the procedure reported by G. Chen et al. [89] CeO_2 tubes were obtained from $Ce(OH)CO_3$ precursor. The $Ce(OH)CO_3$ was synthesized by reacting hexahydrated cerium nitrate with urea, in a typical experiment 0.17 g of $Ce(NO_3)_3.6H_2O$ (99.9%) and 0.36 g of urea were added to 80 mL of water under vigorous magnetic stirring. This solution was placed into a 100 mL wide-mouthed jar which was closed and kept at 80ºC for 24 hours. The solution was then cooled to room temperature. The white precipitates were colleted by centrifugation (4500 rpm), washed with distilled water and dried at 60 ºC. The $Ce(OH)CO_3$ rods obtained above were re-dispersed into 20 mL of water, upon addition of 2.4 g of NaOH, the mixture was stirred during 30 minutes and then kept at room temperature. After 4 days of aging, the light yellow precipitate was dispersed in HNO_3 solution (1 M), recovered by centrifugation (4500 rpm), whased with distilled water and absolute ethanol, respectively, and then dried at 60 ºC in air.

A3) Y_2O_3

a) Y_2O_3 nanotubes synthesis: Y_2O_3 nanotubes were prepared by microwave oven

In a typical procedure 0.6 g of yttrium nitrate hexahydrated (Aldrich, 99.99 %) was dissolved in 50 mL of water and approximately 4 g of NaOH (1 M) was added until the pH reaches the 12.12 value, this mixture remained 0.5 h under magnetic stirring and 1 h in the ultrasonic stirring, respectively. The white colloidal suspension was placed in a proper autoclave and received a thermal treatment at 150ºC during 9 h; the power of the microwave oven was set to 600 W. The white powder formed was calcined at 700 ºC during 3 h.

b) Y_2O_3 tubes synthesis: Y_2O_3 tubes were prepared by adding ammonium hydroxide and conventional hydrothermal synthesis

In this case, 0.40 g of yttrium oxide and 0.05 g of europium oxide were dissolved in 6 mL of nitric acid (3 M), then 15 mL of ammonium hydroxide (25 %, 0.91 gcm^{-3}) was added, pH~12, subsequently, in order to achieve pH higher than 13, this suspension was centrifuged and then the white precipitates were re-dispersed in 10 mL of ammonium hydroxide (25 %, 0.91 gcm^{-3}). This solution was placed in an autoclave and followed by a hydrothermal treatment at 160 ºC during 48 h.

Then the precipitates were collected by centrifugation, washed with ethanol (2 times), water (2 times) and dried at 60 ºC in air. The calcination was performed at 700 ºC during 3 h.

Appendix B – Techniques used for characterisation in this thesis

B1) Excitation (PLE), emission photoluminescence (PL) and life times

Luminescence can be divided into two realms: *fluorescence* and *phosphorescence*. *Fluorescence* is defined as light emission from a sample with a decay time in order of nanoseconds (10^{-9} s), whereas *phosphorescence* is light emission that persists (greater than ~ 10^{-6} s) from a sample, after the excitation is removed. Popularly, they are often called together under "fluorescence spectroscopy".

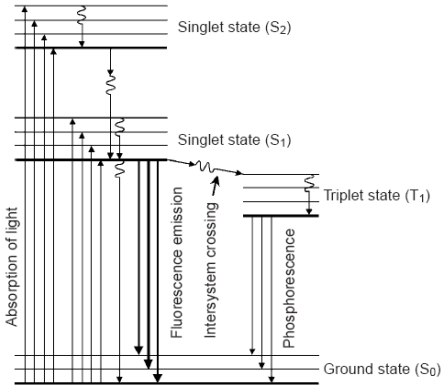

Figure B1 - Jablonski diagram of absorption and emission of light in a molecule. Phosphorescence occurs when an electron flips its spin (intersystem crossing), a "forbidden transition", which occurs more slowly than "allowed" transitions [57].

Fluorescence spectroscopy has found use in the following applications: protein conformation and transport; trace levels of biologically active compounds and carcinogens; quality-assurance of medications; monitoring of drug-delivery and interactions; properties of macromolecules and nanoparticles; photoreactivity of organic compounds; detection of chemical reactions; structure-property relations; monitoring pollutants in air, water, and soil; photoluminescence and photoluminescence excitation; and manufacturing quality-control.

a) Experimental conditions used in this thesis

Emission and excitation spectra were recorded between 11 K and room temperature on a Fluorolog®-3 Model FL3–2T, the system (depicted in **Figure B2**) consists of the following components: a 450 W xenon lamp and its power supply, inside a housing, double excitation spectrometer (Triax 320), fitted with a 1200 grooves/mm grating blazed at 330 nm, a single

emission spectrometer (Triax 320), fitted with a 1200 grooves/mm grating blazed at 500 nm, a R928 photomultiplier and all necessary electronics and software.

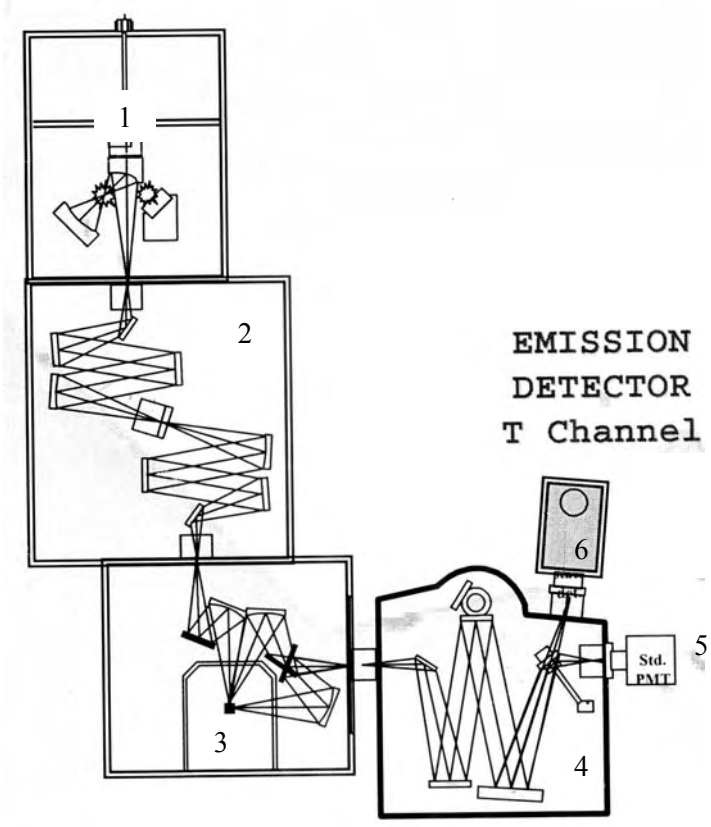

Figure B2 – Schematic representation of the configuration used for steady-state measurements: 1) Xe lamp and mirrors, 2) double excitation monochromator, 3) cryostat and sample, 4) emission monochromator, 5) UV-Vis detector (PMT) and 6) NIR detector.

Brief description of some spectrometer components:

i) Light sources

As light source we used a 450 W Xenon short-arc mounted vertically in an air-cooled housing. Light collection and focusing by off-axis mirror for maximum efficiency at all wavelengths. A typical emission spectrum of the above cited Xenon lamp is presented in Figure B3.

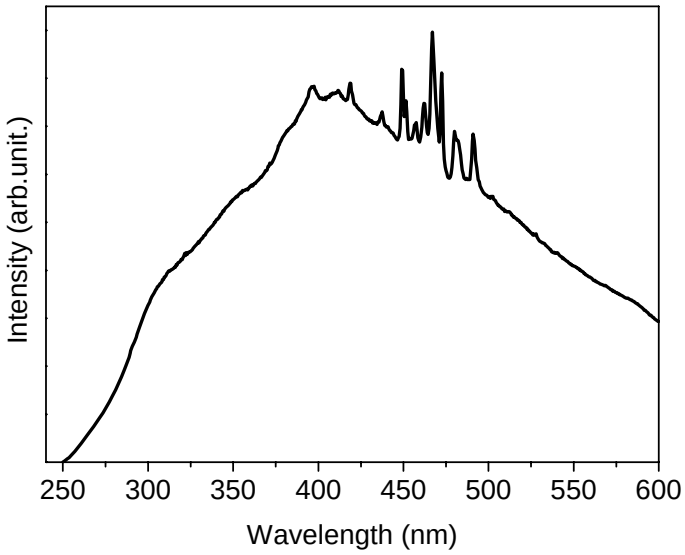

Figure B3 – Typical emission spectra of a Xenon lamp

Excitation spectra were corrected from 240 to 580 nm for the spectral distribution of the lamp intensity using a photodiode reference detector. Emission spectra were also corrected for the spectral response of the monochromators and the detector using typical correction spectra provided by the manufacturer.

For upconversion tests we used a 980 nm (1 W) laser diode excitation from ThorLabs® [238].

ii) Monochromator

As can be observed the monochromator system is in a Czerny-Turner set up. In the common Czerny-Turner design, the broad band illumination source (A) is aimed at an entrance slit (B), Figure B4. The amount of light energy available for use depends on the intensity of the source in the space defined by the slit (width * height) and the acceptance angle of the optical system. The slit is placed at the effective focus of a curved mirror (the collimator, C) so that the light from the slit reflected from the mirror is collimated (focused at infinity). The collimated light is refracted by the prism or diffracted from the grating (D) and then is collected by another mirror (E) which refocuses the light, now dispersed, on the exit slit (F). At the exit slit, the colors of the light are spread out (in the visible this shows the colors of the rainbow). Because each color arrives at a separate point in the exit slit plane, there are a series of images of the entrance slit focused on the plane. Because the entrance slit is finite in width, parts of nearby images overlap. The light leaving the exit slit (G) contains the entire image of the entrance slit of the selected color plus parts of the entrance slit images

of nearby colors. A rotation of the dispersing element (D) causes the band of colors to move relative to the exit slit, so that the desired entrance slit image is centered on the exit slit. The range of colors leaving the exit slit is a function of the width of the slits. The entrance and exit slit widths are adjusted together.

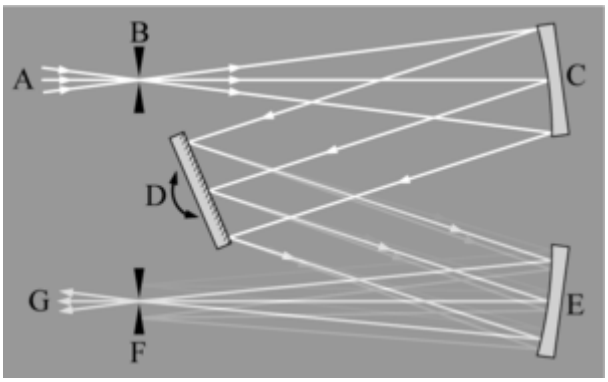

Figure B4 - Diagram of a Czerny-Turner monochromator

iii) Gratings

When a diffraction grating is used, care must be taken in the design of broad band monochromators because the diffraction pattern has overlapping orders. Sometimes extra, broadband filters are inserted in the optical path to limit the width of the diffraction orders so they do not overlap. Sometimes this is done by using a prism in one of the monochromators of a dual monochromator design.

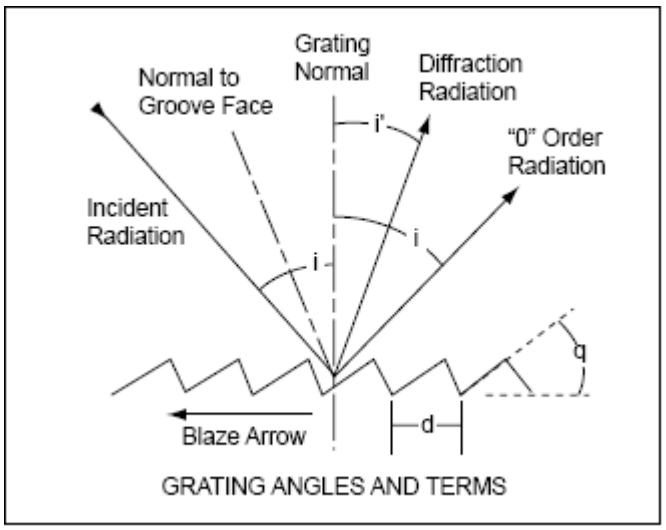

Figure B5 – Cross section of a grating

The slope of the triangular groove in a ruled grating is typically adjusted to enhance the brightness of a particular diffraction order. This is called blazing a grating (the wavelength

for which the reflection and diffraction angles are equal is defined as blazed wavelength). Ruled gratings have imperfections that produce faint "ghost" diffraction orders that may raise the stray light level of a monochromator.

The relationship between the grating spacing and the angles of the incident and diffracted beams of light is known as the grating equation. When a wave propagates, each point on the wavefront can be considered to act as a point source, and the wavefront at any subsequent point can be found by adding together the contributions from each of these individual point sources. An idealised grating is considered here which is made up of a set of long and infinitely narrow slits of spacing d. When a plane wave of wavelength λ is incident normally on the grating, each slit in the grating acts as a point source propagating in all directions. The light in a particular direction, θ, is made up of the interfering components from each slit. Generally, the phases of the waves from different slits will vary from one another, and will cancel one another out partially or wholly. However, when the path difference between the light from adjacent slits is equal to the wavelength, λ, the waves will all be in phase. This occurs at angles θ_r which satisfy the relationship $d\sin\theta_r/\lambda=n$ where *d* is the separation of the slits and *n* is an integer. Thus, the diffracted light will have maxima at angles θ_r given by:

$$d \sin \theta_r = n\lambda \tag{1}$$

If a plane wave is incident at an angle θ_i, the grating equation is given by:

$$d(\sin \theta_r + \sin \theta_i) = n\lambda \tag{2}$$

The light that corresponds to direct transmission (or specular reflection in the case of a reflection grating) is called the zero order, and is denoted $n = 0$. The other maxima occur at angles which are represented by non-zero integers *n*. Note that *n* can be positive or negative, resulting in diffracted orders on both sides of the zero order beam.

The angular dispersion of a grating can be obtained by differentiating the equation (2) and keeping the incident angle constant:

$$\frac{d\theta_r}{d\lambda} = \frac{n}{d \cos \theta_r} \text{ (rad/nm)} \tag{3}$$

The ability to separate two closely spaced spectral lines is expressed in terms of a linear dispersion (D):

$$D = \frac{dy}{d\lambda} = \frac{Fd\theta_r}{d\lambda} \text{ (nm/mm)} \tag{4}$$

where y is the distance d showed at Figure B5.

The resolution or resolving power of monochromator R is the ability to distinguish separate entities adjacent spectral features (absorption bands or emission lines). The definition for resolution is:

$$R = \frac{\lambda}{d\lambda} = n\lambda \qquad (5)$$

where dλ the wavelength difference measured between line (or peak) centers, determined by the value Δλ for which exists constructive interference at λ and destructive interference at λ+Δλ, *n* is the diffraction order and N the total number of diffraction grooves of the grating. To have high resolution (0.1 nm) on a g with 1800 gr/mm the dispersion of the monochromator must be low (1 nm/mm) and slits must be 100 μm opened. If the dispersion is larger, to keep the same resolution, the slits aperture must be reduced, which means that not enough light will enter.

iv) time resolved luminescence:

In time resolved luminescence, excitation occurs via a pulsed lamp (or laser) and a time delay is applied before measurement. In this way, the short lived background luminescence is not considered during measuring the long-lived metal-centered luminescence.

Time-resolved measurements were carried out using a 1934D3 phosphorimeter coupled to the Fluorolog®-3 and a Xe-Hg flash lamp (6 μs/pulse half width and 20-30 μs tail) was used as excitation source.

Besides these components above described, the temperature of 11 K was reached using a He closed-cycle cryostat from APD Cryogenics-HC2. A Lakeshore 330 auto tuning temperature controller and a resistance heater at the cold end of the cryostat allow controlled variation of temperature with a precision of 0.1 ºC. Vacuum system composed by rotary and diffusion pumps (from Edwards Company) was used to obtain pressure at range of 10^{-5}-10^{-6} Torr.

b) Absolute emission quantum yield (QY)

The absolute quantum yield is defined as:

$$QY = \frac{number\ of\ \ photons\ \ emitted}{number\ of\ \ photons\ \ absorbed}$$

Several experimental methods can be used for determination of emission quantum yield, such utilization of white standards powders [239,240] and integrating spheres [241, 242].

Measurements of the absolute emission QY are carried out in air atmosphere, using an integrating sphere for quantum yield measurement system C9920-02 from Hamamatsu Company. In this equipment the emission wavelength can be monitored between 300 to 950 nm, and the excitation wavelength between 250 and 8000 nm, with a bandwidth of 10nm and spot size of approximately 8 mm. The sample holder is a 17 mm diameter dish made of quartz.

This sphere is hollow and coated on its internal surface with a diffusely reflecting material. Photons created within the sphere are channelled, after reflections from the surface, to the exit port, Figure B6.

The intensity detected at the exit is directly proportional to the total light flux created within the sphere. It does not depend on the angular distribution of the signal or the orientation of the emitting dipoles in the sample. Such a flux can be generated by a light source, e.g., lamp or a LED, or produced by a thin luminescent pellet or film, after absorption of a pump radiation. In the present study, we use a 150 W Xenon lamp coupled to a monochromator. The incident beam is guided through the entrance aperture, with an optical fiber, onto the sample placed at the bottom of the sphere. Near normal incidence has been used for all measurements. The reflected signal from the incident beam is directed towards the exit aperture. A baffle placed between the sample and the exit port prevents the PL signal from directly reaching the detector. The PL signal, scattered within the sphere, is measured at the exit with a photodiode, preceded by a cut-off filter.

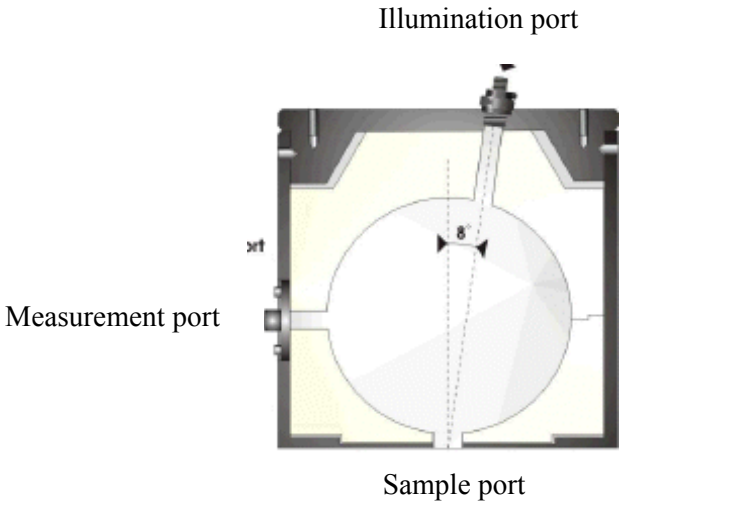

Figure B6 – Schematic drawing of internal region of C9920-02 integrating sphere

The theory of the integrating sphere originates in the theory of radiation exchange within an enclosure of diffuse surfaces. Consider the radiation exchange between two differential elements of diffuse surfaces:

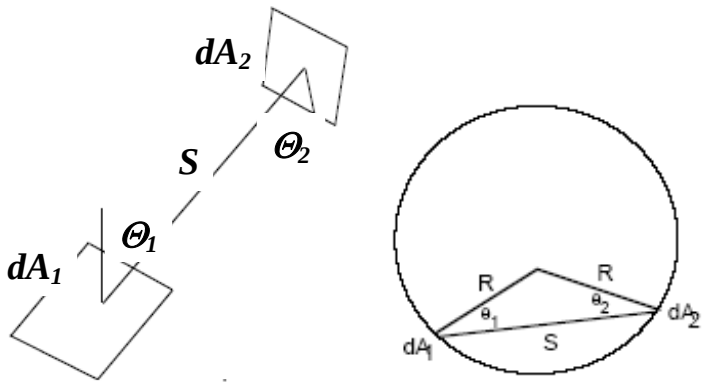

Figure B7– Reflections inside the integrating sphere

The fraction of energy leaving dA_1 and arriving at dA_2 is known as the exchange factor $dF_{d_1-d_2}$.

$$dF_{d_1-d_2} = \frac{\cos\theta_1 \cos\theta_2}{\pi S^2} dA_2 \qquad (6)$$

Where θ_1 and θ_2 are measured from the surface normal and S is the light path inside the sphere:

$$S = 2R\cos\theta_1 = 2R\cos\theta_2 \quad (7)$$

Thus independent of viewing angle and the distance between the areas:

$$dF_{d_1-d_2} = \frac{dA_2}{4\pi \times R^2} \quad (8)$$

Therefore, the fraction of flux received by dA_2 is the same for any radiating point on the sphere surface. If the infinitesimal area dA_1 instead exchanges radiation with a finite area A_2:

$$dF_{d_1-d_2} = \frac{1}{4\pi \times R^2}\int_{A_2} dA_2 = \frac{A_2}{4\pi \times R^2} \quad (9)$$

Since this result is also independent of dA_1:

$$F_{d_1-d_2} = \frac{A_2}{4\pi \times R^2} = \frac{A_2}{A_S} \quad (10)$$

The fraction of radiant flux received by A_2 is the fractional surface area it consumes within the sphere where A_s is the integrating sphere total area. Thus the integrating sphere radiance is:

$$R = \frac{\varphi_i \rho}{\alpha A} \times \frac{\rho}{1-\rho(1-f)} \quad (\text{W.m}^{-2}\text{.sr, Watt per square per steradian}) \quad (11)$$

where the first term is the diffuse surface radiance, the second is sphere multiplier (accounts for R increase due to multiple reflections) and:

- φ_i: input flux
- ρ: reflectance
- A: illuminated area
- α: total projected solid angle from the surface
- (1-f): faction of flux received by the sphere that is not consumed at the port openings

The emission quantum yield is given by [242]:

$$QY = y^{-1}\frac{X_{samp} - (\rho + T)X_{sphere})}{(1-\rho-T)X_{exc})} \quad (12)$$

where X_{samp} is the total emission intensity measured when the wavelength excitation directly irradiates the sample, X_{sphere} is the intensity measured when the wavelength excitation impinges on the sphere walls diffusely irradiating the sample, and X_{exc} is the intensity measured without sample and filter in place (lamp signal). ρ and T are, respectively, the reflectance and transmittance of the sample at the incident wavelength. ρ is extracted from the Equation 11; T is measured from the absorption spectrum of the sample. In the above expression for QY, only reflection of the first interface between air/surface is taken into

account. The ‘‘normalization’’ term, y, accounts for the spectral response of the sphere, $S_{sphere}(\lambda)$, the quantum efficiency of the Si photodiode over the near-UV-visible spectrum, $G(\lambda)$, and the transmission spectrum of the cut-off filter, $F(\lambda)$:

$$y = \frac{\left\{ \frac{S_{sphere}(\lambda) L(\lambda) G(\lambda) F(\lambda)}{S_{lamp}(\lambda)} d\lambda \right\}}{\left\{ \frac{S_{sphere}(\lambda_{ex}) G(\lambda_{ex})}{S_{lamp}(\lambda_{ex})} \oint L(\lambda) d\lambda \right\}} \qquad (13)$$

In Equation 13, $S_{lamp}(\lambda)$ is the emission spectrum of a tungsten lamp measured outside the sphere, $S_{sphere}(\lambda)$ is measured at the exit port of the sphere, when the tungsten lamp irradiates the inside of the sphere through the entrance aperture, and $L(\lambda)$ is the emission spectrum of the sample.

In our experiments three measurements were made for each sample so that the average value is reported. This method is accurate to within 10%.

B2) XRD

The XRD patterns presented in this thesis were recorded using a **Philips X’Pert MPD powder X-ray diffractometer.** This equipment has a goniometer in Bragg-Brentano 2θ/θ setup another [119]. The samples were exposed to the CuK_{α} radiation (1.54 Å) in a 2θ range between 1 and 60º with a step of 0.04 and acquisition time of 40 s per step. Commercial lanthanum hexaboride was used as standard for position and shape lines calibration of the XRD patterns from $Gd_2O_3:Eu^{3+}$ nanotubes, nanorods and microcrystals.

B3) Scanning Electronic Microscopy (SEM)

The scanning electron microscope (SEM) is a type of electron microscope that images the sample surface by scanning it with a high-energy beam of electrons in a raster scan pattern. The electrons interact with the atoms that make up the sample producing signals that contain information about the sample's surface topography, composition and other properties such as electrical conductivity [243].

The types of signals produced by an SEM include secondary electrons, back-scattered electrons (BSE), characteristic X-rays, light (cathodoluminescence), specimen current and

transmitted electrons. Secondary electron detectors are common in all SEMs, but it is rare that a single machine would have detectors for all possible signals. The signals result from interactions of the electron beam with atoms at or near the surface of the sample. In the most common or standard detection mode, secondary electron imaging or SEI, the SEM can produce very high-resolution images of a sample surface, revealing details about less than 1 to 5 nm in size. Due to the very narrow electron beam, SEM micrographs have a large depth of field yielding a characteristic three-dimensional appearance useful for understanding the surface structure of a sample. A wide range of magnifications is possible, from about 10 times (about equivalent to that of a powerful hand-lens) to more than 500,000 times, about 250 times the magnification limit of the best light microscopes. Back-scattered electrons (BSE) are beam electrons that are reflected from the sample by elastic scattering. BSE are often used in analytical SEM along with the spectra made from the characteristic X-rays. Because the intensity of the BSE signal is strongly related to the atomic number (Z) of the specimen, BSE images can provide information about the distribution of different elements in the sample. For the same reason, BSE imaging can image colloidal gold immuno-labels of 5 or 10 nm diameter which would otherwise be difficult or impossible to detect in secondary electron images in biological specimens. Characteristic X-rays are emitted when the electron beam removes an inner shell electron from the sample, causing a higher energy electron to fill the shell and release energy. These characteristic X-rays are used to identify the composition and measure the abundance of elements in the sample.

The SEM images presented in this thesis were acquired in a **Scanning Electron Microscope HR-FESEM Hitachi SU-70**: Schottky emission electron gun (FESG) for extended daily servicing, Accelerating voltage from 500V to 30kV, minimum landing voltage of 100V, secondary electron image resolution of 1nm at 15KV, probe current 1pA-100nA, magnification range of x30 to 800.000x, conventional and in-lens secondary electron SE detectors and in-lens backscattered electron BSE detector. For elemental analysis we used a thin window **B-U Bruker QUANTAX 400 EDS spectrometer** for elemental analysis: Peltier cooled slew window 10mm, B-U XFlash 4010 EDS detector, energy resolution of <133 eV, X-ray pulse count rate up to 275.000cps, standard less/standard qualitative and quantitative EDS on-line, interactive and sequentially programmed analysis and multi-element maps and off-line work.

For SEM analysis the powders were dispersed in ethanol or distilled water, thus this suspension was dropped onto a thin glass substrate previously fixed onto a SEM holder. In order to reduce charge accumulation effect a carbon layer was also deposited.

B4) Transmission Electronic Microscopy (TEM)

In a TEM microscope the ray of electrons is produced by a pin-shaped cathode heated up by current. The electrons are vacuumed up by a high voltage at the anode. The acceleration voltage is between 50 and 150 kV. The higher it is, the shorter are the electron waves and the higher is the power of resolution. But this factor is hardly ever limiting. The power of resolution of electron microscopy is usually restrained by the quality of the lens-systems and especially by the technique with which the preparation has been achieved. Modern gadgets have powers of resolution that range from 0.2 – 0.3 nm. The useful resolution is therefore around 300,000 x. [244]

After passing the object the scattered electrons are collected by an objective. Thereby an image is formed, that is subsequently enlarged by an additional lens-system (called projective with electron microscopes). The thus formed image is made visible on a fluorescent screen or it is documented on photographic material. Photos taken with electron microscopes are always black and white. The degree of darkness corresponds to the electron density (= differences in atom masses) of the candled preparation. There are two basic modes of TEM operation, namely the bright-field mode, where the transmitted beam contributes to the image, and the dark-field imaging mode, in which the beam is excluded. The size of the objective aperture in bright-field mode directly determines the information to be emphasized in the final image. When the size is chosen so as to exclude the diffracted beams, one has the configuration normally used for low-resolution defect studies, so-called diffraction contrast. In this case, a crystalline specimen is oriented to excite a particular diffracted beam, or a systematic row of reflections, and the image is sensitive to the differences in specimen thickness, distortion of crystal lattices due to defects, strain and bending.

TEM and electron diffraction measurements were done on H-9NA (TEM) microscope over nanotubes or nanorods samples on amorphous carbon-Fomvar® grid support. These samples were previously dispersed in distilled water (0.5 mg/mL) with ultrasonic stirring during 10 min; the TEM grid was deep coated in this suspension and dried in air.

B5) AFM

The Atomic Force Microscope was developed to overcome a basic drawback with STM - that it can only image conducting or semiconducting surfaces. The AFM, however, has

the advantage of imaging almost any type of surface, including polymers, ceramics, composites, glass, and biological samples.

G. Binnig et al. [245] invented the Atomic Force Microscope in 1985. Their original AFM consisted of a diamond shard attached to a strip of gold foil. The diamond tip contacted the surface directly, with the interatomic Van der Waals forces providing the interaction mechanism. Detection of the cantilever's vertical movement was done with a second tip - an STM placed above the cantilever.

AFM probe deflection

Today, most AFM equipments use a laser beam deflection system, introduced by M. Meyer and N. M. Amer [246], where a laser is reflected from the back of the reflective AFM lever and onto a position-sensitive detector, Figure B8. AFM tips and cantilevers are microfabricated from Si or Si_3N_4. Typical tip radius is from a few to 10s of nm.

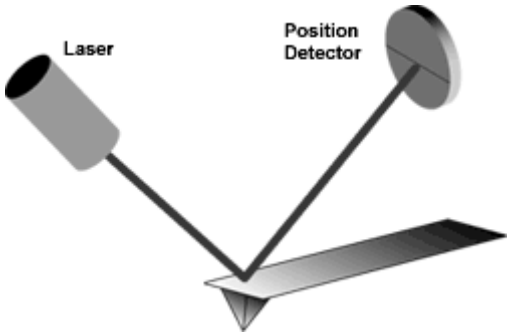

Figure B8 - Beam deflection system, using a laser and photodector to measure the beam position

Measuring forces

Because the atomic force microscope relies on the forces between the tip and sample, knowing these forces is important for proper imaging. The force is not measured directly, but calculated by measuring the deflection of the lever, and knowing the stiffness of the cantilever. Hook's law gives F = -kz, where F is the force, k is the stiffness of the lever, and z is the distance the lever is bent. Figure B9 shows a typical force-distance curve between the tip and surface.

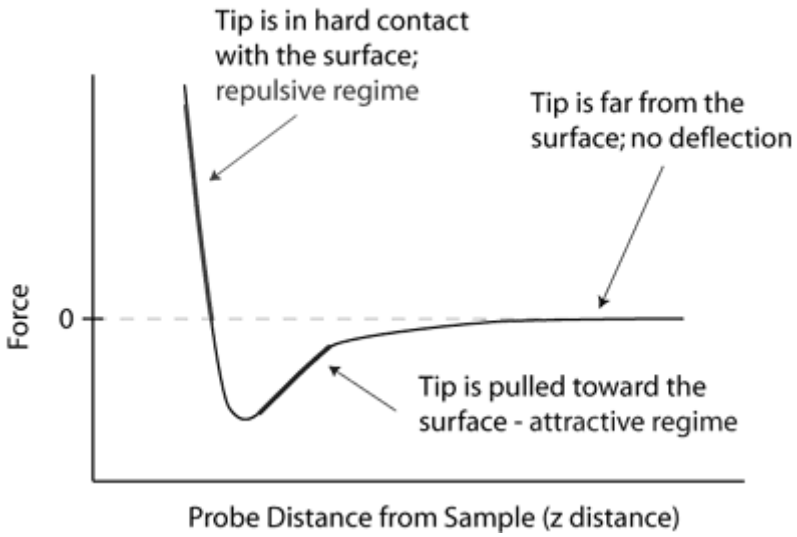

Figure B9– Force-distance curve

AFM modes of operation: [247,248]

Because of the versatility of AFM equipments, it has been applied to a large number of research topics. The Atomic Force Microscope has also gone through many modifications for specific application requirements.

a) Contact Mode

The first and foremost mode of operation, contact mode is widely used. As the tip is raster-scanned across the surface, it is deflected as it moves over the surface corrugation. In constant force mode, the tip is constantly adjusted to maintain a constant deflection, and therefore constant height above the surface. It is this adjustment that is displayed as data. However, the ability to track the surface in this manner is limited by the feedback circuit. Sometimes the tip is allowed to scan without this adjustment, and one measures only the deflection. This is useful for small, high-speed atomic resolution scans, and is known as variable-deflection mode.

Because the tip is in hard contact with the surface, the stiffness of the lever needs to be less that the effective spring constant holding atoms together, which is on the order of 1 - 10 nN/nm. Most contact mode levers have a spring constant of < 1N/m.

b) Lateral Force Microscopy (LFM)

LFM measures frictional forces on a surface. By measuring the “twist” of the cantilever, rather than merely its deflection, one can qualitatively determine areas of higher and lower friction.

c) Noncontact mode

Noncontact mode belongs to a family of AC modes, which refers to the use of an oscillating cantilever. A stiff cantilever is oscillated in the attractive regime, meaning that the tip is quite close to the sample, but not touching it (hence, “noncontact”). The forces between the tip and sample are quite low, on the order of pN (10^{-12} N). The detection scheme is based on measuring changes to the resonant frequency or amplitude of the cantilever.

d) Dynamic Force / Intermittent-contact / “tapping mode” AFM

This mode is commonly referred to as “tapping mode” and it is also referred to as intermittent-contact or, the more general term, Dynamic Force Mode (DFM).

A stiff cantilever is oscillated closer to the sample than in noncontact mode. Part of the oscillation extends into the repulsive regime, so the tip intermittently touches or “taps” the surface. Very stiff cantilevers are typically used, as tips can get “stuck” in the water contamination layer.

The advantage of tapping the surface is improved lateral resolution on soft samples. Lateral forces such as drag, common in contact mode, are virtually eliminated. For poorly adsorbed specimens on a substrate surface the advantage is clearly seen.

e) Force Modulation

Force modulation refers to a method used to probe properties of materials through sample/tip interactions. The tip (or sample) is oscillated at a high frequency and pushed into the repulsive regime. The slope of the force-distance curve is measured which is correlated to the sample's elasticity. The data can be acquired along with topography, which allows comparison of both height and material properties.

e) Phase Imaging

In Phase mode imaging, the phase shift of the oscillating cantilever relative to the driving signal is measured. This phase shift can be correlated with specific material properties that effect the tip/sample interaction. The phase shift can be used to differentiate areas on a

sample with such differing properties as friction, adhesion, and viscoelasticity. The technique is used simultaneously with DFM mode, so topography can be measured as well.

f) Experimental conditions used to acquire the AFM images

The measurements were performed in samples with a regular patterned surface using a Veeco "Multimode" AFM with Nanoscope IIIA controller. The topography images were recorded in the contact or tapping modes. The imaging conditions (setpoint, gains, driving frequency and driving amplitude) were routinely set using standard procedure for contact or tapping modes. The scan velocity was always kept at 0.5 Hz (12 μm/s).

B6) Thermogravimetry (TGA)

TGA analyses were carried out using a Shimadzu TGA 50 instrument with a heating rate of 10 °C min^{-1} under a continuous air stream with a flow rate of 10 cm^3 min^{-1}.

B7) Elemental analysis

Determination of Eu^{3+}, Er^{3+} and Yb^{3+} elements was performed using inductively coupled plasma atomic emission spectroscopy (ICP-AES), ISO 11885

B8) Attenuated total reflection Fourier transformed infrared (ATR-FTIR)

ATR-FTIR spectra were recorded using with a Matson 7000 FTIR spectrometer with experimental setup in transmittance mode, 256 scans, resolution 8 and signal gain 10.

B9) Raman spectroscopy

FT-Raman spectra were collected on a Bruker RFS 100 instrument, at room temperature with a YAG:Nd laser coherent laser source (1064 nm , 50 mW).

B10) Adsorption and desorption of nitrogen gas

The nitrogen adsorption-desorption isotherms were measured at 77 K, using a Micromeritics Gemini® equipment. Prior to analysis the powdered samples were pre-treated at 150 ºC. The BET specific surface areas were calculated for p/p_0 in the range 0.015-0.15. The pore size distribution (PSD) curves were calculated from the desorption branches of the isotherms using the Barrett-Joyner- Halenda method.

B11) Contact angle

Contact angles between water and pristine or modified surface nanotubes were acquired on Data Physics OCA20 equipment.

B12) Zeta potential

Most particles dispersed in an aqueous system will acquire a surface charge, principally either by ionization of surface groups, or adsorption of charged species. These surface charges modify the distribution of the surrounding ions, resulting in a layer around the particle that is different to the bulk solution [249]. If the particle moves, under Brownian motion for example, this layer moves as part of the particle. The zeta potential is the potential at the point in this layer where it moves past the bulk solution. This is usually called the slipping plane. The charge at this plane will be very sensitive to the concentration and type of ions in solution.

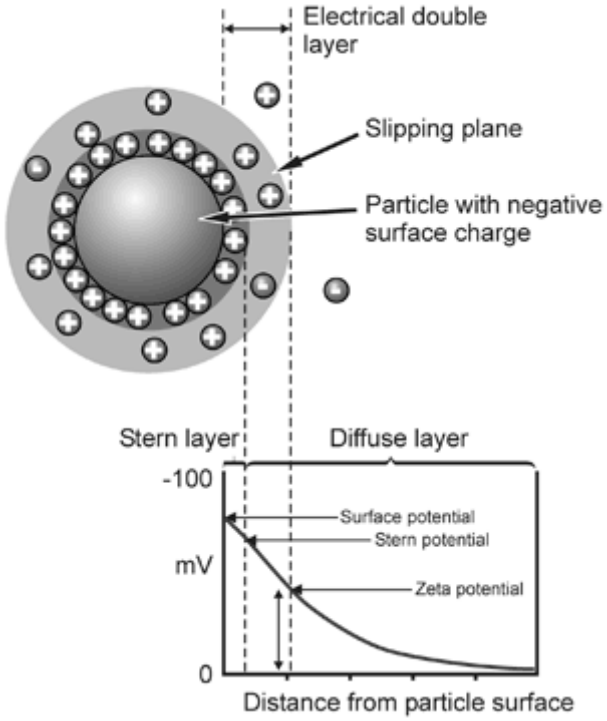

Figure B10– Schematic representation of zeta potential [249]

Zeta potential is one of the main forces that mediate interparticle interactions. Particles with a high zeta potential of the same charge sign, either positive or negative, will repel each other. Conventionally a high zeta potential can be high in a positive or negative sense, i.e. <-30mV and >+30mV would both be considered as high zeta potentials. For molecules and particles that are small enough, and of low enough density to remain in suspension, a high zeta potential will confer stability, i.e. the solution or dispersion will resist aggregation. The

Faraday gold sol made in the 1850's now in the science museum in London, is still a stable dispersion, particle aggregation being slowed to an imperceptible rate due to it's high zeta potential.

Zeta potential is measured by applying an electric field across the dispersion. Particles within the dispersion with a zeta potential will migrate toward the electrode of opposite charge with a velocity proportional to the magnitude of the zeta potential. This velocity is measured using the technique of laser Doppler anemometry [250]. The frequency shift or phase shift of an incident laser beam caused by these moving particles is measured as the particle mobility, and this mobility is converted to the zeta potential by inputting the dispersant viscosity, and the application of the Smoluchowski or Huckel theories [249]. These theories are approximations useful for most applications. More recent models are available which can give a more exact conversion, but require more knowledge of the chemistry of the dispersion.

For the zeta potential measurement a conventional capillary electrophoresis device was used. The system consisted of a standard glass rectangular cell with section of 10×1 mm. The rectangular U-shaped capillary tube was attached to a translation stage. Two electrodes made of platinum wire were added to the ends of the tube. The electrodes were connected to the DC power supply. Aqueous suspension with concentration of approximately 0.1 mg /mL was used.

Appendix C – UV-Vis Absorption

The measurement of absorption spectra in semiconductors constitutes an important aspect of materials characterisation. It provides information not only on the band gap, but the measurements also provide information on direct and indirect transitions, the distribution of states, and the energy position of defects and impurity levels. UV/Vis absorbance spectra were acquired from nanotubes in powder or in dispersion on a Jasco V 560 UV/VIS spectrometer. The absorbance spectrum from nanotubes dispersion was recorded in a quartz cell (1 cm path length), and hexane or ethanol were used as blank. The optical absorption coefficient α was calculated according to $\alpha = (A\rho)/lc$, where A is the absorbance of the sample, ρ the mass density (for instance 7.28 gcm^{-3} for CeO_2), l the path length (1 cm), and c the concentration of the nanotubes suspension (< 0.2 $mgcm^{-3}$). Descriptions of the processes involved in the gap determination are summarized as follows:

a) Direct and indirect band gap absorption

Considering a case of an electron raised from the top of the valence band to the bottom of the conduction band due the absorption of a photon in a direct transition, there is no change in momentum. Strictly, there is a small change in **k** due to finite momentum of the photon, which is equal to h/λ. An indirect transition due absorption of an photon, involve a large change in the momentum, due to absorption or emission of a phonon.

This process can be described by the equation:

$$\varepsilon_{ph} \pm \varepsilon_p = \varepsilon_g \qquad (14)$$

and the change in momentum is given by:

$$\Delta k = k_p \qquad (15)$$

where k_p is the wavevector of the phonon and ε_{ph} and ε_p are the photon and phonon energies, respectively. Therefore, an optical or acoustic phonon with the right energy and momentum must be involved in an indirect transition [130].

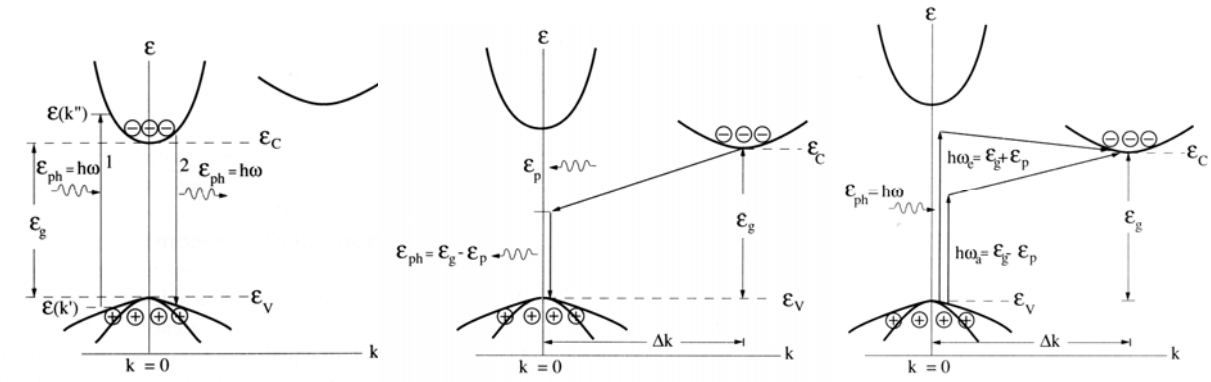

A) B) C)

Figure C1. Illustration of band-to-band of absorption and recombination processes in A) direct band gap semiconductor and B) and C) indirect band gap semiconductor

It can be shown that the transition probability per unit volume per unit time for a an allowed direct transition is given by

$$P(\hbar\omega) = \frac{q^2|A|^2\left(2m_r^*\right)^{3/2}p_{cv}^2}{4\pi m_0^2\hbar^4}\left(\hbar\omega - \varepsilon_g\right)^{1/2} \tag{16}$$

where p_{cv} is the matrix element of the momentum operator and m_r^* is the reduced mass given by:

$$m_r^* = \frac{m_e^* m_h^*}{m_e^* + m_h^*} \tag{17}$$

When the k-selection rule is obeyed, $|p_{cv}|^2=0$ unless k'=k''.

Since the absorption of a photon of energy $\hbar\omega$ is involved in a direct transition, it is important to calculate the absorption coefficient α. Assume that a monochromatic photon flux $\Im_i$, given by:

$$\Im_i = \frac{|S|}{\hbar\omega} \text{ (photons/cm}^2\text{.s)} \tag{18}$$

is incident on the crystal. Here |S| is the radiation energy crossing unit area in unit time, or the Poyting vector. The transmitted intensity $\Im_d$ is then:

$$\Im_d = \frac{|S|}{\hbar\omega} - P(\hbar\omega)d \tag{19}$$

where d is the thickness sample. The second term represents the number of photons absorbed per unit time pert unit area, normal to the incident light in a thickness d. Equation 19 can be written as:

$$\Im_d = \frac{|S|}{\hbar\omega} e^{-\alpha d} \cong \frac{|S|}{\hbar\omega}(1-\alpha d) \tag{20}$$

for small αd. Thus

$$\alpha(\hbar\omega) = \frac{P\hbar\omega}{|S|} \tag{21}$$

the average value of the Poynting vector over a period of the electromagnetic wave can be expressed as

$$|S| = \frac{1}{2} n_r \varepsilon_0 c \omega^2 |A^2| \tag{22}$$

where n_r is the refractive index of the crystal. Substituting 14 and 22 in 21 leads to:

$$\alpha(\hbar\omega) = C_1 n_r^{-1} \left(\frac{2m_r^*}{m_0}\right)^{3/2} \frac{f_{CV}}{\hbar\omega} (\hbar\omega - \varepsilon_g)^{1/2} \tag{23}$$

where:

$$C_1 = \frac{q^2 m_0^{1/2}}{4\pi\hbar^2 \varepsilon_0 c} \tag{21}$$

and

$$f_{CV} = \frac{2p_{cv}^2}{m_0} \tag{24}$$

expressing $\hbar\omega$ and ε_g in eV,

$$\alpha(\hbar\omega) = 2.64\times10^5 n_r^{-1} \left(\frac{2m_r^*}{m_0}\right)^{3/2} \frac{f_{CV}}{\hbar\omega} (\hbar\omega - \varepsilon_g)^{1/2} \quad (\text{cm}^{-1}) \tag{25}$$

f_{CV} is called the oscillator strength for the transition. It has a value approximately equal to 20 eV in most semiconductors. Therefore (for instance f_{CV} =23 eV) we get:

$$\alpha(\hbar\omega) = 5.6\times10^4 \frac{(\hbar\omega - \varepsilon_g)^{1/2}}{\hbar\omega} \qquad (\text{cm}^{-1}) \tag{26}$$

Similarly for forbidden transition, the transition probability is given by:

$$P(\hbar\omega) = \frac{q^2 |A|^2 (2m_r^*)^{5/2} f_{cv}'}{12\pi m_0^2 \hbar^4} (\hbar\omega - \varepsilon_g)^{3/2} \tag{27}$$

It is important to note that the probability is proportional to $(\hbar\omega - \varepsilon_g)^{3/2}$. The absorption coefficient is given by

$$\alpha(\hbar\omega) = C_2 n_r^{-1} \left(\frac{2m_r^*}{m_0}\right)^{5/2} \frac{f_{CV}'}{\hbar\omega} (\hbar\omega - \varepsilon_g)^{3/2} \tag{28}$$

where:

$$C_2 = \frac{q^2 m_0^{1/2}}{6\pi\hbar^2 \varepsilon_0 c} \tag{29}$$

and $f_{CV}^{'}$ is the oscillator strength for the forbidden transition, and it is value is much less than unity. Again, if $\hbar\omega$ and ε_g are expressed in eV:

$$\alpha(\hbar\omega) = 1.76\times10^5 n_r^{-1}\left(\frac{2m_r^*}{m_0}\right)^{5/2} \frac{f_{cv}^{'}}{\hbar\omega}\left(\hbar\omega - \varepsilon_g\right)^{3/2} \quad (\text{cm}^{-1}) \tag{30}$$

b) Indirect intrinsic transitions:

The momentum or wavevector change required in an indirect transition may be provided by single or multiple phonons, although the probability of the latter to occur is very small. Conservation of momentum requires

$$k'' \pm k_p = k^{'} \pm k_{ph} \tag{31}$$

where *k''* and *k'* are the electron wavevectors for the final and initial states, k_p is the wavevector of the phonon, and k_{ph} is the wavevector of the absorbed photon.

Since the latter is small, the conservation of momentum for an indirect transition can be expressed as:

$$k'' - k' = \pm k_p \tag{32}$$

Similarly, the conservation of energy for the two cases of phonon emission and absorption can be expressed as:

$$\hbar\omega_e = \varepsilon_C - \varepsilon_V + \varepsilon_p \tag{33}$$

$$\hbar\omega_a = \varepsilon_C - \varepsilon_V - \varepsilon_p \tag{32}$$

$$N(\varepsilon_v) = \frac{1}{2\pi^2\hbar^3}\left(2m_h^*\right)^{3/2}\left|\varepsilon_V\right|^{1/2} \tag{34}$$

$$N(\varepsilon_c) = \frac{1}{2\pi^2\hbar^3}\left(2m_e^*\right)^{3/2}\left|\varepsilon_c - \varepsilon_g\right|^{1/2} \tag{35}$$

Substituting 33 or 32 in 35

$$N(\varepsilon_c) = \frac{1}{2\pi^2\hbar^3}\left(2m_e^*\right)^{3/2}\left|\hbar\omega - \varepsilon_g \pm \varepsilon_p + \varepsilon_V\right|^{1/2} \tag{36}$$

The coefficient is proportional to the product of the densities of initial states and final states integrated over all possible combination of states separated by $\hbar\omega \pm \varepsilon_p$; α is also proportional to the probability of interacting with phonons, which is itself a function of

$f(N_p)$ of the number N_p of phonon of energy N_p. The number of phonons is giver by Bose-Eistein statistics. Hence,

$$\alpha(\hbar\omega) = Af(N_p)\int_0^{-(\hbar\omega-\varepsilon_g\pm\varepsilon_p)}|\varepsilon_V|^{1/2}\left(\hbar\omega-\varepsilon_g\pm\varepsilon_p+\varepsilon_v\right)^{1/2}d\varepsilon_v$$

for a transition with phonon absorption and

$$\alpha_a(\hbar\omega)\propto\frac{\left(\hbar\omega-\varepsilon_g+\varepsilon_p\right)^2}{e^{\varepsilon_p/k_BT}-1} \tag{37}$$

for a photon energy $\hbar\omega>\left(\varepsilon_g-\varepsilon_p\right)$. Similarly, for a transition with phonon emission the absorption coefficient is given by:

$$\alpha_e(\hbar\omega)\propto\frac{\left(\hbar\omega-\varepsilon_g-\varepsilon_p\right)^2}{1-e^{\varepsilon_p/k_BT}} \tag{38}$$

For $\hbar\omega>\left(\varepsilon_g+\varepsilon_p\right)$. Since for $\hbar\omega>\left(\varepsilon_g+\varepsilon_p\right)$both phonon emission and absorption are possible, under these conditions:

$$\alpha(\hbar\omega)=\alpha_a(\hbar\omega)+\alpha_e(\hbar\omega) \tag{39}$$

The two terms here represents contributions from transitions involving phonon absorption and emission respectively, and have different coefficients of proportionality and temperature dependences. For allowed transition n=2. Also multiple phonon processes can occur, leading to additional pairs of terms in the equation 12. If a plot of $(\alpha^{1/2})$ versus $(h\nu)$ forms a straight line, it can normally be inferred that there is an indirect band gap, measurable by extrapolating the straight line to the $\alpha=0$ axis (assuming $h\nu_{ph}\approx 0$).

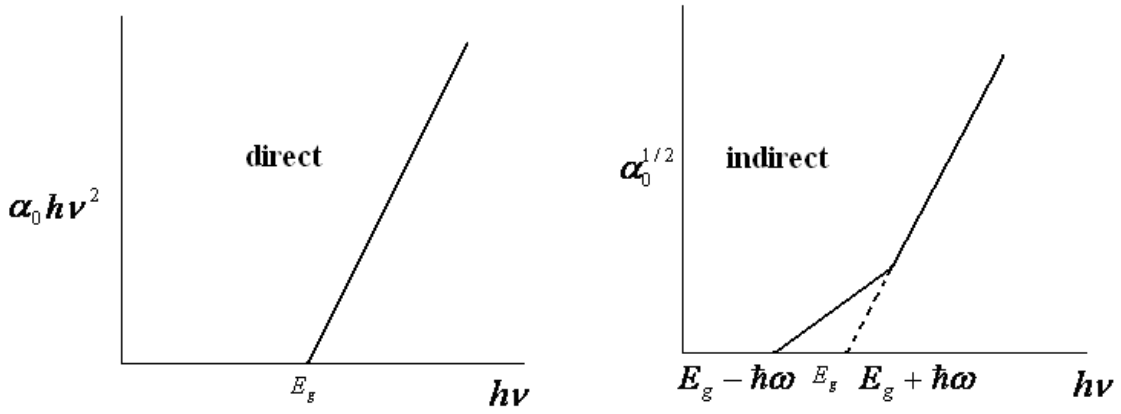

A) B)

Figure C2 – Example of plots for A) direct and B) indirect band gap calculation

Bibliography

1 http://old.iupac.org/reports/periodic_table/

2 B. Geijer, *Annalen für die Freunde der Naturlehre* **9**, 229 (1788)

3 A. G. Ekeberg, *Annalen für die Freunde der Naturlehre* **32**, 63 (1799)

4 A. P. Vink, Doctorate thesis, Delft University of Technology, Delft (2000)

5 A. J. Freeman and R. E. Watson, *Phys. Rev.* **127**, 2058 (1962)

6 G. Racah, *Phys. Rev.* **76**, 1352 (1949)

7 S. Hüfner, Optical Spectra of Transparent Rare Earth Compounds, 1st edition (Academic Press, New York, 1978)

8 J.-C. G. Bünzli, *Lanthanide Probes in Life, Chemical and Earth Science* (Elsevier, Amsterdam, 1995)

9 M. T. Hutchings, D. K. Ray, *Proc. Phys. Soc.* **81**, 663 (1963)

10 A. K. Raychaudhuri, D. K. Ray, *Proc. Phys. Soc*. **90**, 839 (1967)

11 B. G. Wybourne, *Spectroscopic Properties of Rare Earths* (Interscience, New York, 1965)

12 G. Racah, *Phys. Rev.* **63**, 367 (1943)

13 G. Racah, *Phys. Rev.* **76**, 1352 (1949)

14 O. L. Malta, L. D. Carlos, *Quim. Nova* 26, 889 (2003)

15 G. H. Dieke, *Spectra and Energy Levels of Rare Earth Ions in Crystals* (John Wiley & Sons, New York, 1968)

16 I. I. Sobelman, *Atomic Spectra and Radiative Transitions*, 2nd edition (Springer-Verlag, Berlin, 1991)

17 B. R. Judd, *Phys Rev.* **127**, 740 (1962)

18 G. S. Ofelt, *J. Chem. Phys*. **37**, 511 (1962)

19 S. Bhushan, *Luminescence and its applications* (Allied Publishers, Delhi, 1997)

20 J. R. Lakowicz, *Principles of fluorescence spectroscopy* (Springer, New York, 2006)

21 M. H. Kostova, Doctorate thesis, Universidade de Aveiro, Aveiro (2007)

22 D. A. Marques, Doctorate thesis, Universidade de Aveiro, Aveiro (2004)

23 R. A. S. André, Doctorate thesis, Universidade de Aveiro, Aveiro (2002)

24 J. P. J. Rainho, Doctorate thesis, Universidade de Aveiro, Aveiro (2002)

25 M. J. Weber, *Phys. Rev.* **171**, 283 (1968)

26 G. Liu, X. Chen, *Handbook on the Physics and Chemistry of Rare Earths*, **37**, 99 (2007)

27 B. Mercier, C. Dujardin, G. Ledoux, C. Louis, O. Tillement, *J. Appl. Phys.* **96**, 650 (2004)

28 B. Mercier, G. Ledoux, C. Dujardin, D. Nicolas, B. Masenelli, P. Mélinon, G. Bergeret, *The J. Chem. Phys.* 1**26**, 044507 (2007)

29 M. Jia, J. Zhang, S. Lu, J. Sun, Y. Luo, X. Ren, H. Song, X. J. Wang, *Chem. Phys. Lett.* **38**, 193, (2004)

30 T. Igarashi, M. Ihara, T. Kusunoki, K. Ohno, T. Isobe, M. Senna, *Appl. Phys. Lett.* **76**, 1549 (2000)

31 P. A. Tanner, *J. Nanosci. Nanotech.* **5**, 1455 (2005)

32 H. P. Christensen, D. R. Gabbe, H. P. Jenssen, *Phys. Rev. B* **25**, 1467 (1982)

33 R. S. Meltzer, S. P. Feofilov, B. Tissue, H. B. Yuan, *Phys. Rev. B* **60**, R14012 (1999)

34 I. Avramov, M. Michailov, *J. Phys.: Condens. Matter* **20,** 295224 (2008)

35 C. C. Yang, M. X. Xiao, W. Lic, Q. Jiang, *Sol. Stat. Comm***. 139**, 148 (2006)

36 H. Lamb, *Proc. Math. Soc. London* **13**, 187 (1882)

37 A. Tamura, *Phys. Rev. B* **52**, 2688 (1995)

38 A. Tamura, K. Higeta, T. Ichinokawa, *J. Phys. C: Solid State Phys.* **15**, 4975 (1982)

39 X. Bai, H. Song, G. Pan, X. Ren, B. Dong, Q. Dai, L. Fan, *J. Nanosci. Nanotechnol.* **9**, 2677 (2009)

40 G. K. Liu, H. Z. Zhuang, X. Y. Chen, *Nano Lett.* 2, **5**, 535 (2002)

41 X. Y. Chen, Z. Zhuang, G. K. Liu, S. Li and R. S. Niedbala, *J. Appl. Phys.* 94, **9**, 5559 (2003)

42 G. K. Liu, X. Y. Chen, H. Z. Zhuang, S. Li, R. S. Niedbala, *J. Sol, Stat, Chem.* **171**, 123 (2003)

43 B. Mercier, C. Dujardin, G. Ledoux, C. Louis, O. Tillement, P. Perriat, *J. Lumin.* **119–120**, 224 (2006)

44 L. Liu, E. Ma, R. Li, G. Liu, X. Chen, *Nanotech.* **18**, 15403 (2007)

45 C. Liu, J. Liu, K. Dou, *J. Phys. Chem. B* **110**, 20277 (2006)

46 R. S. Meltzer, K. S. Hong, *Phys. Rev. B* 61, **5,** 3396 (2000)

47 R. S. Meltzer, K. W. Jang, K. S. Hong, Y. Sun, S. P. Feofilov, *J. Alloy Compounds* **250**, 279 (1997)

48 B. M. Tissue, B. Bihari, *J. Fluoresc.* **8**, 289 (1998)

49 B. M. Tissue, *Chem. Mater.* **10**, 2837 (1998)

50 F. Wang, X. Liu, *Chem. Soc. Rev.* **38**, 976 (2009)

51 F. Auzel, *Chem. Rev.* **104**, 139 (2004)

52 H. Lin, G. Meredith, S. Jiang, X. Peng, T. Luo, N. Peyghambarian, *J. Appl. Phys.* **93**, 1 (2003)

53 H. Guo, N. Dong, M. Yin, W. Zhang, L.Lou, S. Xia, *J. Phys. Chem. B* **108**, 19205 (2004)

54 A. S. Oliveira, M. T. de Araujo, A. S. Gouveia-Neto, J. A. Medeiros Neto, A. S. B. Sombra, Y.Messaddeq, *Appl. Phys. Lett.* **72**, 753 (1998)

55 J. Freek Suijver, *Upconversion Phosphors* (Wiley-VCH Verlag GmbH & Co. KGaA, 2008)

56 S. Li, H. Feindt, A. C. Sutorik, M. S. Baliat, R. M. Laine, R. S. Niedbala, *Nanoscience and Nanotechnology in Perspective* (Tsinghua University Press, Beijing, 2007)

57 P. Elumalai, P. Atkins, J. Paula, *Atkins' Physical Chemistry*, (Oxford University Press, 2002)

58 Y. P. Fang, A. W. Xu, L. P. You, R. Q. Song, J. C. Yu, H. X. Zhang, Q. Li, H. Q. Liu, *Adv. Funct. Mater.* **13**, 955 (2003)

59 C. R. Stanek, K. J. McClellan, B. P. Uberuaga, K. E. Sickafus, M. R. Levy, R. W. Grimes, *Phys. Rev. B* **75**, 134101 (2007)

60 Q. Tang, Z. Liu, S. Li, S. Zhang, X. Liu, Y. Qian, *J. Crystal Growth* **259**, 208 (2003)

61 S. S. Lee, S. H. Byeon, *Materials Science and Engineering B* **133**, 77 (2006)

62 A. Tang, N.A. Kotov, M. Giersig, *Science* **297**, 237 (2002)

63 Z. G. Yan, C. H. Yan, *J. Mater. Chem.* **18**, 5046 (2008)

64 M. Born, J. E. Mayer, *Z. Phys.* **75**, 1 (1932)

65 P. Martin, S. C. Parker, D. C. Sayle, G. W. Watson, *Nano Lett.* **7**, 543 (2007)

66 K. Binnemans, C. Gorller-Walrand, *Chem. Rev.* **102**, 2303 (2002).

67 C. Feldmann, T. Justel, C. R. Ronda, P. J. Schmidt, *Adv. Func. Mater.* **13**, 511 (2003)

68 J.-C. G. Bünzli, C. Piguet, *Chem. Soc. Rev.* **34**, 1048 (2005)

69 L. D. Carlos, R. A. S. Ferreira, V. de Zea Bermudez, S. J. L. Ribeiro, *Adv. Mater.* **21**, 509 (2009)

70 X. Bai, H. Song, G. Pan, Z. Liu, S. Lu, W. Di, X. Ren, Y. Lei, Q. Dai, L. Fan, *Appl. Phys. Lett.* **88**, 143104 (2006)

71 L. Wang, Y. Li, *Nano Lett.* **6**, 1645 (2006)

72 W. Li, X. Wang, Y. Li, *Chem. Commun.* 164 (2004)

73 G. Jia, K. Liu, Y. Zheng, Y. Song, M. Yang, H. You, *J. Phys. Chem. C* **113**, 6050 (2009)

74 G. Liu, G. Hong, X. Dong, J. Wang, *J. Alloys Comp.* **466**, 512 (2008)

75 N. Li, K. Yanagisawa, *J. Sol .State Chem.* **181**, 1738 (2008)

76 L. Yang, Y. Tang, X. Chen, Y. Li, X. Cao, *Mater. Chem. Phys.* **101**, 195 (2007)

77 Q. Tang, J. Shen, W. Zhou, W. Zhang, W. Yu , Y. Qian, *J. Mater. Chem.* **13**, 3103 (2003)

78 M. Yada, M. Mihara, S. Mouri, M. Kuroki, T. Kijima, *Adv. Mater.* **14**, 309 (2002)

79 M. Yada, C. Taniguchi, T. Torikai, T. Watari, S. Furuta, H. Katsuki, *Adv. Mater.* **16**, 1448 (2004)

80 F. Zhang, D. Zhao, *ACS Nano* **3**, 159 (2009)

81 X. Wang, Y. Li, *Chem. Eur. J.* **9**, 5627 (2003)

82 X. Bai, H. Song, L. Yu, L. Yang, Z. Liu, G. Pan, S. Lu, X. Ren, Y. Lei, L. Fan, *J. Phys. Chem. B* **109**, 15236 (2005)

83 Q. Kuang, Z. W. Lin, W. Lian, Z. Y. Jiang, Z. X. Xie, R. B. Huang, L. S. Zheng, *J. Sol. Stat. Chem.* **180**, 1236 (2007)

84 R. O. Fuentes, F. F. Munõz, L. M. Acuna, A. G. Leyva, R.T. Baker*, J. Mater. Chem.* **18**, 5689 (2008)

85 W. Q. Han, L. Wu, Y. Zhu, *J. Am. Chem. Soc.* **127**, 12814 (2005)

86 K. L. Yu, G. L. Ruan, Y. H. Ben, J. J. Zou, *Mater. Sci. Eng. B* **139**, 197 (2007)

87 C. Tang, Y. Band, B. Liu, D. Golberg, *Adv. Mater.* **17**, 3005 (2005)

88 K. Zhou, Z. Yang, S. Yang, *Chem. Mater.* **19**, 1215 (2007)

89 G. Chen, C. Xu, X. Song, W. Zhao, Y. Ding, S. Sun, *Inorg. Chem.* **47**, 723 (2008)

90 D. Zhang, H. Fu, L. Shi, J. Fang, Q. Li, *J. Sol. Stat. Chem.* **180**, 654 (2007)

91 A. W. Xu, Y. P. Fang, L. P. You, H. Q. Liu, *J. Am. Chem. Soc.* **125**, 1494 (2003)

92 X. Wang, J. Zhuang, Y. Li, *Eur. J. Inorg. Chem.* 946 (2004)

93 N. Li, K. Yanagisawa, *J. Sol. Stat. Chem* .**181**, 1738 (2008)

94 Y. Mao, J. Y. Huang, R. Ostroumov, K. L. Wang, J. P. Chang, *J. Phys. Chem. C* 112, 2278 (2008)

95 Y. Mao, J. Bargar, M. Toney, J. P. Chang, *J. Appl. Phys.* **103**, 094316 (2008)

96 M. K. Devaraju, S. Yin, T. Sato, *Nanotech.* **30**, 3055302 (2009)

97 D. Shi, J. Lian, W. Wang, G. Liu, P. He, Z. Dong, L. Wang, R. C. Ewing, *Adv. Mater.* **18**, 189 (2006)

98 G. Wu, Y. Lin, X. Y. Yuan, T. Xie, B. C. Cheng, L. D. Zhang, *Nanotech.* **15**, 568 (2004)

99 F. Cui, J. Zhang, T. Cui, S. Liang, L. Ming, Z. Gao, B. Yang, *Nanotech.* **19**, 065607 (2008)

100 G. Wu, L. Zhang, B. Cheng, T. Xie, X. Yuan, *J. Am. Chem. Soc.* **126**, 5976 (2004)

101 L. G. Rovira, J. M. S. Amaya, M. L. Haro, E. del Rio, A. B. Hungria, P. Midgley, J. J. Calvino, S. Bernal, F. J. Botana, *Nano Lett.* **9**, 1395 (2009)

102 H. J. Fan, U. Gösele, M. Zacharias, *Small* **3**, 1660 (2007)

103 R. H. Baughman, A. A. Zakhidov, W. A. de Heer, *Science* **297**, 787 (2002)

104 R. Tenne, *Nat. Nanotechnol.* **1**,103 (2006)

105 X. Wang, Y. Li, *Inorg. Chem*. **45**, 7522 (2006)

106 K. Byrappa, M. Yoshimura, *Handbook of Hydrothermal Technology* (Noyes Publications, USA, 2001)

107 K. Hiroaki, F. Sachiko, S. Komarneni, J. Japan Soc. Powder and Powder Metall. **49**, 884 (2002)

108 K. L. Wong, G. L. Law, M. B. Murphy, P. A. Tanner, W. T. Wong, P. K. S. Lam, M. H. W. Lam, *Inorg. Chem.* **47**, 5190 (2008)

109 V. K. Rai, A. Rai, *Appl. Phys. B.* **86**, 333 (2007)

110 S. K. Singh, K. Kumar, S.B. Rai, *Sensors and Actuators A: Physical* **149**, 16 (2009)

111 L. Yang, S. Quan, Y. Yang, Z. Li, W. Wang, L. Guo, *Sol. State Commun.* (2009), doi:10.1016/j.ssc.2009.07.013

112 L. Aigouy, M. Mortier, J. Gierak, E. Bourhis, *Phys. Chem. Glasses: Eur. J. Glass Sci. Technol. B* **47**, 83 (2006)

113 L. Aigouy, P. Lalanne, J. P. Hugonin, G. Julie, V. Mathet, M. Mortier, *Phys. Rev. Lett.* **98**, 153902 (2007)

114 A. Cuche, B. Masenelli, G. Ledoux, D. Amans, C. Dujardin, Y. Sonnefraud, P. Mélinon, S. Huant, *Nanotech.* **20**, 015603 (2009)

115 X. Q Fu, C.Wang, H. C. Yu, Y. G. Wang, T. H. Wang, *Nanotech.* **18**, 145503 (2007)

116 C. J. T. Grotthuss, *Ann. Chim.* **58**, 54 (1806)

117 D. Barreca, A. Gasparotto, C. Maccato, C. Maragno, E. Tondello, E. Comini, G. Sberveglieri, *Nanotech.* **18**,125502 (2007)

118 T. Radhika, S. Sugunan, *Catal. Commun*. **8**, 150 (2007)

119 http://epswww.unm.edu/xrd/xrdbasics.pdf

120 L. Liu, X. Chen, *Nanotech.* **18**, 255704 (2007)

121 L. Liu, E. Ma, R. Li, X. Chen, *J. Nanosci. Nanotechnol.* **8**, 1398 (2008)

122 X. Chen, E. Ma, G. Liu, M. Yin, *J. Phys. Chem. C* **111**, 9638 (2007

123 X. Chen, E. Ma, G. Liu, *J. Phys. Chem. C* **111**, 10404 (2007)

124 E. Downing, L. Hesselink, J. Ralston, R. Macfarlane, *Science* **273**, 1185 (1996)

125 L. Wang, Y. Li, *Nano Lett.* **6**, 1645 (2006)

126 A. Bettencourt-Dias, *Dalton Trans.* 2229 (2007)

127 K. T. Yong, I. Roy, M. T. Swihart, P. N. Prasad, *J. Mater. Chem.* **19**, 4655 (2009)

128 Z. Chen, H. Chen, H. Hu, M. Yu, F. Li, Q. Zhang, Z. Zhou, T. Yi, C. Huang, *J. Am. Chem. Soc.* **130**, 3023 (2008)

129 W. M. Yen, W. C. Scott, A. L. Schawlow, *Phys. Rev.* **136**, A271 (1964)

130 E. A. Davis, N. F. Mott, *Phylos. Mag.* **22**, 903 (1970)

131 Z. K. Heiba, L. Arda, Y. S. Hascicek, *J. Appl. Cryst.* **38**, 306 (2005)

132 M. R. Levy, C. R. Stanek, A. Chroneos, R. W. Grimes, *Sol. Stat. Sci.* **9**, 588 (2007)

133 A. M. Pires, M. R. Davolos, C. O. Paiva-Santos, E. B. Stucchi, J. Flor, *J. Solid Stat. Chem.* **171**, 420 (2003)

134 C. Chang, Q. Zhang, D. Mao, *Nanotech.* **17**, 1981 (2006)

135 C. Chang, D. Mao, *Int .J. of Chem. Kinetics* 75 (2007)

136 B. Antic, M. Mitric, D. Rodic, Y. Zhong, Y. Artemov, S. Bogdanovich, J.R. Riedman, *Phys. Rev. B* **58**, 3212 (1998)

137 R. M. Moon, W. C. Koehler, *Phys. Rev. B* **11**, 1609 (1975)

138 R. B. Hunt, R. G. Pappalardo, *J. Lumin.* **34**, 133 (1985)

139 M. Buijs, A. Meyerink, G. Blasse, *J. Lumin.* **37**, 9 (1987)

140 B. Henderson, G. F. Imbusch, *Optical Spectroscopy of Inorganic Solids* (Oxford, 1989)

141 P. Dorenbos, *J. Lumin.* **111**, 89 (2005)

142 D. Ananias, S. Ferdov, F. A. A. Paz, R. A. S. Ferreira, A. Ferreira, C. F. G. C. Geraldes, L. D. Carlos, Z. Lin, J. Rocha, *Chem. Mater.* **20**, 205 (2008)

143 T. Igarashi, M. Ihara, T. Kusunoki, K. Ohno, T. Isobe, M. Senna, *Appl. Phys. Lett.* **76**, 1549 (2000)

144 R. M. Rason, E. Evangelou, C. B. Thomas, *Appl. Phys. Lett.* **72**, 2663 (1998)

145 D. K. Williams, B. Bihari, B. M. Tissue, J. M. McHale, *J. Phys. Chem. B* **102**, 916 (1998)

146 G. A. Hebbink, J.W. Stouwdam, D. N. Reinhoudt, F. C. J. M. Van Veggel, *Adv. Mater.* **14**, 1147 (2002)

147 E. Zych, A. Meijerink, C. M. Donegá, *J. Phys.: Condens. Mater.* **15**, 5145 (2003)

148 W. V. Schaik, G. Blasse, *Chem. Mater.* **4**, 410 (1992)

149 S. R. Cordero, P. J. Carson, R. A. Estabrook, G. F. Strouse, S. K. Buratto, *J. Phys. Chem. B* (2000)

150 X. Chen, E. Ma, G. Liu, M Yin, *J. Phys. Chem. C* **111**, 9638 (2007)

151 A. Meijerink. C. D. Donega, A. Ellens, J. Sytsma, G. Blasse, *J. Lumin.* 58, 26 (1994)

152 T. Hirai, T. Orikoshi, *J. Colloid Interface Sci.* **269**, 103 (2004)

153 L. Yang, S. Quan, Y. Yang, Z. Li, W. Wang, L. Guo, *Solid State Commun.* in press (2009)

154 Q. Ye, A. M. Cassell, H. Liu, K. J. Chao, J. Han, M. Meyyappan, *Nano Lett.* 4 1301 (2004)

155 A. J. Austin, C. V. Nguyena, Q. Ngo, *J. Appl. Phys.* **99**, 114304 (2006)

156 G. Yang, J. Tang, S. Kato, Q. Zhang, L. C. Qin, M. Woodson, J. Liu, J. W. Kim, P. T. Littlehei, C. Park, O. Zhou, *Appl. Phys. Lett.* **87**, 123507 (2005)

157 Y. Ebenstein, T. Mokari, U. Banin, *J. Phys. Chem.* B **108,** 93 (2004)

158 V. Lulevich, W. A. Ducker, *Appl. Phys. Lett.* **87,** 214107 (2005)

159 A. Gaiduk, R. Kuhnemuth, M. Antonik, C. A. M. Seidel, *Chem. Phys. Chem.* **6,** 976 (2005)

160 L. Novotny, B. Hecht, *Principles of Nano-Optics,* 1st ed. (Cambridge University Press, Cambridge, 2006)

161 Z. H. Kim, S. H. Ahn, B. Liu, S. R. Leone, *Nano Lett.* **7,** 2258 (2007)

162 X. Y. Lin, F. Creuzet, H. Arribart, *J. Phys. Chem.* **97**, 7272 (1993)

163 H. J. Butt, B. Cappella,M. Kappl, *Surf. Sci. Rep.* **59**, 1 (2005)

164 H. Gottlich, W. M. Heckel, *Ultramicroscopy* 61, 145 (1995)

165 H. A. Pohl, *J. Appl. Phys.* **22**, 869 (1951)

166 H. A. Pohl, *Dielectrophoresis* (Cambridge University Press, Cambridge, 1978)

167 T. B. Jones, *Electromechanical of Particles* (Cambridge University Press, Cambridge, 1995)

168 J. S. Seybold, *Introduction to RF propagation* (John Wiley, New York, 2005)

169 G. Yang, et al *Appl. Phys. Lett.* **87**, 123507 (2005)

170 J. Tang, B. Gao, H. Geng, O. D. Velev, L. C. Qin, O. Zhou, *Adv. Mater.* **15**, 1352 (2003)

171 H. W. Lee, S. H. Kim, Y. K. Kwak, E. S. Lee, C. S. Han, *Sensors Actuators* A **125**, 41 (2005)

172 Y. Liu, J. H. Chung, W. K. Liu, R. S. Ruoff, *J. Phys. Chem.* B **110,** 14098 (2006)

173 J. Zhang, J. Tang, G. Yang, Q. Qiu, L. C. Qin, O. Zhou, *Adv. Mater.* 16, 1219 (2004)

174 M .Buijs, G. Blasse, *J. Lumin*. **34**, 263 (1986)

175 C. Molina, P. J. Moreira, R. R. Gonçalves, R. A. Sá Ferreira, Y. Messaddeq, S. J. L. Ribeiro, O. Soppera, A. P. Leite, P. V. S. Marques, V. de Zea Bermudez, L. D. Carlos, *J. Mater. Chem.* **15**, 3937 (2005)

176 D. C. Oliveira, C. Molina, C. M. S. Vicente, E. Pecoraro, R. A. Sá Ferreira, R. Nogueira, P. S. André, M. S. Li, V. de Zea Bermudez, Y. Messaddeq, S. J. L. Ribeiro, L. D. Carlos, *Chem. Mater*. in press.

177 N. Vandamme, J. Schauwaert, E. Janssens, E. Vanderweert, P. Lievens, V. V. Haesendock, *Surf. Sci.* **558**, 57 (2004)

178 A. Trovarelli, C. de Leitenburg, M. Boaro, G. Dolcetti, *Catal. Today* **50**, 353 (1999)

179 X. Liu, K. Zhou, L. Wang, B. Wang, Y. Li, *J. Am. Chem. Soc.* **131**, 3140 (2009)

180 J. Chen, S. Patil, S. Seal, J. F. Mcginnis, *Nature* **1**, 142 (2006)

181 C. Pan, D. Zhang, L. Shi, J .Fang, *Eur. J. Inorg. Chem.* **15**, 2429 (2008)

182 G. Blasse, A. Bril, *J. Chem. Phys.* **47**, 5139 (1967)

183 H. P. Zhou, Y. W. Zhang, H. X. Mai, X. Sun, Q. Liu, W. G. Song, C. H. Yan, *Chem. Eur. J.* **14**, 3380 (2008).

184 N. Kornblum, H. E. DeLaMare, *J. Am. Chem. Soc.* **73**, 880 (1951)

185 Y. W. Wang, Y. S. Duh, C. M. Shua, *Process Saf. Prog.* **26**, 299 (2007)

186 R. A. Sheldon, J. K. Kochi, *Metal-catalyzed oxidations of organic compounds* (Academic Press, USA, 1981)

187 E. Danoczy, J. Paallukacs, D. Gal, Ber. Bunsenges. *Phys. Chem.* **97**, 554 (1993)

188 E. Ganin, I. Amer, *J. Mol. Catal. A: Chem.* **116**, 323 (1997)

189 B. Murugan, A. V. Ramaswamy, *J. Am. Chem. Soc.* **129**, 3062 (2007)

190 J. O. Edwards, R. Curci, *Catalytic Oxidations with Hydrogen Peroxide as Oxidant* (Kluwer Academic Press, Dordrecht, 1992)

191 M. N. Timofeeva, S. H. Jhung, Y. K. Hwang, D. K. Kim, V. N. Panchenko, M. S. Melgunov, Y. A. Chesalov, J. S. Chang, *Appl. Catal. A: General* **317** ,1 (2007)

192 M. Salavati-Niasari, P. Salemi, F. Davar, *J. Mol. Catal. A: Chem.* **238**, 215 (2005)

193 J. D. Koola, J. K. Kochi, *J. Org. Chem.* **52**, 4545 (1987)

194 M. Salavati-Niasari, F. Farzaneh, M. Ghandi, *J. Mol. Catal. A: Chem.* **186**, 101 (2002)

195 C. Tang, Y. Bando, D. Golberg, R. Ma, *Angew. Chem .Int. Ed.* **44**, 576 (2005)

196 F. Marabelli, P. Wachter, *Phys. Rev. B* **36**, 1238 (1987)

197 P. Patsalas, S. Logothetidis, L. Sygellou, S. Kennou, *Phys. Rev. B* **68**, 035104 1 (2003)

198 M. D. H. Alonso, A. B. Hungrıa, A. M. Arias, J. M. Coronado, J. C. Conesa, J. Soria, M. F. Garcia, *Phys. Chem. Chem. Phys.* **6**, 3524 (2004)

199 S. Tsunekawa, T. Fukuda, *J. Appl. Phys.* **87**, 1318 (2000)

200 Y. W. Zhang, R. Si, C. S. Liao, C. H. Yan, C. X. Xiao, Y. Kou, *J. Phys. Chem. B* **107**, 10159 (2003)

201 E. A. Davis, N. F. Mott, *Phylos. Mag*. **22**, 903 (1970)

202 N. F. Mott, E. A. Avis, *Electronic Processes in non-crystalline materials* (Oxford University Press, Oxford, 1979)

203 P. Bhattacharya, *Semiconductor Optoelectronic Devices* (Ed. Prentice Hall International Editions, New Jersey, 1994)

204 N. Imanaka, H. Toshiyuki, G. Y. Adachi, *Chem. Mater.* **15**, 2289 (2003)

205 J. Rocha, P. Ferreira, L. D. Carlos, A. Ferreira, *Angew. Chem. Int. Ed.* **39**, 3276 (2000)

206 M. H. Kostova, R. A. S. Ferreira, D. Ananias, L. D. Carlos, J. Rocha, *J. Phys. Chem. B* **110**, 15312 (2006)

207 C. Sun, Hong Li, H. Zhang, Z. Wang, L. Chen, *Nanotech.* **16**, 1454 (2005)

208 H. E. Heidepriem, D. Ehrt, *Opt. Mater.* **15**, 7 (2000)

209 G. Blasse, W. Schipper, J. J. Hamelink, *Inorg. Chim. Acta* **189**, 77 (1991)

210 A. H. Morshed, M. E. Moussa, S. M. Bedair, R. Leonard, S. X. Liu, N. E. Masry, *Appl. Phys. Lett.* **70**, 1647 (1997)

211 C. Chunlin, Y. Shayan, L. Zhikai, L. Meiyong, M. Nuofu, *Chin. Sci. Bullet.* **48**, 1198, (2003)

212 M. Nolan, S. C. Parker, G. W. Watson, *Surf. Sci.* **595**, 223 (2003)

213 L. D. Carlos, R. A. S. Ferreira, J. P. Rainho, V. Z. Bermudez, *Adv. Func. Mater.* **12**, 819 (2002)

214 D. W. Cooke, B. L. Bennett, R. E. Muenchausen, J. K. Lee, M. A. Nastasi, *J. Lumin.* **106**, 125 (2004)

215 A. G. Macedo, R. A. S. Ferreira, D. Ananias, M. S. Reis, V. S. Amaral, L. D. Carlos, J. Rocha, Effects of phonon confinement on anomalous thermalisation, energy transfer and upconversion in Ln^{3+}-doped Gd_2O_3 nanotubes, *aceptted Adv. Funct. Mater.* (2010)

216 K. L. Wong, G. L. Law, M. B. Murphy, P. A. Tanner, W. T. Wong, P. K. S. Lam, M. H. W. Lam, *Inorg. Chem*. **47**, 5190 (2008)

217 F. Söderlind, H. Pedersen, R. M. Petoral, P. O. Käll, K. Ovdal, *J. Colloid Interface Sci.* **288**, 140 (2005)

218 Z. Chen, H. Chen, H. Hu, M. Yu, F. Li, Q. Zhang, Z. Zhou, T. Yi, C. Huang, *J. Am. Chem. Soc.* **130**, 3023 (2008)

219 H. Zou, S. Wu, J. Shen, *Chem. Rev.* **108**, 3893 (2008)

220 A. C. Esteves, M. C. Neves, A. Barros-Timmons, E. Bourgeat-Lami, L. Liz-Marzán, T. Trindade, *J. Nanosc. Nanotech.* **6**, 414 (2006)

221 L. Liu, E. Ma, R. Li, G. Liu, X Chen, *Nanotech.* **18**, 01540 (2007)

222 W. Stöber, A. Fink, E. Bohn, *J. Colloid Interface Sci.* **26**, 62 (1968)

223 K. Landfester, *Macromol. Rapid Communic.* **22**, 896 (2001)

224 E. Bourgeat-Lami, J. L. Luna-Xavier, A.Guyot, *Mater. Res. Symp. Proc.* **628**, CC3.5 (2000)

225 A. Garcia-Murillo, C. L. Le, C. Dujardin, C. Pedrini, J. Mugnier, *Opt. Mater.* **16**, 39 (2001)

226 N. B. Colthup, L. H. Daly, S. E. Wiberley, *Introduction to Infrared and Raman Spectroscopy*, 3rd Edition, (Academic Press, 1990)

227 F. Li, S. Zhou, L. Wu, *J. Appl. Polymer Sci.* **98**, 2274 (2005)

228 J. Asua, *Prog. Polym. Sci.* **27**, 1283 (2002)

229 J. Zhang, G. Gao, M. Zhang, D. Zhang, C. Wang, D. C. Zhao, F. Q. Liu, *J. Colloid Interface Sci.* **301**, 78 (2006)

230 E. Bourgeat-Lami, J. Lang, *J. Colloid Interface Sci.* **197**, 293 (1998)

231 S. Reculusa, C. Mingotaud, E. Bour geat-Lami, E. Duguet, and S. Ravaine, *Nano Lett.* **4**, 1677 (2004)

232 M. Buijs, A. Meyerink, G. Blasse, *J. Lumin.* **37**, 9 (1987)

233 R. B. Hunt, R. G. Pappalardo*, J. Lumin.* **34**, 133 (1985)

234 H. M. Lee, Y. N. Kim, B. H. Kim, S. O. Kim, S. O. Cho, *Adv. Mater.* **20**, 2094 (2008)

235 R. C. Chikate, K. W. Jun, C. V. Rode, *Polyhedron* **27**, 3, 933 (2008)

236 M. R. Alexander, G. Beamson, C. J. Blomfield, G. Leggett, T. M. Duc, *J. Electron Spectroscopy and Related Phenomena* **121**,19 (2001)

237 M. S. Lim, K. Feng, X. Chen, N. Wu, A. Raman, J. Nightingale, E. S. Gawalt, D. Korakakis, L. A. Hornak, A. T. Timperman*, Langmuir* **23**, 2444 (2007)

238 http://www.thorlabs.com

239 Wrighton et al. *J. Phys. Chem.* **78**, 2229 (1974)

240 A. Brill, A. W. De Jager-Veenis, *J. Electrochem. Soc.* **123**, 396 (1976)

241 H. Mattoussi, H. Murata, C. D. Merritt, Y. Iizumi, J. Kido, Z. H. Kafafi, *J. Appl. Phys.* **86**, 2642 (1999)

242 N. C. Greenham, I. D. W. Samuel, G. R. Hayes, R. T. Phillips, Y. A. R. R. Kessener, S. C. Moratti, A. B. Holmes, R. H. Friend, *Chem. Phys. Lett.* **241**, 89 (1995)

243 G. I. Goldstein, D. E Newbury, P. Echlin, D. C. Joy, C. Fiori, E. Lifshin, *Scanning electron microscopy and x-ray microanalysis* (Plenum Press, New York, 1981)

244 http://www.biologie.uni-hamburg.de/b-online/e03/03e.htm

245 G. Binnig, C. F. Quate, C. H. Gerber, *Phys. Rev. Lett.* **56**, 930 (1986)

246 M. Meyer, N. M. Amer, *App. Phys. Lett.* **56**, 2100 (1990)

247 D. Sarid, *Scanning Force Microscopy, Oxford Series in Optical and Imaging Sciences,* (Oxford University Press, New York, 1991)

248 F. J. Giessibl, *Rev. Mod. Phys.* **75**, 949 (2003)

249 Malvern Instruments, Documentation for Zetasizer 1000/2000/3000: Principles of operation, Manual Number MAN 0152, Issue 1.1, 1996

250 http://www.dantecdynamics.com/Default.aspx?ID=1358t

251 http://www.nima.co.uk